Search for the neutral Higgs Bosons of the Minimal Supersymmetric Standard Model in the $\tau_{\text{lep}}\tau_{\text{had}}$ decay mode with the ATLAS experiment

von
Sascha Thoma

Dissertation

zur Erlangung des Doktorgrades der

Fakultät für Mathematik und Physik

der Albert-Ludwigs-Universität Freiburg im Breisgau

Dekan:	Prof. Dr. Andreas Buchleitner
Referent:	Prof. Dr. Karl Jakobs
Korreferent:	Prof. Dr. Tobias Schätz
Prüfer (Theoretische Physik):	JProf. Dr. Harald Ita
Prüfer (Experimentalphysik):	Prof. Dr. Gregor Herten
Eingereicht im Januar 2013	
Datum der mündlichen Prüfung	21. Februar 2013

Contents

View into the LHC tunnel

(CERN-AC-0504028 01 © 2009 CERN)

Chapter 1

Introduction

The objective of elementary particle physics is to study the smallest constituents of matter and their interactions. Using this knowledge one hopes to understand the origin of the universe and what it is made of. The theoretical foundation of elementary particle physics is the *Standard Model*, which has been developed over the past 60 years. At its current stage of development, this model describes all currently known elementary particles, the half-integer spin *fermions*, and three of the four known interactions, namely the strong, the weak and the electromagnetic interaction. An important concept of the Standard Model is the existence and conservation of certain symmetries. As a consequence, interactions among fermions are mediated through spin-1 particles, the *bosons*. However, a self-consistent theoretical description of these symmetries including massive bosons cannot be realised by just adding appropriate mass terms to the theory by hand. Instead the so-called *Higgs mechanism* needs to be embedded into the model to dynamically generate those masses. This mechanism introduces a new particle, the famous *Higgs boson*, that all massive particles interact with. Many properties of the Higgs boson are fixed by the mechanism. However, its mass is a free parameter of the Standard Model and can only be constrained by theory and measurements, favouring low masses.

In the recent decades the Standard Model has been extremely successful in predicting experimental findings with high precision and in explaining already known phenomena. However, apart from its great success, some observations revealed the limitations of this model. Gravity,

for example, cannot be incorporated into the Standard Model. Furthermore, it is not possible to unify the strong and the electroweak forces at high energies, just as this could be done with the electromagnetic and weak interactions. But the description of all of these forces by a single one in a *Grand Unified Theory* (GUT) would be highly desirable. It would be the next step towards a *Theory Of Everything* (TOE), a single model to describe all known interactions, including gravity. Another issue of the Standard Model is the *Hierarchy problem*: the model parameters require an extreme ad hoc fine-tuning in order to avoid the occurrence of divergences in specific calculations. Further limitations became apparent when measurements of the cosmic microwave background, performed with the *Wilkinson Microwave Anisotropy Probe* spacecraft (WMAP), were evaluated and interpreted in combination with other experimental results [1]. This revealed that the particle content of the Standard Model only contributes about 4.6% to the total energy and matter density of the universe. The remaining density must be due to some sort of *cold dark matter* and *dark energy*, which both are of unknown origin.

All deficits of the Standard Model imply that this model is incomplete and therefore needs to be extended or replaced. The most popular extensions are the group of supersymmetric theories, usually denoted as *Supersymmetry* (*SUSY*). Part of their popularity is due to the fact, that within those models a unification of the electroweak and strong forces seems possible. In addition, they often provide a natural explanation for the existence of cold dark matter.
The underlying concept of supersymmetry is the existence of an additional symmetry that connects each particle of the Standard Model to a supersymmetric partner with identical quantum numbers apart from the spin. Since none of these new particles has been observed so far, their masses must be larger than those of their Standard Model partners. Thus, the additional symmetry seems to be broken, if realised in nature.
In addition to the partners, supersymmetry usually predicts more than just one Higgs boson as a more complex version of the Standard Model Higgs mechanism is required to generate all the masses.

Given our current understanding of the generation of mass in the Standard Model or in supersymmetry, a major goal of modern experimental particle physics is hence to find direct evidence for the existence of one or more Higgs bosons. For this purpose they must be created in particle collisions which requires extremely high energy densities. Such energies can be provided by the *Large Hadron Collider* (LHC), which is built at the outer periphery of Geneva (Switzerland). The LHC accelerates protons (p) and collides them at particular interaction points. The centre-

of-mass energies of these collisions are currently $\sqrt{s} = 7$–$8\,\text{TeV}$, which is sufficient to create heavy particles with masses up to the TeV scale at acceptable rates.

At one of the interaction points the *ATLAS* experiment[1)] is located. This multipurpose detector is capable of detecting and measuring the properties of all Standard Model particles that are produced in p–p collisions, except for neutrinos. Using these information one hopes to find indications for the existence of the Higgs boson.

And in fact, in July 2012 the two LHC experiments ATLAS and CMS[2)] found evidence for a new bosonic resonance with a mass of about $125\,\text{GeV}/c^2$. At the current stage of investigations, the properties of this new particle are in good agreement with those of a neutral Higgs boson of the Standard Model or supersymmetric theories. The proof that this actually is the Higgs boson that physicists have looked for decades now would be a tremendous success for both, theoretical and experimental particle physics. A particular feature of the resonance is that there is no clear evidence for the $\tau^+\tau^-$ and $b\bar{b}$ decay modes, yet, although first indications have been presented recently [2, 3]. However, it is exactly these decay modes that are very probable for a Standard Model Higgs boson with a mass of about $125\,\text{GeV}/c^2$ and are even enhanced for many parameter configurations in supersymmetric models. Therefore, these two decay channels are of special interest for further studies, like the one presented here.
In this thesis a search for the neutral *Higgs bosons* A, h and H of the *Minimal Supersymmetric extension of the Standard Model* (MSSM) in the $\tau^+\tau^-$ decay mode is presented. The complete process considered here is the $pp \to h/A/H \to \tau_{\text{lep}}\tau_{\text{had}}$ process, where τ_{lep} denotes a τ lepton decay into an electron or muon and appropriate neutrinos and τ_{had} the decay of a τ lepton into hadrons and a τ neutrino. Among the different $\tau^+\tau^-$ decay modes this final state realises a good compromise between a clean signal signature, a high decay probability and an acceptable resolution of the reconstructed Higgs boson mass. The search strategy was optimised for the particular properties of the neutral Higgs bosons in the MSSM, assuming specific parameter choices that were proposed in Ref. [4] and are denoted as the m_h^{max} *benchmark scenario*. In this scenario the dominant production mechanisms for the neutral Higgs bosons are the b-quark associated production mode and the gluon-fusion process. The p–p collision data analysed for this search was recorded by the ATLAS detector during the years 2010 and 2011 at a centre-of-mass energy of $\sqrt{s} = 7\,\text{TeV}$.

The structure of this document is as follows: the theoretical foundation that this thesis rests on, the Standard Model and the MSSM, is described in Chapter 2. The focus here lies on the

[1] A Toroidal LHC ApparatuS
[2] Compact Muon Solenoid

description of hadron collisions, the properties of the neutral Higgs bosons of the MSSM and their implications on Higgs boson searches. The experimental setup, the LHC and the ATLAS experiment, is described in Chapters 3 and 4. Chapter 5 describes how hadron collisions and the detector can be simulated, given the theoretical framework that was introduced before. Such simulations are vital for the understanding of real collision data and their correct interpretation. Based on the knowledge about the detector, the reconstruction of particles and event properties using the recorded or simulated detector signals is discussed in Chapter 6. The search for the neutral Higgs bosons of the MSSM is presented in Chapter 7. The search strategy is discussed and motivated, using the theoretical basis and the analysis of simulated data. In addition, this chapter describes several techniques through which the simulated data of various background processes can be validated against or replaced by real collision data. The results of this search are interpreted statistically within the context of the MSSM, and consequences on this model are discussed. Furthermore, the analysis presented here has been statistically combined with further searches for the neutral MSSM Higgs bosons performed with the ATLAS experiment. These additional searches are briefly summarised in Chapter 8 and the results of the combination are presented and discussed. A final summary is given in Chapter 9.

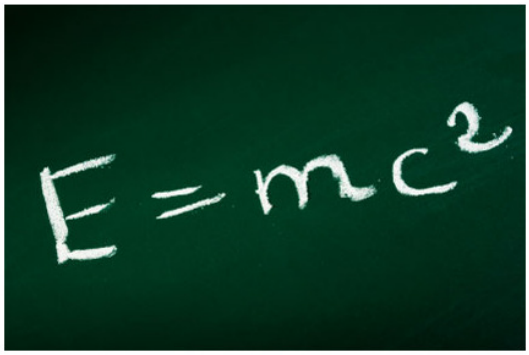

Chapter 2

Theoretical Framework

This chapter intends to introduce the theoretical foundations that the results presented in this thesis are based on. It is not meant to be complete in any way and a more detailed discussion of the underlying theories can be found in Refs. [5] and [6], that most parts of this chapter are based on. Throughout this thesis natural units are used, which means $\hbar = c = 1$. Therefore, masses, energies and momenta are given in units of GeV.

In the first section several underlying concepts are introduced. Some of these concepts are based on the experimental observations that the elementary constituents of matter carry half-integer spins. Therefore they obey the Fermi–Dirac statistics and their wave functions change sign under parity transformations. Such particles are called *fermions*. In contrast, interactions among the fermions are mediated through the exchange of integer spin particles, called *bosons*. Those follow the rules of Bose–Einstein statistics.

2.1. Free Fields and Gauge Interactions

In quantum field theories, particles are characterised by *quantum fields*. Their propagation and interactions can be described by the *Lagrange* formalism. In this formalism the *Lagrange density* $\mathscr{L}$, or *Lagrangian*, of a field is determined by its kinetic and potential energies T and V,

respectively:

$$\mathscr{L} = T - V\,. \tag{2.1}$$

For a free scalar field ϕ or a free fermion field ψ both with masses m this results in the expressions [5]

$$\begin{aligned} \mathscr{L}_{\text{Klein–Gordon}} &= \tfrac{1}{2}\partial_\mu\phi\,\partial^\mu\phi^* + \tfrac{1}{2}m\phi^*\phi\,, \\ \mathscr{L}_{\text{Dirac}} &= \bar{\psi}(i\gamma_\mu\partial^\mu - m)\psi\,. \end{aligned} \tag{2.2}$$

The field $\bar{\psi} = \psi^\dagger\gamma_0$ is the *Dirac adjoint field*, and the matrices γ_μ are the *gamma* or *Dirac matrices*. A detailed description of the latter can be found in Ref. [5], for example.

Given these Lagrangians, the equations of motion can be obtained by applying the *Euler–Lagrange equation*

$$\partial_\mu\left(\frac{\partial L}{\partial(\partial_\mu\phi)}\right) - \frac{\partial L}{\partial\phi} = 0\,. \tag{2.3}$$

For the Lagrangians of Equation (2.2) this results in

$$\begin{aligned} (\partial_\mu\partial^\mu + m^2)\phi &= 0\,, \\ (\gamma_\mu\partial^\mu - m^2)\psi &= 0\,, \end{aligned} \tag{2.4}$$

which are the *Klein–Gordon equation* for the free boson field and the *Dirac equation* for the free fermion field, respectively. These equations can be thought of as relativistic generalisations of the Schrödinger equation. The simplest possible solutions are

$$\begin{aligned} \phi &= e^{\pm ip_\mu x^\mu}\,, \\ \psi &= u(\vec{p})\,e^{\pm ip_\mu x^\mu}\,. \end{aligned} \tag{2.5}$$

Here $u(\vec{p})$ is a four-component *Dirac spinor* that depends on the momentum of the fermion field. These plane wave solutions form a basis for the Fourier components of any general fields that solve the equations 2.4. Such general solutions also incorporate annihilation and creation operators.

To describe the nature of weak interactions, as done in Section 2.3.1, a chirality projection operator can be defined as

$$P = P_L = \frac{1}{2}(1-\gamma^5)\,, \tag{2.6}$$

where $\gamma_5 = \gamma_1\gamma_2\gamma_3\gamma_4$ is the product of the Dirac matrices γ_μ. With this operator a fermion field ψ

can be split into a *right*- and a *left*-handed component:

$$\psi = \frac{1}{2}(1-\gamma^5)\psi + \frac{1}{2}(1+\gamma^5)\psi = \psi_L + \psi_R\,. \tag{2.7}$$

The definition of a projection operator to split the fields into these components is not needed if a particular representation of the Dirac matrices is chosen. In this so-called *Weyl* or *chiral* representation a four-component Dirac spinor field ψ can directly be written as a vector of two complex objects $\psi^T = (\xi_\alpha\, \chi^{\dagger\dot{\alpha}})$, where ξ_α is a two-component left-handed *Weyl spinor* and $\chi^{\dagger\dot{\alpha}}$ a two-component right-handed one. The spinor indices of the upper and lower components are usually labelled as greek symbols ($\alpha = 1,2$) and as greek symbols with dots ($\dot{\alpha} = 1,2$), respectively, to indicate the different behaviour of the upper and lower components of ψ with respect to electroweak interactions. Using this representation the Dirac Lagrangian can be written as

$$\mathscr{L}_{\text{Dirac}} \;=\; i\xi^\dagger\bar{\sigma}^\mu\partial_\mu\xi + i\chi^\dagger\bar{\sigma}^\mu\partial_\mu\chi - M(\xi\chi + \xi^\dagger\chi^\dagger)\,. \tag{2.8}$$

Here the σ-matrices are determined by the two-dimensional identity matrix $\mathbf{1}$ and the three Pauli matrices $\vec{\sigma}$ of the same dimension:

$$\bar{\sigma}^\mu \;=\; (\mathbf{1}, -\vec{\sigma})\,. \tag{2.9}$$

In the Lagrangian formalism interactions among fields are represented by terms that connect several fields and which are added to the free field Lagrangians of Equation (2.2). Given the knowledge of these terms and hence the full Lagrangian the interaction *cross section* σ of a given process can be derived by calculating the transition probability from the initial to the final state. However, a complete calculation of this probability is not possible in general. Using perturbation theory a good approximation of the correct result can be achieved, even when just taking lower orders of the perturbation series into account. In this approach the transition probability to a given order is then given by the square of the sum of all terms in the series up to that order. This square of sums is denoted as the *Matrix element*. Each of the terms in the perturbation series can be depicted by a *Feynman diagram*, named after their inventor R. Feynman. These diagrams allow for a simple and intuitive visualisation of complicated expressions and processes.

However, if interaction terms are introduced by hand in an arbitrary way, higher order terms in the perturbation series, like those including loops of virtual particles, usually lead to diver-

gences in the calculations and therefore to unphysical expressions for measurable quantities. This problem can be solved by a re-interpretation of the parameters of the theory, like masses and couplings, as bare quantities and not as the physical quantities that can be measured in experiments. In this case the divergences can be absorbed in redefinitions of the bare parameters. Physical observables, however, will still remain finite since only differences to a given reference point, the *renormalisation scale*, can be measured.

This *renormalisation* procedure does not only solve the issue with the divergences, it also demonstrated that the coupling parameters of the theory are not constant. Instead they depend on the energy scale of a given process and therefore are usually denoted as *running coupling constants*. This behaviour could be confirmed by various measurements.

Given the above considerations, the renormalisability of a theory is a necessary condition for a meaningful description of measurable quantities. In this context M.Veltman and G. 't Hooft showed that a quantum field theory is always renormalisable if it is *locally gauge invariant* [7]. This principle of local gauge invariance is based on the concept that physical processes and their properties are preserved under transformations of certain symmetries, that seem to be realised in nature. Transferred to the Lagrangian formalism this means that the Lagrangian must be invariant, i.e. does not change, if the particle fields undergo local gauge transformations of the particular symmetry groups.

The simplest example for local gauge invariance is the invariance of the free fermion field Lagrangian of Equation (2.4) under transformations of the symmetry group $U(1)$[1]. The elements of this group can be described as phase transformations of the fields

$$\psi \rightarrow \psi e^{i\alpha(x)} . \tag{2.10}$$

Local gauge invariance requires the transformation angle α to depend on the space-time coordinates x. Applying this transformation changes the derivative part of the kinetic term in the Lagrangian $\mathscr{L}_{\text{Dirac}}$ of Equation (2.2) to

$$\partial_\mu \psi \rightarrow e^{i\alpha(x)} \partial_\mu \psi + i e^{i\alpha(x)} \psi \partial_\mu \alpha(x) . \tag{2.11}$$

The additional term proportional to $\partial_\mu \alpha(x)$ shows that the Lagrangian of Equation (2.2) changes under local gauge transformation of the symmetry group $U(1)$. Therefore this Lagrangian is not locally gauge invariant and hence not renormalisable.

[1] $U(N)$ is the unitary group of degree N. The elements of this group satisfy $U^\dagger U = 1$.

To restore the local gauge invariance of the theory a new *gauge field* A_μ is introduced and its transformation properties are set to

$$A_\mu \to A_\mu + \frac{1}{e}\partial_\mu \alpha(x)\,, \tag{2.12}$$

In addition, the ordinary derivative ∂_μ needs to be replaced by the *covariant derivative* D_μ, which is defined as

$$D_\mu = \partial_\mu - ieA_\mu\,. \tag{2.13}$$

Using these definitions, the modified, gauge invariant Lagrangian for a massless fermion field becomes

$$\mathscr{L} = i\bar{\psi}\gamma^\mu \partial_\mu \psi - \frac{1}{4}F_{\mu\nu}F^{\mu\nu} + e\bar{\psi}\gamma^\mu A_\mu \psi\,. \tag{2.14}$$

In this equation the kinetic term of the gauge field A_μ is expressed in terms of the field strength tensor $F_{\mu\nu}$. For a general gauge group with i generators and antisymmetric structure constants f^{ijk} this tensor is given by

$$F_i^{\mu\nu} = \partial_\mu A_\nu^i - \partial_\nu A_\mu^i - g f^{ijk} A_\mu^j A_\nu^k, \tag{2.15}$$

The last term in Equation (2.14) shows that by requiring local gauge invariance, an interaction of the fermion fields with the gauge boson field with coupling strength e can be introduced in the Lagrangian in a renormalisable way.

2.2. The Higgs Mechanism

At this stage, a remaining problem of gauge invariant theories is that an explicit mass term for the new gauge field is forbidden. Such a term would be of the form $^1/_2\, m^2 A_\mu A^\mu$ and therefore not local gauge invariant. However, the gauge field masses can be generated dynamically by the *Higgs mechanism*, that was initially proposed in 1964 by P. Higgs [8–12]. For this purpose the existence of an additional *Higgs field* is postulated, that all massive particles interact with. The physical mass eigenstate that is associated with the new field is the *Higgs boson*.

The Higgs mechanism can be described using a model of a complex scalar field, $\phi = (\phi_1 + i\phi_2)/\sqrt{2}$, and its Lagrangian

$$\mathscr{L} = (\partial_\mu \phi)^* \partial^\mu \phi - \mu^2 \phi^* \phi - \lambda(\phi^* \phi)^2\,. \tag{2.16}$$

The parameter μ in this equation can be interpreted as the mass of the scalar field, if one assumes that $\mu^2 > 0$. The last term describes the self-interaction of the scalar field with coupling strength $\lambda > 0$. Following the discussion in the previous section, this Lagrangian can be made invariant under $U(1)$ transformations of the Higgs field if the partial derivative is substituted by the covariant derivative of Equation (2.13) and if a gauge field A_μ, satisfying Equation (2.12), is introduced. In this case the Lagrangian of Equation (2.16) becomes

$$\mathscr{L} = D_\mu \phi^* D^\mu \phi - \frac{1}{4} F_{\mu\nu} F^{\mu\nu} - \mu^2 \phi^* \phi - \lambda (\phi^* \phi)^2 . \tag{2.17}$$

The last two terms in Equation (2.17) determine the scalar interaction potential $V = \mu^2 \phi^* \phi + \lambda (\phi^* \phi)^2$, that is usually denoted as the *Higgs potential*. To generate mass for the gauge field, the parameter μ^2 is to be interpreted as a bare parameter of the theory and not as the mass of the Higgs field. In that case the choice $\mu^2 < 0$ is valid. Fig. 2.1 shows the shape of the Higgs potential projected onto a plane for both choices, positive and negative μ^2. The case $\mu^2 < 0$ shows, that the minimum of the potential is not at the origin anymore. Instead, there is a circle of minima in the ϕ_1–ϕ_2 plane, which is given by $\phi_1^2 + \phi_2^2 = v^2$, with $v^2 = -\mu^2/\lambda$. The field ϕ can now be expanded around a minimum $v = v_0$ in terms of fields η and θ, which results in the expression

$$\phi(x) = \sqrt{\frac{1}{2}} v_0 + \eta(x) + i\theta(x) . \tag{2.18}$$

For this field the interaction potential is not symmetric anymore and the symmetry of the original model is *spontaneously broken* by the choice of the new ground state. Using the Taylor expansion for ϕ as given in Equation (2.18), the Lagrangian of this theory can be written as

$$\mathscr{L} = \frac{1}{2}(\partial_\mu \eta)^2 + \frac{1}{2}(\partial_\mu \theta)^2 - v_0^2 \lambda \eta + \frac{1}{2} e^2 v_0^2 A_\mu A^\mu - e v_0 A_\mu \partial^\mu \theta + \ldots \tag{2.19}$$

The fourth term in this equation represents an effective mass term with mass $m = e v_0$ for the field A_μ that is generated by spontaneously breaking the symmetry. This is done in a way that preserves the local gauge invariance of the Lagrangian. Therefore, every theory in which the particles retrieve their masses by the Higgs mechanism will stay renormalisable.

In addition to the generation of mass, the Higgs mechanism introduces a massive scalar field η, the Higgs boson, and a massless scalar field θ. Such massless scalars, denoted as *Goldstone bosons*, are always created, when a symmetry is spontaneously broken. This is stated by the *Goldstone Theorem* that has been proven in Ref. [13]. In general, however, these additional bosons can be hidden by appropriate gauge transformations and are interpreted as the longitudi-

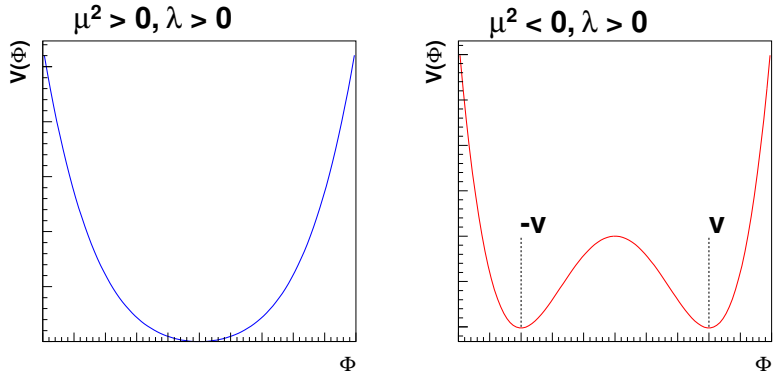

(a) (b)

Figure 2.1.: Projection of the Higgs potential $V(\phi) = \mu^2\phi^*\phi + \lambda(\phi^*\phi)^2$ onto a plane. Figure (a) and (b) show the shape for positive and negative μ^2, respectively. λ is chosen positive.

nal polarisation degrees of freedom of the massive gauge bosons.

2.3. The Standard Model of Particle Physics

The Standard Model of particle physics is a relativistic quantum field theory based on the concepts discussed in the previous sections. It describes the properties of all known elementary constituents of matter and the elementary particles that mediate three of the four known interactions amongst them, namely the strong, the weak and the electromagnetic forces.

The building blocks of matter are the six *leptons* and six *quarks*, each with a corresponding anti-particle. The leptons that carry electric charge -1 are the *electron* e, the *muon* μ, the τ *lepton*. The corresponding three neutrinos, namely ν_e, ν_μ and ν_τ, are charge-less. Quarks, on the other hand, have fractional charges. The *up-type* quarks u, c and t all have electric charge $^{+2}/_3$, the *down-type* quarks d, s and t have charge $^{-1}/_3$. All these particles can be sorted in three *generations* in ascending order of mass. This is indicated in Table 2.1, where all the fermions described the Standard Model are listed together with their quantum numbers with respect to electromagnetic interactions.

The total gauge symmetry of the Standard Model is the combination of the symmetry groups $U(1)_Y \otimes SU(2)_L \otimes SU(3)_C$. These symmetry groups are the $U(1)_Y$ group with a quantum number called *hypercharge* Y, the group $SU(2)_L$[2)] with quantum number *weak isospin* I_W and the $SU(3)_C$

[2] $SU(N)$ is the special unitary group of degree N. Its elements satisfy $UU^\dagger = 1$ and $det(U) = 1$.

	Fermions			Quantum Numbers		
Generation	I	II	III	I_3	Y	Q
Leptons	$\begin{pmatrix} \nu_{e_L} \\ e_L \end{pmatrix}$	$\begin{pmatrix} \nu_{\mu_L} \\ \mu_L \end{pmatrix}$	$\begin{pmatrix} \nu_{\tau_L} \\ \tau_L \end{pmatrix}$	$^1/_2$ $-^1/_2$	-1 -1	0 -1
	ν_{e_R}	ν_{μ_R}	ν_{τ_R}	0	0	0
	e_R	μ_R	τ_R	0	-2	-1
Quarks	$\begin{pmatrix} u_L \\ d'_L \end{pmatrix}$	$\begin{pmatrix} c_L \\ s'_L \end{pmatrix}$	$\begin{pmatrix} t_L \\ b'_L \end{pmatrix}$	$^1/_2$ $-^1/_2$	$^1/_3$ $^1/_3$	$^2/_3$ $-^1/_3$
	u_R	c_R	t_R	0	$^4/_3$	$^2/_3$
	d_R	s_R	b_R	0	$-^2/_3$	$-^1/_3$

Table 2.1.: The particle content of the Standard Model and their quantum numbers with respect to electroweak interactions. The three generations of leptons and quarks are the building blocks of matter. The left handed fields are arranged in doublets of the weak isospin. The forces in between them are mediated through the bosons. The Higgs boson provides masses to fermions and bosons. The quantum numbers of electroweak interactions are the hypercharge Y and the third component of the weak isospin I_3. The electric charge is determined by the relation $Q = I_3 - {}^Y/_2$.

group of strong interaction with *colour charge C* as quantum number. The mass eigenstates of the corresponding gauge bosons are the massive $W^{\pm}$ and *Z bosons*, the massless *photon* γ and eight massless *gluons*. In order to generate these masses and those of the fermions one massive *Higgs boson* is predicted by the Standard Model.

The total Lagrangian of the Standard Model can be written as

$$\mathscr{L}_{\mathrm{SM}} = \mathscr{L}_{\mathrm{QCD}} + \mathscr{L}_{\mathrm{EW}} + \mathscr{L}_{\mathrm{Higgs}} + \mathscr{L}_{\mathrm{Yukawa}}\,. \tag{2.20}$$

The individual terms describing the kinematics and the gauge interactions of the elementary particles will be discussed in the next sections.

2.3.1. Electroweak Interactions

The common description of electromagnetic and weak interactions by one gauge theory with symmetry group $U(1)_Y \otimes SU(2)_L$ is based on the work of Glashow, Weinberg and Salam, who retrieved the Nobel prize for their work in 1979 [14–16].

To describe the parity violating nature of weak interactions the left- and right-handed components of the fields, which can be projected out like shown in Equation (2.7), are treated differently: only the left-handed components of the fields carry weak isospin charge and are arranged in doublets of the weak isospin symmetry group $SU(2)_L$. The right-handed fields do not carry weak isospin charge and stay singlets under the $SU(2)_L$ symmetry transformations. Therefore, the electroweak theory is often called a *chiral gauge theory*. In addition to a possible weak isospin charge, all fermion fields except the right-handed neutrinos carry weak hypercharge of the $U(1)_Y$ gauge group. The arrangement of the fermions into doublets and singlets of weak isospin is indicated in Table 2.1. In addition, the weak isospin and hypercharge quantum numbers as well as the resulting electric charge of the fermions are listed.

The ordering of the leptons into the doublets of weak isospin is straightforward. In contrast, experiments demonstrated that weak interactions between quarks can proceed through *flavour changing charged currents*: not only transitions like $u \to d$ have been observed, but also transitions in between different generations, like $u \to s$. Therefore, the quark eigenstates participating in electroweak interactions must be superpositions of their mass eigenstates. To describe this behaviour an additional mixing matrix for the quark fields denoted as the *CKM matrix* has been introduced by Cabibbo, Kobayashi and Maskawa. With this matrix, labelled M_{CKM} here, the

quark field eigenstates of electroweak theory, q', can be related to their mass eigenstates, q, by

$$\begin{pmatrix} d' \\ s' \\ b' \end{pmatrix} = M_{\mathrm{CKM}} \times \begin{pmatrix} d \\ s \\ b \end{pmatrix} . \tag{2.21}$$

The *CKM* matrix is a transformation of the $SU(3)$ symmetry group and prohibits transitions within the triplets $(d\,s\,b)$ and $(u\,c\,t)$, i.e. flavour changing neutral currents. This effect is called the *GIM* mechanism, named after Glashow, Iliopoulos and Maiani [17], which is needed to be in agreement with the measured lifetime of the proton. A complex phase of the matrix elements allows to describe the *CP* violating nature of electroweak interactions.

Lagrangian of Electroweak Interactions

Starting from the free field Lagrangian for the fermions, local gauge invariance under $SU(2)_L$ and $U(1)_Y$ transformations requires the introduction of a gauge boson triplet $W^{1,2,3}$ and one gauge field B, respectively, all with appropriate transformation properties. The covariant derivative of this theory is given by

$$D_\mu = \partial_\mu + i\,\frac{g}{2}\tau_i W^i_\mu + i\,\frac{g'}{2} Y B_\mu \,, \tag{2.22}$$

where the constants g' and g determine the coupling strengths of the fermions to the gauge bosons B and W^i, respectively. The Y and the τ_i in Equation (2.22) denote the generators of the gauge groups $U(1)_Y$ and $SU(2)_L$, respectively. The latter are usually represented by the Pauli matrices σ_i. Given this covariant derivative the total Lagrangian of electroweak interactions can be written in terms of the weak isospin doublets of left-handed fields, represented by $(a\,b)_L$, and the right-handed singlet fields, a_R and b_R:

$$\begin{aligned} \mathscr{L}_{\mathrm{EW}} \;=\; & i\,(\bar{a}\;\bar{b})_L\;\gamma_\mu D^\mu \begin{pmatrix} a \\ b \end{pmatrix}_L + i\,\bar{a}_R\,\gamma_\mu D^\mu\, a_R + i\,\bar{b}_R\,\gamma_\mu D^\mu\, b_R \\ & -\tfrac{1}{4}\,W^i_{\mu\nu} W_i^{\mu\nu} - \tfrac{1}{4}\,B_{\mu\nu} B^{\mu\nu} \,. \end{aligned} \tag{2.23}$$

Again the kinetic terms of the gauge fields W^i and B are expressed in terms of their field strength tensors $W^i_{\mu\nu}$ and $B_{\mu\nu}$. Their definition follows Equation (2.15), given the appropriate structure constants f^{abc} of the gauge groups $SU(2)$ and $SU(1)$.

2.3.2. Electroweak Symmetry Breaking

Given the discussion in Section 2.2, explicit mass terms for the gauge bosons of electroweak theory are forbidden, since these violate local gauge invariance. Instead the $U(1) \otimes SU(2)$ must be broken spontaneously to generate those masses. For this purpose a Higgs doublet of weak isospin, ϕ, is introduced

$$\phi = \begin{pmatrix} \phi_\alpha \\ \phi_\beta \end{pmatrix} = \frac{1}{\sqrt{2}} \begin{pmatrix} \phi_1 + i\phi_2 \\ \phi_3 + i\phi_4 \end{pmatrix} . \tag{2.24}$$

The Lagrangian of this Higgs doublet is given by

$$\mathscr{L}_{\text{Higgs}} = D_\mu \phi^\dagger D^\mu \phi - \mu^2 \phi^\dagger \phi - \lambda (\phi^\dagger \phi)^2 . \tag{2.25}$$

According to Section 2.2 the parameter μ^2 can be chosen negative ($\mu^2 < 0$) to spontaneously break the $U(1) \otimes SU(2)$ symmetry. This results in a non-trivial ground state for the Higgs doublet, which can be chosen as

$$\phi_0 = \frac{1}{\sqrt{2}} \begin{pmatrix} 0 \\ v \end{pmatrix} \neq \begin{pmatrix} 0 \\ 0 \end{pmatrix} . \tag{2.26}$$

The vacuum expectation value v of the Higgs boson is connected to the Fermi coupling G_F by $v = (\sqrt{2} G_F)^{-1/2}$ [5, 18]. As G_F was determined precisely from muon decay measurements [19–22], the value of v could be predicted to $v \approx 246\,\text{GeV}$. In contrast, the mass of the Higgs boson could not be predicted as the self interaction strength of the Higgs boson is not related to any quantity that could be measured.
The choice of the new ground state as given in Equation (2.26) generates the masses for the gauge bosons.

Due to the $SU(2)$ structure of weak isospin the masses of the gauge bosons are described by a mass matrix for the fields W_i and B. The corresponding mass eigenstates can be obtained by diagonalising this matrix. However, the mass eigenstates already have been observed, they are the massive $W^\pm$ and Z bosons and the massless photon γ. In order for the theory to be in agreement with the experimental observations of a massless photon, the $U(1)_{em}$ symmetry of electromagnetic interactions must be preserved when the electroweak symmetry is broken. Hence the quantum numbers of the Higgs doublet must be chosen appropriately. In that case the electromagnetic quantum number Q is connected to the third component of weak isospin I_3 and the weak hypercharge Y by the requirement $Q = I_3 - {}^{Y}/_{2}$, and the Higgs boson must be electrically neutral ($Q = 0$). The resulting mixing of the fields B and W^i can parameterised by

the *weak mixing angle* [5]

$$\theta_W := \sin^{-1}\left(\frac{g'}{\sqrt{g^2+g'^2}}\right) = \cos^{-1}\left(\frac{g}{\sqrt{g^2+g'^2}}\right), \tag{2.27}$$

With this definition the mass eigenstates are connected to the gauge bosons by

$$\begin{aligned} W_\mu^\pm &= \tfrac{1}{\sqrt{2}}(W_\mu^1 \mp i W_\mu^2), \\ \begin{pmatrix} A_\mu \\ Z_\mu \end{pmatrix} &= \begin{pmatrix} \cos\theta_w & -\sin\theta_w \\ \sin\theta_w & \cos\theta_w \end{pmatrix} \begin{pmatrix} B_\mu \\ W_\mu^3 \end{pmatrix} \end{aligned} \tag{2.28}$$

The masses of the observed gauge bosons are determined by the coupling constants g and g' and the vacuum expectation value of the Higgs boson:

$$\begin{aligned} M_{W^\pm} &= \tfrac{1}{2} v g\,. \\ M_Z &= \tfrac{1}{2} v \sqrt{g^2+g'^2}\,. \end{aligned} \tag{2.29}$$

As these masses are large with measured values of $M_{W^\pm} \approx 80.4\,\text{GeV}$ and $M_{Z^\pm} \approx 91.2\,\text{GeV}$ [18], the existence of the W and Z bosons has been predicted before these particles were discovered experimentally at the UA1 and UA2 experiments [23, 24].

To also generate the masses of the fermions in a gauge invariant way, additional *Yukawa coupling terms* are introduced that connect the fermion fields to the Higgs field. For a fermion b, of which the left handed component is part of the weak isospin doublet $(a\,b)_L$ and the right-handed component is the singlet b_R, the Yukawa term is given by

$$\mathscr{L}_{Yukawa} = -G_b \left[\left(\bar{a}\,\bar{b}\right)_L \phi\, b_R + \bar{b}_R\, \phi^\dagger \begin{pmatrix} a \\ b \end{pmatrix}_L \right]. \tag{2.30}$$

The masses of the upper components a of weak isospin doublets are generated by analogous terms in which ϕ is replaced by $-i\tau_2\phi^*$ and b_R by a_R. From Equation (2.30) follows that in order to generate distinct masses for each fermion f, a new coupling constant G_f needs to be introduced.

2.3.3. Quantum Chromodynamics

The strong interactions of quarks and gluons are described by *Quantum Chromodynamics* (*QCD*), which was developed in the 1970s. The symmetry of this theory is represented by the $SU(3)_C$ group of *colour charge*. The fermions that participate at strong interactions are the quarks, that either carry one of the three colours or anti-colours. Leptons do not interact strongly and therefore are not colour charged.

Lagrangian of Quantum Chromodynamics

The requirement of local gauge invariance under $SU(3)_C$ symmetry requires a covariant derivative of the form

$$D_\mu = \partial_\mu + i g_s \lambda_i G^i_\mu \,, \tag{2.31}$$

where the λ_i are the eight generators of the $SU(3)_C$ symmetry group, which are usually represented by the *Gell-Mann matrices*. A definition for these matrices can be found in Ref. [5], for example. Due to this number of generators, eight gluon gauge fields G^i are required to ensure local gauge invariance. With the covariant derivative of Equation (2.31) and by defining the quark colour triplets q_f for each of the six quark flavours f, the Lagrangian of the strong interactions can be written as

$$\mathscr{L}_{\mathrm{QCD}} = \sum_{\text{flavours } f} i \bar{q}_f \gamma_\mu D^\mu q_f - \frac{1}{4} G^i_{\mu\nu} G^{\mu\nu}_i \,. \tag{2.32}$$

The tensor $G^i_{\mu\nu}$ is the gauge invariant gluonic field strength tensor as defined in Equation (2.15), with the $SU(3)_C$ structure constants f^{ijk} and the coupling constant of strong interactions.

Consequences on the SU(3) Structure

The symmetry group $SU(3)_C$ is non-abelian, i.e. their elements and generators do not commute. This leads to additional terms in the Lagrangian if a gauge transformation is applied to the fermion fields and the ordinary derivative is replaced by the covariant derivative. To compensate these terms the gluon fields G^i are defined to transform differently from the field in Equation (2.12): An additional contribution $-f_{ijk}\,\alpha^j\,G^k_\mu$ is required to recover the gauge invariance of the Lagrangian. This transformation behaviour is reflected by the last term of the field strength tensor definition of Equation (2.15), $-g f^{ijk} G^j_\mu G^k_\nu$, which represents a self-interaction term among the gluons. The corresponding coupling strength is given by the coupling constant of strong interactions. The interpretation of this self-interaction is that gluons carry colour charge themselves, a colour and an anti-colour, and therefore allow for colour exchanges in between

quarks. This has important consequences on the behaviour of the running coupling constant of Quantum Chromodynamics, α_s, which can be parameterised with the expression [5]

$$\alpha_s(Q^2) = \frac{1}{\beta_0 \ln\left({}^{Q^2}/_{\Lambda^2}\right)} . \tag{2.33}$$

In this equation, Q^2 denotes the energy scale of the interaction process, Λ the typical energy scale of strong interactions and β_0 a constant computed by Gross, Wilczek and Politzer [25, 26].

At low distances (high energies) the running coupling constant of strong interactions gets small and therefore quarks and gluons interact very weakly at these conditions. This is known as the *asymptotic freedom* of quarks and gluons.

On the other hand, the strong coupling constant gets very large at large distances (low energies). Therefore, if quarks get separated the potential energy between them increases up to some threshold at which it is energetically more favorable that a quark–anti-quark pair is created. For this reason quarks cannot be observed in isolation, instead they cluster to colour neutral groups of quarks, the *hadrons*. This phenomenon is known as *colour confinement*, the process of the creation of quark–anti-quark pairs and the clustering to hadrons is denoted as *hadronisation* or *fragmentation*. The resulting hadrons do not solely consist of the *valence quarks* that built up the hadron. In addition, there is an indefinite number of *sea (anti-)quarks* and gluons that carry some part the momentum of the hadron and constantly exchange colour charge among themselves.

2.3.4. Phenomenological Models for Hadron Collisions

The characteristics of the strong force have important consequences on the description of p–p scattering. This description is based on the *factorisation theorem*, which states that the interactions of hadrons can be factorised into the hard scattering of the initial partons and the soft processes that connect the partons participating at the hard interaction with the incoming and outgoing colour-neutral hadrons. This is illustrated in Fig. 2.2, which shows a Feynman diagram for a p–p interaction with hadrons in the final state.

Parton Content of Hadrons

Since protons are composite objects consisting of *partons*, quarks and gluons, it is unknown which of these partons participate at some interaction process and what fraction of the momentum of the proton this parton occupied. Therefore, hadronic interactions are usually described by phenomenological models in a probabilistic approach. The parton content and their momentum

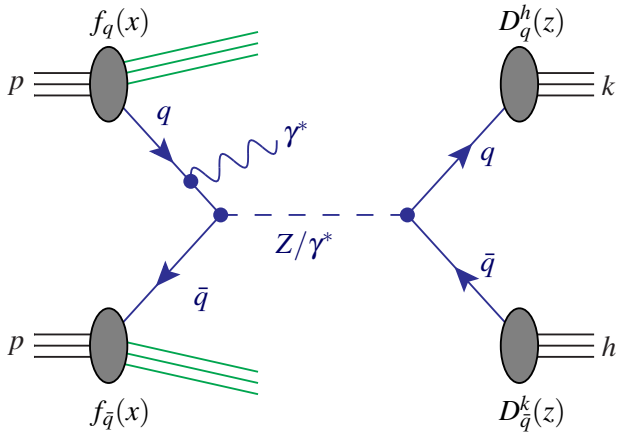

Figure 2.2.: Feynman diagram for p–p scattering. The hard scattering process of the participating partons is shown in blue. The parton density functions $f_{q,\bar{q}}(x)$ parameterise the parton content of the proton as a function of their relative momentum fraction. The fragmentation functions $D_{q,\bar{q}}^{h,k}$ parameterise the hadronisation of quarks. The outgoing fragments of the proton form the underlying event of the collision, which is indicated in green.

distributions inside a hadron are parameterised by the *parton density functions* (PDF), which can be interpreted as the probability of finding a specific parton inside the hadron with a particular fraction of the momentum of the hadron. Given these parameterisations the total cross section for hadron interactions can be expressed as a convolution of the interaction cross sections for the hard scattering process of the partons and their corresponding parton density functions. For the scattering of an electron e off a proton p with quark density functions f_q, for example, the cross section can be written as

$$\sigma(pe^- \to X) = \sum_q \int_0^1 f_q(x)\, \sigma(qe^- \to X)\, dx. \tag{2.34}$$

The interpretation of this equation is as follows: the cross section of the hard scattering process, i.e. the interaction of the electron with one of the quarks inside the proton, is given by $\sigma(qe^- \to X)$. To reflect the lack of knowledge about the flavour and colour charge of the participating quark, the cross sections for all possible quark flavours and colour charges, q, must be summed, weighted by the probability $f_q(x)$ to find such a quark inside the proton with a given momentum fraction $x = {}^{p_q}/_{p_p}$. Since this momentum fraction is unknown, too, the parameter x is to be integrated over the whole possible range from zero to one.

The parton density functions can be measured in electron–hadron collisions, for example. As

the energy of the electron can be controlled with high precision, only the properties of the partons remain unknown. However, the kinematic range of such experiments is usually constrained to a limited phase space. Nevertheless, parameterisations of the parton densities can be defined and using an evolution formalism the parameters can be determined using fits to the measurements performed at low energies [27–29]. The resulting approximations of parton density functions are then further extrapolated to higher energies. For the quark density f_q known at energy scale Q the *Dokshitzer–Gribov–Lipatov–Altarelli–Parisi evolution equation* (DGLAP) is given by [5,27–29]

$$\frac{d}{d\log Q^2} f_q(x,Q^2) = \frac{\alpha_s}{2\pi} \int_x^1 f_q(y,Q^2)\, P_{qq}\left(\frac{x}{y}\right) \frac{dy}{y} + \dots \tag{2.35}$$

This equation again has a probabilistic interpretation, based on the processes that proceed inside the hadron. It reflects that the origin of a quark with energy fraction x could have been another quark with energy fraction y (where $y > x$) that radiated off a gluon. The probability to find such a quark inside the hadron is given by the parton density function $f_q(y,Q^2)$, which is to be weighted by the probability for this quark to radiate off a gluon. This latter probability can be expressed in terms of the strong coupling constant, α_s, and the *Altarelli–Parisi splitting function* $P_{qq}(x/y)$. As again the exact momentum fraction of the parent parton is unknown, the parameter y is to be integrated over all possible values from x to 1. Since there exist further processes that also might result in the quark of interest to be produced, Equation (2.35) needs to be extended with appropriate terms for each of the additional processes, indicated by the "…".

Parton Showers

Higher-order corrections to the hard scattering process are the emission of gluons by the initial and final state partons (ISR and FSR). These gluons carry colour charge and therefore might radiate or split into further partons themselves, leading to *parton showers*. However, the very large number of partons produced in the parton showering process makes a detailed calculation of these higher-order corrections impractical or even impossible. In addition, the collinear emission of partons leads to divergences in the calculations. Therefore, partons showers are usually described using a phenomenological approach. Since the underlying process is the splitting of a parton into a pair of other partons, the parton showering can be related to the evolution of the parton density functions, that is also based on the same splitting processes. The iterative application of the Altarelli–Parisi splitting functions $P_{qq}(x/y)$ of Equation (2.35) leads to a sufficiently good description of the showering of a primary parton. The splitting is performed up to some a-priori arbitrary cut-off scale Q^2, which is usually chosen around 1 GeV.

Hadronisation and Jets

As a consequence of the confinement all final state partons produced in the hard scattering and the subsequent parton showering process will hadronise to the colour neutral hadrons. Usually several of these hadrons are produced in the hadronisation process that distribute the energy of the initial parton among themselves and that all share the same general direction. Furthermore, the radiation of gluons also dominantly results in collinear emissions. Therefore, the object that one usually observes in the final state are collimated *hadron jets*.

The mathematical description of the hadronisation process using perturbation theory is not possible. The reason is that the strong coupling constant grows with large distances at which the hadronisation takes place, which is in contradiction with the concept of perturbation theory that is only valid for small coupling strengths. Therefore, this process needs to be described with phenomenological models. For this purpose, the complete evolution of a process is factorised into the hard scattering process and the hadronisation of quarks and gluons into the final state particles. A common approach is to parameterise the latter with *fragmentation functions*. These fragmentation functions, $D_q^h(z)$, can be interpreted as probability densities to find a particular hadron h with momentum fraction $z = {}^{E_h}/_{E_q}$ inside the particle jet of a quark q. Analogous to the case of parton density functions, the interaction cross section of a process resulting in hadrons in the final state can be written as the cross section for the hard interaction process that is summed over all possible quark flavours that might have produced the hadrons and integrated over the momentum fractions of the hadrons:

$$\sigma(q_1 q_2 \to hX) = \sum_q \int_0^1 \sigma(e^+e^- \to q\bar{q}) \, [D_q^h(z) + D_{\bar{q}}^h(z)] \, dz \, . \tag{2.36}$$

However, this somehow simple approach to describe hadronisation becomes insufficient if also correlations among the final state particles are of interest. In addition, the description of decay chains increase the complexity of such calculations. Hence, other models are used in such cases to describe the hadronisation.

One of these is the more complex *string model* [30]. In this approach a pair of quark and anti-quark are connected by a colour string. The potential energy of this string increases with the distance in between the quarks and at some given energy threshold, which is of the order of hadron masses, the string breaks up to generate a new pair of quarks. Gluons are treated separately in this model as nodes in the strings that carry some energy and momentum.

Another approach to describe hadronisation is pursued by the *cluster models*. Their approach is based on the preconfinement property of perturbative QCD, that was discovered by Amati and

Veneziano [31]. They observed that at scales much lower than the hard interaction scale, the partons inside a shower are clustered to colour-neutral groups. These clusters subsequently decay to the finally observed hadrons, independently on the energy scale of the hard interaction process.

The measurement of the fragmentation functions and the determination of the parameters of the cluster and string models can be performed the easiest by analysing electron–positron collisions with final states containing hadron jets.

Underlying Event

A further consequence of the inner structure of hadrons is that not only the primary hard scattering process might proceed when protons collide. Additional particles produced in *multiple parton interactions* (MPI), like additional elastic gluon–gluon scattering, and in the hadronisation of the *proton remnants* accompany the hard interaction. These additional contributions to a collision event are summarised as the *underlying event* and several phenomenological models exist to describe its contribution to the event activity [32, 33]. Since most of the processes involved include low momenta transfers, a perturbative treatment of the underlying event description is not possible.

2.4. Supersymmetric Extensions to the Standard Model

The Standard Model is very successful in describing the interactions of quarks and leptons and in predicting the outcome of many experiments. Nevertheless, various observations and measurements revealed the limitations of this model. Such observations are, for example:

- Several experiments, like *Super-Kamiokande*, *KamLAND* and *MINOS*, were able to prove the oscillation of neutrinos from one lepton flavour to another [34–37]. This indicates that neutrinos have mass, which is not foreseen in the Standard Model.

- Measurements of the cosmic microwave background with the *Wilkinson Microwave Anisotropy Probe* (WMAP) were combined with further experimental results to estimate the matter and energy density of the universe [1]. This combination revealed that the baryonic matter, that can be described by the Standard Model, only contributes about 4.6% to the total energy density of the universe. Hence, some additional sort of *dark matter* must exist, which was measured to contribute additional 22.9%. Since up to now this dark matter could only be observed through its gravitational interactions with ordinary matter, it is expected to consist of so-called *WIMPs*[3], massive particles that only interact through gravity and weak interactions. However, the large amount of dark matter cannot be described by the Standard Model, even with massive neutrinos. The remaining $\approx 72.5\%$ of the energy density of the universe is made of *dark energy*. Up to now the nature of dark matter and dark energy and their properties are unknown.

- Quantum corrections to the Higgs boson mass lead to divergent contributions. In the Standard Model a stringent fine-tuning of several parameters is required to accomplish cancellations of the divergent terms. This need is denoted as the *fine-tuning problem*. Closely related to the fine-tuning problem it the *hierarchy problem*: given the measured value for the vacuum expectation value of the Higgs field and the cancellations of divergences due to the fine-tuning, the mass of the Standard Model Higgs boson is expected to be very low compared to the Planck mass. There is no obvious reason for the large difference of these quantities.

- In the Standard Model the running coupling constants of the electroweak and strong forces do not unify at high energies. Therefore, the Standard Model cannot be the *Grand Unified Theory*. Furthermore, gravity cannot be embedded into the existing model.

[3] *Weakly Interacting Massive Particles*

To solve these issues several extensions to the Standard Model have been proposed. One of these is the group of *Supersymmetric extensions to the Standard Model* (*SUSY*) [6]. The most important properties of these theories are summarised in Section 2.4.1. A special case important for the search presented in this thesis is the Minimal Supersymmetric Standard Model that is described in Section 2.4.2.

2.4.1. Supersymmetric Theories

Supersymmetric theories introduce an additional symmetry between the particles of the Standard Model and new postulated partner particles. These *superpartners* are identical to the Standard Model particles in terms of mass and internal quantum numbers apart from their spin: the superpartners of bosons are fermions and vice versa. However, no supersymmetric particles have been observed up to now and therefore their masses must be larger than those of their Standard Model partners. This implies that supersymmetry must be a broken symmetry. The additional symmetry can be described by a *supersymmetry transformation* operator Q operating on an additional quantum number. This operator turns a fermionic state into a bosonic one and vice versa:

$$Q\ |\text{Fermion}\rangle = |\text{Boson}\rangle\,, \qquad Q\ |\text{Boson}\rangle = |\text{Fermion}\rangle\ . \tag{2.37}$$

With the above choice of mass and quantum numbers for the superpartners these models do not suffer from the fine-tuning problem: the loop contributions of fermions and bosons to the Higgs boson mass have opposite signs and hence the divergences introduced by the Standard Model particles cancel with those of their superpartners to all orders of the perturbation series.

The solution to the fine-tuning problem is not the only advantage of supersymmetry. To enforce the stability of the proton supersymmetric models postulate an additional discrete symmetry, the *R-parity*. The definition of the corresponding quantum number is such that the R-parity is +1 for particles and -1 for supersymmetric particles. As this quantum number is multiplicatively conserved the *Lightest Supersymmetric Particle* (*LSP*) is stable. In most supersymmetric models this particle is massive, electrically neutral and interacts only weakly. Therefore, the LSP in these models might be responsible for the amount of cold dark matter that is observed in the universe.

The representation of the fields in supersymmetric theories are the *supermultiplets*. Each supermultiplet describes both at once, a fermion and a boson field of the same internal quantum numbers with respect to the $U(1)_Y \otimes SU(2)_L \otimes SU(3)_C$ gauge group. For the theoretical description of supersymmetry, it is very convenient to use the Weyl notation that has been introduced

in Section 2.1: the Dirac matrices are defined in the Weyl representation and therefore a fermion field can be described by two two-component Weyl spinors. In this representation a *chiral* or *scalar* supermultiplet describes a single Weyl fermion with two spin helicity states and a complex scalar field, i.e. two real spin-0 scalars. Such supermultiplets represent the leptons and quarks and their superpartners. These scalar superpartners are called *sfermions* ("scalar fermions"). Hence, the superpartners of quarks are the *squarks*, those of leptons are *sleptons*. Since the left- and right-handed components of a fermion field are separate two-component Weyl fermions that couple differently to the gauge bosons of electroweak interactions, two complex scalar superpartners are postulated for each fermion. Despite the fact that the sfermions are spin-0 particles, they are denoted as left- or right-handed fields to indicate their affiliation to the left- or right-handed fermions. The gauge interactions for these left- and right-handed sfermions are identical to those of their Standard Model partners.

A *gauge* or *vector* supermultiplet describes a massless Standard Model gauge boson with spin 1 and a massless spin-$^1/_2$ Weyl fermion, the *gaugino*. The superpartners of the gauge boson fields W^i are the *winos*, the partner of the gauge field B is the *bino*. After spontaneous breaking of electroweak symmetry they mix to the mass eigenstates *zino* and *photino*. If gravity is included in the supersymmetric model the graviton with spin 2 is assigned a superpartner with spin $^3/_2$, the *gravitino*.

The Higgs sector of supersymmetric theories requires two chiral supermultiplets to generate the masses of fermions, as will be described later. One multiplet gives mass to up-type quarks (H_u), the other to down-type quarks and the electrically charged leptons (H_d). The fermionic superpartners of the Higgs fields are denoted as *higgsinos*.

The minimal particle content of supersymmetric models is shown in Table 2.2. To identify the affiliation of the superpartners but to still be able to distinguish them from the Standard Model particles they are denoted by the same symbols, but with a tilde: The superpartner of the left-handed electron e_L is the left-handed selectron $\widetilde{e}_L$, for example. Since the chiral supermultiplets are defined with left-handed two-component Weyl spinors, the conjugates of the right-handed fields are listed in this table.

Supersymmetric interactions among the chiral supermultiplets can be introduced as a function of the *superpotential* W, which is a holomorph in the scalar fields. The derivatives of this superpotential with respect to the scalar fields determine the Yukawa couplings of the scalar fields, i.e. the sfermions, to the fermion fields of the theory. Furthermore, the superpotential introduces explicit mass terms for fermions. However, due to the requirement of local gauge invariance most of these are forbidden and only the mass terms for the higgsinos remain valid.

Chiral supermultiplets						
Names		Spin 0	Spin 1/2	$SU(3)_C$	$SU(2)_L$	$U(1)_Y$
squarks, quarks	Q	$(\,\widetilde{u}_L\,\widetilde{d}_L\,)$	$(\,u_L\,d_L\,)$	3	2	$^1/_6$
	$\bar{u}$	$\widetilde{u}_R^*$	$u_R^\dagger$	$\bar{3}$	1	$^{-2}/_3$
	$\bar{d}$	$\widetilde{d}_R^*$	$d_R^\dagger$	$\bar{3}$	1	$^1/_3$
sleptons, leptons	L	$(\,\widetilde{\nu}\,\widetilde{e}_L\,)$	$(\,\nu\,e_L\,)$	1	2	$^{-1}/_2$
	$\bar{e}$	$\widetilde{e}_R^*$	$e_R^\dagger$	1	1	1
Higgs, higgsinos	H_u	$(\,H_u^+\,H_u^0\,)$	$(\,\widetilde{H}_u^+\,\widetilde{H}_u^0\,)$	1	2	$^{+1}/_2$
	H_d	$(\,H_d^0\,H_d^-\,)$	$(\,\widetilde{H}_d^0\,\widetilde{H}_d^-\,)$	1	2	$^{-1}/_2$

Gauge supermultiplets					
Names	Spin 1/2	Spin 1	$SU(3)_C$	$SU(2)_L$	$U(1)_Y$
gluino, gluon	$\widetilde{g}$	g	8	1	0
winos, W bosons	$\widetilde{W}^\pm$, $\widetilde{W}^0$	$W^\pm$, W^0	1	3	0
bino, B boson	$\widetilde{B}^0$	B^0	1	1	0

Table 2.2.: The minimal particle content of supersymmetric theories and their quantum numbers. The upper part of the table lists the chiral multiplets representing the Standard Model fermions and their superpartners, as well as the fields of the Higgs sector. In the lower part the gauge supermultiplets are listed. These describe the Standard Model gauge bosons and their fermionic counterparts.

Soft Supersymmetry Breaking

Since no supersymmetric particles have been observed so far supersymmetry must be broken if realised in nature. In this case one of the main task of experimentalists and theorists is to find the responsible mechanism. Several models have been proposed of how supersymmetry breaking might proceed, but up to now there is no consensus. A common feature of all the proposals is that the symmetry is broken in a *soft* way: all additional contributions to the SUSY Lagrangian only contain mass terms and parameters with positive mass dimensions and the dimensionless terms in the Lagrangian remain unchanged. With this requirement the quadratic divergences to the Higgs mass are not reintroduced and therefore soft SUSY breaking models still provide a solution to the fine-tuning and hierarchy problems.

An analysis of the most general SUSY breaking Lagrangian that fulfills the above requirements reveals that the soft supersymmetry breaking sector adds a total of $O(100)$ new free parameters to the theory [38]. Some of these parameters can be constrained by sensible assumptions which are derived from existing measurements and hence soft SUSY breaking cannot be introduced in an arbitrary way. Taking into account the additional constraints on the parameters, assuming the absence of phases and mixing of fermion generations and assuming the universality of the first and second generations of sfermions the number of free parameters can be reduced to $O(20)$ [6, 39]. Such models with restricted parameter space are easier to investigate and therefore are denoted as *phenomenological* models.

In addition to the explicit approach to just add soft supersymmetry breaking terms to the Lagrangian, several proposals have been made how supersymmetry might be broken spontaneously. All approaches introduce new particles and interactions at high mass scales and further constraints on the masses and mixing angles are predicted. These constraints further reduce the number of free parameters to $O(5)$.

R-Parity

The most general form of the superpotential introduces lepton number and baryon number violating interactions to the SUSY Lagrangian. Those interactions result in flavour changing neutral currents and hence allow for the decay of the proton. However, since the proton is measured to be stable with a lower limit on its lifetime of the order of $O(10^{33})$ years [40] the corresponding couplings are either very weak or absent. In order to avoid the need for fine-tuning of those couplings, S. Glashow and S. Weinberg proposed a discrete ad-hoc symmetry that protects the proton from decaying [41]. This symmetry is either the *Matter parity* or the *R-Parity*, of which the latter is more restrictive. For a particle the multiplicatively conserved quantum number P_R

with respect to R-Parity is determined by its spin quantum number S, lepton number L and baryon number B by

$$P_R = (-1)^{3\times(B-L)+2S}. \tag{2.38}$$

A further consequence of this definition, apart from the stability of the proton, is that particles within the same supermultiplet have different R-Parity charges: sparticles have $P_R = -1$, all particles of the Standard Model and the scalar Higgs bosons have $P_R = +1$. Therefore, the conservation of R-Parity gives rise to particular features of a supersymmetric model:

- Sparticles do not mix with particles.
- Sparticles are always produced in pairs.
- The lightest sparticle, the LSP with $P_R = -1$, is stable.
- Other instable sparticles decay into final states containing an odd number of LSPs.

In many supersymmetric models the LSP is the lightest of the four neutralinos, i.e. the mass eigenstates resulting from the mixing of the neutral higgsinos, the bino and the neutral wino. This neutralino interacts only weakly with the Standard Model particles and therefore the conservation of R-Parity results in a dark matter candidate in such models. In addition, final states including neutralinos lead to interesting experimental signatures with large missing transverse momentum, as the neutralinos will traverse any detector undetected.

2.4.2. The Minimal Supersymmetric Standard Model

The *Minimal Supersymmetric Standard Model* (MSSM) [42, 43] is a supersymmetric extension of the Standard Model with minimal particle content and R-parity conservation. The lightest of the neutralinos is usually assumed to the LSP of the MSSM. As a consequence of R-parity conservation this neutralino is stable and provides a dark matter candidate.

Using the supermultiplet definitions of Table 2.2, the superpotential of the MSSM is given by

$$W_{\text{MSSM}} = \widetilde{\bar{u}}\, y_u\, \widetilde{Q} H_u - \widetilde{\bar{d}}\, y_d\, \widetilde{Q} H_d - \widetilde{\bar{e}}\, y_e\, \widetilde{L} H_d + \mu\, H_u H_d\,, \tag{2.39}$$

where the y_i are Yukawa coupling matrices in the 3×3 family space [6]. In this equation several indices are suppressed. The term $\widetilde{\bar{u}} y_u \widetilde{Q} H_u$, for example, can be written out as

$$\widetilde{\bar{u}}\, y_u\, \widetilde{Q} H_u = \widetilde{\bar{u}}^{ia} (y_u)_i^j\, \widetilde{Q}_{j\alpha a} (H_u)_\beta\, \varepsilon^{\alpha\beta}\,, \tag{2.40}$$

where i, j are family indices, α and β weak isospin indices and $a = 1, ..., 8$ a colour index. The term proportional to μ is the supersymmetric version of the Higgs boson mass in the Standard Model. Other terms like $\widetilde{\bar{u}} y_u \widetilde{Q} H_d^*$ and $\widetilde{\bar{d}} y_d \widetilde{Q} H_u^*$ are not allowed, which follows from the most general form of the superpotential for supersymmetric theories. Therefore, two distinct Higgs doublets are required to generate masses of up- and down-type fermions.

In the MSSM, supersymmetry is broken explicitly. The most general soft SUSY breaking Lagrangian of the MSSM that conserves matter parity and local gauge invariance is given by [6]:

$$\begin{aligned}
\mathscr{L}^{\text{soft}}_{\text{MSSM}} = \quad & -\left(M_3 \widetilde{g}\widetilde{g} + M_2 \widetilde{W}\widetilde{W} + M_1 \widetilde{B}\widetilde{B} + \text{c.c.}\right) \\
& -\left(\widetilde{\bar{u}} a_u \widetilde{Q} H_u - \widetilde{\bar{d}} a_d \widetilde{Q} H_d - \widetilde{\bar{e}} a_e \widetilde{L} H_d + \text{c.c.}\right) \\
& -\widetilde{Q}^\dagger m_Q^2 \widetilde{Q} - \widetilde{L}^\dagger m_L^2 \widetilde{L} - \widetilde{\bar{u}} m_{\bar{u}}^2 \widetilde{\bar{u}}^\dagger - \widetilde{\bar{d}} m_{\bar{d}}^2 \widetilde{\bar{d}}^\dagger - \widetilde{\bar{e}} m_{\bar{e}}^2 \widetilde{\bar{e}}^\dagger \\
& -m_{H_u}^2 H_u^* H_u - m_{H_d}^2 H_d^* H_d - (b H_u H_d + \text{c.c.}) \, .
\end{aligned} \tag{2.41}$$

The first three terms provide masses to the gluinos, winos and binos. The matrices $a_{u,d,e}$ are 3×3 matrices in family space that introduce trilinear couplings between the scalar fields. The matrices $m_{Q,L,\bar{u},\bar{d}}$ are 3×3 matrices in family space that explicitly provide masses to squarks and sleptons. These explicit mass terms for sfermions might explain why the sparticles are heavier than their Standard Model partners. A mixing between right- and left-handed sfermions might be realised if the mass matrices $m_{Q,L,\bar{u},\bar{d}}$ are non-diagonal. The last line in Equation (2.41) contributes to the mass terms of the Higgs bosons. Adding $\mathscr{L}^{\text{soft}}_{\text{MSSM}}$ to the SUSY Lagrangian explicitly breaks supersymmetry.

With the superpotential and the soft supersymmetry breaking Lagrangian given above the gauge couplings of electroweak and strong interactions can be unified at high energies. This behaviour of the gauge couplings in the MSSM is compared to their behaviour in the Standard Model in Fig. 2.3.

2.4.3. The Higgs Sector of the MSSM and Electroweak Symmetry Breaking

The scalar potential of the two Higgs doublets of the MSSM is given by the terms in Equations (2.39) and (2.41) that only depend on the scalar Higgs boson fields. To dynamically generate masses for the Standard Model particles the minimum of this potential must be chosen such that the ground state breaks electroweak symmetry and electromagnetism remains unbroken, of which the latter condition implies that $H_u^+ = H_d^- = 0$. Analogous to the generation of mass in

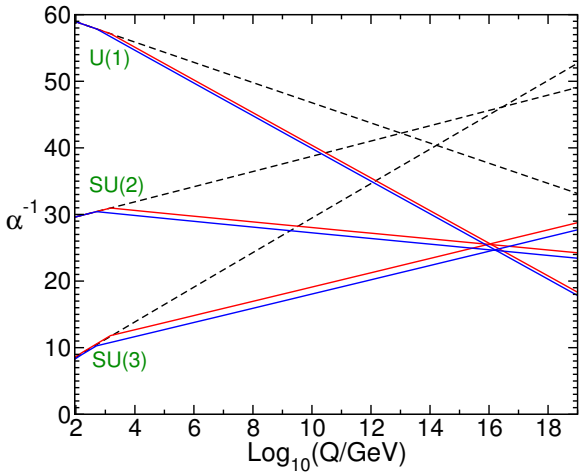

Figure 2.3.: Comparison of the inverse of the running coupling constants $\alpha^{-1}(Q)$ in the Standard Model (dashed lines) and the MSSM (solid lines). The calculations are performed at second order in perturbation theory. In between the red and blue lines the universal sparticle mass is varied from 500 GeV up to 1.5 TeV, and the coupling constant of strong interactions $\alpha_{SU(3)}(m_Z)$ is varied between 0.117 and 0.121. [6]

the Standard Model, this can be realised by assuming a negative squared mass term for the scalar Higgs boson fields. Assuming that the scalar potential is bound from below, a negative squared mass term requires the following two conditions to be satisfied [6]

$$\begin{aligned} 2b &< 2\,|\mu|^2 + m_{H_u}^2 + m_{H_d}^2\,, \\ b^2 &> (|\mu|^2 + m_{H_u}^2)\,(|\mu|^2 + m_{H_d}^2)\,. \end{aligned} \tag{2.42}$$

Both equations can only be solved simultaneously if $m_{H_u}^2 \neq m_{H_d}^2$. Furthermore, they imply that electroweak symmetry cannot be broken without the contributions due to the SUSY breaking Lagrangian, i.e. the term proportional to b.

After choosing a new ground state and breaking the electroweak symmetry, the two Higgs boson fields obtain non-trivial vacuum expectation values $v_u = < H_u^0 >$ and $v_d = < H_d^0 >$. The ratio of these values is used to define an angle β as

$$\tan\beta = \frac{v_u}{v_d}\,. \tag{2.43}$$

Using this quantity $\tan\beta$ and an additional mixing angle α the gauge-eigenstate fields of the

Higgs boson doublets can be related to the mass eigenstates. From the eight degrees of freedom of the two Higgs doublets, three are Goldstone bosons that are interpreted as the longitudinal polarisation degrees of freedom of the massive Z and $W^{\pm}$ bosons. Therefore, five observable Higgs boson are predicted by the MSSM, that are denoted as h, H, A and $H^{\pm}$. Of these, the mass eigenstates h and H are CP–even and electrically neutral scalars that result from the mixing of the fields H_u^0 and H_d^0 with mixing angle α. By convention their masses are chosen such that $m_h < m_H$. The Higgs boson A is electrically neutral and CP–odd. In addition to the three neutral Higgs bosons, two electrically charged mass eigenstates $H^{\pm}$, with $H^- = H^{+*}$, are predicted. Given the relations between the gauge-eigenstate fields and mass eigenstates and the scalar Higgs boson potential, the following expressions for the Higgs boson masses can be derived [6]

$$\begin{aligned} m_A^2 &= 2b/\sin(2\beta) = 2|\mu|^2 + m_{H_u}^2 + m_{H_d}^2 , \\ m_{h,H}^2 &= m_A^2 + m_Z^2 \mp \sqrt{(m_A^2 - m_Z^2)^2 + 4 m_Z^2 m_A^2 \sin^2(2\beta)} , \\ m_{H^{\pm}}^2 &= m_A^2 + m_W^2 . \end{aligned} \tag{2.44}$$

The "$-$" in the second equation results in the expression for the mass of h, m_h, and the "$+$" in that for H, m_H. Equation (2.44) shows that the masses m_A, m_H and $m_{H^{\pm}}$ increase with large values for the soft supersymmetry breaking parameter b and therefore are not constrained. The mass of h, on the other hand, is bound from above and at tree level one finds that $m_h < m_Z$. However, additional quantum corrections add further contributions to the mass and therefore increase this upper bound. Especially contributions from stop and top loops, a possible mixing of right- and left-handed top squarks and, at large $\tan\beta$, contributions from b- and $\widetilde{b}$-quark loops lead to larger possible values of m_h. Assuming that all masses contributing to those loop corrections are less than 1 TeV, the upper threshold on m_h is increased to $m_h \lesssim 135$ GeV [6]. Additional supermultiplets or larger sfermion masses might further contribute to the maximum allowed value of m_h.

The couplings of the Higgs bosons to the gauge bosons behave as shown in Fig. 2.4. Couplings of two Higgs bosons to two gauge bosons are not important for the results presented in this thesis. Therefore, these are not listed; a complete list of couplings can be found in Ref. [39], for example. The Fig. 2.4 shows that either the couplings of h to ZZ and WW or those of H are suppressed, depending on the magnitude of $(\beta - \alpha)$. For the respective other boson with non-suppressed couplings to ZZ and WW these couplings are equivalent to those of a Standard Model Higgs boson with the same mass – in that case it is often called a *Standard Model–like Higgs boson*.

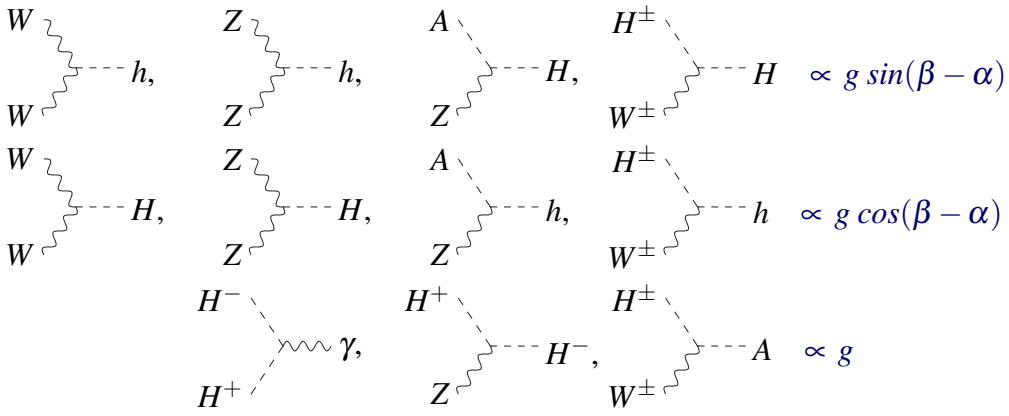

Figure 2.4.: Coupling strengths of the Higgs bosons of the MSSM to the gauge bosons. The parameter g denotes the weak coupling constant and α the mixing angle of the two *CP*–even Higgs boson fields h and H.

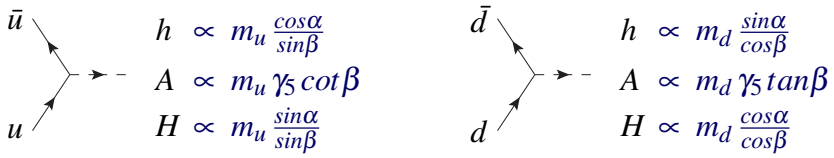

Figure 2.5.: Coupling strengths of the neutral Higgs bosons h, A and H to up- and down-type fermions. α denotes the mixing angle of the two *CP*–even Higgs boson fields h and H, γ_5 is one of the Dirac γ matrices.

Since A is *CP*–odd, the tree-level couplings AZZ and AWW are forbidden by *CP* invariance.

The couplings of the neutral Higgs bosons to fermions scale at tree-level as shown in Fig. 2.5. With increasing $\tan\beta$ the couplings of the A boson to down-type fermions are enhanced and those to up-type fermions are suppressed. The same statements hold for either h and H, depending on the magnitudes of α and β, and hold with inverted logic for the respective other boson. The coupling strengths of the electrically charged Higgs bosons are not important for this thesis, but can be found in Ref. [39], for example.

The Decoupling Limit: $m_A \gg m_Z$

At tree level the mixing angle α of the *CP*–even Higgs bosons can be expressed in terms of the parameter $\tan\beta$, the mass of the Z boson and the masses of the three neutral Higgs bosons. In the *decoupling limit*, i.e. for $m_A \gg m_Z$, these expressions show that the magnitude of α approaches

$\beta - \pi/2$. Since in that case $\cos(\beta - \alpha)$ approaches zero, the h boson couples to gauge bosons with the same coupling strength as a Standard Model Higgs boson of the same mass. On the other hand, the Higgs boson H decouples from the W and Z bosons in that limit.

Furthermore, it can be shown that in the decoupling limit the Higgs bosons $H^{\pm}$, A and H are nearly degenerate in mass. The mass of the h boson, m_h, approaches the maximum allowed value, which at tree level is the Z mass.

2.4.4. The $m_h^{\max}$ Benchmark Scenario of the MSSM

Due to the various degrees of freedom that are introduced by the soft supersymmetry breaking Lagrangian of Equation (2.41) the interpretation of experimental results becomes difficult, even for the phenomenological MSSM. For this reason several benchmark scenarios were elaborated, each representing a whole set of models with specific phenomenological characteristics. Many of the SUSY breaking parameters are fixed in these scenarios and the remaining parameter space is low-dimensional and therefore can be analysed more easily.

One of the benchmark scenarios for the MSSM is the *$m_h^{\max}$ benchmark scenario* [4] that will be used to quote results throughout this thesis. In this scenario the sfermion, gaugino and gluino masses as well as Higgs boson bilinear coupling μ are fixed. The parameters in the $\widetilde{t}$ and $\widetilde{b}$ sector are adjusted to values that maximise the mass m_h for a given choice of the parameters $\tan\beta$ and m_A. This guarantees conservative exclusion bounds from the LEP experiments.

The particular assumptions and choices for the supersymmetry parameters are in detail [4]: there is no mixing among the sfermions and all of their masses are equal; this universal mass is set to M_{SUSY} =1 TeV. The Higgs mixing parameter is chosen positive and set to μ =200 GeV. The gluino and gaugino masses are universal each and set to fixed values $m_{\widetilde{g}} = 0.8 * M_{SUSY}$ =800 GeV and $M_2 = 0.2 * M_{SUSY}$ =200 GeV, respectively. The trilinear Higgs-sfermion couplings are assumed to be equal in the sbottom and stop sector, $A_b = A_t$. The values of A_t that maximise m_h for the above choices of the other parameters and for given values of m_A and $\tan\beta$ are usually expressed in terms of the stop mixing parameter $X_t := A_t - \mu/\tan\beta$. Given the fixed parameter values listed above a maximum value for m_h is obtained with the choice $X_t^{OS} = 2 * M_{SUSY}$ =2 TeV, which was derived using the Feynman-diagrammatic approach and the on-shell renormalisation scheme.

The remaining free parameters in this model that determine the Higgs sector at tree level are the mass of the *CP*–odd and neutral Higgs boson, m_A, and the ratio of the vacuum expectation values of the two Higgs doublets, $\tan\beta$. The behaviour of the Higgs boson masses m_h and m_H in the $m_h^{\max}$ benchmark scenario as a function of m_A are shown in Fig. 2.6 for two different values

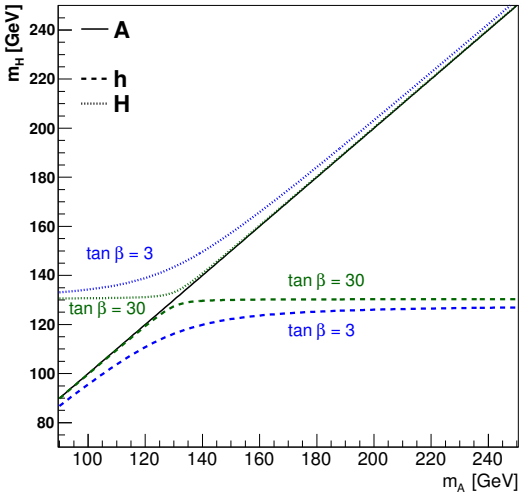

Figure 2.6.: Masses of the neutral Higgs bosons in the m_h^{max} scenario as a function of the parameter m_A and for values of the parameter $\tan\beta$ of $\tan\beta = 3$ (light-blue) and $\tan\beta = 30$ (dark green). The calculations include the complete one-loop and the dominant two-loop quantum corrections and are provided by Ref. [44].

of $\tan\beta$. For high masses m_A the heavier Higgs bosons, A and H, are nearly degenerate in mass and m_h is maximised. This effect is enhanced with increasing values of $\tan\beta$.

2.5. Higgs Physics at the LHC

Production and Decay of Standard Model Higgs Bosons

The processes relevant for the production of a Standard Model Higgs boson at the LHC are shown in Fig. 2.7. The corresponding cross sections of these processes are shown in Fig. 2.8 (a) as a function of the assumed Higgs boson mass. The gluon-fusion production mechanism has the largest cross section over the whole Higgs boson mass range. The cross section for the Vector Boson Fusion production is lower, but the two jets in forward directions and with large transverse momenta that are produced in this process provide a remarkable final state signature. This signature can be exploited in Higgs boson searches and in that case it compensates to some degree for the lower production cross section. Another important production process is the production of the Higgs boson in association with a W or Z boson, often denoted as Higgs-strahlung. The decays of the vector bosons into final states containing electrons or muons provide a clean signature inside the detector that can be used to find and to identify those production processes.

The various decay modes and their branching ratios of a Standard Model Higgs boson are shown in Fig. 2.8 (b). For low Higgs boson masses the $b\bar{b}$ decay mode is dominant, but the search for this mode is challenging as b-jets are difficult to identify. The search for this decay mode is mainly performed in the context of Higgs-strahlung production, like it is done in Ref. [45]. Other production processes, like the gluon-fusion process, do not provide any leptons and therefore the resulting final states are barely discriminable from purely hadronic interactions. For larger Higgs boson masses above the threshold of $\simeq 2 * m_W$ the decay into W^+W^- dominates. The most exceptional final state of this decay mode and hence the most promising one to search for is the one containing two leptons of different flavour, i.e. one electron and one muon. The decay of the Higgs boson into two Z bosons occurs with a much lower branching ratio as the decay into W^+W^-. However, the subsequent Z boson decays into four leptons result in a remarkably clean final state signature. Therefore this decay mode is often referred to as the "golden" channel for Higgs boson searches. The Higgs boson decay into a pair of massless photons only proceeds through loops of virtual particles. Although the probability for this decay is very small, this channel provides a very clean signal signature and a good control over the various background processes.

Production and Decay of the Neutral Higgs Bosons of the MSSM

In the MSSM the couplings of the neutral Higgs bosons to the fermions and bosons can differ dramatically from those in the Standard Model, especially for large values of $\tan\beta$. Due to

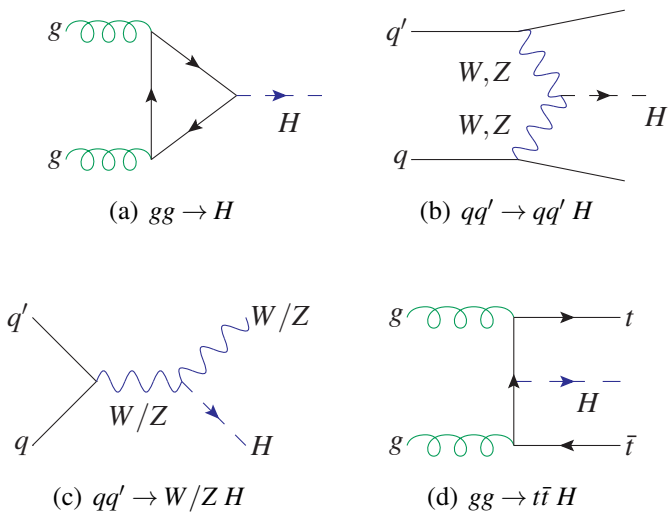

Figure 2.7.: Dominant production processes for the Higgs boson of the Standard Model. These are the gluon-fusion (a), the Vector Boson Fusion (b), the Higgs-strahlung (c) and the $t\bar{t}$ associated (d) production processes, in descending order regarding their cross sections.

the suppressed couplings of either h or H to ZZ and W^+W^- in large regions of the $(m_A, \tan\beta)$-parameter space and due to the absence of those couplings for A the searches for the neutral Higgs bosons in the ZZ and W^+W^- decay modes might be ineffective. In addition, the Vector Boson Fusion production mode, while being important for the Standard Model Higgs boson searches, might be suppressed for one of the *CP*–even Higgs bosons and is non-existent for A. On the other hand, the enhanced coupling to down-type fermions for large values of $\tan\beta$ can strongly increase the production rate of the neutral Higgs bosons through certain production mechanisms.

The mechanisms mainly affected by the enhanced couplings are the *gluon-fusion process* and the *b-quark associated production* of the neutral MSSM Higgs bosons. The corresponding production cross sections are shown in Fig. 2.9 for two different values of $\tan\beta$. At moderate and large values for the parameter $\tan\beta$ these cross sections exceed those of the Vector Boson Fusion production and Higgs-strahlung process by several orders of magnitude [39].
The gluon-fusion production has an overall large cross section, independent of the MSSM parameter choice. This process dominates the Higgs boson production for low masses m_A and low values of $\tan\beta$. The cross section increases with large values of $\tan\beta$ due to enhanced contributions of b-quark loops, which become the dominant contribution for values of $\tan\beta$ of ten and above [39]. In addition, squark loop contributions increase the production cross section even

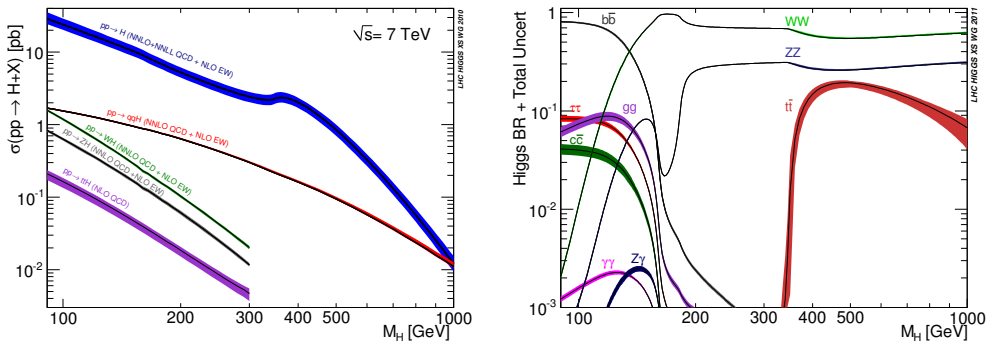

(a) Production modes (b) Decay modes

Figure 2.8.: Cross sections for the most important production mechanisms of a Standard Model Higgs boson at the LHC (a) and the corresponding branching ratios (b). The bands indicate the uncertainties on these properties due to uncertainties in the theory predictions. For the production cross sections the figure provides additional information about the perturbative order of the calculations. The figures are taken from Ref. [44].

further when compared to the gluon-fusion production cross section in the Standard Model. The corresponding leading-order Feynman diagram to this process is shown in Fig. 2.10 (a).
For larger masses m_A and large values of the parameter $\tan\beta$ the b-quark associated production mode dominates the Higgs boson production. The Feynman diagrams for the most relevant processes are shown in Fig. 2.10 (b-d). In the five-flavour scheme, additional contributions to the Higgs boson production are due to the process shown in Fig. 2.10 (e). Especially for large values for $\tan\beta$ these processes have large cross sections due to the enhanced couplings to b-quarks. The b-jets that are produced in most of them provide a particular signature that can be exploited in Higgs boson searches. However, this is very challenging since these b-jets usually exhibit very low transverse momenta and therefore are difficult to identify.

The dominant decay mode of the neutral MSSM Higgs bosons is the decay into $b\bar{b}$-quark pairs with a branching ratio close to 90%. However, the main production mechanisms in the MSSM, the gluon-fusion and the b-quark associated production, do not provide any outstanding signatures like electrons, muons or forward-directed jets with large transverse momenta that can be used to identify these events. Such signatures are, for example, provided by the Higgs boson production via Higgs-strahlung off a W or Z boson, which are of minor importance in the MSSM.
In contrast, the $\mu^+\mu^-$ decay mode provides a very clean final state signature. The two high energetic muons can be identified easily and due to the good energy resolutions for muons the Higgs boson mass can be reconstructed with a very high mass resolution. However, the probability for

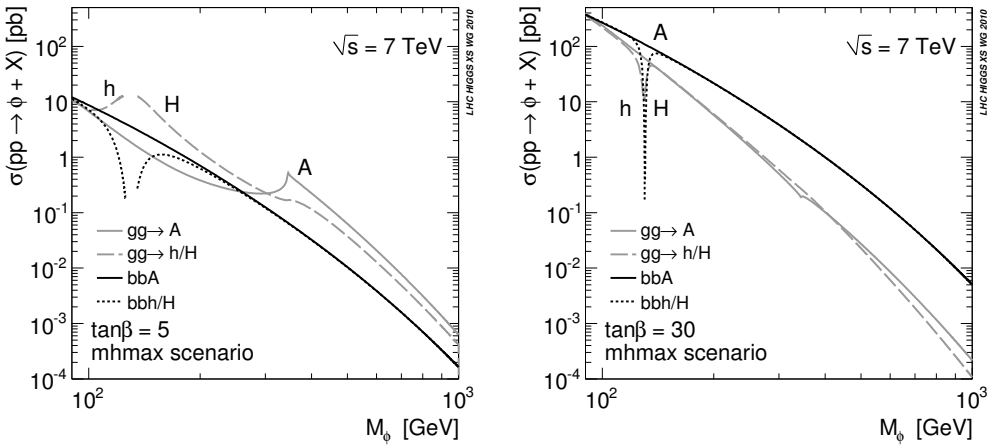

(a) $\tan\beta = 5$ (b) $\tan\beta = 30$

Figure 2.9.: Total production cross sections of the neutral Higgs bosons of the MSSM, assuming the $m_h^{\max}$ benchmark scenario. Cross sections for the gluon-fusion process and the b-quark associated production mode are given for values of $\tan\beta = 5$ in figure (a) and $\tan\beta = 30$ in figure (b). The b-quark associated production cross section has been calculated within the so-called five-flavour scheme. For both production modes at least NLO PDFs have been used and a center-of-mass energy of $\sqrt{s} = 7\,\text{TeV}$ was assumed. The figures are taken from Ref. [44].

the Higgs boson to decay into $\mu^+\mu^-$ is only about 0.04% whereas for the $Z/\gamma^* \to \mu^+\mu^-$ background process, which exhibits the same final state signature and has a larger production cross section, the same probability is much higher ($\simeq$3.4%). Therefore, the challenge for searches for this final state is to find a small resonance located on top of a large background distribution.

The $\tau^+\tau^-$ decay mode of the neutral Higgs bosons is a very promising process for Higgs boson searches in the context of the MSSM. Due to the enhancement of the Higgs boson couplings to τ leptons in large regions of the MSSM parameter space, the decay probability for the process $h/A/H \to \tau^+\tau^-$ can reach values up to 10%. Every possible final state of the $\tau^+\tau^-$ system can be taken into account for the Higgs boson searches, namely the final states resulting from two leptonic τ decays, one leptonic and one hadronic τ decay and from two hadronic τ decays.

Of the previously listed final states the fully hadronic decay mode of the $\tau^+\tau^-$ system is most challenging. This final state for the two τ leptons occurs with a large probability of about 42% and no high-energetic electron or muon is produced. Therefore, the search for this final state heavily depends on the identification efficiency for the hadronic decays of τ leptons and the corresponding misidentification probability for quark and gluon initiated jets. A big challenge

in the search for this final state is to understand and suppress the background due to multi-jet production processes. In addition, the energy measurements for hadronic τ decay products is very challenging and therefore the reconstructed Higgs boson mass suffers from a low resolution.

The final state easiest to identify results from the fully leptonic decay mode of the $\tau^+\tau^-$ system. Especially the decay into one electron and one muon can be identified easily and distinguished from the $Z/\gamma^* \to e^+e^-$ and $Z/\gamma^* \to \mu^+\mu^-$ background processes, that both have large production cross sections. On the other hand, the probability for the corresponding decay of the $\tau^+\tau^-$ system is very low ($\approx$6%). Since four neutrinos are produced in the two leptonic τ decays, the Higgs boson mass is reconstructed with a low resolution.

A very promising final state for Higgs boson searches in the $\tau^+\tau^-$ decay mode is realised if one τ lepton decays hadronically and the other one into an electron or a muon. The corresponding decay probability of the $\tau^+\tau^-$ system is about 46% in total and about 23% for each of the final states containing either an electron or a muon. The identified electron or muon can be utilised to strongly reduce the contribution of multi-jet background processes. In addition to a lepton, the final state contains three neutrinos and the hadronic decay products of a τ lepton, which result in a resolution for the reconstructed Higgs boson mass of intermediate quality. Details about the search for the neutral Higgs bosons of the MSSM in this final state are presented in Chapter 7. A summary of the searches for the other $\tau^+\tau^-$ final states and the $\mu^+\mu^-$ decay mode of the Higgs bosons, as well as the results of a statistical combination of all these searches is given in Chapter 8.

2.6. Existing Constraints on the Parameters of the Higgs Sector

Although not constrained a-priory, the parameter $\tan\beta$ is restricted by the requirement that the Yukawa couplings of the Higgs bosons to fermions must not get too large. Therefore, the parameter $\tan\beta$ is restricted to the range $1.5 < \tan\beta < 50-60$ in constrained MSSM models [6, 39].

Measurements of the anomalous magnetic moment of the muon prefer large values of $\tan\beta$, a positive μ and/or small masses of the sparticles [46].

In 2012 the BaBar experiment found evidence for enhanced decay rates for the process $\bar{B} \to D^{(*)}\tau^-\bar{\nu}_\tau$, that in combination exceeded the predictions of the Standard Model by approximately $3.4\,\sigma$ [47]. Furthermore, the two experiments BELLE and BaBar measured branching ratios for the fully leptonic decay $B \to \tau^-\bar{\nu}_\tau$ that also exceed the Standard Model predictions [48, 49]. Hence, these experimental results might be an indication for new physics beyond the Standard

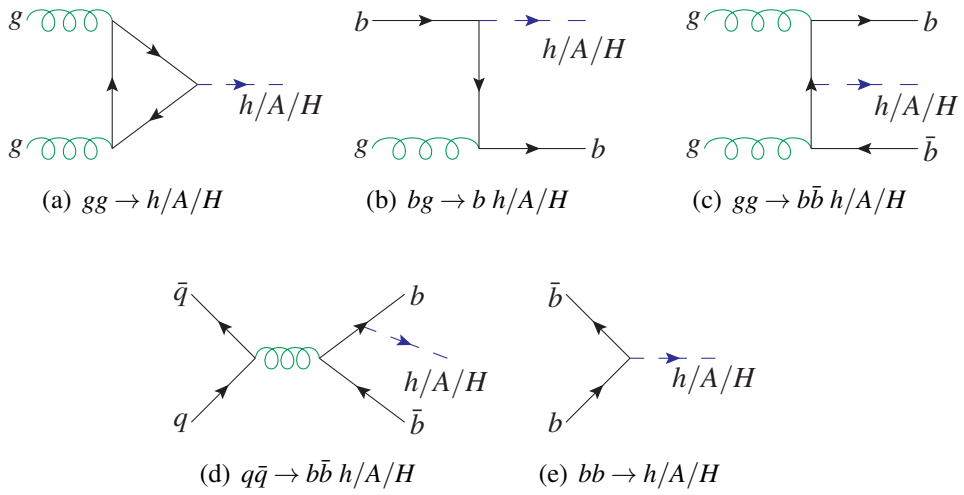

Figure 2.10.: Dominant production processes for the neutral Higgs bosons of the MSSM. The gluon-fusion production to lowest order in perturbation theory is shown in figure (a). The lowest-order Feynman diagrams contributing to the b-quark associated production mode are shown in figures (b-d). In the five-flavour scheme, additional contributions to the Higgs boson production are due to the process shown in figure (e).

Model and therefore have been interpreted in Ref. [47] in the context of models involving two Higgs doublets, such as the MSSM. More precisely, the authors investigated two Higgs doublet models in which one doublet provides masses to up-type fermions and the other doublet to down-type fermions and which preserve an additional symmetry to avoid flavour changing neutral currents at tree-level. The conclusion of the authors is that the experimental outcomes cannot be explained simultaneously by any of these models. Assuming the results of the BELLE and BaBar experiments can be confirmed with higher significance, such models can be ruled out with a probability of 99.8%.
Since the MSSM is a Higgs doublet model featuring the above properties, it might be ruled out, as well. However, the m_h^{max} benchmark scenario of the MSSM might still be a useful model as it represents any two Higgs doublet model in which the neutral Higgs bosons obtain enhanced couplings to down-type fermions.

Restrictions to the allowed parameter space in the $(m_A, \tan\beta)$ plane have been set by direct searches for a neutral Higgs boson of the Standard Model or the MSSM.

At the *Large Electron Positron Collider* (LEP) the experiments ALEPH, DELPHI, L3 and

OPAL searched for neutral Higgs bosons of the MSSM produced in the processes $e^+e^- \to Zh$ and $e^+e^- \to Ah$. No evidence for the existence of such Higgs bosons was observed and therefore a lower limit on the mass m_h of the h boson was set. Interpreted in the m_h^{max} benchmark scenario and assuming $m_A > m_Z$, the experimental results imply that $m_h >$92.8 GeV at 95% confidence level [50]. In addition, values of $\tan\beta$ in the range $0.7 < \tan\beta < 2.0$ could be excluded at the same confidence level.

In 2012 the two LHC experiments ATLAS and CMS independently from each other discovered a new boson and presented their results in Refs. [51] and [52]. Both experiments found an excess of data beyond the predicted Standard Model background rates in their searches for a Standard Model Higgs boson produced via the gluon-fusion, Vector Boson Fusion and Higgs-strahlung processes. The searches were performed for the decay modes $H \to \gamma\gamma$, $H \to ZZ^* \to 4\ell$, $H \to WW^* \to e\nu\mu\nu$, $H \to \tau^+\tau^-$ and $H \to b\bar{b}$. For both experiments, the significance of the observed excess exceeded 5 σ and the most probable mass of the new neutral boson was measured to be within the range 124–127 GeV[4)]. The rates at which this new particle has been produced and the decay modes it has been observed in indicate that it might be the long-sought Higgs boson[5)] and only the slightly larger rates in the $H \to \gamma\gamma$ decay mode might be an indication for physics beyond the Standard Model.
Evidence for the existence of the new particle was also presented by the experiments *DØ* and *CDF*, both located at the *Fermi National Accelerator Laboratory* (Fermilab). In 2012 these experiments observed an excess of data above the background predictions in their combined search for neutral Higgs bosons produced in association with a W or Z bosons and decaying into a $b\bar{b}$ quark pairs [53]. The observed excess was most significant in the mass range between 120 GeV and 135 GeV, with a local significance of 3.3 σ[6)].

The observations of the new boson have been interpreted in the context of the MSSM, which restricts the parameter space of constrained supersymmetric models [54, 55]. Since the A boson does not directly couple to WW and ZZ the observed particle cannot be interpreted as this CP–odd Higgs boson of the MSSM. The most favoured interpretation for the observed excess in

[4]The best fit value for the mass is $125.2 \pm 0.3\,(\text{stat}) \pm 0.6\,(\text{sys})$ GeV for the search with the ATLAS experiment with a significance of 7.0 σ [3]. The mass fitted by the CMS experiment is $125.8 \pm 0.4\,(\text{stat}) \pm 0.4\,(\text{sys})$ GeV with a significance of 6.9 σ [2].

[5]The signal strengths expressed in the parameter μ that were fitted to the excess were $\mu = 1.35 \pm 0.24$ for the searches with the ATLAS experiment [3] and $\mu = 0.88 \pm 0.21$ for the searches with the CMS experiment [2], where $\mu = 1.0$ corresponds to the signal strength of a Standard Model Higgs boson.

[6]The significance of the excess was 3.1 σ when taking into account the so-called *look-elsewhere effect*.

the context the MSSM is that the new particle corresponds to the light *CP*–even Higgs boson h. The observed production and decay rates suggest that in this case h must have Standard Model-like coupling strengths to gauge bosons. The mass range in which the new boson has been observed does not exceed the upper bound on the mass m_h that holds in MSSM-like models ($m_h \lesssim 135$ GeV). Otherwise such models could have been ruled out by the observations. However, the observed mass is far beyond the mass of the Z boson which requires a large mass for the top squark and a large trilinear coupling in the Higgs-stop sector. The observed decay rate into two photons suggests a low mass for the τ sleptons. Both, the observed mass and decay rates, prefer a large mass of the *CP*–odd Higgs boson, m_A, and therefore the masses and couplings of the Higgs sector should behave like in the decoupling limit. In addition to these constraints and indications, an upper bound on the parameter $\tan\beta$ can be derived, if the observations are interpreted in the m_h^{max} benchmark scenario. In that case the remaining free parameter space in the $(m_A, \tan\beta)$ plane would be a narrow band at low $\tan\beta$ values.
It is important to note that these considerations only hold for the MSSM; in other supersymmetric models the constraints derived from the observations could be far more or far less stringent.

An alternative interpretation for the observed excess in the context of the MSSM is that the new particle corresponds to the heavier *CP*–even Higgs boson H. In this case the H boson must feature Standard Model-like properties and the masses of the A and h bosons, m_A and m_h, are required to be very low. Further details on this interpretation can be found in Ref. [55].

The above considerations indicate that the MSSM is still consistent with any measurement performed to date. Considering the enhanced or suppressed couplings of the neutral MSSM Higgs bosons to third generation fermions, the $\tau^+\tau^-$ and $b\bar{b}$ decay modes are of special interest for further investigations. A precise measurement of the corresponding branching ratios or a measurement of the production rate of the new boson in association with b-quarks would be important to finally validate or rule out the MSSM.

Furthermore, additional neutral Higgs bosons are predicted by the MSSM with particular properties regarding their production and decay modes. At the ATLAS experiment dedicated searches for these were mainly focussing on the $\tau^+\tau^-$ decay mode of the neutral Higgs bosons produced in the gluon-fusion or b-quark associated production modes, as these are the enhanced processes for moderate and large values of $\tan\beta$ [56]. To date no significant excess of data above the predicted Standard Model background was observed in these searches. This lead to the exclusion of a large area in the $(m_A, \tan\beta)$-parameter plane of the MSSM, which is shown in Fig. 2.11 (a), assuming Higgs boson production and decay rates in the m_h^{max} benchmark scenario. The results

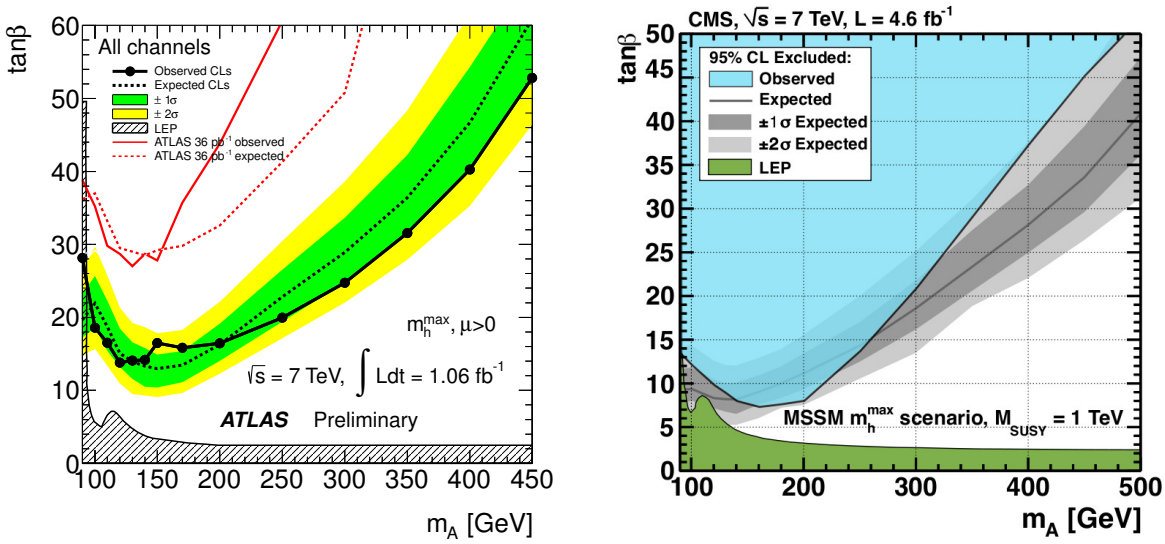

(a) ATLAS Collaboration (b) CMS Collaboration

Figure 2.11.: Former 95% CL upper exclusion limits on $\tan\beta$ as a function of the parameter m_A set by the ATLAS (a) and CMS (b) experiments. The results are derived from direct searches for the neutral Higgs bosons of the MSSM in the $h/A/H \to \tau^+\tau^-$ decay mode. The production modes considered are the gluon-fusion and the b-quark associated production of the Higgs bosons. The searches performed by the ATLAS collaboration included a data set corresponding to an integrated luminosity of $1.06\,\text{fb}^{-1}$. The amount of data included in the searches performed by the CMS collaboration is significantly larger ($4.6\,\text{fb}^{-1}$), therefore a direct comparison of the results is not straightforward. Figures were taken from Refs. [56] and [57].

presented in this figure were obtained using a dataset corresponding to an integrated luminosity of about $1.06\,\text{fb}^{-1}$, recorded in the first half of 2011 at a centre-of-mass energy of $\sqrt{s} = 7\,\text{TeV}$. An update on this search using the full data set recorded in 2011 is presented in Chapters 7 and 8. Equivalent searches have been performed by the CMS collaboration [57]; the area of the $(m_A, \tan\beta)$ plane that could be excluded by these is shown in Fig. 2.11 (b), also assuming the m_h^{max} benchmark scenario. Since the searches performed by the CMS collaboration included a significantly larger data set, a direct comparison of the results presented by the two experiments requires care.

The LHC accelerator

(CERN-DI-0503019 © 2005 CERN)

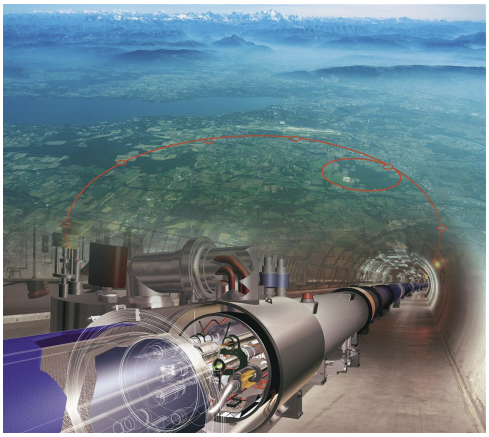

Chapter 3

The Large Hadron Collider

The *Large Hadron Collider* (*LHC*) is a huge particle accelerator ring located at the *CERN laboratory*[1)] next to Geneva (Switzerland). The storage ring is built inside the former *Large Electron–Positron Collider* (LEP) tunnel that has a circumference of about 27 km and is buried 50 to 175 meters below ground. A schematic illustration of the LHC accelerator complex is shown in Fig. 3.1.

The LHC is designed to accelerate and store bunches of protons or heavy ions and to bring them to collision at specific interaction points. For this purpose the accelerator and storage ring must be kept under a constant high vacuum in order to avoid collisions of the beams with gas molecules inside the beam pipe. At the interaction points several experiments are located that study the properties of those collisions. These experiments are the *LHCb*, *ALICE*, *CMS* and *ATLAS* experiments. The results presented in this thesis are based on *proton–proton (p–p) collision* data recorded with the ATLAS detector that is described in Chapter 4.

Although collisions of electrons and positrons are much cleaner and easier to study, the amount of energy loss due to synchrotron radiation, which is proportional to the mass m of the accelerated particle as m^{-4}, is very large for such light particles. Protons, on the other hand, are much heavier and therefore the energy loss is kept at an acceptable level.

The protons accelerated with the LHC stem from a hydrogen source. From there they are

[1] Organisation européenne pour la recherche nucléaire (European organization for nuclear research)

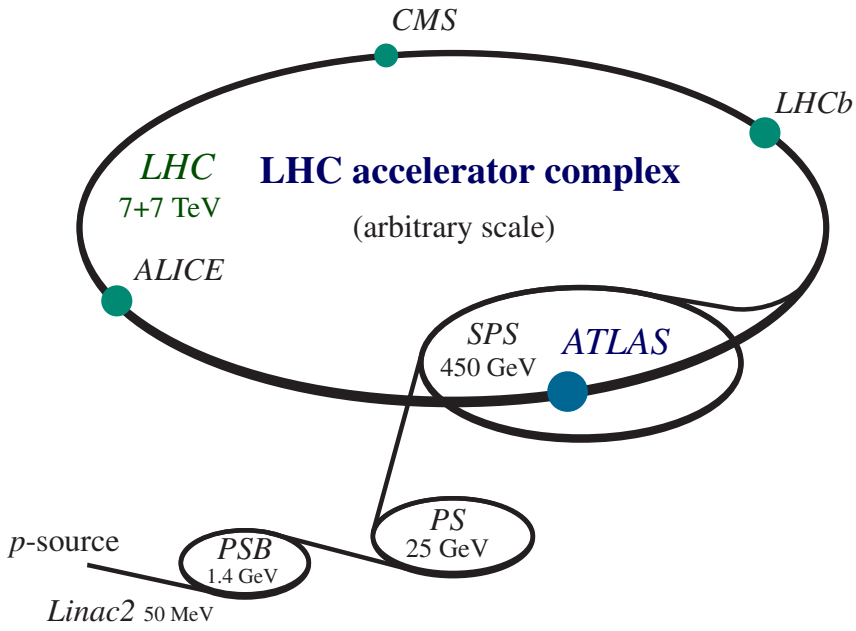

Figure 3.1.: Schematic view at the CERN accelerator complex and the experiments that are located at the four interaction points.

accelerated in a linear accelerator, the *Linac2*, to energies of about 50 MeV, and then further to energies of 1.4 GeV, 25 GeV and 450 GeV by the *Proton Synchrotron Booster* (*PSB*), the *Proton Synchrotron* (*PS*) and the *Super Proton Synchrotron* (*SPS*), respectively. This accelerator chain is illustrated in Fig. 3.1. With an energy of 450 GeV the protons are injected into the LHC ring and accelerated to their final collision energy. Given the fixed diameter of the tunnel, the maximum energy per proton beam that can be achieved is limited by the strength of the magnets that keep the beams on their circular orbit. At the LHC, 1232 super-conducting dipole magnets with a length of around 15 m each generate a magnetic field with a strength of ≈8.33 T. With this field strength an energy of 7 TeV per proton beam can be realised. To keep the magnets super-conducting they have to be kept at a constant temperature of about 1.9 K. Additional 392 quadrupole magnets with lengths ranging from 5 to 7 meters provide magnetic fields with field gradients of 233 $^{\mathrm{T}}/_{\mathrm{m}}$ each. These magnets are required to focus the proton beams.

The storage ring is capable of storing 2808 proton bunches that consist of up to 10^{11} protons each. The nominal distance of two successive bunches, the *bunch spacing*, is therefore just about 25 ns, which corresponds to a *bunch crossing frequency* of roughly 40 MHz.

The large amount of bunches with many protons and the short bunch spacing in between them

give rise to a huge number of collisions taking place in a given time interval. To quantify this rate the *instantaneous luminosity* of a storage ring can be defined, which is a measure of how many particles cross a given area per time interval. Assuming a gaussian beam profile with widths σ_x and σ_y in x- and y-direction, respectively, and given the numbers of stored bunches N_B and protons per bunch N_p as well as the bunch crossing frequency f as measured per second, the luminosity L is proportional to

$$L \propto \frac{N_p^2 N_B f}{4\pi \sigma_x \sigma_y}. \tag{3.1}$$

For a particular process with cross section σ the expected number of events per second is then given by

$$\mathrm{N}_{events} = L\sigma\,. \tag{3.2}$$

During its first three years of operation, the LHC aims to operate at instantaneous luminosities of about $10^{33}\,\mathrm{cm}^{-2}\mathrm{s}^{-1}$ for p–p collisions, and about one order of magnitude higher, roughly $10^{34}\,\mathrm{cm}^{-2}\mathrm{s}^{-1}$, after this period.

Operation during the Years 2010 and 2011

The accelerator has been designed to provide an energy of 7 TeV per beam. However, just a few days after the first successful circulation of proton beams, on the 10th of September 2008 [58], the LHC was shut down as a consequence of a magnet quench incident. After about one year of repairs operations were resumed on the 20th of November 2009 [59], and 3 days later the first p–p collisions were recorded [60]. A beam energy of 3.5 TeV was established on 30th of March, 2010, and the planned research program began [61]. Although the design goals for the beam energy could not be accomplished, the current centre-of-mass energy of 7 TeV outperforms the former record of 1.96 TeV, set by the Tevatron accelerator. An energy of 3.5 TeV per beam has been used for the whole data taking period up to the end of 2011 which is relevant for the results presented in this thesis. The instantaneous luminosity during this data taking period already exceeded the initial design goals and reached peak values of up to $3.61 \times 10^{33}\,\mathrm{cm}^{-2}\mathrm{s}^{-1}$. In total, the data that has been accumulated by the LHC in 2010 and 2011 corresponds to an integrated luminosity of $5.61\,\mathrm{fb}^{-1}$.

Pile-up

The previously defined high rate of p–p collisions results in huge amounts of data delivered to ATLAS. Very often, however, the time in between collisions is shorter than the finite response

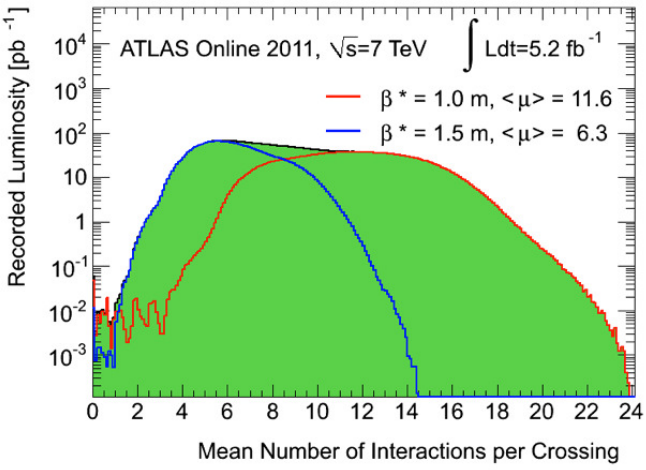

Figure 3.2.: Average number of interactions per bunch crossing for the data recorded with the ATLAS detector in 2011 [62]. The total inelastic p–p interaction cross section that has been assumed is 71.5 mb. Entries at $\mu \approx 0$ arise from so-called *pilot bunches*, i.e. single proton bunches, that were present during the commissioning phase of the LHC.

time of the detector elements and read-out electronics. Therefore, the energy depositions from one collisions event might influence the energy measurements in an event of the subsequent bunch crossing. This effect is referred to as *out-of-time pile-up*.

In addition, another source of pile-up, the *in-time pile-up*, arises from the high particle densities inside the proton bunches. Due to these densities far more than just one p–p interaction is expected per bunch crossing and therefore any interesting hard interaction is accompanied by several additional inelastic p–p collisions. These additional collisions mainly comprise low momentum transfers, resulting in so-called *minimum bias* events. Hence, in-time pile-up gives rise to superpositions of several physics processes that are recorded as one interaction event.

The luminosity-weighted distribution of the mean number of interactions per bunch crossing, μ, for the data taken at the end of 2010 and in 2011 is shown in Fig. 3.2. The individual entries are calculated as $\mu = L \times \sigma_{\text{inel}}/(n_{\text{bunches}} \times f)$, using the measured instantaneous luminosity L, the inelastic p–p interaction cross section σ_{inel}, the number of colliding bunches N_{bunches} of p–p collisions and the bunch crossing frequency f [62]. The figure is shown for data taken before and after a technical stop in September 2010, when the profile and focussing structure of the beam has changed. These properties can be described in terms of two quantities of which one is the so-called amplitude function of the beam, β, with function value β^* at the interaction point.

View at the ATLAS detector

(CERN-EX-0702041 © 2007 CERN)

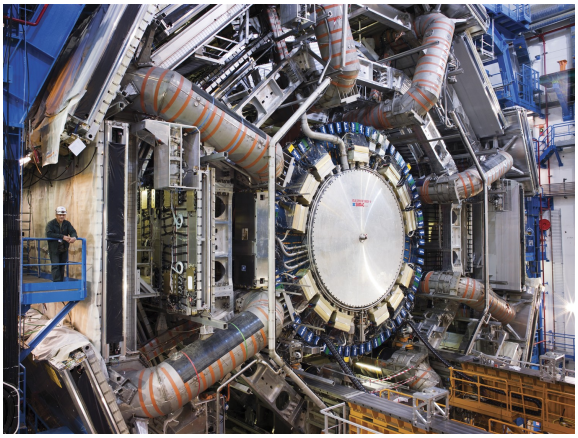

Chapter 4

The ATLAS Experiment

The *ATLAS detector* is a multi-purpose detector that is installed at one of the interaction points (*Point 1*) of the LHC accelerator ring. The active components of this detector can be grouped into three categories: The *tracking system*, the *calorimeter system* and the *muon detector system*. Each component of these categories consists of a cylindric central part that is built around the LHC beam axis, the *barrel*, and two disc structures at each side of a barrel, the *end-caps*. By construction, the barrel components measure the properties of particles traversing the detector volume at large angles with respect to the beam axis. The end-caps, on the other hand, measure the properties of particles at low angles. In addition, two separate magnetic systems, a *toroid* and a *solenoid magnet system*, are installed to bend the flight path of electrically charged particles. In total the length of the detector, including the barrel, end-caps and magnets, is about 46 meters, its total diameter is about 22 meters. All the components sum up to a total weight of about 7000 tons.

Each sub-detector has been designed to measure specific particle properties. The innermost layer of the detector, i.e. the layer which is closest to the interaction point, is the tracking system that is described in Section 4.2. The components of this sub-detector measure the directions and momenta of electrically charged particles. The tracking detectors are surrounded by the calorimeter system (see Section 4.3) that has been designed for exact energy measurements of both, electromagnetically and strongly interacting particles. Hence, the two components that the

calorimeter consists of are denoted as the *electromagnetic* and the *hadronic calorimeter*. The *Muon Spectrometer* (see Section 4.4) again is a tracking device and constitutes the outermost active detector components. Its main purpose is to measure the momenta of muons, that pass the calorimeters with minimal energy losses. Hence, with all detector components being operative, all known particles of the Standard Model, except neutrinos, can be detected. Since the neutrinos pass the detector elements undetected, their presence is only indicated indirectly by an imbalance in the momentum distribution in the plane transverse to the beam axis: Summing all measured particle momenta in the transverse plane gives an estimate of the amount of *missing transverse momentum* that has been carried away by un-detected particles. In order for this quantity to be an accurate measure of the momentum carried away, the detector needs to cover the complete solid angle. Therefore, a major design goal for the detector architecture was to achieve maximum possible *hermeticity*. The ATLAS calorimeter system, for example, covers the solid angle down to $\approx 1^\circ$ towards the beam axis and the complete ϕ range in the transverse plane.

The reliability of all subsystems described above, and therefore the data taking efficiency of the ATLAS experiment, was outstanding during the first two years of operation; from the 5.61 fb^{-1} of data that were delivered by the LHC, a total of 5.25 fb^{-1} could be recorded.

A schematic overview of the complete detector and its sub-detector systems is given in Fig. 4.1. The following sections provide a brief overview on the individual detector components and their functionality. A far more detailed description can be found in Refs. [63–65], for example.

4.1. The ATLAS Coordinate System

To uniquely identify directions and positions within the detector volume a particular coordinate system is defined. This coordinate system uses the nominal interaction point as its origin. The z-axis of this system is given by the LHC beam direction. The positive x-axis is defined as pointing from the interaction point to the centre of the LHC ring whereas the positive y-axis is defined as pointing upwards. Polar angles θ are measured with respect to the beam direction and azimuthal angles ϕ are defined in the transverse plane. The pseudorapidity η can be defined as a function of the polar angle θ by $\eta = -\ln\tan(\theta/2)$. The advantage of this quantity is that distances in η, usually denoted as $\Delta\eta = \eta_1 - \eta_2$, are invariant under Lorentz boosts in beam direction. Transverse momenta are computed from the three-momenta $\vec{p}$ as $p_T = |\vec{p}|\sin\theta$. Geometrical distances ΔR within the detector volume are defined as $\Delta R^2 = (\Delta\eta)^2 + (\Delta\phi)^2$, where $\Delta\phi$ and $\Delta\eta$ are the distances in the coordinates ϕ and η, respectively.

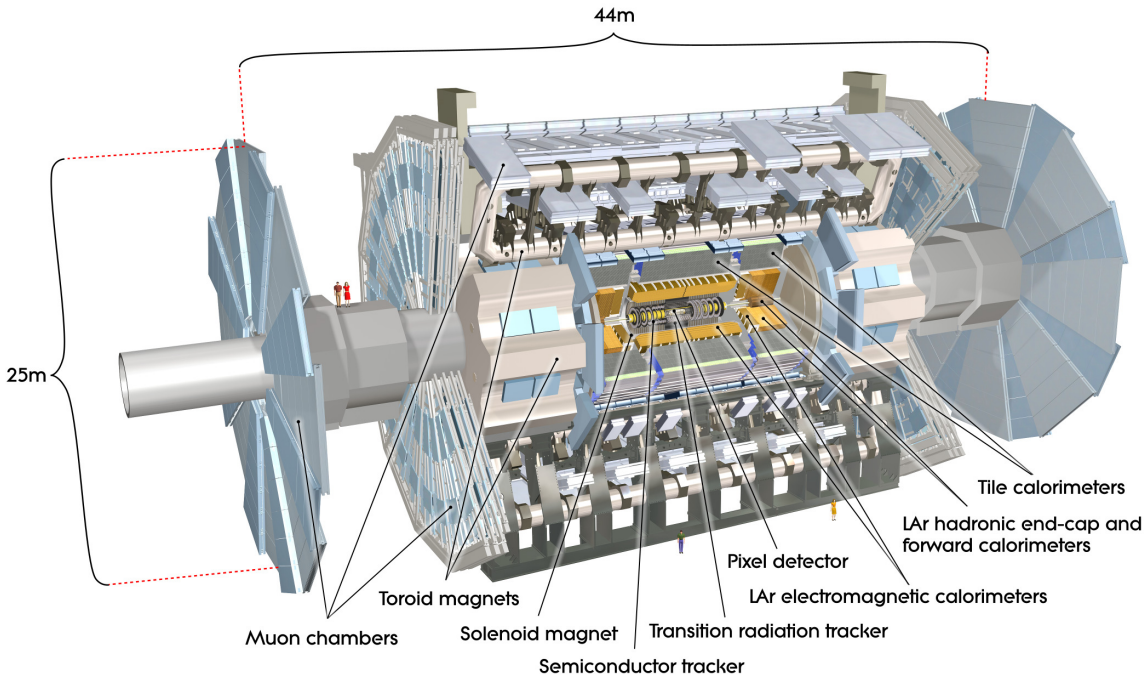

Figure 4.1.: The ATLAS detector and the individual subsystems. The Inner Detector is built around the beam axis at a very low distance and is surrounded by a solenoid magnet. These tracking devices are enclosed by the electromagnetic and the hadronic calorimeter. The muon detector system with its toroid magnet system constitutes the outermost layer of the detector. Figure taken from Ref. [63].

4.2. The Tracking System

The detector parts closest to the beam axis constitute the ATLAS tracking system, that is shown in detail in Fig. 4.2. The individual components, which are usually summarised as the *Inner Detector*, are the *Pixel Detector*, the *Semiconductor Tracker* and the *Transition Radiation Tracker*, in the order of growing distance to the interaction point, respectively. All of these components are designed to provide precise measurements of the direction and transverse momenta of electrically charged particles. Using these information also the origin of a particle, i.e. the so-called *vertex* of the interaction the particle has been produced in, can be reconstructed. The Inner Detector has outer radius of 1.15 m and a total length of 7 m.

In order to measure the momenta of charged particles the tracking devices need to be permeated with a magnetic field. Therefore, the tracking detectors are surrounded by a solenoid magnet system with dimensions of about 2.5 m in diameter and 5.3 m in length. This solenoid generates a magnetic field with a strength of 2 T that bends the flight path of electrically charged particles. The transverse momenta of these particles can then be reconstructed from the measured curvature of the trajectories. Due to the high magnetic field strength and with the full Inner Detector operational resolutions for transverse momentum measurements of $\sigma_{p_T}/_{p_T} = 0.05\% p_T \oplus 1\%$ are possible [64].

4.2.1. The Pixel Detector

The tracking detector closest to the beam pipe is the semiconductor *Pixel Detector*. The active components of this device are modules with external lengths of 63 mm and widths of 19 mm each. The modules consist of pixel sensors that each contain a total of 47232 pixels. The minimum size of such a pixel is $50 \times 400\,\mu\text{m}^2$ in $R\phi \times z$ and $R\phi \times R$ in the barrel and end-caps, respectively. Three barrels with radii of 5.05 cm, 8.85 cm, and 12.25 cm, respectively, cover the central part of the detector and contain a total number of 1456 of these modules. To achieve the best possible hermetic coverage the modules are overlapping on their support structure. The forward region in solid angle is covered by three disks that are positioned on either side of the barrel. These discs with radii ranging from 8.88 cm to 14.96 cm contain a total number of 288 modules. Given these numbers the barrels and end-cap pixel detectors contain 1744 modules. Communication in between the modules and read-out system is realised with 46080 readout channels.

This Pixel Detector provides information of up to three precision position measurements for each electrically charged particle that traverses the central detector volume within the pseudorapidity range of $|\eta| = 2.5$. The intrinsic accuracies for such measurements in the barrel are $10\,\mu$m

in the R–ϕ plane and 115 μm in z direction. The corresponding precisions of the end-cap discs are 10 μm and 115 μm, respectively. With its close distance to the interaction point the Pixel Detector provides essential information to precisely reconstruct the position of interaction vertices and the closest distances of tracks of long-lived particles, such as b-hadrons, to the interaction vertex.

4.2.2. The Semiconductor Tracker

The pixel detector is surrounded by the *Semiconductor tracker* (*SCT*). The active detector components of the SCT are modules that consist of pairs of single sided p–on–n type micro-strip sensors that are glued back-to-back with a relative rotation of 40 mrad. Each of these sensors has a thickness of 285 μm and contains 768 active silicon strips. The strips have a length of 12 cm and an average strip pitch of 80 μm each. Two additional strips at the edge of each sensor are inactive. The modules allow for measurements in R–ϕ with an intrinsic resolution of 17 μm. The intrinsic accuracies per module for measurements in z-direction are 580 μm in the barrel, in the end-cap disks measurements in R-direction can be performed with accuracies of 580 μm.

The four cylindrical barrels of the SCT contain 2112 modules each and cover the central detector region up to $|\eta| < 1.4$. On either side of the barrel there are nine disk layers positioned that extend the coverage to the range $|\eta| = 2.5$. These discs contain additional 1976 modules. The barrel and end-cap modules are arranged such that a particle that traverses the solid angle covered by the SCT will cross the volume of at least four module layers.

4.2.3. The Transition Radiation Tracker

The outermost component of the Inner Detector is the *Transition Radiation Tracker* (*TRT*). The active elements of the TRT are gaseous straw tubes with radii of 4 mm and lengths of 144 cm and 37 cm in the barrel and end-caps, respectively. The non-flammable gas mixture inside the tubes is based on *Xe* gas and can be ionised by electrically charged particles that traverse the tube. The charges that are freed are collected by an anode wire in the middle of each straw.

The barrel part of the TRT consists of three rings that cover the central detector region up to $|\eta| = 0.8$. The rings are built of 32 modules, that contain in between 329 and 793 straws each. In total the barrel contains 52544 straw tubes that form 73 layers. The tubes in this region are interleaved with polypropylene fibres that serve as inert material and induce the transition radiation.

Two additional sets of 12 and 8 wheels, respectively, are placed on each side of the barrel

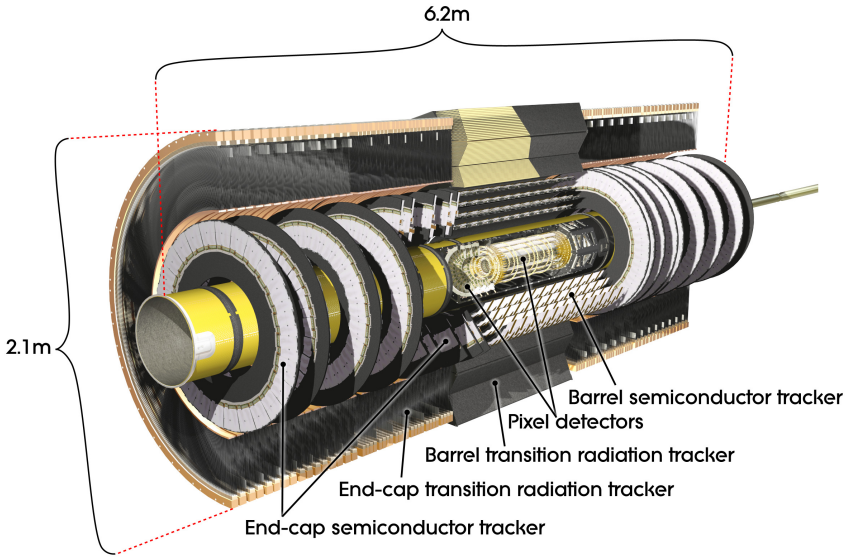

Figure 4.2.: The Inner Detector of the ATLAS experiment. The innermost subsystem is the Pixel Detector that is surrounded by the Semiconductor Tracker (SCT). The outermost layer is the Transition Radiation Tracker (TRT). Figure taken from Ref. [63].

rings and expand the coverage of the TRT to up to $|\eta| < 2.0$. Each of the wheels consists of eight layers of straw tubes which results in a total number of 122880 straws per end-cap. In this part of the TRT foils of polypropylene are placed in between the layers and serve as inactive material.

Due to its layout the barrel part of the TRT only provides information in the plane transverse to the beam axis, i.e. in R–ϕ direction. For the corresponding coordinate measurements the intrinsic accuracy is 130 μm per straw. This comparably low resolution is compensated to some degree by the fact, that each charged particle that passes the TRT volume will traverse in between 22 and 36 straw tubes.

Since the amount of transition radiation that a charged particle emits is roughly proportional to the Lorentz factor $\gamma = {}^{E}/_{mc^2}$, the amount of radiation and the number of high energetic depositions can be used to discriminate electrons from the heavier leptons and hadrons.

4.3. The Calorimeter System

The ATLAS calorimeter system is designed to measure the energy of electromagnetically and hadronically interacting particles with very high precision. In addition, all of its components

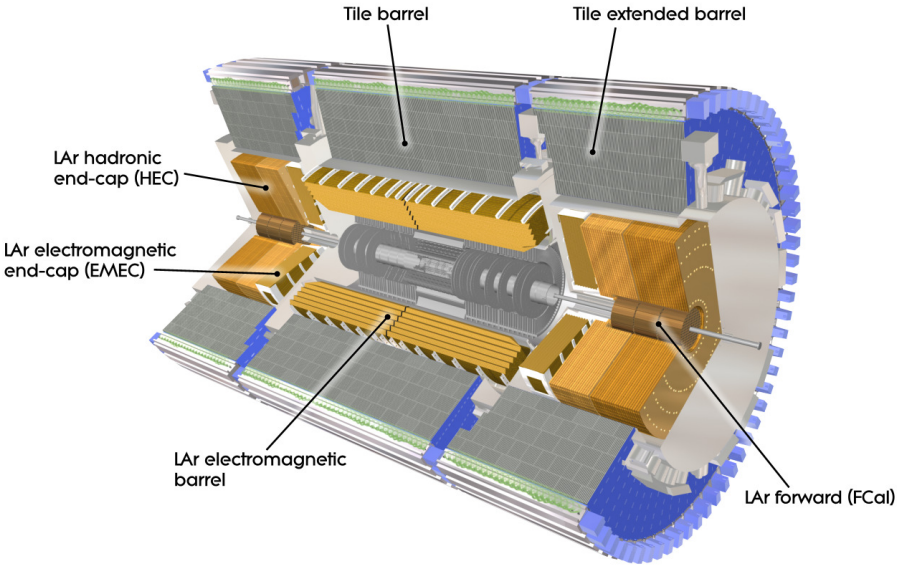

Figure 4.3.: The ATLAS calorimeter system. Figure taken from Ref. [63].

feature a high granularity. Therefore, not only the amount of energy that has been deposited can be analysed, but also the lateral and longitudinal shapes of these depositions. This information is used to distinguish particles of different type. An overview on both the electromagnetic and hadronic calorimeter components of ATLAS is shown in Fig. 4.3.

4.3.1. The Electromagnetic Calorimeter

The Inner Detector and the solenoid magnets are enclosed by the *Electromagnetic Calorimeter* (EMCal) that consists of several layers of calorimetric detector devices.

The *presampler* is the innermost calorimeter system. It consists of an active liquid-argon (LAr) layer with a thickness of 1.1 cm in the barrel and 0.5 cm in the end-caps. The barrel components cover the central region up to $|\eta| < 1.51$. This coverage is extended by the end-caps, that reach from 1.5 up to 1.8 in $|\eta|$. The presampler is used to correct for the energy that electrons and photons loose by interactions with the Inner Detector material.

In the central detector region, the presampler is surrounded by two identical half-barrels that are separated by a small gap of 4 mm at $z = 0$. They cover a range up to $|\eta| < 1.475$. The end-cap calorimeters that enclose the barrel are divided into two coaxial wheels each. The inner two wheels cover the region from 1.375 to 2.5 in $|\eta|$, the outer ones range from 2.5 to 3.2 in $|\eta|$.

All of the barrel and end-cap components consist of up to three layers of high granularity *LAr electromagnetic sampling calorimeters*. These layers are constructed in an accordion-shaped pattern to provide full coverage in ϕ-direction without azimuthal crack regions. Within this accordion structure the active LAr cells alternate with lead plates that serve as absorber material.

The first of these layers, the *first sampling*, has a very high granularity in η-direction of $\Delta\eta = 0.025$ over the whole covered range. This allows for precise position and shower shape measurements and therefore leads to a good distinction between energy depositions of electrons and photons from those of pions. The second layer, the *main sampling*, is the thickest component of the electromagnetic calorimeter. In this part of the calorimeter electromagnetically interacting particles deposit most of their energy. The third and final layer of the electromagnetic calorimeter is the *back layer* that has a coarse structure.

Detailed information on the granularities of the three layers are given in the upper part of Table 4.1.

The material distribution of the electromagnetic calorimeter in units of the radiation length X_0[1)] as a function of $|\eta|$ is shown in Fig. 4.4. Its minimal thickness is $22\,X_0$ in the barrel and $>24\,X_0$ in the end-caps and therefore any electromagnetically interacting particle will nearly loose all of its energy in this part of the calorimeter.

The intrinsic resolution of energy measurements with the electromagnetic calorimeter was measured using electron, photon and pion beams [66, 67]. The measured resolution is

$$\frac{\sigma(E)}{E} = \frac{a}{\sqrt{E}} \oplus b, \quad \text{with} \begin{cases} a = 10\%\,,\ b = 0.2\% & (\text{barrel}), \\ a = 10.0 - 12.5\%\,,\ b = 0.6\% & (\text{end}-\text{caps}). \end{cases} \tag{4.1}$$

4.3.2. The Hadronic Calorimeter

The hadronic *Tile Calorimeter* (TileCal) is wrapped around the electromagnetic calorimeter. It consists of a large center barrel reaching up to $|\eta| < 1.0$ and two smaller cylinders on each side of the barrel that cover the range $0.8 < |\eta| < 1.7$. Each of these components is divided azimuthally into 64 modules that are built of steel layers (absorber material) and polystyrene scintillating tiles (active material).

The intermediate $|\eta|$ range in between 1.5 and 3.2 is covered by the *Hadronic End-cap Calorimeter* (HEC). The HEC consists of two wheels on each side of the barrel that are lo-

[1]The radiation length is the mean distance at which an electron has lost all but $1/e$ of its energy due to bremsstrahlung.

Electromagnetic Calorimeter				
	Barrel		End-cap	
	$\Delta\eta \times \Delta\phi$	$\lvert\eta\rvert$ Coverage	$\Delta\eta \times \Delta\phi$	$\lvert\eta\rvert$ Coverage
Presampler	0.025×0.1	$\lvert\eta\rvert < 1.52$	0.025×0.1	$1.5 < \lvert\eta\rvert < 1.8$
1st Layer	$0.025/8 \times 0.1$	$\lvert\eta\rvert < 1.4$	0.050×0.1	$1.375 < \lvert\eta\rvert < 1.425$
	0.025×0.025	$1.4 < \lvert\eta\rvert < 1.475$	0.025×0.1	$1.425 < \lvert\eta\rvert < 1.5$
			$0.025/8 \times 0.1$	$1.5 < \lvert\eta\rvert < 1.8$
			$0.025/6 \times 0.1$	$1.8 < \lvert\eta\rvert < 2.0$
			$0.025/4 \times 0.1$	$2.0 < \lvert\eta\rvert < 2.4$
			0.025×0.1	$2.4 < \lvert\eta\rvert < 2.5$
			0.1×0.1	$2.5 < \lvert\eta\rvert < 3.2$
2nd Layer	0.025×0.025	$\lvert\eta\rvert < 1.40$	0.050×0.025	$1.375 < \lvert\eta\rvert < 1.425$
	0.075×0.025	$1.40 < \lvert\eta\rvert < 1.475$	0.025×0.025	$1.425 < \lvert\eta\rvert < 2.500$
			0.1×0.1	$2.5 < \lvert\eta\rvert < 3.2$
3rd Layer	0.050×0.025	$\lvert\eta\rvert < 1.35$	0.050×0.025	$1.5 < \lvert\eta\rvert < 2.5$

Hadronic Calorimeter				
	Barrel		End-cap / Extended Barrel	
	$\Delta\eta \times \Delta\phi$	$\lvert\eta\rvert$ Coverage	$\Delta\eta \times \Delta\phi$	$\lvert\eta\rvert$ Coverage
HEC			0.1×0.1	$1.5 < \lvert\eta\rvert < 2.5$
			0.2×0.2	$2.5 < \lvert\eta\rvert < 3.2$
TileCal	0.1×0.1	$\lvert\eta\rvert < 1.0$	0.1×0.1	$0.8 < \lvert\eta\rvert < 1.7$
(Last Layer)	0.2×0.1	$\lvert\eta\rvert < 1.0$	0.2×0.1	$0.8 < \lvert\eta\rvert < 1.7$
			$\Delta x \times \Delta y$ [cm]	$\lvert\eta\rvert$ Coverage
FCal 1			3.0×2.6	$3.15 < \lvert\eta\rvert < 4.30$
			$\approx \times 4$ finer	$3.10 < \lvert\eta\rvert < 3.15$
			$\approx \times 4$ finer	$4.30 < \lvert\eta\rvert < 4.83$
FCal 2			3.3×4.2	$3.24 < \lvert\eta\rvert < 4.50$
			$\approx \times 4$ finer	$3.20 < \lvert\eta\rvert < 3.24$
			$\approx \times 4$ finer	$4.50 < \lvert\eta\rvert < 4.81$
FCal 3			5.4×4.7	$3.32 < \lvert\eta\rvert < 4.60$
			$\approx \times 4$ finer	$3.29 < \lvert\eta\rvert < 3.32$
			$\approx \times 4$ finer	$4.60 < \lvert\eta\rvert < 4.75$

Table 4.1.: Granularity and coverage of the electromagnetic and hadronic calorimeter components [63].

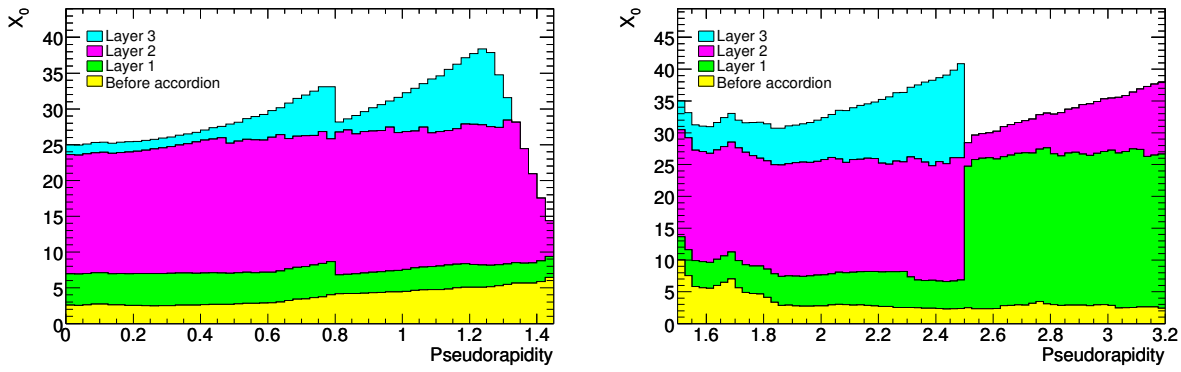

(a) Barrel

(b) End-caps

Figure 4.4.: Thickness of the electromagnetic calorimeter layers and the amount of material in front of the calorimeter in the barrel region (a) and the end-cap region (b). All values are given in units of the radiation length X_0. Figures taken from Ref. [63].

cated behind the electromagnetic calorimeter end-caps. Each wheel is further divided into two segments in depth which results in a total of four layers per end-cap. The wheels consist of parallel copper plates that are interleaved with liquid-argon gaps.

The larger discs of the HEC surround the smaller discs of the *Forward Calorimeter* (FCal). The FCal consists of three modules per end-cap and covers the range $3.1 < |\eta| < 4.9$. The first module is made of copper and is mainly used to measure electromagnetic energy deposits. The other two modules are made of tungsten and predominantly measure the energy deposits of hadronically interacting particles.

The granularities of the individual hadronic calorimeter components are listed in the lower part of Table 4.1.

The energy resolutions of the individual components have been measured using a pion test beam [63]. These measurements show an energy resolution for charged pions of

$$\frac{\sigma(E)}{E} = \frac{a}{\sqrt{E}} \oplus b, \quad \text{with} \begin{cases} a = 52\% \,,\; b = 3\% & \text{(EMCal and TileCal)}, \\ a = 71\% \,,\; b = 5.8\% & \text{(HEC)}, \\ a = 94\% \,,\; b = 7.5\% & \text{(FCal)}. \end{cases} \tag{4.2}$$

The thickness of the hadronic calorimeter components in units of the interaction length λ[2] is

[2] One interaction length is defined as the mean distance that a number of relativistic charged hadrons can pass in a certain material until their number is reduced by the factor 1/e due to inelastic hadronic interactions.

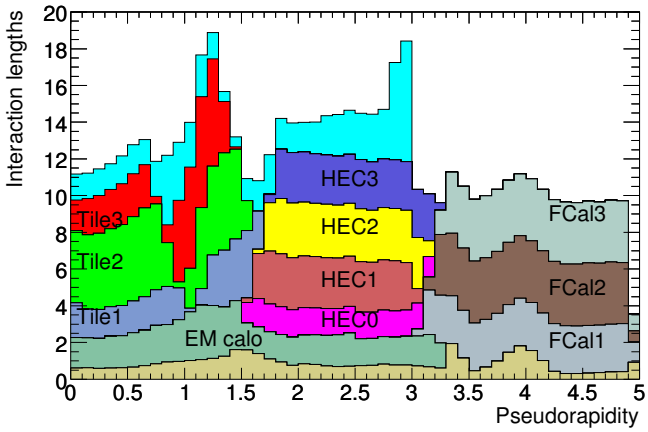

Figure 4.5.: Material budget of the different ATLAS calorimeter systems and the material in front of the calorimeters. All values are given in units of the interaction length λ. In addition the total amount of material in front of the first active Muon Spectrometer layer is shown up to $|\eta| = 3.0$ (cyan). Figure taken from Ref. [63].

shown in Fig. 4.5 as a function of $|\eta|$. Given the large amount of material, nearly any strongly interacting particle, even such with high energies, looses its complete energy in this part of the detector.

4.4. The Muon Spectrometer and the Toroid Magnets

The *Muon Spectrometer* is designed to detect charged particles that traverse the Inner Detector and the calorimeter systems without being absorbed and to measure their momenta. Except for rare cases of particle *punch throughs* these are mainly muons. An overview of the muon detector system is shown in Fig. 4.6.

The performance goal of the Muon Spectrometer is to achieve transverse momentum resolutions of $\sigma_{p_T}/p_T = 10\%$ for muons with transverse momenta of $p_T = 1$ TeV [64]. The magnetic field that is required for these momentum measurements is provided by eight large air-core toroid magnets in the barrel region that are positioned radially and symmetrically around the beam axis. The coils have a length of 25.3 m and inner and outer diameters of 9.4 m and 20.1 m, respectively. Two additional end-cap toroid magnets consist of eight coils with an axial length of 5 m each and a radial extension of 1.65 – 10.7 m. The field strength created by the toroid system varies from 0.15 T to 2.5 T in the barrel region, depending on the radius R and azimuthal angle ϕ. In the

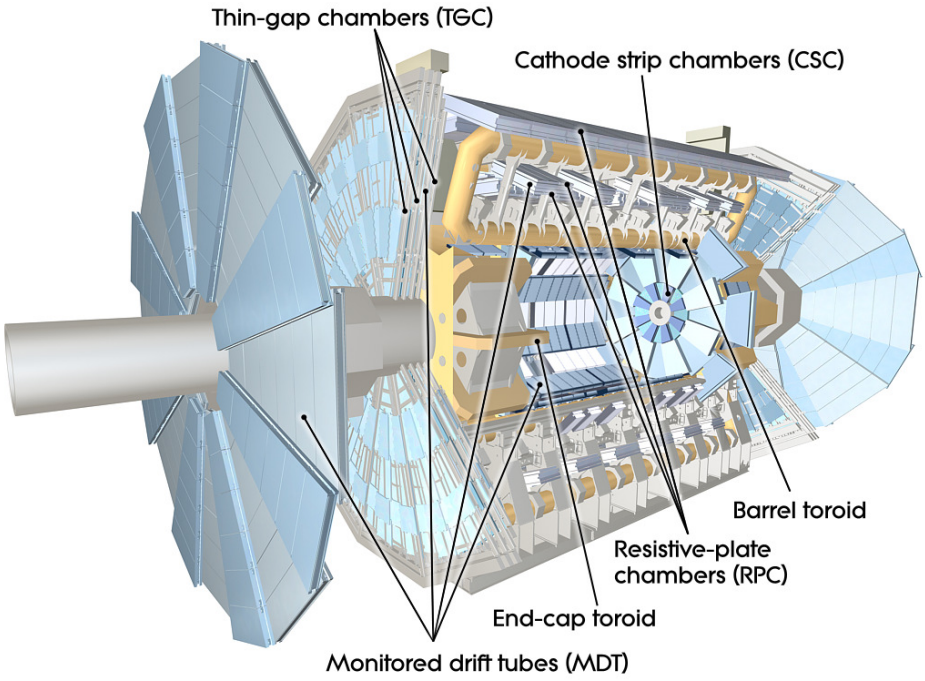

Figure 4.6.: The muon detector system of the ATLAS detector. Figure taken from Ref. [63].

end-cap region the field strength ranges from 0.2 T to 3.5 T.

The central region of the Muon Spectrometer consists of three cylindrical layers of tracking chambers of several different types that are located in between and on top of the eight toroid magnet coils. These layers with radii of approximately 5 m, 7.5 m and 10 m provide the information to precisely reconstruct the trajectories of electrically charged particles and to measure their momenta. Each of the layers consists of sixteen chambers.

The two end-cap muon chamber layers are constructed as four large wheels perpendicular to the z-axis that are positioned in front and behind the two end-cap toroid magnets. They are located at distances of $|z| \approx$7.4 m, 10.8 m, 14 m and 21.5 m from the interaction point, respectively.

The high-precision momentum measurement in this detector system is performed by *Monitored Drift Tube chambers* (MDT). They consist of three to eight layers of pressurised drift tubes with diameters of 30 cm. The chambers cover a range up to $\eta < 2.7$, except for the innermost layer in the forward region. In this region, for $2 < |\eta| < 2.7$ and close to the interaction point, the expected counting rates are beyond the limits for a safe operation of the MDTs. Therefore,

in this area the MDTs are replaced by *Cathode-Strip Chambers* (CSC). The CSCs are multi-wire proportional chambers that measure the coordinates of a trajectory from the charges induced on the cathode strips.

In addition to measuring the momenta of charged particles, the Muon Spectrometer is designed to provide fast information on the multiplicity of muon tracks and their approximate energy range. These properties are measured by *trigger chambers* that cover the whole range in $|\eta|$ up to 2.4 and the full ϕ range. In the barrel region up to $\eta < 1.05$ the trigger chambers consist of three layers of *Resistive Plate Chambers* (RPCs). These RPCs are built of two resistive plates that are placed in parallel to each other at a distance of 2 mm. Ionising particles that pass the gas in between the plates will free electric charge, that, due to the high electric field strength in between the plates, is amplified before it is collected. The muon trigger system that is used in the end-cap for the range $1.05 < |\eta| < 2.4$ consists of four layers of *Thin Gap Chambers* (TGC). TGCs are multi-wire proportional chambers that provide good time resolution and are capable of working at high event rates. In addition to their trigger capability, they are used to determine the azimuthal coordinate of charged particle tracks which complements the measurement of the MDTs in radial direction.

4.5. The Trigger System

At instantaneous luminosities of $10^{34}\,\mathrm{cm}^{-2}\mathrm{s}^{-1}$ that the LHC has been designed for, p–p interactions will occur at a rate of approximately 1 GHz. Recording every of these interaction events is technically not possible and, in addition, would result in uncontrollable amounts of data. Furthermore, most p–p collision events involve only low momentum transfers and hence are not relevant for the physics program of the ATLAS experiment. For these reasons a *three stage trigger system* has been developed to filter out the potentially relevant interaction processes. The three stages of this system are denoted as *Level 1* (L1), *Level 2* (L2) and *Level 3* or *Event Filter* (L3, EF). They are configured such that the rate at which the interactions are finally recorded is about 200 Hz. This rate is sufficient low for the ATLAS read-out and storage system to record the full event information.

Due to the high initial interaction rate, the L1 trigger system must be implemented at hardware level. To reduce the readout time required to gather the relevant information from the detector elements and to minimise the event processing time, only a subset of the ATLAS detector systems is used at this trigger stage. The components of the Inner Detector are not read out. The calorimeters, however, are used with reduced granularity to reconstruct energy depositions and

shower properties of hadronically and electromagnetically interacting particles. Muon candidates are identified using the trigger chambers of the Muon Spectrometer, namely the RPCs and TGCs. Based on these information events are pre-filtered that contain particular signatures, like large missing or total transverse energy or particles like muons, electrons, photons, jets or τ leptons with large transverse momenta. For those events that contain such features one or more *Regions of Interest* (RoIs) are defined. These contain η- and ϕ-coordinates and potential additional information about interesting properties of each event. The RoIs are further analysed by the *Central Trigger Processor* (CTP) and a final L1 trigger decision is made. The pre-selection of events based on the L1 trigger decision reduces the event rate to approximately 75 kHz.

Events passing the L1 trigger requirements are further processed by the L2 and L3 trigger stages, that are summarised as the *High-Level Trigger system* (HLT). The L2 trigger is seeded by the RoIs and further improves the identification quality of event and particle properties. It refines the event information stored in a RoI by acquiring additional information from the detector components, this time using the full granularity of the calorimeters within the regions defined in the RoI. The decisions based on this information reduce the event rate to below 3.5 kHz. The final decision, if an event is to be recorded, is made by the event filter (EF). At this trigger stage offline algorithms are used to analyse the information from the calorimeter using its full granularity, the muon detector systems and the complete Inner Detector to fully reconstruct an interaction event. According to the decisions made by the EF trigger system the event rate is reduced to approximately 200 Hz, at which the events are finally recorded.
The work flow of the trigger system is summarised in Fig. 4.7.

4.6. Forward Detectors and Luminosity Measurements

The luminosity measurements for the ATLAS experiment are performed by additional detectors. These are placed at large distances to the interaction point and very close to the beam axis in order to measure event activities in the very forward directions.
The measured integrated luminosity delivered by the LHC and recorded with the ATLAS detector is shown on the left-hand side in Fig. 4.8. The same figure also shows the measured peak luminosities on the right.

4.6.1. The LUCID Detectors

The relative and absolute luminosity measurement is primarily performed by Cherenkov detectors denoted as *"Luminosity Measurement using Cherenkov Integrating Detector"* (*LUCID*). The

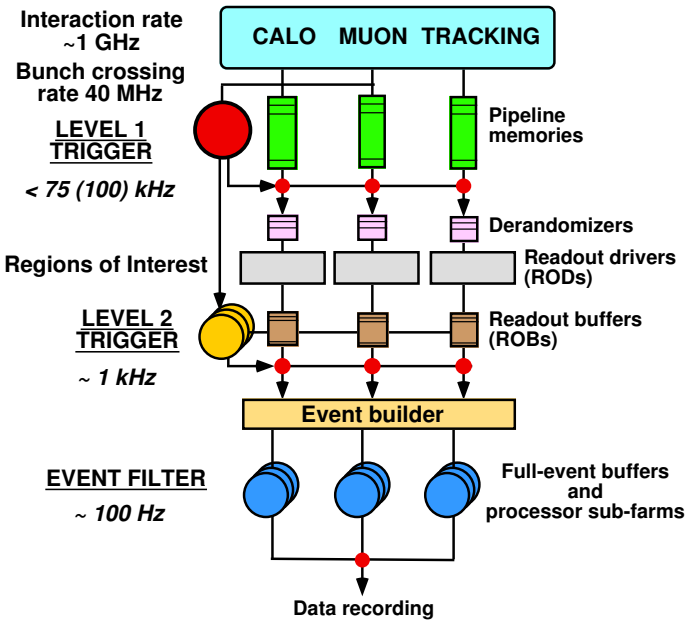

Figure 4.7.: The ATLAS trigger chain. Figure taken from [64].

two LUCID detectors are located at a distance of $|z| = 17\,\text{m}$ to the interaction point and consist of an array of twenty Cherenkov tubes each. These tubes are gas filled aluminium vessels with photo-multiplier tubes. By analysing the pulse-height of the tube signals the number of particles that pass a LUCID detector can be computed at each bunch crossing. Since this number is proportional to the number of p–p interactions that took place in a bunch crossing the instantaneous luminosity can be determined. Even a simpler method, the counting of tubes measuring a signal above a certain threshold, can be used to determine the luminosity with acceptable uncertainties.

4.6.2. The ZDC Detector

Two *Zero-Degree Calorimeters* (ZDC) are located at a distance of $|z| \approx 140\,\text{m}$ to each side of the interaction point. These tungsten-quartz sampling calorimeters are designed to detect neutral particles at a polar angle of $\approx 0^\circ$. Hence, they measure the production rate of such particles in forward direction which can also be used to determine the luminosity.

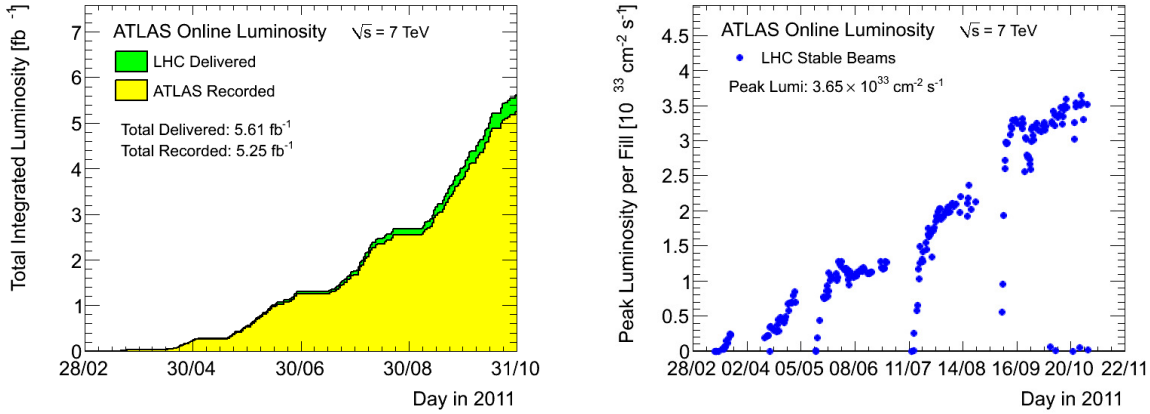

Figure 4.8.: The total integrated luminosity (left) delivered by the LHC (green area) and recorded by the ATLAS experiment (yellow area) in 2011 and the peak instantaneous luminosity per day (right) during the same data taking period. The figures are taken from [68].

4.6.3. The ALFA Detectors

In addition to the measurements with the LUCID detectors, the absolute luminosity is measured with the *Absolute Luminosity For ATLAS detectors* (ALFA). The ALFA detectors are scintillating fibre tracking devices that detect elastically scattered protons. The underlying concept of the luminosity measurement using ALFA is that the total p–p interaction cross section and the elastic-scattering amplitude in forward direction are connected by the optical theorem. Since this theorem is only valid at very small angles, the ALFA detectors are located at distances of $|z| \approx 240\,\text{m}$ from the interaction point and very close to the beam axis. This allows for measurements at angles towards the beam axis down to $3\,\mu\text{rad}$.

4.7. Official ATLAS Software

This section provides a short overview on programs and tools that were used to derive the results presented in this thesis.

The ATHENA Framework

The interpretation of the detector response as physics objects and event properties is implemented in several algorithms, that will be described in Chapter 6. All those algorithms are contained in

a single framework, denoted as *ATHENA* [69], that is written and maintained by the ATLAS collaboration using the *C++* programming language. In addition to reconstruction and identification algorithms, ATHENA contains several Monte Carlo event generators to simulate all those physics processes that are relevant for p–p collisions, a detector simulation to imitate the ATLAS detector response to those simulated interactions and many more programs. Furthermore, a data model has been developed to store the simulated or recorded event information and to store reconstructed objects and event properties. Hence, this framework contains many different and complex tools, and therefore an easy but powerful configuration method needed to be implemented. In ATHENA scripts written in the *Python* programming language are used to configure, activate or deactivate the different programs contained in ATHENA.

Detector Simulation based on GEANT

The ATLAS detector simulation is based on the *GEANT* program [70], that simulates the transition of particles through matter. Every component of the ATLAS detector is modelled using this program, accurately describing the geometry and material properties of the real detector [71]. However, the positions of individual elements are misaligned to reflect the limited knowledge about the corresponding positions in the real detector (*misalignment*). Using this detector model GEANT simulates the traversion of all particles produced in a simulated p–p collision through the detector volume. This is done from the inside of the detector to the outside, taking into account the geometry of the individual detector components, the interaction of the particles with the detector material and effects originating from the magnetic fields. The response of the active detector elements to the traversing particles is simulated in this process and stored like it was data from real physics collisions.

The ROOT Framework

Based on the physics objects and event properties that were reconstructed for an event, a final interpretation of this event as a certain physics process and the selection of particular processes can be attempted. This is implemented in dedicated analysis algorithms, that also can be incorporated into the ATHENA framework. In that case, an analysis may use all the tools included in the ATHENA framework and the full event information provided by its data model. Most of these tools and programs, however, are not required at this final stage of the event analysis. Furthermore, the high complexity of the ATLAS data model adds no benefit for most analyses and in addition increases the event processing time. A common approach is hence to use a simpler data model and less tools to analyse the data, of which all are provided by the *ROOT* frame-

work [72]. This object oriented framework is also written in the *C++* programming language and has originally been developed by R. Brun and F. Rademakers. The purpose of ROOT is to provide mathematical algorithms and small data structures relevant for the analysis of physics data.

A simulated p–p collision event

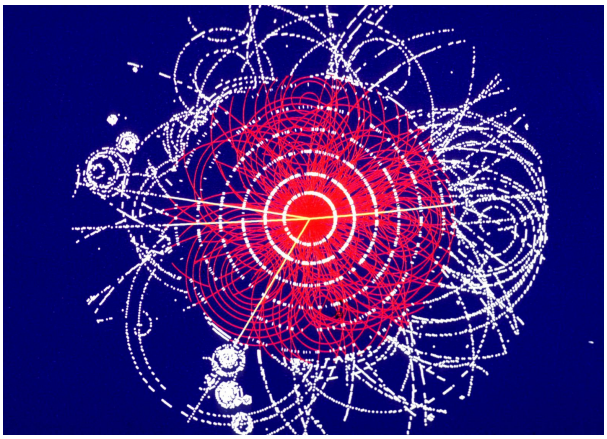

Chapter 5

Simulation of Hadron Collisions

The analysis of *simulated p–p collisions* is essential for the complete understanding of real physics collisions data. Such studies are necessary to develop analysis and event reconstruction strategies. In addition, the properties of real collision data can be compared to the expectations.

The simulation of p–p collisions implies that all relevant processes that might occur in these collisions need to be simulated accurately. This is done by *Monte Carlo* (MC) *event generators*. Using these programs a statistically sufficient amount of *events* is produced for each process. An event is a collection of four-momenta for all the final state particles that are produced in the interaction. The events are passed to the detector simulation, that is described in Section 4.7, to mimic the response of the detector to the final state particles. The event samples, one for each process, are combined according to the individual cross sections. The resulting combination of events is a statistically representative sample of simulated p–p collisions.

Event Generation

The simulation of events for a particular p–p interaction process is performed by Monte Carlo (MC) event generators. These programs start with the computation of the hard scattering process. The kinematics of the colliding partons are selected by sampling the PDF set of the protons at the energy scale of the hard interaction. The properties of the final state particles, like their

momenta and spin configurations, are determined according to probabilities that are derived from the matrix element calculations using the full Lagrangian of the theory. Hence, the precision of such simulations depends on the order in perturbation theory that the calculation in use has been performed. Additional initial and final state radiation and the hadronisation of partons cannot be treated by the matrix element calculations, as already stated in Section 2.3.4. Therefore, these two processes are treated by separate algorithms or programs.

The hadronisation of partons is usually simulated by algorithms that implement either the string or the cluster model that were described in Section 2.3.4.

Initial and final state radiation are modeled by *parton showering* algorithms. These implement the iterative splitting procedure of partons that is described in Section 2.3.4 to produce the final state parton jets. The cut-off scale, at which the splitting of the partons is terminated, depends on the implementation of the algorithm and is of the order of 1 GeV. However, certain processes and phase space regions might be overemphasised due to the splitting procedure. This occurs if the splitting of a parton results in two partons that are far separated. In that case the simulation of a process containing n final state parton jets results in an event containing $n+1$ of those jets. But such events are usually covered by the explicit simulation of events containing $n+1$ final state partons, using the full matrix element calculations. To avoid this double counting of processes and the resulting double-counting in certain phase space regions several *matching schemes* have been developed [73]. These matching schemes define a quantity Q for the final state partons, like an angle in between them, and a corresponding cut-off value $\hat{Q}$. This cut-off value splits the available phase space into two parts, of which one is assigned to the matrix element calculation ($Q > \hat{Q}$) and the other to the parton showering process ($Q < \hat{Q}$). If a parton splitting results in two far separated partons satisfying $Q > \hat{Q}$ the event with originally n parton jets by definition turns into an event with $n+1$ parton jets. Therefore this event is discarded. If the splitting results in two partons satisfying $Q < \hat{Q}$ the event topology is preserved and the event is retained. The same statements hold for events that are generated using the matrix element calculation, but with inverted logic regarding the rejection of events. Hence, the quantity Q and its cut-off value determine, if an event with particular kinematics for the final state partons is covered by the matrix element calculation or the parton showering procedure.

The treatment of parton radiation using the showering approach can be directly applied to the emission of partons in the final state. Starting from the energy scale of the hard interaction, the primary parton and all partons produced by the splitting loose their energy down to a cut-off scale. However, for the description of initial state radiation this procedure cannot be applied directly, because for the incoming primary partons the final momenta at the end of the parton

shower are already determined by the matrix element calculation. Therefore, the evolution must be applied in reverse direction in time and energy scale, which is known as the *backwards evolution* approach [74]. The momentum fractions of the incoming partons participating at the hard interaction are chosen according to the PDF set at the energy scale of the hard process. The evolution of the showering starts at the same energy scale and is propagated backwards. Hence, at each splitting the parton gains energy. Constraints on this reverse evolution are given by the requirement of momentum and energy conservation taking into account the energy scale of the hard scattering subprocess and the center-of-mass energy of the proton collisions.

The decays of unstable particles are usually treated with simple probabilistic approaches. However, for a detailed description of particular decays, like those of τ leptons, this approach is not sufficient. In such cases they can be simulated by dedicated programs that take into account the matrix element of the particular decays and spin correlations among the final state particles [75, 76].

Since only the hard interaction is simulated by a Monte Carlo event generator, the simulated events are enveloped in a very clean environment. At realistic data taking conditions, however, the hard interaction is accompanied by the underlying event and several pile-up events. The underlying event activity is therefore simulated with separate algorithms and programs, like PYTHIA or JIMMY [32, 33]. To account for additional pile-up events, several minimum bias events are simulated and the resulting final state particles are added on top of the event record of the hard interaction [32]. As the data taking conditions and therefore the average number of pile-up interactions per bunch crossing might change with time, the complete sample of simulated events is usually re-weighted to match the distribution of this quantity in data.

Monte Carlo Event Generators in Use

The Monte Carlo generators used to simulate the production of the neutral MSSM Higgs bosons in the gluon-fusion and the b-quark associated production processes are POWHEG [77] and Sherpa [78], respectively.

The production of W and Z/γ^* bosons in association with jets is simulated using the AlpGen [79] event generator, that calculates the hard scattering process with leading-order matrix elements for up to five additional jets. The MC@NLO [80] event generator is used to simulate the $t\bar{t}$ production process, electroweak di-boson samples, i.e. WW, WZ and ZZ production, and the Single-top production through the s- and t-channel and in association with W bosons. The loop-induced $gg \to WW$ processes are generated using gg2WW [81].

To simulate parton showers and the hadronisation of quarks the AlpGen and MC@NLO generators are interfaced with the HERWIG [82] program. Furthermore the activity of the underlying event is simulated using JIMMY [33].

All of the above Monte Carlo event generators implement either the MLM matching [73] or the CKKW matching [83] between the parton showers and the hard interaction process. The PDF sets that are used for the event generation are provided by the *CTEQ*[1)] collaboration. MC@NLO uses the PDF set named CT10 [84], AlpGen and Sherpa use the set CTEQ6L1 [85].

The decay of τ leptons is usually simulated using the TAUOLA program [76]. Only the Sherpa event generator incorporates its own program HADRONS++ to accurately treat the τ lepton decays. The programs PHOTOS [75] and PHOTONS++, of which the latter is part of the Sherpa event generator, add QED radiation to hadron and τ lepton decays.

Signal Modelling

In Chapter 7 a search for the neutral Higgs bosons of the MSSM is presented. This search assumes masses, decay widths and branching ratios for h, A and H according to the m_h^{max} benchmark scenario. The listed properties are computed using the program FeynHiggs [86]. The calculation employed the coupling constants, parton distribution functions and scale choices as proposed in Ref. [44].

Depending on the remaining free MSSM parameters m_A and $\tan\beta$ any signal distribution is a compositions of three distributions, one for each of the bosons h, A and H. However, signal events are not simulated for all three Higgs bosons as their properties are very similar and do not affect the search for the final states considered here. In addition, event and detector simulation are very time expensive and result in large data sets. For these reasons only event samples for the production of the *CP*–odd Higgs boson A have been simulated and the same samples are employed for the modelling of H and h production. Hence, any possible spin correlation of the decay products due to the different *CP* quantum numbers of the Higgs bosons are neglected. These effects are expected to be small.

The Higgs boson production modes considered are the gluon-fusion mode and the b-quark associated production. Samples for the production of A in these modes are generated for several masses m_A in the range of 90 GeV to 500 GeV and for $\tan\beta = 20$. For each point in the $(m_A, \tan\beta)$ grid the three samples for h, A and H are added according to their masses and production cross sections. The cross sections have been calculated using HIGLU [87], ggh@nnlo [88] for the gluon-fusion process and the *Santander matching scheme* [89] for the b-quark associated

[1] Coordinated Theoretical-Experimental Project on QCD

production process, which combines the four-flavour and five-flavour calculations presented in Refs. [90, 91] and Ref. [92], respectively. Since only samples for a discrete selection of masses could be simulated, the simulated samples with m_A closest to the computed masses m_H and m_h are used for the modelling of H and h, respectively.

The simulation of the A boson production has been performed only for the one value of $\tan\beta = 20$ and hence the increase of the natural widths of h, A and H with $\tan\beta$ is not taken into account. This increase, however, is of the order of 1 GeV in the relevant $\tan\beta$ range and much lower than the experimental resolution of the Higgs boson mass, which is of the order 10 GeV and above for the final state considered here. Therefore, the increase of the natural width with $\tan\beta$ can be neglected in this search.

Energy clusters reconstructed with the anti-k_t algorithm

(Image taken from Ref. [93])

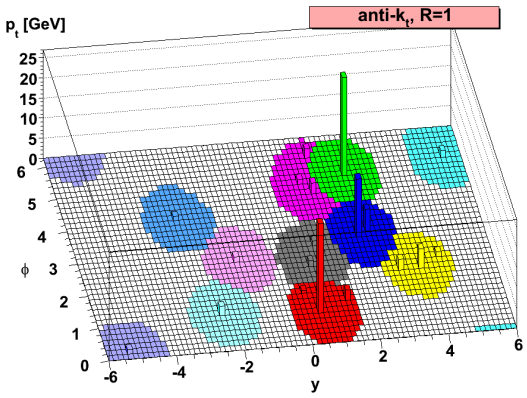

Chapter 6

Event Reconstruction and Particle Identification

The data analysed – either the simulated data or the data recorded with the ATLAS detector – are raw signals originating from the detector response to traversing particles. The interpretation of these signals as particles and event properties is performed with the help of several algorithms. Each of them combines the signals delivered by several detector components to either reconstruct and identify certain particle types or to reconstruct important event properties. The reconstructed particles and properties are the essential information required to identify the underlying physics process of a p–p collision.

The following sections introduce the particles and event properties that are important for the search for the neutral Higgs bosons of the MSSM in the $\tau^+\tau^-$ decay mode and summarise the techniques to reconstruct and identify them.

Comparison of Objects in Simulated Events and Data

The description of p–p collision data heavily depends on the simulation of the individual ATLAS detector components and their response to interacting particles. This simulation, however, cannot be perfect since the exact position and orientation of the detector parts, their relative *alignment*,

is only known to limited precision. In addition, the detector noise and the response of the active detector elements cannot be simulated perfectly. Therefore, the reconstruction and identification efficiencies for several objects as well as reconstructed energies and momenta differ slightly in simulated and real collision data. To account for these differences, corrections have been derived by comparing object and event properties in simulated events to those in real data for processes that are easy to identify and to select in data. Further details on the corrections for the individual objects will be given in the corresponding sections.

In the search presented here, these corrections are applied to all processes that are estimated using Monte Carlo predictions.

6.1. Reconstruction of Tracks

The reconstruction of tracks of electrically charged particles is a basic ingredient for the more sophisticated particle and event reconstruction techniques. Given the Inner Detector geometry, the track reconstruction is limited to the pseudorapidity range $|\eta| < 2.5$.

An *inside-outside technique* is used to combine the individual signals in the Inner Detector components, denoted as *hits* in the following, to form a combined particle track [94]. Each track is initially seeded by a group of three adjoining hits in the silicon detectors. By moving away from the interaction point, further hits that might be caused by the same charged particle are subsequently added to the track. The compatibility of the hits with the existing track is evaluated using a combinatorial Kalman filter. From the resulting silicon detector tracks those with reconstructed transverse momenta below 400 MeV are discarded. All other tracks are extended into the TRT and additional hits reconstructed from the measured timing information are assigned to them. Finally, the resulting extended tracks are refitted using the full information from all the tracking systems. This inside-outside approach is very efficient in reconstructing tracks caused by particles that are produced close to the beam spot [94].

The complementary *back-tracking* technique is used to reconstruct additional tracks of charged particles mainly produced at some distance to the interaction point [94]. These tracks are seeded by track segments reconstructed in the TRT. They are extended by moving towards the interaction point and adding hits from the silicon detectors. If no additional hits in the silicon detector can be assigned, a track is reconstructed as a so-called TRT-standalone track.

6.2. Vertex Reconstruction

The common origin of particles produced in the same p–p interaction is denoted as the *interaction vertex*. Vertices can be reconstructed by grouping the tracks of those electrically charged particles that might have been produced in the same interaction. The vertex coordinates in the x- and y-directions can be determined very precisely as these coordinates are constrained by the very small beam spread in these directions. In z-direction, however, the beam spot expansion is much larger and therefore the determination of this coordinate is more challenging.

The detailed procedure of the vertex reconstruction in the ATLAS experiment is described in Ref. [95]. Initially, all reconstructed tracks satisfying certain quality criteria are extrapolated towards the beam line. The global maximum in the distribution of their z-coordinates at the point of closest approach to the nominal interaction point is used as a vertex seed. Based on this seed all vertices are reconstructed using an iterative approach. In each iteration step a χ^2 fit is performed using the seed coordinates and all near-by tracks to determine the vertex position and to check the compatibility of the tracks with the vertex position. In this fit a three-dimensional constraint is given by the beam spot position. Those tracks for which the fit yields $\chi^2 < 49$ are considered to be compatible with the seed and hence are associated to that vertex. The remaining tracks are used to seed a new vertex. The above procedure is repeated until no additional vertices are found. From the thus reconstructed vertices those are discarded that have been assigned only one charged particle track.

As a consequence of the large amount of pile-up events produced under nominal data taking conditions at the LHC, a large number of vertices are reconstructed in each recorded event. However, only the position of the hard interaction process, involving large momenta and energy transfers, is of interest. This vertex is denoted as the *primary interaction vertex* in the following. A quantity to distinguish it from vertices involving low momenta transfers is the sum of squared momenta of all associated tracks, $\sum p_T^2$. The primary vertex is defined as the vertex for which this sum is largest.

Given the coordinates of the primary vertex, the *impact parameter* of a track can be computed. The impact parameter is defined as the minimum distance of the primary vertex to the trajectory of the track that has been extrapolated towards the beam spot. For particles directly produced in the hard interaction process this distance is expected to be low. Such particles can be separated from those produced in decays of long-lived particles, for example, and therefore have larger impact parameters. The *transverse impact parameter* of a track is defined as the minimum distance of the primary vertex to the extrapolated track in the plane transverse to the beam axis. The z-coordinate of the track at this point of closest approach is referred to as the *longitudinal*

impact parameter. The *significance* of an impact parameter is defined as the ratio of the impact parameter to its estimated error.
The impact parameter of a track and its significance are important quantities used by several of the more sophisticated particle reconstruction techniques.

6.3. Electrons and Photons

The reconstruction and identification of electrons and photons is mainly based on the analysis of their energy depositions in the electromagnetic calorimeter. These depositions are reconstructed as *energy clusters*, groups of close-by calorimeter cells which contain a certain minimum amount of energy. Additionally, for electrons traversing the central detector region ($|\eta| < 2.5$), a track reconstructed in the Inner Detector is expected to match the cluster position. Details about the electron and photon identification procedure can be found in Ref. [96].

Energy clusters in the central detector region ($|\eta| < 2.47$) are reconstructed using a *sliding window algorithm*. This algorithm positions a rectangular area of fixed size inside the middle layer of the electromagnetic calorimeter in such a way that the energy contained inside the area is maximised. The individual depositions inside this window with energies above a certain threshold are grouped to form a cluster. All clusters with total transverse energy above 2.5 GeV are further considered as electron or photon candidates.

Electron candidates are taken to be those clusters for which a track in the Inner Detector ($|\eta| < 2.5$) is found to be compatible with the cluster position. The tracks taken into account must not be matched to a conversion process $\gamma^* \to e^+e^-$. The compatibility criteria are defined using the geometrical distance of the cluster position and the impact point of the track when extrapolated to the middle layer of the calorimeter. In this extrapolation a possible loss of energy due to bremsstrahlung and hence a possible change in the direction of the electron is taken into account. The maximum allowed distance in η-direction is $\Delta\eta = 0.05$. In azimuthal direction the maximum distance $\Delta\phi$ of track and cluster must not exceed 0.1 on the side where the track bends due to the Inner Detector magnetic field, and 0.05 on the opposite side. An additional requirement on the ratio of cluster energy to track momentum of $E/p < 10$ rejects heavier hadrons reconstructed as electron candidates. If no track can be found that satisfies the above criteria the cluster is considered a photon candidate.

After matching the tracks to the clusters, the latter are refined using larger window sizes. The resulting energies of the electron and photon candidates are re-computed taking into account the estimated loss of energy in the material in front and beyond the electromagnetic calorimeter,

the measured energy of the reconstructed cluster and an estimate of the energy that has been deposited outside the cluster. This calibration procedure takes only the energy depositions and the properties of the electromagnetic calorimeter into account. Therefore, it is denoted as a calibration at the *electromagnetic energy scale* (*EM scale*). The calibration corrections have been derived from electron test-beam measurements using detector components of the electromagnetic calorimeter barrel [66, 97–99]. The four-momenta of central electrons are defined using the energy computed for the calibrated cluster and the direction of the associated track.
The energy scale and resolution of electrons were measured in $Z/\gamma^* \to e^+e^-$ and ${}^{J}/_{\psi} \to e^+e^-$ events selected from the data [96]. As the masses and widths of the Z boson and the ${}^{J}/_{\psi}$ particle are well known, these measurements were used to improve the knowledge of the energy scale and resolution of electrons. Correction factors for both quantities as well as the corresponding uncertainties were derived from the measurements. Typical corrections to the energy scale of simulated electrons reconstructed within the central detector region ($|\eta|<2.5$) are of the order of $(\pm)1-4\%$ [96]. The smearing corrections to the energy of simulated electrons that correct for the small discrepancies observed in the energy resolution of electrons are typically of the order of $(\pm)1-3\%$ [96].

Additional quality requirements are imposed on the clusters and associated tracks of the candidates in order to separate true electrons and photons from hadronic backgrounds and to reject electrons that were produced in photon conversion processes [96]. These η and energy dependent selection cuts are defined in three different quality levels, denoted as *loose*, *medium* and *tight*, with decreasing identification efficiencies and increasing expected jet rejection factors[1)] of about 500, 5000 and 50000, respectively [96]. The *loose* selection only uses information on the shower shape in the middle layer of the electromagnetic calorimeter and the hadronic leakage energy. For the *medium* selection these information are complemented by information from the strip layer, additional track quality requirements and a refined track–cluster matching. Further information on the ratio of the energy of the electron to its momentum, ${}^{E}/_{p}$, the number of low and high energetic hits in the TRT, the number of hits in the innermost layer of the pixel detector and information on reconstructed vertices of γ conversions are used in the *tight* selection.

In the forward direction ($2.5 < |\eta| < 4.9$) no tracking detectors are available and therefore the electron identification is based solely on calorimeter information. Electrons directed towards the forward detector region are not employed in the search presented here. Details on their reconstruction and identification can be found in Ref. [96].

[1]The rejection r is defined as the inverse of the selection efficiency ε, i.e. $r = {}^{1}/_{\varepsilon}$.

Using a "tag-and-probe" method, the electron reconstruction and identification efficiencies were measured in $Z/\gamma^* \to e^+e^-$ events selected from the data and compared to the efficiencies in simulated events [96]. The results of these measurements are shown in Fig. 6.1 for the reconstruction efficiency and the identification efficiencies of the *medium* and *tight* quality criteria as a function of the pseudorapidity of the electron and integrated over $20\,\text{GeV} < E_\text{T} < 50\,\text{GeV}$. Good agreement is observed within uncertainties. To account for the small deviations observed, p_T- and η-dependent correction factors for the reconstruction and identification efficiencies of simulated electrons were derived [96]. The identification efficiency corrections, for example, range from values of 1% up to values of 13%.

6.4. Muons

For the reconstruction and identification of muons with the ATLAS detector a variety of strategies has been developed [100]. The different strategies reconstruct *Stand-alone*, *Combined* and *Segmented Tagged muons*, depending on what information provided by the Inner Detector and the Muon Spectrometer are used.

Stand-alone muons are formed from tracks that are reconstructed solely in the Muon Spectrometer. The direction and the impact parameter of a muon at the interaction point are determined by an extrapolation of the Muon Spectrometer track back to the beam line. In this process a possible energy loss of the muon inside the calorimeters and potential multiple scattering processes are taken into account.

A combined muon is based on a successful combination of a reconstructed Inner Detector track and a stand-alone muon. The compatibility of both tracks is evaluated using a χ^2 test. The properties of the muon are determined by combining the measurements in both sub-detector systems and two different techniques are applied for this combination. In the first approach the combined muon track properties are computed as the weighted average of the two individual measurements. In the second approach the combined track is determined by a new fit to all hits associated to the track in the Inner Detector and the Muon Spectrometer. The average efficiency of this muon reconstruction technique has been measured in $Z/\gamma^* \to \mu^+\mu^-$ data and amounts to about 93% [100].

Segment tagged muons are seeded by Inner Detector tracks with momenta above a certain threshold. Each track is extrapolated to the muon system and identified as a muon if straight track segments in the precision muon chambers are found at a close distance to the extrapolated trajectory. The efficiency for the identification of muons that were reconstructed by either the

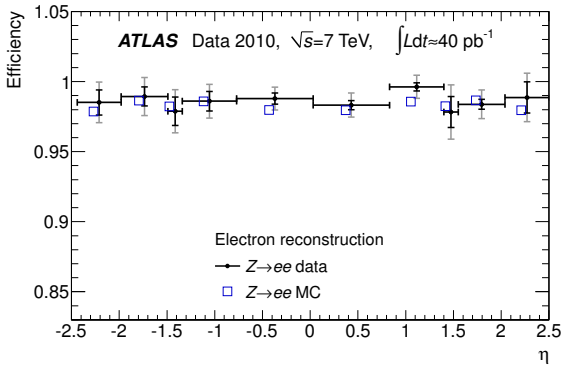

(a) Reconstruction

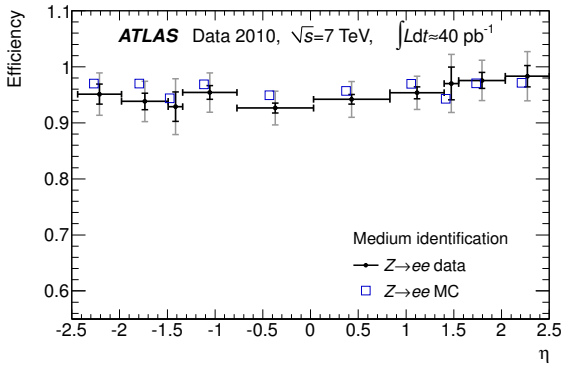

(b) *Medium* quality identification

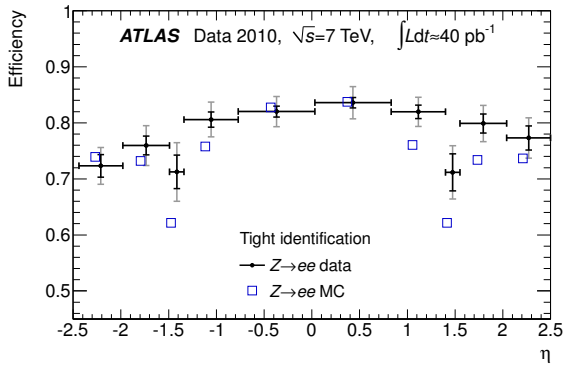

(c) *Tight* quality identification

Figure 6.1.: Figure (a) shows the reconstruction efficiency for electrons in $Z/\gamma^* \to e^+e^-$ events selected from the data and in simulation as a function of the pseudorapidity of the electron energy cluster and integrated over $20\,\text{GeV} < E_\text{T} < 50\,\text{GeV}$. Figure (b) shows the identification efficiency for electrons in the same event samples for the *medium* (b) and *tight* (c) identification criteria as a function of the pseudorapidity of the electron energy cluster and integrated over $20\,\text{GeV} < E_\text{T} < 50\,\text{GeV}$. The results for the data are shown with their statistical (inner error bars) and total (outer error bars) uncertainties. The statistical error on the efficiencies in the simulated sample – shown as open squares – are negligible. The data points are slightly displaced to make the plot more readable. The figures are taken from Ref. [96].

combined or the segment tagged reconstruction technique is about 97% in $Z/\gamma^* \to \mu^+\mu^-$ data [100].

The reconstruction of segmented tagged and combined muons relies on the reconstruction of tracks in the Inner Detector and hence is limited to the range $|\eta| < 2.5$. However, the combination of measurements in two independent sub-detector systems improves the p_{T} resolution for reconstructed muons and reduces the background from muons that are produced in pion decays or inside the calorimeter.

In several detector regions the identification of muons is very challenging. At $\eta = 0$, several services of the Inner Detector and calorimeters are positioned inside the Muon Spectrometer. Therefore, this region is only partially equipped with muon chambers, resulting in a low muon identification efficiency. In addition, muons passing through the transition region between the barrel and the end-caps ($|\eta| = 1.2$) do traverse only one chamber of the muon system.

The muon momentum resolution and scale have been measured in $Z/\gamma^* \to \mu^+\mu^-$ events selected in data and corrections have been derived [101].
The muon momentum resolution was extracted from the width of the di-muon mass distribution in $Z/\gamma^* \to \mu^+\mu^-$ decays. Furthermore, the independent momentum measurements for muons from $Z/\gamma^* \to \mu^+\mu^-$ and $W(\to \mu\nu_\mu)$+jets decays performed with the Inner Detector and the muon detector system were compared to determine the momentum resolution.
Scale corrections for the momenta of simulated muons were extracted from comparisons of the average invariant di-muon mass in the $Z/\gamma^* \to \mu^+\mu^-$ events selected in data to the well known Z boson mass [100].

Using a "tag-and-probe" method, the muon reconstruction and identification efficiencies were measured in $Z/\gamma^* \to \mu^+\mu^-$ decays selected from data [100]. The efficiencies in simulated events and in real collision data show good agreement within uncertainties. This is shown for the reconstruction efficiency of combined muons in Fig. 6.2. To account for the small deviations observed, p_{T}-, η- and ϕ- dependent correction factors for the reconstruction and identification efficiencies of simulated muons were derived.

6.5. Lepton Isolation Criteria

Electrons and muons produced in decays of heavy particles, like those from Z boson decays, are usually isolated from other particles that would cause additional energy depositions in the calorimeter and from close-by tracks. Several variables can be defined to reflect the degree of

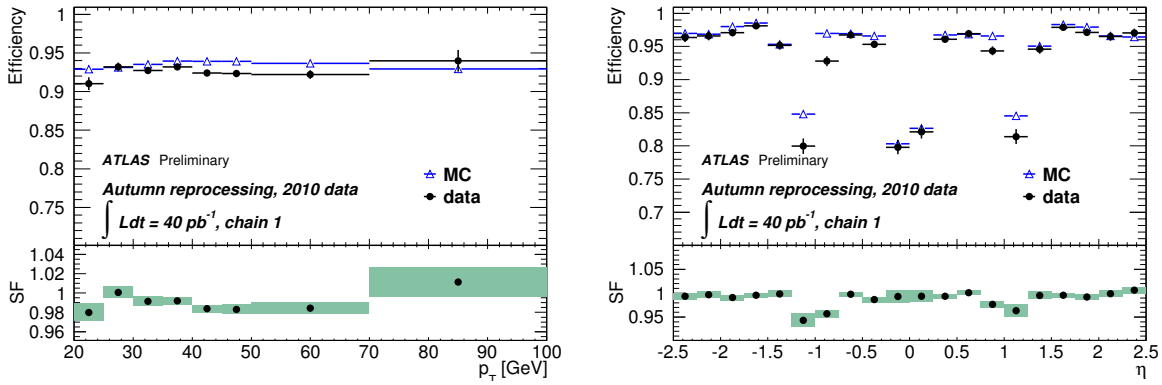

(a) p_{T} dependent

(b) η dependent

Figure 6.2.: Reconstruction efficiencies and correction factors for combined muons reconstructed with the techniques described in the text (labelled "chain 1" in the figures) as a function of the muon p_{T} (a) and η (b). The upper part of the figures show the efficiencies measured in data (dots) and simulated events (open triangles). The corresponding correction factors ("SF") are shown in the lower part of the figures. The figures are taken from Ref. [100].

isolation [96, 100].

The isolation of a lepton from close-by tracks, $p_{\mathrm{T}}^{\Delta\mathrm{R}=0.4}$, is computed as the scalar sum of transverse momenta of all tracks located within a cone with radius parameter $\Delta\mathrm{R} = 0.4$ around the lepton direction. Only tracks are taken into account that satisfy $p_T > 1$ GeV and that are associated to the same primary vertex as the lepton. Furthermore, the track of the lepton itself is excluded from the sum.

The isolation from additional energy deposits in the calorimeter, denoted as $E_{\mathrm{T}}^{\Delta\mathrm{R}=0.2}$, is computed from the energy deposited in the calorimeter within a cone with radius parameter $\Delta\mathrm{R} = 0.2$ around the lepton direction. The energy deposited by the lepton itself is not taken into account in the computation of this quantity. Corrections to the isolation variable are applied depending on the number of reconstructed primary vertices as energy depositions resulting from pile-up events might bias the computed isolation [100]. Further corrections are applied to the isolation variables for electrons. Electrons with large transverse momenta tend to deposit some of their energy outside the narrow cluster window used to reconstruct the electron candidates. Hence, some of their energy leaks into the cone around the electron direction used to compute the calorimeter isolation. This effect leads to a bias and is corrected for.

The relative track and calorimeter isolation variables for combined muons, defined as the ratio of the isolation variable over the muon p_{T}, are shown in Fig. 6.3. The muons were obtained

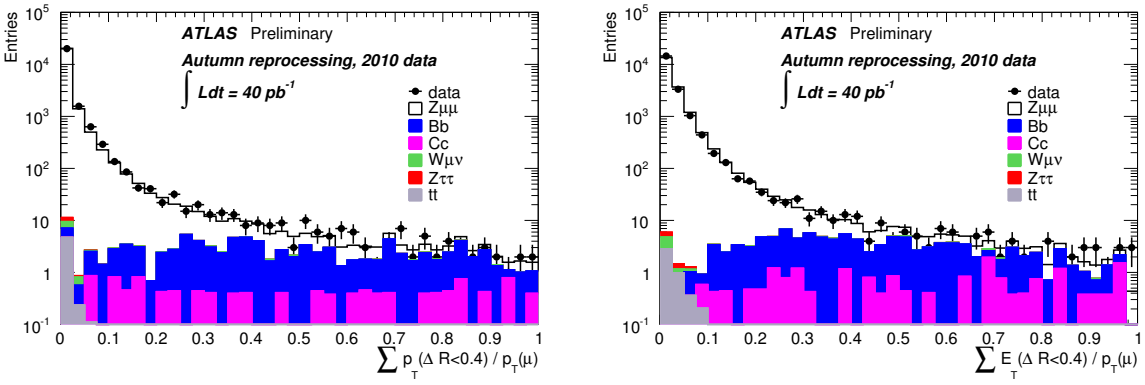

(a) Relative track isolation

(b) Relative calorimeter isolation

Figure 6.3.: Relative track (a) and calorimeter (b) isolation variables for muons selected in data compared to the expectations from simulation. The isolation variables shown here were computed from the activity within a cone with radius parameter $\Delta R = 0.4$ around the muon candidate. The figures are taken from Ref. [100].

from $Z/\gamma^* \to \mu^+\mu^-$ decays selected in data and from simulation using a "tag-and-probe" method and are required to satisfy $p_T > 20\,\text{GeV}$ [100]. Excellent agreement of the distributions in simulated events and data is observed for both isolation variables. As a consequence, the selection efficiencies for real and simulated muons agree within uncertainties.

6.6. Jets

Hadronic particle jets are reconstructed using the anti-k_t algorithm [93]. The energy clusters that seed the jet candidates are reconstructed with the so-called *topological clustering algorithm* [102]. *Topological clusters* are seeded by calorimeter cells with a large signal to noise ratio above a certain threshold t_{Seed}. Neighbouring cells are added to the cluster if their signal to noise ratio is above a lower threshold t_{low}. Those added cells with signal to noise ratios above a medium threshold $t_{\text{medium}} > t_{\text{low}}$ serve as additional seeds to iteratively expand the cluster. When no further neighbouring seed cells can be found, the clustering is finished by adding all direct neighbour cells on the outer perimeter of the cluster that feature a signal to noise ratio above a certain threshold t_{cell}. Given this procedure, the resulting topological clusters contain a variable number of cells.

The direction of a topological cluster is defined as the barycentre of all associated cells. Its total corrected energy is given by the sum of energies deposited in the cells, corrected for possible

energy losses in front of the calorimeter. The anti-k_t algorithm sequentially combines nearby topological clusters within a distance of $\Delta R = 0.4$ from each other. This is done in a way that soft energy depositions tend to cluster with hard ones. Therefore, if a hard cluster is separated from any other hard cluster by a large distance, it accumulates all the soft clusters within a distance $\Delta R = 0.4$. If the distance of two hard clusters is within $0.4 < \Delta R < 0.8$, all soft clusters in between them are split among the hard ones, and if their distance is lower than 0.4 they will form one single jet. Soft clusters that are far separated from hard clusters may combine among themselves.

The calorimeter response to hadrons is lower than its response to electrons or photons. In addition, the amount of energy that hadrons loose in the inactive detector parts differs from the corresponding energy loss of electrons and photons. Therefore, a detailed calibration scheme for energy depositions of hadronic particle jets has been developed [103]. The *Local Cluster Weighting* (LCW) calibration applies dedicated energy corrections to clusters of either electromagnetic or hadronic energy depositions. These corrections take into account the lower calorimeter response to hadrons, their particular energy losses within the inactive detector material and detector signals below the applied noise thresholds.

On top of this LCW calibration an additional jet energy calibration is applied as a function of the kinematic variables p_T and η of a jet. This *jet energy scale* (JES) calibration has been derived from a combination of test beam results, the analysis of simulated events and in-situ measurements in p–p collisions [104, 105].

6.7. τ Leptons

With their large mass of 1.777 GeV, τ leptons are the only known leptons that decay into hadrons [18]. The average lifetime of a τ lepton is about 2.9×10^{-13} seconds and therefore they usually decay at a very close distance to the primary vertex.

The leptonic decays of τ leptons, denoted as τ_{lep}, are characterised by either one electron or one muon and two neutrinos. Hence, reconstructed electrons and muons are used to tag these decay modes. In the following, the corresponding processes $\tau \to e\nu_e\nu_\tau$ and $\tau \to \mu\nu_\mu\nu_\tau$ will be denoted as τ_e and τ_μ, respectively. Their branching ratios are BR(τ_e)≈17.9% and BR(τ_μ)≈17.4% [106].
The remaining branching ratio of ≈64.7% corresponds to hadronic τ decays. These will be summarised as τ_{had} in the following. Nearly all of these hadronic decays result in final states containing either one or three charged pions, several neutral pions and a ν_τ neutrino. The corre-

sponding branching ratios are approximately 49.5% and 15.2% for the decay into one and three charged pions, respectively. Only in very rare cases more than three charged pions are produced in a τ lepton decay. Given these decay modes, the signature of the visible hadronic τ decay products in the detector is a collimated calorimeter shower and one or three associated tracks. This signature is very similar to that of quark or gluon jets and therefore the main challenge in the identification of the hadronic τ decays is the rejection of these.

The τ_{had} candidates are seeded by reconstructed jets with transverse momenta above 10 GeV [107]. The coordinates in η and ϕ of a τ_{had} candidate are determined by the coordinates of the topological clusters of calorimeter cells that are associated to the seeding jet. The energy of a τ_{had} candidate is computed from the topological clusters and calibrated using a dedicated τ energy calibration factor [107] – the jet energy scale cannot be employed for τ_{had} candidates as the hadronic decays of τ leptons result in specific, known compositions of charged and neutral pions.

As the number of associated tracks is an important information used in the τ_{had} identification, the τ_{had} reconstruction is restricted to the solid angle covered by the Inner Detector ($|\eta| < 2.5$). Tracks reconstructed in the Inner Detector are associated to a τ_{had} candidate if their distance to the τ_{had} flight direction is below $\Delta\text{R} = 0.2$ and if they satisfy the following quality criteria:

- $p_{\text{T}} > 1$ GeV,
- Number of pixel hits ≥ 2,
- Number of pixel and SCT hits ≥ 7,
- $|d_0| < 1.0$ mm, where d_0 denotes the transverse impact parameter of the track,
- $|z_0 \sin\theta| < 1.5$ mm, where z_0 denotes the longitudinal impact parameter of the track.

The associated tracks that satisfy the above conditions are denoted as *core tracks* in the following. Additional *isolation tracks*, defined as the tracks that satisfy the above criteria and lie within a distance of $0.2 < \Delta\text{R} < 0.4$ around the τ_{had} candidate axis, i.e. within the so-called isolation annulus, are used to compute several variables employed in the τ_{had} identification algorithm described below.

The final identification of a τ_{had} jet is based on a selection of variables that describe the properties mentioned before and discriminate the hadronic τ decays against quark and gluon jets. These variables are [108]:

- Track radius (R_{track}): the p_{T} weighted track width, which is calculated as

$$R_{\text{track}} = \frac{\sum_i^{\Delta\text{R}_i<0.4} p_{\text{T},i}\,\Delta\text{R}_i}{\sum_i^{\Delta\text{R}_i<0.4} p_{\text{T},i}}, \tag{6.1}$$

where i runs over all core and isolation tracks assigned to the τ_{had} candidate. The momenta of these tracks are denoted as $p_{\text{T},i}$.

- Leading track momentum fraction (f_{track}): Ratio of the transverse momentum of the core track featuring the largest p_{T} over the transverse momentum of the τ_{had} candidate.

- Core energy fraction (f_{core}): the fraction of transverse energy deposited in the calorimeters within a narrow cone around the τ_{had} flight axis ($\Delta\text{R} = 0.1$) divided by the transverse energy deposited in a larger cone ($\Delta\text{R} = 0.4$). All topological clusters associated to the τ_{had} candidate are considered and calibrated at the electromagnetic energy scale.

- Number of isolation tracks ($N^{\text{iso}}_{\text{track}}$): the number of tracks within the isolation annulus of the τ_{had} candidate ($0.2 < \Delta\text{R} < 0.4$).

- Calorimetric radius (R_{Cal}): the shower width in the electromagnetic and hadronic calorimeter weighted by the transverse energy deposited in each calorimeter part,

$$R_{\text{Cal}} = \frac{\sum_{i\in\{\text{all}\}}^{\Delta\text{R}_i<0.4} E_{\text{T},i}\,\Delta\text{R}_i}{\sum_{i\in\{\text{all}\}}^{\Delta\text{R}_i<0.4} E_{\text{T},i}}, \tag{6.2}$$

  where i runs over cells in all layers of the electromagnetic and hadronic calorimeters.

- Cluster mass ($m_{\text{eff. clusters}}$): the invariant mass computed from the topological clusters associated to the seeding jet. The clusters are calibrated at the LCW energy scale.

- Track mass (m_{tracks}): the invariant mass of the system consisting of all core and isolation tracks.

- Transverse flight path significance ($S^{\text{flight}}_{\text{T}}$): the decay length significance of the secondary vertex[2)] in the transverse plane. The decay length significance is the ratio of the reconstructed signed decay length over its estimated uncertainty. Only core tracks are used for the secondary vertex fit and hence this quantity can only be computed for a τ_{had} candidate that more than one core track is assigned to.

- Leading track IP significance ($S_{\text{lead track}}$): the transverse impact parameter significance of the track associated to the τ_{had} candidate featuring the largest transverse momentum.

[2]The secondary vertex denotes the decay vertex of long-lived particles. The decay length is the distance between the primary and secondary vertices. The sign of this property is determined from the positioning of the primary and secondary vertices with respect to the jet direction.

- First three leading clusters energy ratio ($f_{3\text{ lead clusters}}$): the ratio of the cluster energy of the three clusters that the most energy was deposited in over the total energy of all clusters associated to the τ_{had} candidate.
- Maximum ΔR (ΔR_{max}): the maximal distance ΔR between a core track and the τ_{had} candidate flight axis.

The variables described above are analysed using *Boosted Decision Trees* (BDTs), a multivariate analysis technique that exploits the separation power of all variables and their correlations. Each BDT has been trained for a different category of τ_{had} candidates defined by the number of associated tracks and the number N of reconstructed primary vertices ($N \leq 3$, $3 < N \leq 5$, $5 < N \leq 7$ and $N > 3$). The latter categorisation reduces the dependency of the identification quality on the number of additional pile-up events. The output value of the corresponding BDT for a τ_{had} candidate is used as the discriminating variable to identify τ_{had} jets and to reject quark and gluon jets. Three sets of p_{T}-dependent cuts on these discriminators, denoted as *loose*, *medium* and *tight*, are optimised and calibrated to data [107]. The corresponding signal efficiencies of these selection criteria are approximately 60%, 45% and 30%, respectively.
The τ_{had} jet identification efficiency was measured in $Z/\gamma^* \rightarrow \tau^+\tau^-$ data using a "tag-and-probe" technique [107] and is shown in Fig. 6.4 as a function of the τ_{had} jet p_{T} for τ_{had} candidates with one associated track ("1-Prong") and three associated tracks ("3-Prong"). The measured efficiencies were compared to the expectations and correction factors for the selection efficiency of simulated τ_{had} jets were extracted.
The rejection factors of the τ_{had} identification against quark and gluon jets were measured in a di-jet sample selected in data as the number of probe jets reconstructed as τ_{had} candidates over the number of probe jets reconstructed and identified as a τ_{had} jet [107]. Their values were found to vary from about 20 for the *loose* quality selection to about 300 for the *tight* quality selection. The rejection factors for the *medium* quality selection are shown in Fig. 6.5 as a function of the τ_{had} selection efficiency for true τ_{had} jets[3)]. Only true τ_{had} decays are considered are directed towards the central detector region ($|\eta| < 2.5$).

Electrons and muons are additional background sources for τ decays with one charged pion in the final state. Additional boosted decision trees optimised for four different regions in $|\eta|$ are used to reject electrons. In addition to the track radius (R_{track}), the leading track momentum fraction (f_{track}) and the core energy fraction (f_{core}) that are defined above, further variables are analysed by the BDTs. One of the most discriminating property is the amount of transition radiation emitted in the TRT, which on average is much larger for electrons than for charged pions.

[3]True τ_{had} jets are τ_{had} candidates that can be matched to a true τ_{had} decay at the generator level.

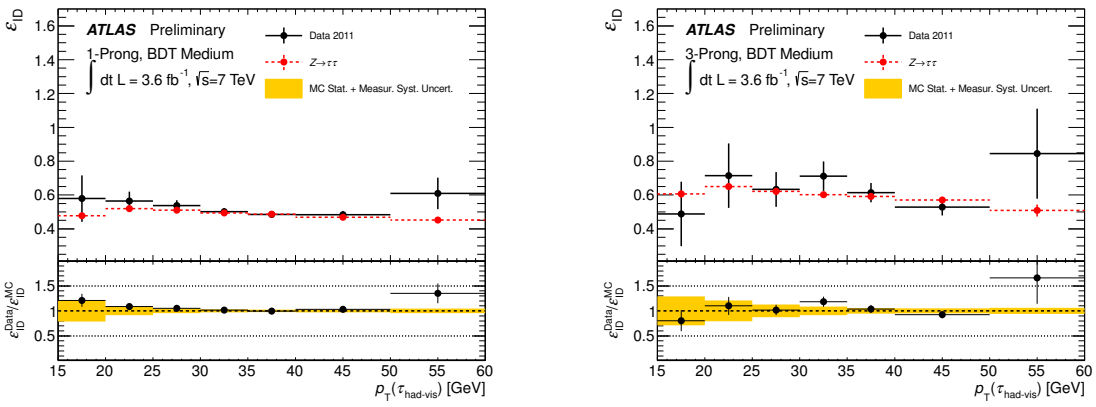

(a) One track (b) Three tracks

Figure 6.4.: Identification efficiencies for τ_{had} jets (ε_{ID}) with one (a) and three (b) associated tracks and for the τ_{had} selection criteria with *medium* efficiency as a function of p_{T}. The errors on the measured efficiencies include systematic and statistical uncertainties, while the errors on the simulated efficiencies are of statistical nature. The correction factors for the selection efficiency of simulated τ_{had} decays are shown at the bottom of each figure. The corresponding error bars show statistical uncertainties. The yellow band includes the systematic uncertainty of the measurement and the statistical uncertainty on the efficiencies in simulated events. The figures are taken from Ref. [107].

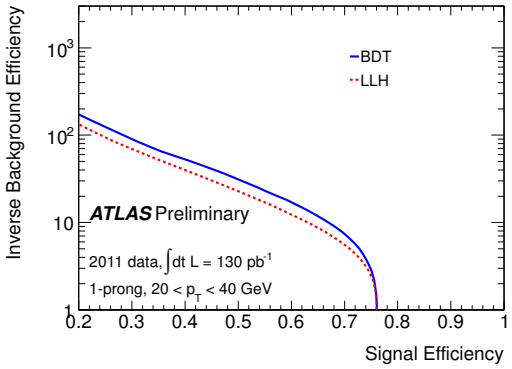

(a) One track and 20 GeV$< p_{\mathrm{T}} \leq$ 40 GeV

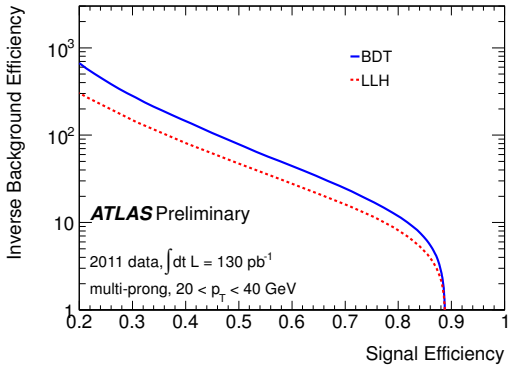

(b) Three tracks and 20 GeV$< p_{\mathrm{T}} \leq$ 40 GeV

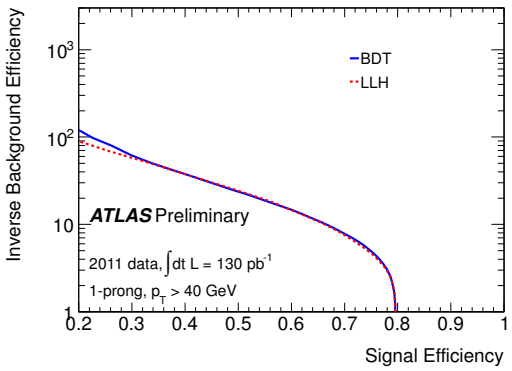

(c) One track and $p_{\mathrm{T}} >$40 GeV

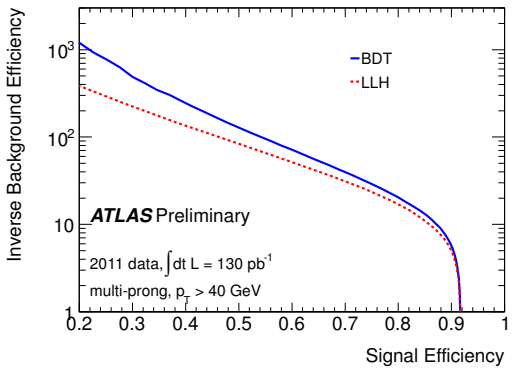

(d) Three tracks and $p_{\mathrm{T}} >$40 GeV

Figure 6.5.: Inverse background efficiency versus the signal efficiency for the τ_{had} identification with *medium* efficiency (BDT) and an additional, likelihood-based τ_{had} identification algorithm (LLH) that is not employed in this thesis. The inverse background efficiencies for τ_{had} candidates with one associated track are shown on the left-hand side, those for candidates with multiple tracks on the right-hand side. The top row shows the inverse efficiencies for candidates with transverse momenta within the range of 20 GeV$< p_{\mathrm{T}} \leq$40 GeV, the bottom row those for candidates with $p_{\mathrm{T}} >$40 GeV. The figures are taken from Ref. [107].

Again, cuts on the BDT discriminator are provided in three quality levels, *loose*, *medium* and *tight*, to discriminate the hadronic τ decays from electrons. These result in signal efficiencies of approximately 95%, 85% and 75%, respectively [107]. Using a "tag-and-probe" technique, the background rejection rate of the discrimination against electrons was measured in $Z/\gamma^* \to e^+e^-$ decays selected in data [107]. A comparison of the measured electron rejection rate to the rejection rate of simulated electrons was used to extract correction factors for the τ_{had} misidentification probability of simulated electrons. For the *medium* quality identification, correction factors of 1.3 ± 0.5, 1.0 ± 1.0, 0.5 ± 0.4 and 2.8 ± 1.3 were derived for τ_{had} candidates reconstructed within the pseudorapidity ranges of $|\eta|<1.37$, $1.37<|\eta|<1.52$, $1.52<|\eta|<2.00$ and $|\eta|>2.00$, respectively.

The detector response to muons is very different from its response to a τ_{had} jet. However, in rare cases a muon might undergo hard bremsstrahlung or might coincidentally overlap with the calorimeter depositions of other particles. In such cases the muon track in combination with a reconstructed energy cluster might be misidentified as a hadronic τ decay. To reject such candidates, a cut-based selection is applied. The information used is that in either of the two cases mentioned above the candidate is very likely to have a track momentum exceeding the energy deposited in the calorimeter. In addition, the fraction of energy deposited by a τ_{had} jet in the electromagnetic calorimeter is larger on average. As opposed to this, a muon deposits its energy more uniformly in the two calorimeter systems. Studies of simulated $Z/\gamma^* \to \mu^+\mu^-$ and $Z/\gamma^* \to \tau^+\tau^-$ events show that approximately 55% of the muons misidentified as *medium* quality τ_{had} jets are rejected by this veto while the τ_{had} selection efficiency is kept at a high level of 96% [107].

6.8. Reconstruction of Missing Transverse Momentum

Several physics processes result in final states containing particles that escape detection. Such particles are the neutrinos of the Standard Model or other stable and only weakly interacting particles that are predicted by several theories. Although such particles evade direct detection, their presence is indicated indirectly by an imbalance in the momentum distribution in the plane transverse to the beam axis. Hence, the reconstruction of this imbalance, denoted as the *missing transverse momentum* ($E_{\text{T}}^{\text{miss}}$), is an essential ingredient in many searches for new physics as well as for measurements of already known processes.

The magnitude of $E_{\text{T}}^{\text{miss}}$ and its direction is computed from the negative vector sum of the momenta of all particles that were reconstructed in an event [109]. If no particle escapes detection, momentum conservation requires a balanced distribution of momenta in the transverse plane and

therefore results in values for $E_{\mathrm{T}}^{\mathrm{miss}}$ close to zero.

The computation of $E_{\mathrm{T}}^{\mathrm{miss}}$ takes into account the contributions of all energy depositions in the calorimeters. Clusters associated with jets or τ_{had} candidates, both satisfying $E_{\mathrm{T}} > 20$ GeV, are calibrated at the hadronic energy scale, whereas calorimeter cells not associated with any object are calibrated at the electromagnetic energy scale. In addition to the contribution of calorimeter clusters, low-p_{T} tracks are taken into account in the computation. This recovers the contribution from momenta of low energetic particles that do not deposit their energy in the calorimeters. Further contributions to $E_{\mathrm{T}}^{\mathrm{miss}}$ are due to muons that were reconstructed in the Muon Spectrometer and the Inner Detector. Their contribution is calculated separately for isolated and non-isolated muons.

The resolution of the $E_{\mathrm{T}}^{\mathrm{miss}}$ measurement is limited by the finite resolution of the energy measurements in the various detector elements, the presence of inactive material and the limited solid angle coverage of the detector. In addition, several sources may lead to contributions to $E_{\mathrm{T}}^{\mathrm{miss}}$ that do not originate from undetected particles. Such sources are, for example, the electronic noise in various detector elements and in the read-out systems as well as cosmic-ray muons traversing the detector volume.

6.9. Identification of *b*-Jets

The identification of jets originating from the hadronisation of *b*-quarks, *b-jets*, play an important role in searches for the neutral Higgs bosons of the MSSM.

Several properties of *b*-jets can be used to identify these and to reject candidates originating from the hadronisation of gluons or lighter quarks. The *b*-hadron produced in the hadronisation of the *b*-quark usually acquires most of the energy of the *b*-quark. Its typical lifetime is about 1.5 ps and therefore it traverses several millimeters up to centimeters of the detector volume before it decays. Measurements show that this long lifetime is due to the small transition probability $b \to u$ and $b \to c$ via flavour changing weak currents, which is reflected by the small CKM matrix elements $|V_{cb}| \simeq 40.9 \times 10^{-3}$ and $|V_{ub}| \simeq 4.15 \times 10^{-3}$ [18]. Another consequence of these probabilities is that the *b*-hadron will most likely decay into a *c*-hadron, which itself may decay further into lighter quarks. As a consequence of these decay chains a large number of charged particle tracks are associated to a *b*-jet on average. All of these reconstructed tracks have their origin very close to the jet flight path and a large impact parameter. Given the long lifetime of *b*-hadrons and the high track multiplicity, the decay vertex of the *b*-hadron can be reconstructed in many cases. Furthermore, an additional vertex of the subsequent *c*-hadron decay

may be found. In contrast, the jets initiated by the hadronisation of gluons or lighter quarks do not contain decay chains or are characterised by a very short lifetime. Therefore, no additional vertices can be reconstructed and the impact parameters of the associated tracks are usually very low. However, the average number of gluon or light quark jets that is produced in p–p collisions is very large and compensates for the good discrimination power of the above properties. Even more difficult is the rejection of c-jets and τ_{had} jets since both of these have significant large lifetimes themselves. However, the probability for these to be produced is lower than that for light quark or gluon jets.

All of the b-jet properties mentioned above are condensed in a set of variables that are analysed with several algorithms.
The *IP3D* algorithm uses a likelihood ratio technique to compare selected input variables to pre-defined distributions for both the b- and light jet hypotheses [110]. These distributions are obtained from the two-dimensional histograms of the signed transverse impact parameter significance and the longitudinal impact parameter significance of the tracks associated with the jet.
The *SV1* algorithm aims to reconstruct the vertex of the b- or c-hadron decay [110]. The search for this vertex starts from two-track pairs that form a vertex passing certain quality criteria. Only tracks are considered which are associated to the jet and are separated from the primary vertex by a certain distance. The two-track vertices are iteratively combined to form a single secondary vertex. During this merging procedure, the compatibility of the tracks with the current secondary vertex position is tested using the vertex fit quality and incompatible tracks are discarded. The following properties of the resulting secondary vertex are then analysed using a likelihood ratio technique:

- The signed decay length significance measured in three dimensions.
- The invariant mass of all tracks associated to the vertex.
- The ratio of the sum of energies of all tracks associated to the vertex to the sum of energies of all tracks associated to the jet.
- The number of reconstructed two-track vertices.
- The distance ΔR between the jet axis and the line joining the primary vertex to the secondary one.

The discriminators of the IP3D and SV1 algorithms can be combined easily as both algorithms use the likelihood ratio method. The resulting combined discriminator is referred to as *IP3D+SV1*.
Similar to the SV1 algorithm, the *SV0* algorithm aims to reconstruct the decay vertex of the b- and c-hadron decays [110]. However, only the information about the signed decay length significance of the reconstructed secondary vertex is used to identify b-jets.

The *JetFitter* algorithm exploits the topology of the weak b- and c-hadron decays inside the jet and tries to compute the flight path of the b-hadron [110, 111]. This is done by using a Kalman filter to find a common line on which the primary, the secondary and the tertiary vertex lie, as well as their position on this line. The advantage of this approach is that the b- and c-hadron decay vertices are not necessarily merged, even when only a single track is attached to each of them. The final discrimination between b-, c- and light jets is based on a likelihood ratio technique using similar input variables as the SV1 algorithm described above, as well as the flight length significance of the fitted vertices.
The algorithm *JetFitterCombNN* uses an artificial neural network to combine the discriminators of the IP3D and JetFitter algorithms [110]. Additional input variables describe the topology of the decay chain.
The discriminators of the IP3D, SV1 and JetFitterCombNN algorithms are further analysed and combined in a neural network, denoted as the *MV1* algorithm [112]. In the search presented here, the output of this algorithm is used as the discriminating variable to identify b-jets and to reject jets of different origin. A requirement on the output, $MV1$, of $MV1 \gtrsim 0.602$ results in a b-jet identification efficiency of about 70% in simulated $t\bar{t}$ events. The rejection factors obtained with this algorithm against light and c-jets in the same event sample are shown in Fig. 6.6 (a) for light jets and (b) for c-jets as a function of the b-jet selection efficiency. For the b-jet selection with 70% efficiency, rejection factors of 130 against light jets and 5 against c-jets are observed.
The b-jet identification efficiency was measured in data as a function of the transverse momentum of the jet using the so-called $p_{\mathrm{T}}^{\mathrm{rel}}$ and system8 methods [112]. The results of these measurements are shown in Fig. 6.7 (a) for the $p_{\mathrm{T}}^{\mathrm{rel}}$ method and in Fig. 6.7 (b) for the system8 method. The efficiencies in data were compared to those observed in simulated events. An overall good agreement is observed within uncertainties, with efficiencies measured in data that are about 5 – 10% lower than those in simulation. From these comparisons efficiency correction factors for the identification of simulated b-jets were derived; these corrections are shown in Fig. 6.7 (c). The correction factors measured with the two methods are found to be consistent with each other within uncertainties.
The misidentification rate of the MV1 algorithm for light jets was measured in data as a function of the p_{T} and $|\eta|$ of the jet. These measurements were performed using the so-called negative tag and sv0mass methods [113]. The results of the measurements performed with the negative tag method are shown in Fig. 6.8 for jets reconstructed within the two pseudorapidity ranges $|\eta|<1.2$ (a) and $1.2<|\eta|<2.5$ (b). The mistag rates measured in data were compared to those in simulated events and correction factors were derived for the two different $|\eta|$ regions and as a

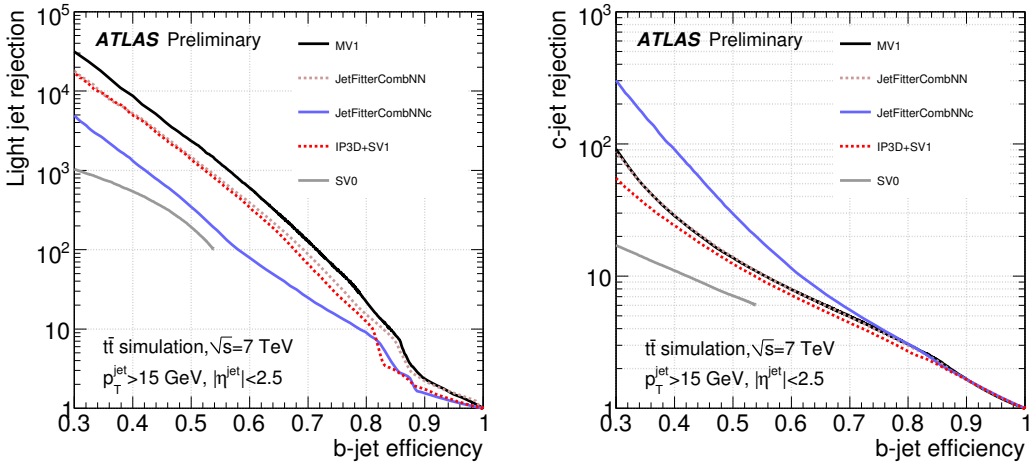

(a) Light jet rejection

(b) c-jet rejection

Figure 6.6.: Light-jet (a) and c-jet (b) rejection in simulated $t\bar{t}$ events as a function of the b-jet selection efficiency and for several b-jet identification algorithms. "JetFitterCombNNc" denotes a c-jet identification algorithm similar to the JetFitterCombNN algorithm. The figures are taken from Ref. [112].

function of the jet p_{T}. These correction factors are shown in Fig. 6.8 (c) and (d).

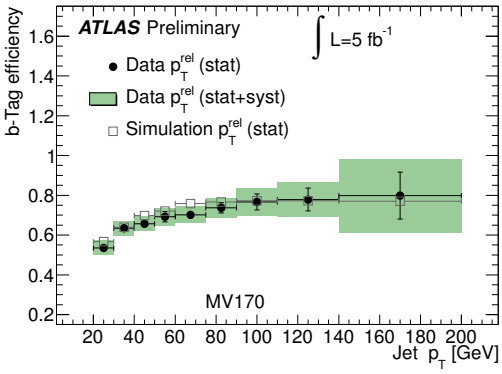

(a) $p_{\mathrm{T}}^{\mathrm{rel}}$ method

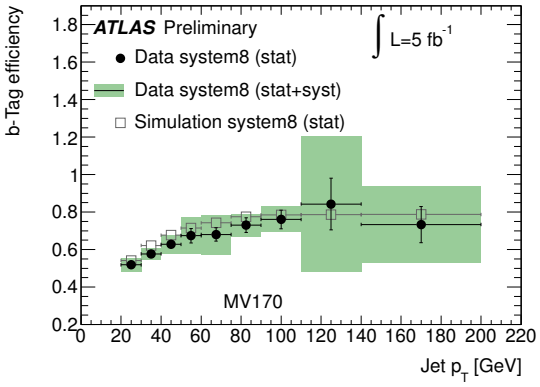

(b) system8 method

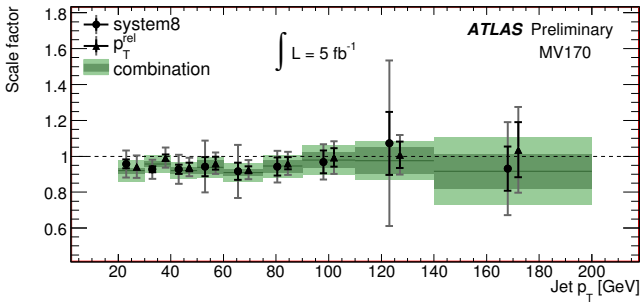

(c) Derived correction factors

Figure 6.7.: The b-jet selection efficiency in data and simulation for the 70% efficiency working point of the MV1 algorithm (MV170) as a function of the jet p_{T}. The efficiencies measured with the so-called "$p_{\mathrm{T}}^{\mathrm{rel}}$" method are shown in figure (a), those measured using the "system8" method in figure (b). The efficiency measurements were used to derive correction factors for the b-jet selection efficiency in simulated events. These correction factors are shown in figure (c) individually for both methods and for their combination. The statistical uncertainty on the combined correction factors are indicated with the dark green band, the light green band shows the total uncertainty. The data points showing the measurements for the two methods are slightly displaced to make the plot more readable. The figures are taken from Ref. [112].

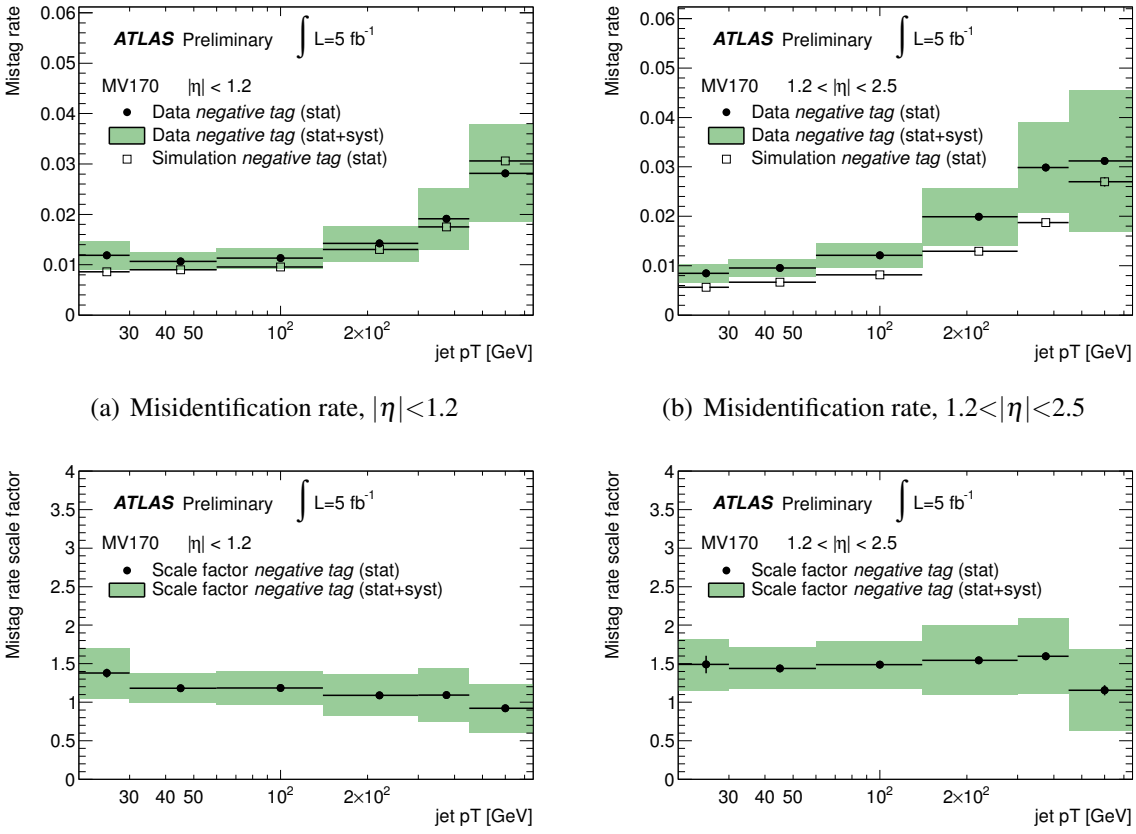

(a) Misidentification rate, $|\eta|<1.2$

(b) Misidentification rate, $1.2<|\eta|<2.5$

(c) Correction factors, $|\eta|<1.2$

(d) Correction factors, $1.2<|\eta|<2.5$

Figure 6.8.: Misidentification efficiency of light jets ("Mistag rate") reconstructed within the pseudorapidity range $|\eta|<1.2$ (a) and $1.2<|\eta|<2.5$ (b) as a function of the jet p_{T}. The rates were measured for the 70% b-jet identification efficiency working point of the MV1 algorithm (MV170) using the so-called "negative tag" method. From these measurements correction factors for the misidentification rate of simulated light jets were extracted. These are shown in figure (c) for the pseudorapidity range $|\eta|<1.2$ and in figure (d) for the pseudorapidity range $1.2<|\eta|<2.5$. The figures are taken from Ref. [113].

$Z/\gamma^* \to \tau^+\tau^-$ event candidate display

(The dominant background to this search [68])

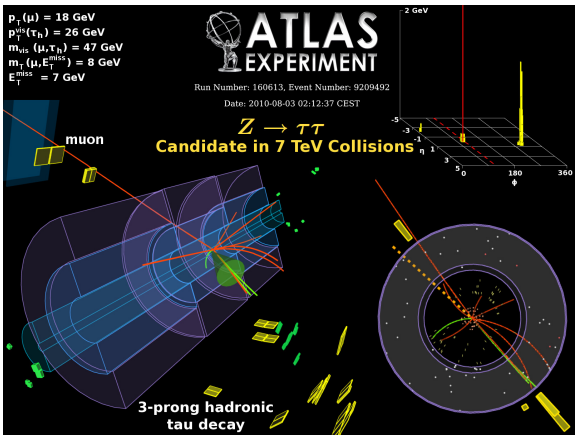

Chapter 7

Search for the Neutral Higgs Bosons of the MSSM in the $\tau_{\text{lep}}\tau_{\text{had}}$ Decay Mode

In this chapter a search for the neutral Higgs bosons of the MSSM in the $\tau^+\tau^-$ decay mode is presented. The p–p collision data used for this search have been collected with the ATLAS detector in the year 2011 at a centre-of-mass energy of $\sqrt{s} = 7$ TeV. The total integrated luminosity of the data set is 4.7 fb^{-1}. Details on the data selection are presented in Section 7.1.

The three neutral Higgs bosons are predominantly produced in the gluon-fusion process and the b-quark associated production mode. The Higgs-strahlung and Vector Boson Fusion production modes are neglected as these are only relevant in certain MSSM parameter regions resulting in Standard Model like couplings for either h or H. Hence, the dedicated searches for a Standard Model Higgs boson are suitable to find a MSSM Higgs boson with such couplings and are considered complementary to the analysis presented here.

The $\tau^+\tau^-$ final states of interest are the $\tau_e\tau_{\text{had}}$ and $\tau_\mu\tau_{\text{had}}$ decay modes of the two τ leptons, with branching ratios of about 23% each. The total processes considered for the search presented here are therefore

$$pp \to (b\bar{b})\, h/A/H \to (b\bar{b})\, \tau_{\text{lep}}\tau_{\text{had}}\,.$$

The following Sections 7.2 and 7.3 discuss the corresponding signal signatures and the rele-

vant Standard Model background processes that might result in similar or identical final states. As neutrinos are produced in the τ lepton decays of the signal processes, the reconstruction of the invariant $\tau^+\tau^-$ mass, i.e. the mass of the Higgs boson, is not straight forward. Therefore, a sophisticated mass reconstruction technique is employed in this search and presented in Section 7.4. Taking the information about the signal signature and background processes into account, the event selection that has been developed to favour the signal topology and to reject background processes is motivated in Section 7.5. The contributions of several background processes to the resulting signal regions are estimated using the Monte Carlo techniques already presented in previous chapters. For dominant backgrounds, however, data-driven estimation or correction techniques have been developed. These are presented in Section 7.6.

The search presented here and further searches for other decay modes of the neutral MSSM Higgs bosons produced in the gluon-fusion and b-quark associated processes have been published in Ref. [114]. A statistical combination of all of these has been performed to maximise the sensitivity of the ATLAS experiment to a possible signal in the recorded data. A brief description of the additional search channels and the results of the combination are presented in the following Chapter 8.

7.1. Data Sample, Data Quality Requirements and Trigger Choice

The results of this search are based on p–p collision data recorded with the ATLAS detector in the year 2011 at a centre-of-mass energy of $\sqrt{s} = 7\,\text{TeV}$. Only data that have been recorded with all components of the ATLAS detector relevant for this search being fully operational are used. The total integrated luminosity of the resulting data set is $4.7\,\text{fb}^{-1}$.

Data Quality Requirements

In order to ensure that the recorded data are true p–p collision events, at least one reconstructed primary vertex is required for each event. Only vertices are taken into account for which at least four reconstructed tracks with transverse momenta above 1 GeV each could be assigned. No requirement on the longitudinal position of the vertex with respect to the nominal beam spot, i.e. its z-coordinate, is applied.

Further data quality criteria are applied in order to suppress sources of missing transverse momentum not originating from p–p collisions, e.g. those resulting from mis-measurements of energy depositions. Such are mainly due to insensitive regions in the electromagnetic LAr

calorimeter that were present during part of the data taking. More details about these requirements can be found in Refs. [115] and [116].

Trigger Selection

Single-lepton triggers are used to pre-select events containing electrons or muons. The corresponding transverse momenta thresholds and identification criteria on the lepton candidates are applied depending on the data taking conditions in order for the triggers not to exceed their assigned bandwidths. Therefore, no events had to be randomly discarded in the event recording procedure, which is commonly known as *prescale*.

Events containing an electron candidate are selected by triggering on energy deposits in the electromagnetic calorimeter that can be associated to tracks in the Inner Detector. The identification criteria applied to the candidates at the higher trigger levels are comparable to those of the offline identification algorithm with *medium* identification efficiency. For early data taking periods with lower instantaneous luminosities lower transverse energy thresholds of $E_T > 20\,\text{GeV}$ were imposed on the electron candidates at trigger level, whereas for later data taking periods higher thresholds of $E_T > 22\,\text{GeV}$ were applied. For the last periods with very high peak instantaneous luminosities, the transverse momentum threshold was not increased any further. Instead, additional requirements on the kinematic variable η and the hadronic energy leakage of the electron candidates were imposed at the Level 1 trigger stage.

Events containing a muon candidate are preselected using a single-muon trigger with a constant transverse momentum requirement of $p_{\text{T}} > 18\,\text{GeV}$ for the whole data set. The candidates are reconstructed using information provided by the trigger chambers of the muon detector system and tracks reconstructed in the Inner Detector. For the last four data taking periods with higher instantaneous luminosities the quality criteria on the muon candidates applied at the Level 1 trigger stage were tightened.

Small differences in the event trigger selection efficiencies are observed in simulated p–p collisions when compared to those in data. The corresponding measurements are mainly performed in $Z/\gamma^* \to \ell^+\ell^-$ and $W \to \ell\nu_\ell$ data and correction factors for simulated trigger decisions have been derived [96, 100]. These factors of 99.5% and 99.2% for events selected by the electron and muon trigger, respectively, are applied to simulated events in the search presented here.

Summary of Data Periods

The individual data taking periods considered for this search are listed in Table 7.1 together with the corresponding trigger choices and recorded integrated luminosities. All trigger names

Period	Runs	Run Range	Electron trigger	Muon trigger	$\int L dt$ (pb^{-1})
B2	3	178044-178109	EF_e20_medium	EF_mu18_MG	11.7
D	22	179725-180481	EF_e20_medium	EF_mu18_MG	161.9
E	5	180614-180776	EF_e20_medium	EF_mu18_MG	48.8
F	15	182013-182519	EF_e20_medium	EF_mu18_MG	136.1
G	28	182726-183462	EF_e20_medium	EF_mu18_MG	537.6
H	13	183544-184169	EF_e20_medium	EF_mu18_MG	259.5
I	23	185353-186493	EF_e20_medium	EF_mu18_MG	324.8
J	9	186516-186755	EF_e20_medium	EF_mu18_MG_medium	226.4
K	16	186873-187815	EF_e22_medium	EF_mu18_MG_medium	561.7
L	44	188921-190343	EF_e22vh_medium1	EF_mu18_MG_medium	1387.7
M	30	190608-191933	EF_e22vh_medium1	EF_mu18_MG_medium	1005.1
Total	208	178044-191933	-	-	4.7 fb^{-1}

Table 7.1.: Data taking periods and individual data taking runs considered for the search presented here. In addition, the corresponding trigger choices and the recorded integrated luminosities are listed. A description of the trigger naming convention is given in the text.

contain the attribute "EF" which denotes the final trigger stage ("Event Filter"). The labelling like "e20" and "mu18" indicates the individual transverse momenta thresholds on the lepton candidate. In case of electron triggers the attribute "vh" indicates additional requirements on the kinematic variable η and the hadronic energy leakage of the electron candidate. The "medium" or "medium1" attribute in case of electron triggers indicates the corresponding identification efficiency of the offline identification algorithm. In case of muon triggers containing the attribute "medium" the final trigger decision is based on a different Level 1 trigger object. "MG" denotes the algorithm that the muon candidates are reconstructed with at trigger level.

7.2. Signal Signature

The $\tau_\mu\tau_{\text{had}}$ and $\tau_e\tau_{\text{had}}$ final states of the signal processes are characterised by either exactly one muon or electron, respectively, and the hadronic decay of the second τ lepton. Since the Higgs bosons of interest are electrically neutral, the light lepton and the τ_{had} jet have zero net electric charge, which implies that their charges are of opposite sign.

The τ leptons are directed back-to-back in the Higgs boson rest frame and hence their decay products including the neutrinos are predominantly directed in opposite directions. Moderate transverse momenta for the Higgs bosons leading to deviations from the back-to-back configuration are realised if in addition to the Higgs boson recoiling jets are produced. The gluon-fusion process, for example, is subject to large radiative corrections that include the production of quark and gluon jets. The transverse momenta of the Higgs bosons produced in the gluon-fusion mode or in association with b-quarks are shown in Fig. 7.1 (a) for two different mass hypotheses. The transverse momenta of the leptons and hadrons produced in the τ decays can be large and depend on the Higgs boson mass, which is shown in Fig. 7.1 (d) – (f). The light leptons are usually isolated from further energy depositions in the calorimeter and from tracks of other electrically charged particles. As a consequence of the neutrinos escaping in opposite directions, only a moderate amount of missing transverse momentum is expected in signal events for low m_A masses. However, since two neutrinos are produced on the side where the τ lepton decays into a light lepton and only one is produced in the hadronic decay, larger values for $E_{\mathrm{T}}^{\mathrm{miss}}$ are possible for large masses m_A. This is shown in Fig. 7.1 (c).

One or two b-jets are produced in the b-quark associated Higgs boson production process. Requiring such b-jets to be identified in the final state might enhance the relative contribution of this signal source to the selected data sample and effectively suppresses several Standard Model background processes. Their identification, however, is challenging, as they have very low transverse momenta in average. This is shown in Fig. 7.1 (b).

7.3. Important Backgrounds Processes

Several Standard Model processes result in final states identical or similar to the signal final states. Such processes contribute as *background processes* to the search presented here. In some of the background processes either one lepton or one τ_{lep} and an additional τ_{had} are produced, and hence these can often hardly be distinguished from the signal process. Processes resulting in final states containing one lepton or one τ_{lep} and one jet are selected if the jet is mistaken for a τ_{had}. In very rare cases background contributions are due to events that contain one true τ_{had} jet and in which a jet is selected as the lepton. Events in which only quark and gluon jets are misidentified as the lepton and the τ_{had} jet are barely mistaken for signal events, given the small corresponding misidentification rates. However, in case of the multi-jet background processes these small rates are compensated by large production cross sections. Further event topologies that might be confused as the signal process are realised in events containing two electrons of

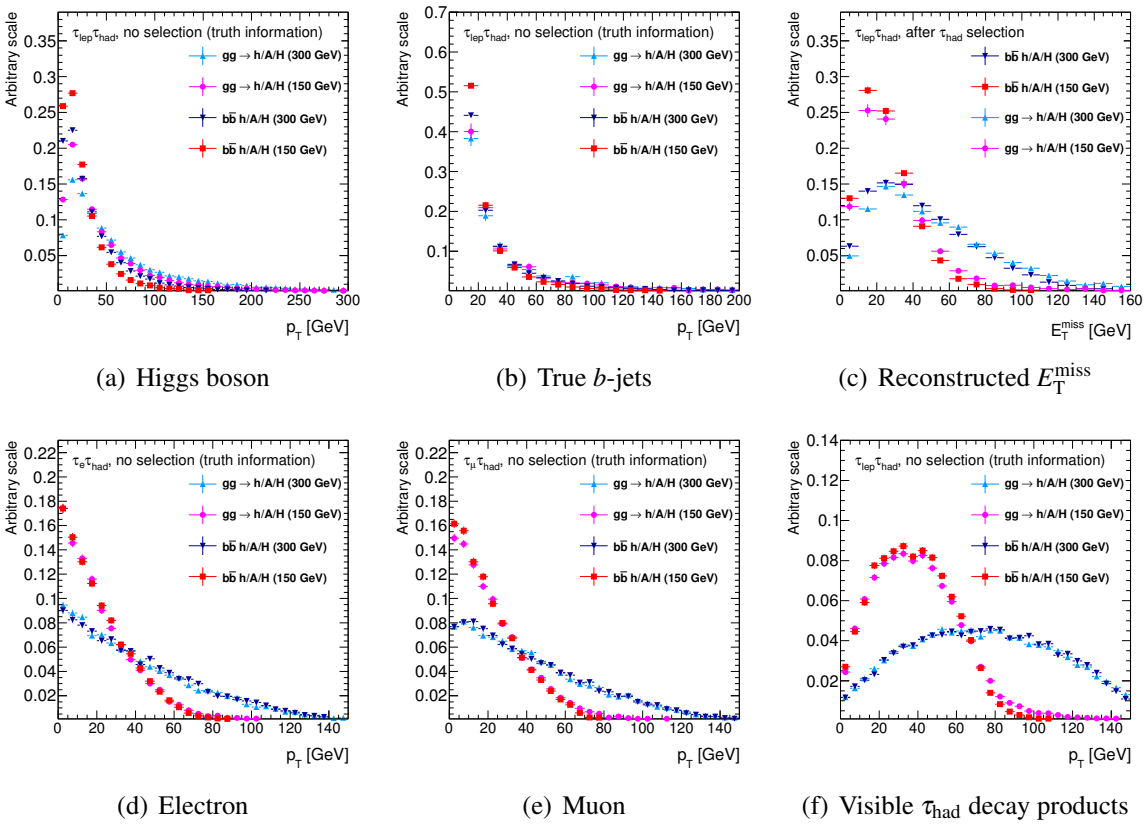

(a) Higgs boson (b) True b-jets (c) Reconstructed $E_{\text{T}}^{\text{miss}}$

(d) Electron (e) Muon (f) Visible τ_{had} decay products

Figure 7.1.: Normalised distributions of the transverse momenta of the Higgs boson (a) and true b-jets (b) in the gluon-fusion ($gg \to h/A/H$) and b-quark associated ($b\bar{b}\,h/A/H$) Higgs boson production processes for two mass hypotheses and $\tan\beta = 20$. The lower row shows the transverse momenta of the Higgs boson decay products, the electron (d), the muon (e) and the visible decay products of the τ_{had} jet (f). All distributions are based on the truth information delivered by the Monte Carlo generator programs. An exception is Figure (c) which shows the reconstructed missing transverse momentum after the τ_{had} jet has been selected.

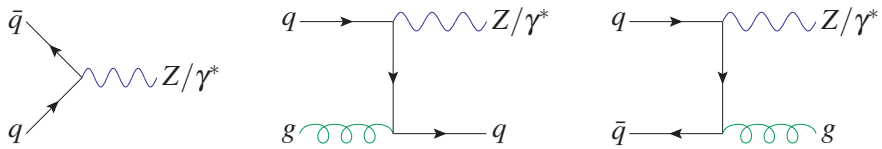

(a) $q\bar{q} \to Z/\gamma^*$ (b) $qg \to q\,Z/\gamma^*$ (c) $q\bar{q} \to g\,Z/\gamma^*$

Figure 7.2.: Dominant tree-level Z boson production mechanisms.

which one is misidentified as the τ_{had} jet. A muon, on the other hand, results in a very different detector signature compared to the signature of a τ_{had} jet. Nevertheless, processes in which two muons are produced might contribute to the total background if one of the muons cannot be reconstructed or identified or does not pass the quality criteria applied in this search. In such cases one muon is selected and a jet might be mistaken for a τ_{had} jet. The same applies to di-electron final states, as well.

The Standard Model processes that contribute significantly as background sources to the search presented here are discussed in the following.

7.3.1. Production of Z Bosons in Association with Jets

The background from Z boson production is especially important for the search presented here. Several decay modes of the Z boson result in final states identical or similar to the signal final states, with the $\tau^+\tau^-$ decay mode being the most important one.
The production of Z bosons proceeds mainly through the tree-level processes $q\bar{q} \to Z/\gamma^*$, $q\bar{q} \to gZ/\gamma^*$ and $qg \to qZ/\gamma^*$. The corresponding Feynman diagrams are shown in Fig. 7.2. The production of Z bosons in association with jets will be denoted as Z/γ^*+jets production in the following. The cross section for the production of Z bosons at the LHC and their subsequent decays into leptons of any flavour is about 5 nb. This number was calculated at NNLO in perturbation theory using the program FEWZ [117]. Processes like $bg \to Z/\gamma^* b$ are especially important for the search for neutral Higgs bosons produced in association with b-jets. However, the relative production rates for b-jets in Z/γ^*+jets processes are lower than those for the signal process as the couplings of Z bosons to down-type fermions are lower than the same couplings of A and either h or H for all relevant values of the parameters m_A and $\tan\beta$.

The decay mode of Z bosons most important for this search is the decay $Z/\gamma^* \to \tau^+\tau^-$. It occurs with a branching ratio of about 3.4% [18] and hence is less probable as the same decay of the neutral Higgs bosons. The subsequent decays $\tau_{\text{lep}}\tau_{\text{had}}$ of the di-τ system results in final states

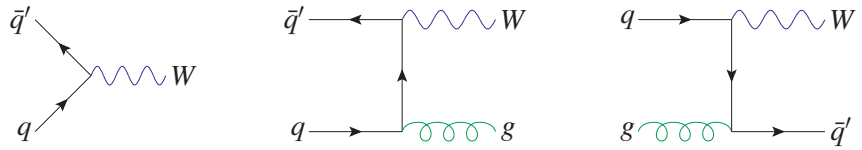

(a) $q\bar{q}' \to W$ (b) $q\bar{q}' \to g\,W$ (c) $qg \to \bar{q}'\,W$

Figure 7.3.: Dominant tree-level W boson production mechanisms.

identical to those of the signal processes. Therefore, this process is an *irreducible* source of background that cannot be suppressed effectively without loosing a significant fraction of the signal at the same time. Nevertheless, the reconstructed invariant mass of the $\tau^+\tau^-$ system reflects the different masses of the Z boson and those of the neutral Higgs bosons. Much less important as a source of background events are Z boson decays in the final states $\tau_{\text{lep}}\tau_{\text{lep}}$ and $\tau_{\text{had}}\tau_{\text{had}}$, of which the former in addition has a low branching ratio of about 6%.

The production of Z bosons and their direct decays into either a pair of electrons or a pair of muons are background processes for the signal final states $\tau_{\text{e}}\tau_{\text{had}}$ and $\tau_{\mu}\tau_{\text{had}}$, respectively. The $Z/\gamma^* \to \mu^+\mu^-$ and $Z/\gamma^* \to e^+e^-$ processes are selected if one of the two leptons is not correctly identified and an additional jet is misidentified as the τ_{had} jet. $Z/\gamma^* \to e^+e^-$ decays further contribute if either one of the two electrons is correctly identified and the respective other mistaken for a τ_{had} jet. In case of the $Z/\gamma^* \to \mu^+\mu^-$ background process this is very unlikely.

Both the $Z/\gamma^* \to \mu^+\mu^-$ and $Z/\gamma^* \to e^+e^-$ processes are summarised as $Z/\gamma^* \to \ell^+\ell^-$ in the following and $\ell = e, \mu$ is implicitly assumed if not stated otherwise.

7.3.2. Production of W Bosons in Association with Jets

The production of W bosons in association with jets, denoted as W+jets production, is one of the dominant backgrounds to the search presented here. W bosons are mainly produced in the tree-level processes shown in Fig. 7.3, i.e. in $q\bar{q}' \to W$, $q\bar{q}' \to g\,W$ and $qg \to \bar{q}'\,W$. The total cross section for W boson production at the LHC is about 10 nb, when taking into account the branching ratio for W boson decays into leptons. This cross section was calculated at NNLO precision using the program FEWZ [117].

The leptonic decay of a W boson into an electron, a muon or a τ_{lep} accompanied by a jet results in a final state comparable to that of the signal processes if the jet is misidentified as the τ_{had} jet. The high jet rejection rate of the τ_{had} identification criteria is compensated by the large W boson production cross section. Former studies have shown that the jet rejection rate is lower

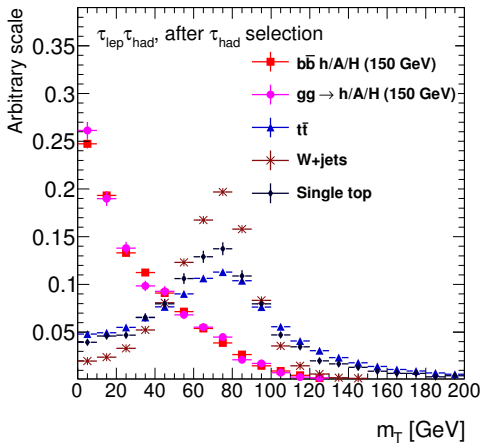

Figure 7.4.: Normalised distributions of the reconstructed transverse mass M_{T} in simulated $t\bar{t}$, single top, $W+$jets and signal events after selection of the τ_{had} jet. The distributions for both Higgs boson production mechanisms are shown for the parameter choice $m_A = 150\,\mathrm{GeV}$ and $\tan\beta = 20$.

in simulated event samples as in the data [118]. To account for this difference, the Monte Carlo predictions for this background need to be corrected; details are presented in Section 7.6.2.
Other final state topologies in which a jet is misidentified as the light lepton are strongly suppressed by the lepton selection criteria and contribute at a negligible level.

Further properties of the W boson production mechanisms are important for the search presented here. Due to processes like $qg \to qW$, the production rate of events with opposite sign electric charges for the selected lepton and τ_{had} jet is higher than the rate of events with same sign charges. Furthermore, the fraction of quark and gluon jets is expected to differ in events with same sign or opposite sign charges. These properties are important for the background estimation techniques that are described in the following sections.

Apart from small contributions due to mis-measured jet energies, the missing transverse momentum that is reconstructed in $W+$jets events is due to the neutrinos produced in the W boson decays. Therefore, the distribution of the invariant mass of the visible W decay products and the missing transverse momentum, denoted as *transverse mass* M_{T}, peaks at values around $\sim m_W$ in $W+$jets events. A comparison of this quantity in simulated $W+$jets events to the distribution in the signal production processes considered here is shown in Fig. 7.4.

7.3.3. t-Quark Pair and Single t-Quark Production

Pairs of t-quarks ($t\bar{t}$) are mainly produced in the processes $gg \to t\bar{t}$ and $q\bar{q} \to t\bar{t}$, shown in Fig. 7.5 (a-c). The total cross section for $t\bar{t}$ production has been calculated at NLO+Next-to-Next-to-Leading-Logarithmic (NNLL) precision [119, 120] and amounts to about 164.6 pb. This cross section is low compared to those of the previously discussed backgrounds. However, by selecting b-jets in order to search for Higgs bosons produced in association with b-quarks, the relative contribution of $t\bar{t}$ production processes to the total background is enhanced.

The decay of a $t\bar{t}$-quark pair can result in final states very similar to those of the signal processes. Through the weak decays of the two t-quarks a pair of τ leptons might be produced. Therefore, final states like $b\bar{b}\,\tau_{\text{lep}}\,\tau_{\text{had}}$ can occur that feature a very signal-like signature. The final states $b\bar{b}\,\tau_{\text{lep}}\,\tau_{\text{lep}}$ and $b\bar{b}\,\tau_{\text{had}}\,\tau_{\text{had}}$ contribute at a low level to the resulting $t\bar{t}$ background. The former of these is disfavoured by the low branching ratios of τ_{lep} decays and the latter is suppressed by the high τ_{had} jet rejection rate of the lepton identification techniques. Furthermore, the $t\bar{t}$ final states $b\bar{b}\,\ell\tau_{\text{had}}$, $b\bar{b}\,\ell$+jets, $b\bar{b}\,\tau_{\text{lep}}$+jets, $b\bar{b}\,\ell\ell$, $b\bar{b}\,\ell\tau_{\text{lep}}$ or $b\bar{b}\,\tau_{\text{had}}$+jets or final states containing quark and gluon jets only might be selected, with about this order of importance considering the corresponding (mis-)identification probabilities and branching ratios.

Single t-quarks are mainly produced in the s-channel process $q\bar{q}' \to t\bar{b}$, the t-channel processes $bq \to q't$ and $qg \to q't\bar{b}$ and the W-associated production mode $bg \to Wt$, denoted as Wt-channel. All these modes are summarised as *single top* production in the following, their Feynman diagrammatic representations are shown in Fig. 7.5 (d-g). The corresponding cross sections of the s-, t- and Wt-channels were calculated at NLO+NNLL QCD precision and amount to 3.9 [121], 58.7 [122], 13.1 pb [123], respectively.

The single top background processes mainly contribute with final states containing a true lepton, i.e. for $t \to b\ell\nu_\ell$ and $t \to b\tau_{\text{lep}}\nu_{\tau_{\text{lep}}}$. and in which a jet is selected as the τ_{had}. The Wt-channel process is selected with a higher efficiency as an additional electron, muon, τ_{lep} or τ_{had} jet might be produced in the W boson decay.

Both the single top and $t\bar{t}$ production processes are summarised as *top production* in the following. The top production processes involving exactly one semi-leptonic t-quark decay, i.e. effectively one leptonic W boson decay, result in final states with large transverse masses M_{T} in average. This is shown in Fig. 7.4 and compared to the distribution of this quantity in the signal processes. The b-jets originating from the t-quark decay feature large transverse momenta whereas the b-jets produced in the signal process have very low transverse momenta. This is shown in Fig. 7.6 for simulated $t\bar{t}$ and single top event samples and both Higgs boson production

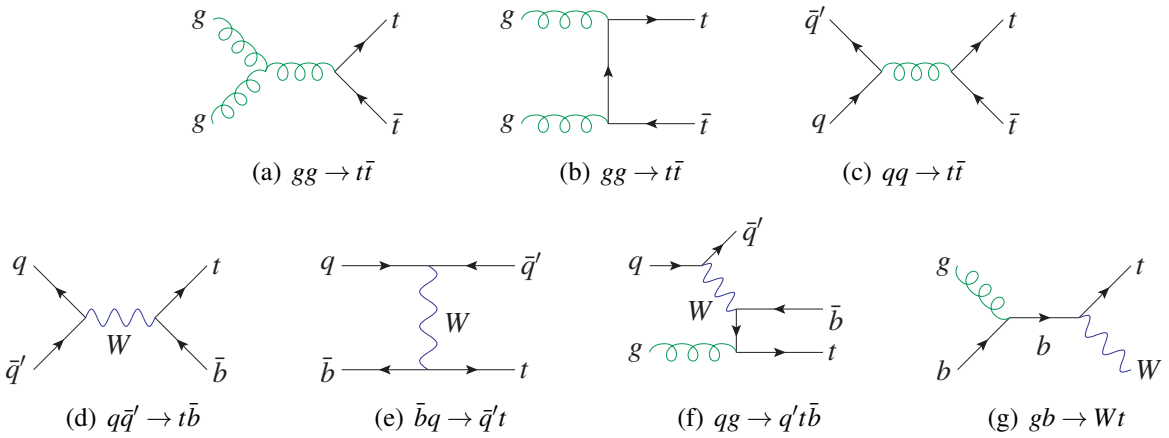

Figure 7.5.: Dominant $t\bar{t}$ (a-c) and single top (d-f) production mechanisms.

mechanisms. Sub-figure (a) shows the transverse momenta of the leading quark or gluon jets in these processes after selecting the τ_{had} jet. The same distribution is shown in sub-figure (b) for jets that passed the b-jet selection criteria and that could be matched to a true b-quark. Both distributions are centered at larger values for the top background processes.

7.3.4. Di-boson Production

Production of two bosons like WW, WZ and ZZ is denoted as *di-boson* production. The total production cross sections of the involved processes are 46.2, 18.0 and 5.6 pb, respectively. These values were calculated at NLO precision using the MC@NLO program [80, 124] and at NNLO precision for the process $gg \to WW$ using gg2WW [81]. The tree-level Feynman diagrams for di-boson production are shown in Fig. 7.7.

WW production can result in final states containing one τ_{had} and one electron, muon or τ_{lep}. The final states of the other processes containing several leptons, τ_{lep} or τ_{had} decays contribute as some of the final state particles might escape detection or identification, resulting in a signal-like event signature. However, due to the comparatively low production cross sections these processes add only small contributions to the total background composition of the search presented here.

7.3.5. Multi-jet Production

A large number of processes in which only quark and gluon jets are produced in the hard interaction are summarised as *multi-jet* production. Examples for such processes are those involving

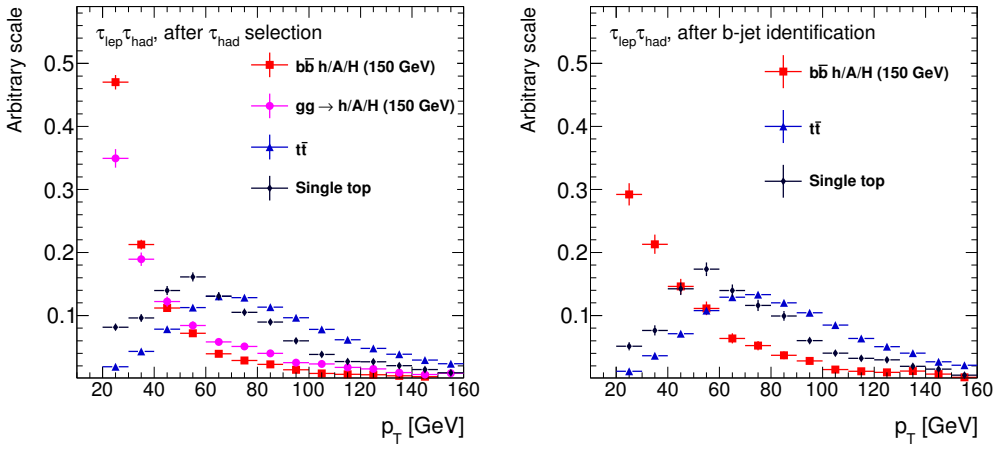

(a) p_{T} of the leading jet (b) p_{T} of true b-jets

Figure 7.6.: Normalised distributions of transverse momenta of the leading jet (a) in simulated $t\bar{t}$, single top and signal events after selecting the τ_{had} jet. Figure (b) shows the transverse momenta of the selected b-jets that could be matched to a true b-quark in the $t\bar{t}$, single top and the b-quark associated Higgs boson production processes. All signal distributions are shown for the parameters $m_A = 150\,\text{GeV}$ and $\tan\beta = 20$.

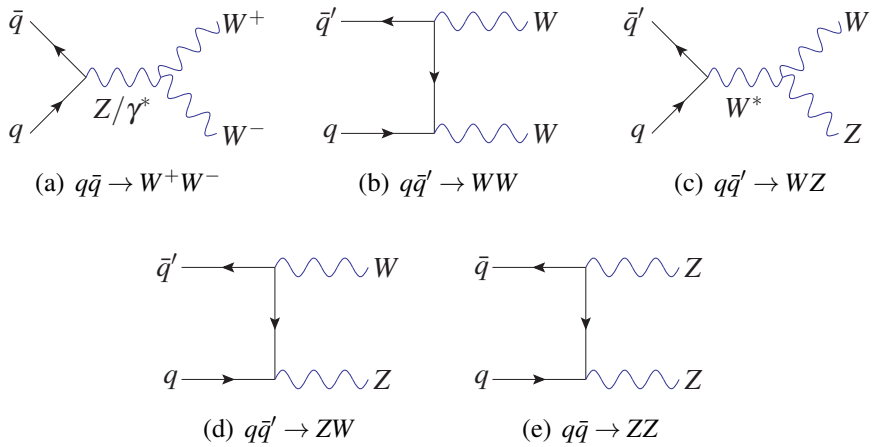

(a) $q\bar{q} \to W^+W^-$ (b) $q\bar{q}' \to WW$ (c) $q\bar{q}' \to WZ$

(d) $q\bar{q}' \to ZW$ (e) $q\bar{q} \to ZZ$

Figure 7.7.: Dominant tree-level di-boson production mechanisms.

only strong interactions like $q\bar{q} \to q'\bar{q}'$ and the production of W/Z bosons with their subsequent hadronic decays, e.g. $W \to q\bar{q}'$.

The multi-jet production processes provide a highly reducible source of background events as for most processes one quark or gluon jet is selected as the light lepton and a second jet as a τ_{had}. The corresponding low misidentification rates are compensated by large production cross sections that exceed the signal production cross sections by many orders in magnitude. In addition, true leptons might be produced in heavy flavour quark decays. In these events, which are expected to dominate the multi-jet background contribution in the search for Higgs bosons produced in association with b-jets, the leptons from heavy flavour quark decays are usually accompanied by additional energy depositions in the calorimeters and close-by tracks of other electrically charged particles. Therefore, isolation requirements imposed on the selected leptons effectively suppress this source of background events. The missing transverse momentum in multi-jet events is predominantly originating from mis-measured jet energies. The corresponding distribution is therefore centered at low values around zero, which can be exploited to suppress this background.

The understanding of this background source is critical for the search presented here. Given their large production cross sections in combination with the expected low event selection efficiencies, the simulation of these processes with sufficient statistics is not applicable with the given resources. Furthermore, the Monte Carlo predictions for the involved processes are subject to large uncertainties on the cross sections and the lepton and τ_{had} misidentification rates of jets. For these reasons a technique, denoted as the *ABCD method*, has been developed to estimate the contribution of the multi-jet background from the p–p collision data themselves. A detailed description of the procedure is given in Section 7.6.5.

7.3.6. Summary of the Background Processes and Cross Sections

A summary of the most important background processes for the search presented here is given in Table 7.2. In addition, their production cross sections are listed, taking into account relevant branching ratios. The multi-jet production cross section is not listed in this table as this background is estimated completely from the data.

7.4. $\tau^+\tau^-$ Mass Reconstruction

As neutrinos are produced in the two τ lepton decays of the signal processes, the reconstruction of the invariant $\tau^+\tau^-$ mass, i.e. the mass of the Higgs boson, is not straight forward. A simple

Process	Cross section [× BR] (pb)	Perturbative Order
$W\to \ell\nu_\ell$+jets ($\ell = e,\mu,\tau$)	10.46×10^3	NNLO [117]
$Z/\gamma^*\to \ell^+\ell^-$+jets ($m_{\ell\ell}$ >40 GeV)	1.07×10^3	NNLO [117]
$Z/\gamma^*\to \ell^+\ell^-$+jets (10 GeV< $m_{\ell\ell}$ <40 GeV)	3.89×10^3	NNLO [117]
$t\bar{t}$	164.6	NLO+NNLL [119, 120]
Single top: t,s and Wt-channel	58.7, 3.9, 13.1	NLO+NNLL [121–123]
Di-boson: WW, WZ and ZZ	46.2, 18.0, 5.6	NLO [80, 124] / NNLO [81]
$gg\to h/A/H\to\tau_{\text{lep}}\tau_{\text{had}}$	28.2	NNLO+NLO [87, 88]
$b\bar{b}\,h/A/H\to\tau_{\text{lep}}\tau_{\text{had}}$	19.5	NNLO [89]

Table 7.2.: Summary of the dominant background processes and their cross sections; relevant branching ratios (BR) are taken into account. Signal cross sections for the parameter choice m_A =120 GeV and $\tan\beta = 40$ are given for comparison.

technique to approximate its true value is to reconstruct the *visible mass* of the $\tau^+\tau^-$ system that is defined as the invariant mass of the visible τ lepton decay products, the identified lepton and the hadrons in the τ_{had} jet. This method neglects the neutrino momenta and therefore suffers from a low mass resolution. A more sophisticated mass reconstruction technique that includes the measured missing transverse momentum in its calculations to account for the neutrino momenta is denoted as the *Missing Mass Calculator* (MMC) [125]. By exploiting the information on $E_{\text{T}}^{\text{miss}}$ and the visible τ lepton decay products and the knowledge gathered from simulated $\tau^+\tau^-$ system decays, a good approximation for the true invariant Higgs boson mass can be computed. This approximation is denoted as the *MMC mass* $m_{\tau\tau}^{MMC}$ in the following.

The $\tau_{\text{lep}}\tau_{\text{had}}$ decay of the $\tau^+\tau^-$ pair is described by the following system of four equations:

$$\begin{aligned}
M_{\tau_1}^2 &= m_{\text{mis}_1}^2 + m_{\text{vis}_1}^2 + 2\sqrt{p_{\text{vis}_1}^2 + m_{\text{vis}_1}^2}\sqrt{p_{\text{mis}_1}^2 + m_{\text{mis}_1}^2} - 2p_{\text{vis}_1}p_{\text{mis}_1}\cos\Delta\theta_{vm_1}\,,\\
M_{\tau_2}^2 &= m_{\text{vis}_2}^2 + 2\sqrt{p_{\text{vis}_2}^2 + m_{\text{vis}_2}^2}\sqrt{p_{\text{mis}_2}^2} - 2p_{\text{vis}_2}p_{\text{mis}_2}\cos\Delta\theta_{vm_2}\,,\\
E_x^{miss} &= p_{\text{mis}_1}\sin\theta_{\text{mis}_1}\cos\phi_{\text{mis}_1} + p_{\text{mis}_2}\sin\theta_{\text{mis}_2}\cos\phi_{\text{mis}_2}\,,\\
E_y^{miss} &= p_{\text{mis}_1}\sin\theta_{\text{mis}_1}\sin\phi_{\text{mis}_1} + p_{\text{mis}_2}\sin\theta_{\text{mis}_2}\sin\phi_{\text{mis}_2}\,.
\end{aligned} \tag{7.1}$$

The $p_{\text{vis}_{1,2}}$, $m_{\text{vis}_{1,2}}$, $\theta_{\text{vis}_{1,2}}$ are the momenta, invariant masses and polar angles of the visible τ

decay products. The E_x^{miss} and E_y^{miss} are the x- and y-components of the missing transverse momentum and $M_{\tau_{1,2}} = 1.777\,\text{GeV}$ are the invariant mass of the τ lepton [18]. The momentum $\vec{p}_{\text{mis}_2}$ of the neutrino produced in the τ_{had} decay and the combined momentum $\vec{p}_{\text{mis}_1}$ and invariant mass m_{mis_1} of the di-neutrino system produced in the leptonic τ decay are the unknowns in these equations. The angles $\Delta\theta_{vm_{1,2}}$ between the vectors $\vec{p}_{\text{mis}_{1,2}}$ and $\vec{p}_{\text{vis}_{1,2}}$ for each of the two τ decay products can be expressed in terms of the other variables.

Given these equations and parameters the invariant mass of the $\tau^+\tau^-$ system cannot be computed analytically as the number of unknowns exceeds the number of constraints. However, some solutions to this system of equations are more likely than others. The information used by the Missing Mass Calculator to evaluate their corresponding probabilities is the three-dimensional angle $\Delta\theta_{3D}$ between the directions of the visible and invisible decay products of a τ lepton.

To find those values for the unknowns resulting in the highest probability for the corresponding solution the system of Equations (7.1) is solved for any point in a grid of the $(\phi_{\text{mis}_1}, \phi_{\text{mis}_2})$ parameter space. An additional scan for m_{mis_1} is performed to account for the unknown invariant mass of the di-neutrino system produced in the leptonic τ decay. The effect of the finite resolution for the missing transverse momentum measurement is taken into account by varying the two components E_x^{miss} and E_y^{miss} with boundaries chosen according to the measured resolution of $E_{\text{T}}^{\text{miss}}$. For each of the resulting scan points the vectors $\vec{p}_{\text{mis}_{1,2}}$ are defined and the angles $\Delta\theta_{3D\ 1,2}$ are computed for the current momenta $\vec{p}_{\text{mis}_{1,2}}$. Given these angles the probability of the current parameter configuration is calculated from probability density functions for $\Delta\theta_{3D\ 1,2}$ that are extracted from simulated $Z/\gamma^* \to \tau^+\tau^-$ decays. Hence, the multi-dimensional parameter scan provides a set of invariant $\tau^+\tau^-$ masses and their corresponding probabilities. These are used to model a probability density distribution for the invariant $\tau^+\tau^-$ mass. The position of the maximum of this distribution defines the final estimate for the MMC mass $m_{\tau\tau}^{\text{MMC}}$.

The performance of the above procedure has been evaluated in Ref. [125]. Simulated $Z/\gamma^* \to \tau^+\tau^-$ events have been compared to simulated Standard Model Higgs boson decays into $\tau^+\tau^-$ ($H \to \tau^+\tau^-$), considering the gluon-fusion production mode of the Higgs bosons and assuming masses of $m_H = 115\,\text{GeV}$ and $130\,\text{GeV}$. All events have been generated with the PYTHIA event generator for $p\bar{p}$ collisions at a centre-of-mass energy of $\sqrt{s} = 1.96\,\text{TeV}$. Events were selected in which the visible decay products of both τ lepton decays satisfy $p_{\text{T}} > 10\,\text{GeV}$. The missing transverse momentum was calculated as the combined transverse momentum of all neutrinos from both τ decays and was required to be above $10\,\text{GeV}$. Since all of these properties were computed at the generator level, an ideal detector resolution was assumed. For events passing the above selection criteria the MMC mass $m_{\tau\tau}^{\text{MMC}}$ was calculated.

For $H \to \tau^+\tau^-$ events ($m_H = 115\,\text{GeV}$) the corresponding distributions are shown in Fig. 7.8 (a) for all possible decay modes of the $\tau^+\tau^-$ system ($\tau_{\text{lep}}\tau_{\text{lep}}$, $\tau_{\text{lep}}\tau_{\text{had}}$ and $\tau_{\text{had}}\tau_{\text{had}}$). All distributions are centered around the true value of the Higgs boson mass, reflecting the good performance of the MMC algorithm. A decrease in the resolution of the reconstructed $\tau^+\tau^-$ mass with increasing number of neutrinos produced in the τ lepton decays is observed which is a consequence of the increasing number of unknowns in the system of Equations (7.1).
A comparison of the $m_{\tau\tau}^{\text{MMC}}$ mass distributions in simulated $Z/\gamma^* \to \tau^+\tau^-$ and $H \to \tau^+\tau^-$ events for $m_H = 115\,\text{GeV}$ and $130\,\text{GeV}$ is shown in Fig. 7.8 (b), assuming the $\tau_{\text{had}}\tau_{\text{had}}$ decay mode of the Z and Higgs bosons. The comparison shows the good performance of the MMC algorithm which is reflected by the clearly distinguishable mass peaks.
Detailed studies of these and further distributions show that the MMC algorithm provides a good approximation of the true invariant Higgs boson mass with resolutions of 13–20% [125], depending on the kinematics and decay modes of the two τ leptons. For resonant $\tau^+\tau^-$ decays, like decays of Z and Higgs bosons, the efficiency to find a solution with the above scan procedure is about 99%, i.e. in less than about 1% of all cases the system of Equations (7.1) cannot be solved for any of the grid points in the $(\phi_{\text{mis}_1}, \phi_{\text{mis}_2})$-parameter space. For non-resonant background processes slightly lower efficiencies are observed, depending on the event kinematics.

7.5. Topological Event Selection

A selection has been developed to prefer events featuring the signal topology and to suppress the backgrounds. The particles used to determine the event properties are reconstructed using the algorithms described in Chapter 6 and selected as presented in Section 7.5.1. Using these objects, a basic signal candidate event selection is defined in Section 7.5.2. Further requirements are applied to the resulting event sample, depending on reconstructed event properties. These additional selections are presented in Sections 7.5.3 and 7.5.4.

7.5.1. Pre-selection of Objects

The following identification and selection criteria are applied to the reconstructed particle candidates. These criteria ensure a high selection efficiency for the signal processes as well as large rejection rates against misidentified particles.

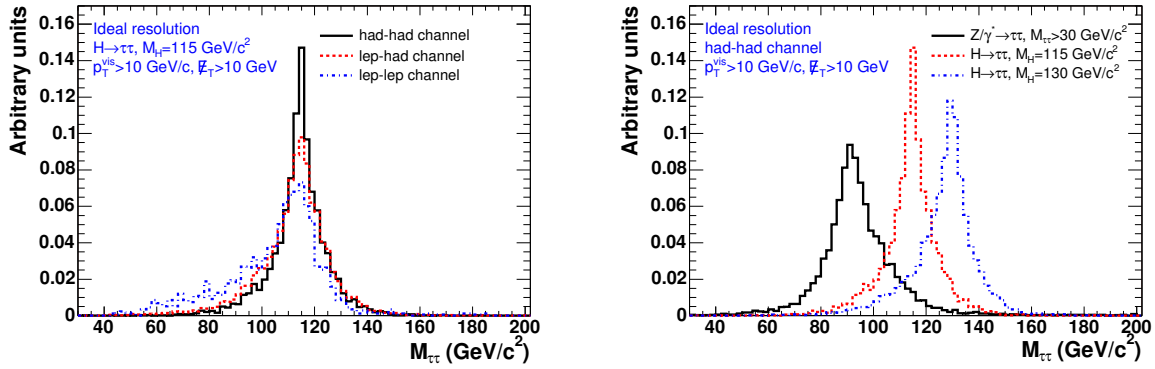

(a) (b)

Figure 7.8.: Figure (a) shows the distribution of the reconstructed MMC mass $m_{\tau\tau}^{\mathrm{MMC}}$ in $H \to \tau^+\tau^-$ events ($m_H = 115\,\mathrm{GeV}$) for the three possible $\tau^+\tau^-$ final states $\tau_{\mathrm{had}}\tau_{\mathrm{had}}$ (solid line), $\tau_{\mathrm{lep}}\tau_{\mathrm{had}}$ (dashed line) and $\tau_{\mathrm{lep}}\tau_{\mathrm{lep}}$ (dashed-dotted line). Figure (b) shows the reconstructed $m_{\tau\tau}^{\mathrm{MMC}}$ mass in simulated $Z/\gamma^* \to \tau^+\tau^-$ and $H \to \tau^+\tau^-$ events for the $\tau_{\mathrm{had}}\tau_{\mathrm{had}}$ final state and Higgs boson masses of $m_H = 115\,\mathrm{GeV}$ and $130\,\mathrm{GeV}$. All results are obtained assuming an ideal detector resolution and all distributions are normalised to a unit area. Both figures are taken from Ref. [125].

Electrons

Electrons are selected with transverse energies of $E_{\mathrm{T}} > 15\,\mathrm{GeV}$ and within the pseudorapidity range $|\eta| < 2.47$, but outside of the transition region between the barrel and end-cap calorimeters ($1.37 < |\eta| < 1.52$). In addition, they are required to pass the *medium* criteria of the electron identification algorithm. The reconstructed isolation variable $E_{\mathrm{T}}^{\Delta\mathrm{R}=0.2}$ must be less than 8% compared to the total electron energy, i.e. the candidate must satisfy the condition $E_{\mathrm{T}}^{\Delta\mathrm{R}=0.2} / E_{\mathrm{T}}^{\mathrm{Cluster}} < 8\%$. The isolation from close-by tracks relative to the reconstructed energy of the electron must be less than 6%, i.e. $p_{\mathrm{T}}^{\Delta\mathrm{R}=0.4} / E_{\mathrm{T}}^{\mathrm{Cluster}} < 6\%$.

Muons

Muons reconstructed within the central detector region ($|\eta| < 2.5$) are selected with transverse momenta of $p_{\mathrm{T}} > 10\,\mathrm{GeV}$. Cosmic-ray muons and those from beam-induced backgrounds are rejected by requiring the longitudinal impact parameter of the associated Inner Detector track to be below 1 cm.

Selection of τ_{had} Jets

Reconstructed τ_{had} candidates are selected within the central detector region ($|\eta| < 2.5$) and with transverse momenta above 20 GeV. In addition, exactly one or three high-quality tracks must be associated to the candidate, resulting in a total measured electric charge of $Q = \pm 1$. The identification quality criteria applied are those with *medium* τ_{had} selection efficiency for the discrimination against both electrons and jets (Boosted Decision Trees). In addition, the cut-based selection to reject muons is applied.

Selection of Jets and b-Jets

Reconstructed jets are selected with $E_T > 20$ GeV and within the pseudorapidity range $|\eta| < 2.5$. Rare events containing jets with associated out-of-time activity or calorimeter noise are discarded [115]. To reject jets produced in pile-up collisions the sum of transverse momenta of all associated tracks is computed. Only jets are taken into account for which at least three-quarters of this sum is due to tracks matched to the primary vertex of the event [126]. For jets produced in pile-up collisions this fraction is lower in average.

The MV1 algorithm is used to identify b-jets. The selection requirement with a high b-jet selection efficiency of about 70% in simulated $t\bar{t}$ events is applied as the transverse momenta of b-jets produced in the signal processes are very low.

Overlap Removal

The interpretation of the detector signatures of particles is not unique. As a consequence one single particle might be reconstructed as several distinct objects. However, a priority ranking of the identification techniques can be defined, based on their reconstruction efficiencies and background rejection power. Muons, for example, are much easier to distinguish from other particles as τ_{had} jets. In defining such a ranking the double counting of particles can be avoided and potential ambiguities are resolved. For the results presented here muon candidates, electron candidates, τ_{had} candidates and jet candidates are selected in this order of priority. If two candidates of the above object types overlap with each other geometrically within a cone with radius parameter $\Delta R = 0.2$, only the one of the higher priority type is maintained for further investigations of the event. The object of the lower priority type is discarded. This procedure is denoted as *overlap removal*.

7.5.2. Basic Event Selection

The data quality requirements described in Section 7.1 are applied to both the simulated and real collision data. A muon or electron is required to trigger the event with trigger choices depending on the instantaneous luminosity conditions (see Section 7.1). Exactly one isolated electron or muon is required in events selected by the electron or muon triggers, respectively. The selected electron needs to further satisfy the *tight* criteria of the electron identification algorithm. From the preselected muons only those are considered for which a reconstructed Inner Detector track and a stand-alone muon track could be combined (combined muons). Furthermore, the selected muon is required to be isolated from additional activity in the Inner Detector and the calorimeter. Similar to the pre-selection of electrons, the isolation criteria imposed on the muon are $E_{\mathrm{T}}^{\Delta\mathrm{R}=0.2}/p_{\mathrm{T}} < 4\%$ and $p_{\mathrm{T}}^{\Delta\mathrm{R}=0.4}/p_{\mathrm{T}} < 6\%$. The transverse momenta thresholds on the selected leptons are raised from those listed in Section 7.5.1 to $p_T > 25\,\mathrm{GeV}$ for electrons and $p_T > 20\,\mathrm{GeV}$ for muons. These thresholds guarantee that the selected leptons reside on the efficiency plateaus of the corresponding trigger selections and therefore threshold effects due to the trigger turn-on behaviour can be avoided.

Events containing a second pre-selected light lepton, i.e. a muon or an electron passing the selection criteria presented in Section 7.5.1, are discarded. This requirement especially suppresses the $Z/\gamma^* \to \ell^+\ell^-$ background processes and results in orthogonal event selections for the searches in the $\tau_{\mathrm{e}}\tau_{\mathrm{had}}$ and $\tau_{\mu}\tau_{\mathrm{had}}$ final states.

In addition to exactly one isolated lepton, exactly one τ_{had} jet of opposite sign electric charge is required to be identified. The charge requirement effectively suppresses background events containing quark or gluon jets that are misidentified as τ_{had} candidates.

An upper threshold on the transverse mass M_{T} is applied to reduce the contribution of $W+$jets and top background processes. This quantity is computed from the missing transverse momentum $E_{\mathrm{T}}^{\mathrm{miss}}$, the transverse momentum p_{T}^{ℓ} of the selected light lepton and the azimuthal distance $\Delta\phi$ in between the directions of those two quantities as

$$M_{\mathrm{T}} = \sqrt{2\, p_{\mathrm{T}}^{\ell}\, E_{\mathrm{T}}^{\mathrm{miss}} (1 - \cos\Delta\phi)}\,. \tag{7.2}$$

A cut at $M_{\mathrm{T}} < 30\,\mathrm{GeV}$ results in a high signal efficiency and an effective background suppression, as can be seen in Fig. 7.4.

At this stage of the event selection the event sample is split into two parts, depending on the presence or absence of an identified b-jet; the resulting event samples are denoted as the *b-tagged* and *b-vetoed* samples, respectively. The requirement for a b-jet enhances the relative

contribution of the b-quark associated Higgs boson production mode to a hypothetical signal in data. Since in the corresponding underlying processes further jets are produced solely in initial or final state gluon radiation processes, their transverse momenta are lower in average than the transverse momentum of the b-jet. Therefore, the b-jet requirement is only tested on the one jet in each event which features the largest transverse momentum. This jet is denoted as the *leading jet* in the following.

7.5.3. Further Requirements on the b-Tagged Event Sample

Events in which the leading jet satisfies the b-jet selection criteria enter the b-tagged sample. The requirement for a b-jet strongly reduces the contributions of several background sources and enhances the fraction of t-quark production processes in the total background composition. In order to reduce the contribution of this background, the transverse momentum of the leading jet is restricted to values below 50 GeV (see Fig. 7.6).
The resulting signal regions containing either selected electrons or muons are dominated by the irreducible $Z/\gamma^* \to \tau^+\tau^-$ and the multi-jet production processes.
A hypothetical signal in these regions would be originating from the b-quark associated production mode only; the gluon-fusion process is strongly suppressed by the b-jet requirement (see Section 7.5.6).

7.5.4. Further Requirements on the b-Vetoed Event Sample

Events in which no jet was reconstructed or in which the leading jet does not satisfy the b-jet identification criteria enter the b-vetoed sample. The multi-jet production processes contribute significantly to the background composition at this stage of the event selection. To reduce this contribution the reconstructed missing transverse momentum is restricted to values above 20 GeV. For multi-jet production processes this variable is centered at low values. This is shown in Fig. 7.9 in which the $E_{\text{T}}^{\text{miss}}$ distribution in data is compared to the expectations for all backgrounds but multi-jet production. The discrepancies at low values for $E_{\text{T}}^{\text{miss}}$ indicate the presence of the multi-jet background.
The final signal regions for the $\tau_{\text{e}}\tau_{\text{had}}$ and the $\tau_{\mu}\tau_{\text{had}}$ final states are dominated by the irreducible $Z/\gamma^* \to \tau^+\tau^-$ background process.
A hypothetical signal would be composed of a mixture of Higgs bosons produced in the gluon-fusion and the b-quark associated production modes.

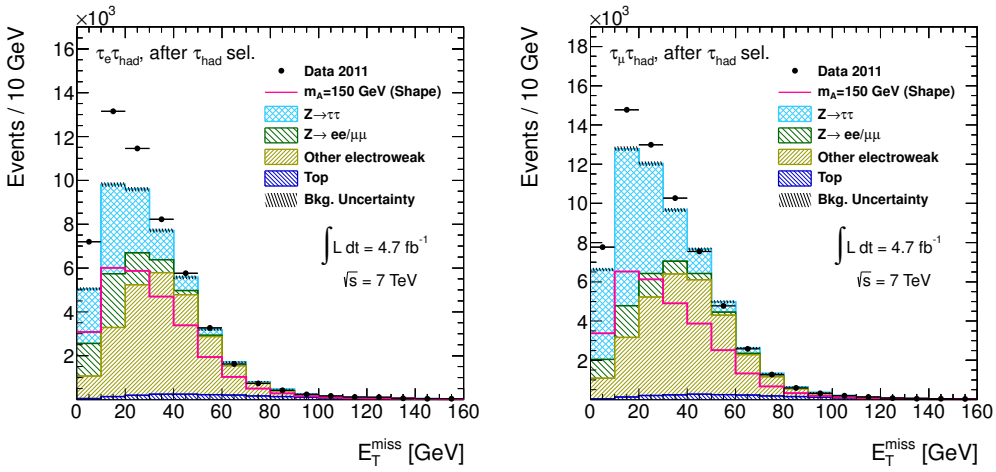

(a) $\tau_e\tau_{had}$ final state (b) $\tau_\mu\tau_{had}$ final state

Figure 7.9.: Missing transverse momentum E_T^{miss} after selecting the τ_{had} jet in event samples containing electrons (a) or muons (b). The data are compared to the background expectations. The contributions of the di-boson and $W+$ jets backgrounds are combined and labelled "Other electroweak". The multi-jet background is not included in the background expectations – its presence is indicated by the discrepancies centered at low values for E_T^{miss}. The expected distribution for a signal is shown for the parameters m_A=150 GeV and $\tan\beta$=20 and normalised to an arbitrary scale. The uncertainties shown are of statistical nature.

7.5.5. Summary of the Event Selection

The topological event selection described above can be summarised as follows:

1. Events are pre-selected using single-lepton triggers and several data quality criteria are applied (see Section 7.1).
2. Either exactly one isolated electron of *tight* quality and satisfying $p_{\text{T}}^{e} > 25\,\text{GeV}$ or one isolated combined muon satisfying $p_{\text{T}}^{\mu} > 20\,\text{GeV}$ is required in events selected by the electron or muon trigger, respectively.
3. Events containing additional muons or isolated *medium* quality electrons with $p_{\text{T}} > 10\,\text{GeV}$ and $p_{\text{T}} > 15\,\text{GeV}$, respectively, are rejected.
4. Exactly one identified τ_{had} with $p_{\text{T}} > 20\,\text{GeV}$ and of opposite sign electric charge with respect to the light lepton is required.
5. The transverse mass, M_{T}, is restricted to $M_{\text{T}} < 30\,\text{GeV}$.
6. The event sample is split according to whether the leading jet passes the b-jet selection criteria (b-tagged sample) or fails to pass these (b-vetoed sample). Additional selection criteria imposed on the resulting event samples are:
   - b-tagged sample: The leading jet, the b-jet, must satisfy $p_T < 50\,\text{GeV}$.
   - b-vetoed sample: The missing transverse momentum is restricted to $E_T^{miss} > 20\,\text{GeV}$.

These selection criteria result in four orthogonal signal regions populated with events containing either electrons or muons and containing leading jets being identified as b-jets or not.

7.5.6. Observed Data and Predicted Event Yields

The numbers of observed data events satisfying the above selection criteria are listed in Table 7.3. The same table contains the expected event yields of the background processes as predicted by simulation. The $t\bar{t}$ and $W+$jets background process normalisations are corrected to data (see Sections 7.6.2 and 7.6.3). The contributions of the $Z/\gamma^* \to \ell^+\ell^-$ background to the b-tagged samples are corrected as described in Section 7.6.4. Data driven predictions for the $Z/\gamma^* \to \tau^+\tau^-$ and multi-jet production processes are derived in the following sections. Signal expectations after the full event selection are shown in Table 7.4 for both Higgs boson production mechanisms and several combinations of the parameters m_A and $\tan\beta$.

$\tau_\mu\tau_{\text{had}}$ final state						
	Data	$Z/\gamma^*\to\tau^+\tau^-$	$W\to\ell\nu_\ell$	$Z/\gamma^*\to\ell^+\ell^-$	Top	di-boson
Common sel.						
e and τ_{had} sel.	81488	23490 ± 90	36850 ± 240	7820 ± 80	2460 ± 11	630 ± 9
Charge req.	63488	23080 ± 90	28240 ± 200	5120 ± 60	2090 ± 10	490 ± 7
$M_{\text{T}} \leq 30\,\text{GeV}$	20426	13850 ± 70	2140 ± 50	1720 ± 35	300 ± 4	68.0 ± 2.6
b-tagged sample						
Passes b-jet req.	429	135 ± 6	33 ± 5	13 ± 4	146 ± 4	2.2 ± 0.5
$p_{\text{T}}^{b\text{-jet}} < 50\,\text{GeV}$	202	76 ± 5	19 ± 4	8.3 ± 2.3	14.5 ± 0.8	0.75 ± 0.33
b-vetoed sample						
Fails b-jet req.	19997	13720 ± 70	2110 ± 50	1710 ± 40	152 ± 4	65.8 ± 2.6
$E_{\text{T}}^{\text{miss}} > 20\,\text{GeV}$	6424	4810 ± 40	781 ± 26	351 ± 16	105.1 ± 2.2	37.5 ± 1.9

$\tau_{\text{e}}\tau_{\text{had}}$ final state						
	Data	$Z/\gamma^*\to\tau^+\tau^-$	$W\to\ell\nu_\ell$	$Z/\gamma^*\to\ell^+\ell^-$	Top	di-boson
Common sel.						
μ and τ_{had} sel.	74200	12250 ± 60	31030 ± 220	10990 ± 90	2290 ± 10	548 ± 9
Charge req.	52630	11970 ± 60	24110 ± 190	7320 ± 80	1940 ± 10	422 ± 7
$M_{\text{T}} \leq 30\,\text{GeV}$	16454	6940 ± 50	1890 ± 50	3110 ± 50	290 ± 4	57.1 ± 2.6
b-tagged sample						
Passes b-jet req.	378	80 ± 5	32 ± 9	29 ± 5	142.4 ± 2.6	2.1 ± 0.4
$p_{\text{T}}^{b\text{-jet}} < 50\,\text{GeV}$	175	39 ± 4	18 ± 8	19 ± 4	15.1 ± 0.8	0.95 ± 0.35
b-vetoed sample						
Fails b-jet req.	16076	6860 ± 50	1860 ± 45	3090 ± 50	151.5 ± 2.8	55.0 ± 2.5
$E_{\text{T}}^{\text{miss}} > 20\,\text{GeV}$	5034	2640 ± 28	740 ± 25	700 ± 20	105.6 ± 2.2	29.3 ± 1.7

Table 7.3.: Numbers of events observed in data and expected numbers of events for simulated Standard Model background processes passing the individual selection criteria. Event yields for simulated samples are normalised to the total integrated luminosity of the data sample ($4.7\,\text{fb}^{-1}$). The $W+$ jets and $t\bar{t}$ production processes are normalised to data as described in Sections 7.6.2 and 7.6.3, respectively. The $Z/\gamma^*\to\ell^+\ell^-$ background contributions to the b-tagged samples are corrected, as well (Section 7.6.4). The final selection criteria ("$p_{\text{T}}^{b\text{-jet}} < 50\,\text{GeV}$" and "$E_{\text{T}}^{\text{miss}} > 20\,\text{GeV}$") additionally imply that the invariant $\tau^+\tau^-$ mass, $m_{\tau\tau}^{\text{MMC}}$, could be reconstructed successfully.

	$\tau_\mu\tau_{\text{had}}$ final state			
Production	b-tagged sample		b-vetoed sample	
($\times BR(\Phi \to \tau_{\text{lep}}\tau_{\text{had}})$)	$\tan\beta$ =20	$\tan\beta$ =30	$\tan\beta$ =20	$\tan\beta$ =30
m_A=150 GeV				
$b\bar{b}\,h/A/H$	20.4 ± 1.4	45.9 ± 3.1	174 ± 4	393 ± 9
$gg \to h/A/H$	1.2 ± 0.4	2.4 ± 0.8	115 ± 4	227 ± 8
m_A=200 GeV				
$b\bar{b}\,h/A/H$	8.5 ± 0.9	19.3 ± 2.1	96.5 ± 3.1	219 ± 7
$gg \to h/A/H$	0.61 ± 0.14	1.09 ± 0.26	54.9 ± 1.4	96.1 ± 2.4
m_A=300 GeV				
$b\bar{b}\,h/A/H$	0.47 ± 0.03	2.53 ± 0.20	26.4 ± 0.7	63.8 ± 1.6
$gg \to h/A/H$	0.26 ± 0.08	0.36 ± 0.09	22.8 ± 0.8	28.8 ± 0.9

	$\tau_e\tau_{\text{had}}$ final state			
Production	b-tagged sample		b-vetoed sample	
($\times BR(\Phi \to \tau_{\text{lep}}\tau_{\text{had}})$)	$\tan\beta$ =20	$\tan\beta$ =30	$\tan\beta$ =20	$\tan\beta$ =30
m_A=150 GeV				
$b\bar{b}\,h/A/H$	15.0 ± 1.2	34.0 ± 2.7	138 ± 4	314 ± 8
$gg \to h/A/H$	1.2 ± 0.4	2.3 ± 0.9	98.9 ± 3.4	195 ± 7
m_A=200 GeV				
$b\bar{b}\,h/A/H$	8.2 ± 0.9	18.6 ± 2.0	21.1 ± 3.0	206 ± 7
$gg \to h/A/H$	0.55 ± 0.15	0.89 ± 0.25	27 ± 1.3	80.5 ± 2.2
m_A=300 GeV				
$b\bar{b}\,h/A/H$	2.04 ± 0.18	4.9 ± 0.4	24.5 ± 0.6	59.5 ± 1.6
$gg \to h/A/H$	0.26 ± 0.10	0.31 ± 0.10	20.3 ± 0.8	26.1 ± 0.8

Table 7.4.: Expected numbers of signal events after the full event selection for the two Higgs boson production mechanisms and several hypotheses for the parameters m_A and $\tan\beta$. Expectations are normalised to the total integrated luminosity of the data sample (4.7 fb^{-1}). Only events are considered for which the invariant $\tau^+\tau^-$ mass, $m_{\tau\tau}^{\text{MMC}}$, could be reconstructed successfully.

7.6. Data-Driven Background Estimation Techniques

The final interpretation of the observed data requires an exact knowledge of the potential signal contributions and the contributions from the various background processes to the signal regions. For all background processes a prediction for these can be derived from simulated event samples. However, such predictions are usually subject to large systematic uncertainties originating from the limited precision of the simulations and the underlying theory models (see Section 7.8).

A different approach is to use the data themselves to estimate the contributions of specific background processes or to correct the Monte Carlo predictions to the data observed in dedicated control regions. For the study presented here several techniques have been used to follow this approach for almost every relevant background. The individual methods and estimates are described in the following sections, the corresponding systematic uncertainties are discussed separately in Section 7.8. A focus is set on the corrections for the $W+$ jets (Section 7.6.2) and $t\bar{t}$ (Section 7.6.3) production processes and the estimation of the multi-jet background contributions from the data (Section 7.6.5), since the corresponding techniques have been developed during the course of this thesis.

7.6.1. $Z/\gamma^* \to \tau^+\tau^-$ Background Estimation using the τ-Embedding Technique

The $Z/\gamma^* \to \tau^+\tau^-$ process forms a largely irreducible background. Hence, an exact prediction for the contributions of this background to the finally selected event samples is essential. A control sample of this process cannot be selected from the data without significant contamination from a hypothetical signal. Therefore, the search presented here relies on the *τ-embedding technique* to estimate the $Z/\gamma^* \to \tau^+\tau^-$ background contributions partially from the data. The τ-embedding method selects $Z/\gamma^* \to \mu^+\mu^-$ events from the data and modifies these: the muons are removed from the data event and replaced by simulated τ leptons with identical kinematics. Hence, in the resulting event only the kinematics and the detector response to the τ decay products are taken from simulations. The underlying event activity, additional jets and the pile-up conditions originate from the real p–p collision.

The embedding procedure is based on several assumptions. The first is that a clean $Z/\gamma^* \to \mu^+\mu^-$ event sample with very high purity and without significant signal contamination can be selected from the data. The second assumption is that the event topology and kinematics of the selected $Z/\gamma^* \to \mu^+\mu^-$ events are identical to those of the $Z/\gamma^* \to \tau^+\tau^-$ process. The latter is true if the difference in masses of τ leptons and muons is neglected, the prior is studied in the following paragraph.

$Z/\gamma^* \to \mu^+\mu^-$ Event Selection

The event selection requires exactly two muons with opposite sign electric charges and transverse momenta above 20 GeV each. A track isolation requirement of $p_{\text{T}}^{\Delta R=0.2}/p_{\text{T}} < 0.2$ largely improves the purity of the resulting event sample. Additionally, the muons are required to have a common primary vertex and the invariant mass of the di-muon system is restricted to values above 55 GeV. This event selection results in a very clean $Z/\gamma^* \to \mu^+\mu^-$ data sample with a purity of approximately 97%, as has been shown with an equivalent event selection in Ref. [127]. Given the very low signal process cross sections and branching ratios for neutral MSSM Higgs boson decays into di-muon pairs, which is of the order of 0.04%, the contamination with a hypothetical signal is expected to be negligible.

Muon Removal Procedure

Based on the selected $Z/\gamma^* \to \mu^+\mu^-$ data the $Z/\gamma^* \to \tau^+\tau^-$ events can be produced. For this purpose, the individual hits assigned to the muon tracks are removed from the event. To remove the energy depositions of the muons in the calorimeters an equivalent $Z/\gamma^* \to \mu^+\mu^-$ event is simulated, taking into account the Z boson kinematics reconstructed from the data event. The simulated detector responses to the muons in this event are used to approximate the energy depositions of the real muons and therefore these depositions are removed from the data event.

τ-Embedding

The Z boson kinematics reconstructed from the data event are further employed to simulate a Z boson decay into a $\tau^+\tau^-$ pair. Since these τ leptons are supposed to replace the muons their kinematics are computed from the momenta of the original muons as $p_\tau = \sqrt{E_\mu^2 - m_\tau^2}$. In this computation the momenta are rescaled to the Z boson rest frame and the different particle masses are taken into account. The resulting simulated $Z/\gamma^* \to \tau^+\tau^-$ event is further processed with TAUOLA to simulate the τ lepton decays and with PHOTOS to add final state radiation off their decay products. In this way a clean $Z/\gamma^* \to \tau^+\tau^-$ event without additional event activity is obtained on which the full ATLAS detector simulation is processed. Detector noise, however, is not simulated as this effect is already included in the data event. The charged particle tracks and the calorimeter depositions in the resulting simulated $Z/\gamma^* \to \tau^+\tau^-$ event are added to the data event from which the muons have been removed. The resulting hybrid event is reconstructed using the usual techniques.

At the current stage of development no trigger is emulated in the τ-embedded $Z/\gamma^* \to \mu^+\mu^-$ data for technical reasons. Therefore, the event yield of this sample is normalised to the event yield obtained for a simulated $Z/\gamma^* \to \tau^+\tau^-$ sample after the visible τ decay products, the light lepton and the τ_{had} jet, have been selected. With this choice no bias is introduced as the τ decay products are taken from simulation in both of the involved event samples.

Method Validation and Purity

The above procedure has been validated extensively in Refs. [128] and [56]. The τ-embedded sample has been compared to simulated $Z/\gamma^* \to \tau^+\tau^-$ events and a good agreement has been observed. Further validation has been performed by embedding simulated muons instead of τ leptons into the $Z/\gamma^* \to \mu^+\mu^-$ data sample. The resulting hybrid sample has been compared to simulated $Z/\gamma^* \to \mu^+\mu^-$ events and no systematic deviations have been observed.

The selected $Z/\gamma^* \to \mu^+\mu^-$ data used for the embedding procedure features a high purity which is a consequence of the good performance of the muon identification techniques and the high production rate of Z bosons in p–p collisions when compared to the background rates. A negligible contamination originates from the $t\bar{t}$ production processes, that also might feature the signature of two isolated muons in final states. This contamination is expected to remain negligible after applying the event selection for the b-vetoed signal regions. After selecting events for the b-tagged event samples, however, the relative amount of $t\bar{t}$ events in the τ-embedded $Z/\gamma^* \to \mu^+\mu^-$ data might be enhanced. To evaluate the purity of the τ-embedded sample in the corresponding signal regions, the magnitude of the potential contamination with $t\bar{t}$ events has been computed. For this purpose, the $Z/\gamma^* \to \mu^+\mu^-$ data event selection and the event selection of the b-tagged signal regions have been applied subsequently to a simulated $t\bar{t}$ event sample. The resulting event yields have been compared to the corresponding event yields of the τ-embedded data. In this way the purity has been estimated to approximately 99% after the full event selection of the b-tagged samples, and to about 96% after the same selection but without restricting the transverse momenta of the leading jets to values below 50 GeV.

7.6.2. Normalisation of the W+jets Background

The contributions of the $W+$ jets production processes to the total background for this search are estimated using simulated event samples. Since the τ_{had} misidentification probability for jets differs in those simulated samples from the true efficiency in data, the estimated event yields after selecting the τ_{had} jet are predicted inaccurately. To correct for this effect, a $W+$ jets control

	$\tau_\mu\tau_{\text{had}}$ Final State		$\tau_e\tau_{\text{had}}$ Final State	
	Opposite Sign	Same Sign	Opposite Sign	Same Sign
$W+$ jets	25350 ± 260	7420 ± 160	18640 ± 220	5400 ± 130
Others	2363 ± 30	744 ± 19	1553 ± 26	424 ± 12
$h/A/H \to \tau_{\text{lep}}\tau_{\text{had}}$ (m_A=150 GeV, $\tan\beta$=20)	82.0 ± 2.9	0.21 ± 0.13	70.8 ± 2.7	0.28 ± 0.15
Data	16078	5801	12494	4810

Table 7.5.: Number of observed events in data and expected event yields in the $W+$jets background control region for the $\tau_\mu\tau_{\text{had}}$ and $\tau_e\tau_{\text{had}}$ final states. "Opposite Sign" and "Same Sign" denote the event samples containing selected light leptons and τ_{had} jets of opposite or same sign electric charges, respectively. All uncertainties shown are of statistical nature. The contributions of the $Z/\gamma^* \to \tau^+\tau^-$, $Z/\gamma^* \to \ell^+\ell^-$, di-boson and Top backgrounds are combined and labelled "Others". The multi-jet background is not included. A hypothetical signal contamination of the data is shown for the parameter choice m_A=150 GeV and $\tan\beta$=20 and includes both production mechanisms.

sample with high purity is selected from the data and a normalisation correction factor for the simulated event sample is derived.

From the data passing the light lepton and the τ_{had} selection criteria events with large transverse masses within the W boson peak region from 70 – 110 GeV are selected. The observed and expected event yields in the resulting control regions containing either electrons or muons and τ_{had} jets of either opposite or same sign electric charges are listed in Table 7.5. A correction for each of these samples is derived by comparing the data to the expected yields in simulated $W+$jets events. In order to not introduce a bias in this comparison, the residual small contaminations from simulated non-$W+$jets processes are subtracted from the data. The potential small contributions from multi-jet production processes, however, cannot be taken into account as the estimation of these require the prior knowledge of all other background contributions. Given the observed data events $n^{e/\mu}_{\text{Data}}$, the number of $W+$jets events $n^{e/\mu}_{W+\text{jets}}$ and events from other processes $n^{e/\mu}_{\text{Others}}$ in the control regions with selected electrons or muons, the corresponding correction factors f^e_W and f^μ_W, respectively, are computed as

$$f^{e/\mu}_W = \frac{n^{e/\mu}_{\text{Data}} - n^{e/\mu}_{\text{Others}}}{n^{e/\mu}_{W+\text{jets}}} \,. \tag{7.3}$$

Given the event yields presented in Table 7.5, the correction factors for the $W+$ jets background in event samples with opposite sign electric charges amount to $f_W^e = 0.587 \pm 0.009$ (stat.) and $f_W^\mu = 0.541 \pm 0.008$ (stat.). Systematic uncertainties on these numbers are discussed in Section 7.8.3. Distinct scale factors in events samples with selected electrons or muons are expected as the different transverse momenta thresholds and isolation quality requirements on the selected light leptons lead to different event kinematics. Furthermore, these requirements lead to different contaminations with multi-jet production processes, which are neglected in the derivation of the scale factors.
The correction factors observed for event samples with same sign electric charges are $f_W^{e,SS} = 0.813 \pm 0.024$ (stat.) and $f_W^{\mu,SS} = 0.682 \pm 0.020$ (stat.). The deviations of those from the factors derived in the regions with opposite sign electric charges result from the different fractions of quark and gluon jets in the corresponding event samples, which is a consequence of the various W boson production processes.

The correction factors derived above are applied to simulated $W+$ jets event samples in the corresponding signal regions and in various control regions for other background estimates. In Fig. 7.10 the transverse mass distributions in data are compared to the expectations from simulations for both the $\tau_e \tau_{had}$ and $\tau_\mu \tau_{had}$ final states, after the τ_{had} jet has been selected and the normalisation correction has been applied to the simulated $W+$ jets event sample. The disagreement at low transverse masses is interpreted to result from the missing multi-jet background contributions that are not included in the background expectations.

The method has been tested for stability by varying the boundary conditions on the transverse mass control region. These have been moved from their nominal values of 70 and 110 GeV to values of 50 and 90 GeV or 90 and 150 GeV. In Table 7.6 the resulting scale factors are compared to the nominal values for event samples with opposite sign charged leptons and τ_{had} jets. Only small deviations within less than two standard deviations of the corresponding statistical uncertainties are observed by modifying the control region definition. To account for these, a conservative systematic uncertainty of 5% is assigned to the normalisation of the $W+$ jets background (see Section 7.8.3).

7.6.3. Normalisation of the $t\bar{t}$ Production Background

The signal region event selections effectively suppress $t\bar{t}$ production processes and only small contributions are predicted by the Monte Carlo simulation, even in the b-tagged event samples. Nevertheless, studied performed during the course of this thesis have shown, that in only about 60% of the remaining $t\bar{t}$ background events a true hadronic τ decay is selected as the τ_{had} jet. The

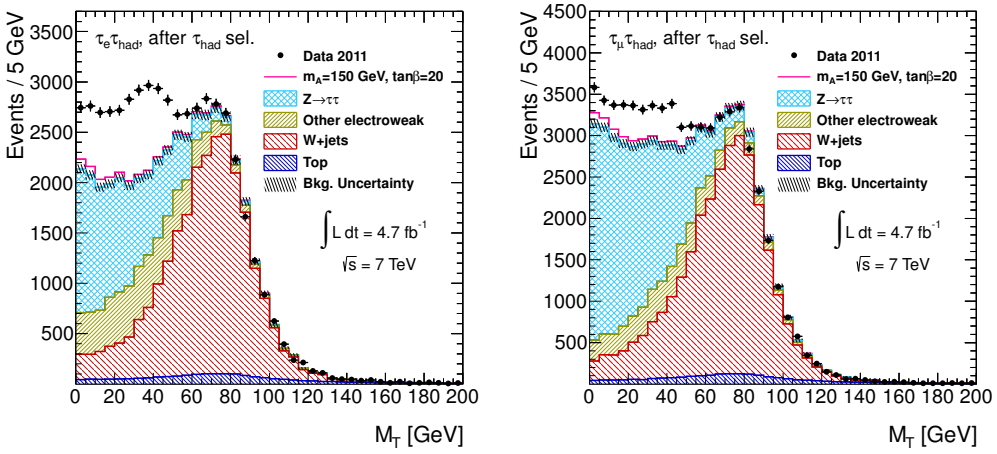

(a) $\tau_e\tau_{had}$ final state (b) $\tau_\mu\tau_{had}$ final state

Figure 7.10.: The transverse mass M_T in the $\tau_e\tau_{had}$ (a) and $\tau_\mu\tau_{had}$ (b) final state event samples after the τ_{had} jet has been selected and the normalisation of the $W+$jets background has been corrected. The data are compared to the background expectation and a hypothetical MSSM signal (m_A=150 GeV and $\tan\beta$=20). The contributions of the di-boson and $Z/\gamma^* \to \ell^+\ell^-$ background processes are combined and labelled "Other electroweak". The disagreement at low transverse masses is interpreted to result from the missing multi-jet background contributions that are not included in the background expectations.

Final	M_T Interval			Maximum	
State	50 – 90 GeV	70 – 110 GeV	90 – 150 GeV	Uncert.	Deviation
$\tau_e\tau_{had}$	0.605 $\pm$ 0.009	0.587 $\pm$ 0.009	0.610 $\pm$ 0.017	3%	4%
$\tau_\mu\tau_{had}$	0.553 $\pm$ 0.007	0.541 $\pm$ 0.008	0.527 $\pm$ 0.013	2%	3%

Table 7.6.: Normalisation correction factors for the $W+$jets background event yields derived from several control regions defined by varying boundary conditions on the transverse mass M_T. Individual factors are given for the $\tau_e\tau_{had}$ and $\tau_\mu\tau_{had}$ final state event samples.

residual 40% of the latter are misidentified quark or gluon jets. As the corresponding misidentification rate in simulated events strongly differs from the true rate in data, the predicted contributions of the $t\bar{t}$ background to the signal regions are overestimated. In order to correct for this a signal free and pure $t\bar{t}$ control region is defined and a normalisation correction factor is derived by comparing the observed event yields in data to those predicted by simulations.

The $t\bar{t}$ control sample is obtained from events satisfying the signal region selection criteria of the b-tagged samples, but without restricting the transverse mass and the transverse momentum of the b-jet. The data control sample is further selected by requiring a second identified b-jet. This requirement does not introduce a bias in the origin of the selected τ_{had} jets, because the relative number of b-jets that are selected as τ_{had} jets is below 5% in $t\bar{t}$ events populating the signal region. A further increase in purity is obtained by requiring a transverse momentum of the leading jet within the range of 50 – 150 GeV. This criterion additionally preserves the orthogonality to the signal regions. The resulting control regions for the $\tau_{\text{e}}\tau_{\text{had}}$ and $\tau_{\mu}\tau_{\text{had}}$ final states are dominated by $t\bar{t}$ production processes with purities above 90%. The corresponding number of events observed in data and the expected contributions from Standard Model processes are presented in Table 7.7. The contributions from $Z/\gamma^{*}\rightarrow\tau^{+}\tau^{-}$ processes have been evaluated using a simulated event sample. The τ-embedded $Z/\gamma^{*}\rightarrow\mu^{+}\mu^{-}$ data might suffer from a small contamination from $t\bar{t}$ production processes, that is significantly enhanced with the control region selection. The use of the τ-embedded sample might therefore lead to a bias in any event yield comparison. A hypothetical contamination from signal events is given for the parameters m_A=150 GeV and $\tan\beta$=20 and contains the contributions from both production mechanisms.

A normalisation correction for the simulated $t\bar{t}$ production processes is derived by comparing the observed data to the expectations. To avoid any bias the residual contaminations from processes other than $t\bar{t}$ production are subtracted from the data. The contamination from multi-jet production processes, however, cannot be taken into account as the estimation of these require the prior knowledge of all other background contributions. Given the observed data events $n^{e/\mu}_{\text{Data}}$, the number of $t\bar{t}$ production events $n^{e/\mu}_{t\bar{t}}$ and events from other processes $n^{e/\mu}_{\text{Others}}$ in the control regions with selected electrons or muons, the corresponding correction factors $r^{e}_{t\bar{t}}$ and $r^{\mu}_{t\bar{t}}$, respectively, are computed as

$$r^{e/\mu}_{t\bar{t}} = \frac{n^{e/\mu}_{\text{Data}} - n^{e/\mu}_{\text{Others}}}{n^{e/\mu}_{t\bar{t}}}\,. \tag{7.4}$$

The normalisation factors derived from the event yields in Table 7.7 are $r^{e}_{t\bar{t}} = 0.82 \pm 0.05$ (stat.) and $r^{\mu}_{t\bar{t}} = 0.94 \pm 0.06$ (stat.) for the $\tau_{\text{e}}\tau_{\text{had}}$ and $\tau_{\mu}\tau_{\text{had}}$ final states, respectively. Again the difference originates from different event kinematics and a potential bias resulting from the neglected

	$\tau_\mu\,\tau_{\text{had}}$ final state	$\tau_e\,\tau_{\text{had}}$ final state	Combined
$t\bar{t}$	361 ± 4	334 ± 4	695 ± 6
Others	25.6 ± 2.4	20.7 ± 2.1	46.3 ± 3.2
$h/A/H \to \tau_{\text{lep}}\tau_{\text{had}}$ (m_A=150 GeV, $\tan\beta$=20)	0.96 ± 0.27	1.89 ± 0.41	2.85 ± 0.49
Data	323	334	657

Table 7.7.: Observed data and expected event yields in the $t\bar{t}$ background control regions for the $\tau_\mu\,\tau_{\text{had}}$ and the $\tau_e\,\tau_{\text{had}}$ event samples, as well as for their statistical combination. All uncertainties shown are of statistical nature. The $Z/\gamma^* \to \tau^+\tau^-$, $Z/\gamma^* \to \ell^+\ell^-$, di-boson, single top and $W+$jets background processes are combined and labelled "Others". The contributions from multi-jet production are not included. A hypothetical signal contamination of the data is shown for the parameter choice m_A=150 GeV and $\tan\beta$=20, and includes the contributions of both production mechanisms.

contributions of multi-jet production processes. Since the expected contributions of the $t\bar{t}$ production processes to the signal regions are small and as the factors quoted above are subject to large statistical uncertainties, the event samples for the two final states are statistically combined and a common normalisation correction is derived. This combination results in a factor of $r_{t\bar{t}} = 0.88 \pm 0.04$ (stat.) that is used to correct the expected $t\bar{t}$ background event yields in all signal regions. Systematic uncertainties on this number are discussed in Section 7.8.3.
In Fig. 7.11 the transverse momenta of the selected b-jets in the b-tagged data sample are compared to the expectations after the corrections to the $t\bar{t}$ and $W+$jets background normalisations have been applied. The distributions are shown individually for the $\tau_e\,\tau_{\text{had}}$ and $\tau_\mu\,\tau_{\text{had}}$ states and without restricting the transverse mass M_{T} and the transverse momentum of the b-jet. Good agreement is observed for large transverse momenta. The disagreement for low transverse momenta is interpreted to result from the missing multi-jet background contributions that are not included in the background expectations.

The method has been validated by testing the stability of the derived scale factor against varying requirements on the transverse mass and the transverse momentum of the leading jet. The modified control regions are defined by a transverse mass within the range of either 0 – 30 GeV, 30 – 70 GeV or 70 – 200 GeV and a transverse momentum of the leading jet within a range of either 50 – 100 GeV or 100 – 150 GeV. Although values for M_{T} in the range of 0 – 30 GeV are unlikely for W boson decays, the corresponding control regions are still dominated by the

	M_{T} Interval			Maximum	
	0 – 30 GeV	30 – 70 GeV	70 – 200 GeV	Uncert.	Deviation
$p_{\mathrm{T}} \in$					
50 – 100 GeV	1.01 $\pm$ 0.14	0.82 $\pm$ 0.08	0.89 $\pm$ 0.06	14%	14%
100 – 150 GeV	0.92 $\pm$ 0.17	0.80 $\pm$ 0.11	0.90 $\pm$ 0.09	18%	9%

Table 7.8.: Measured normalisation correction factors for simulated $t\bar{t}$ event samples. The numbers have been derived from orthogonal control regions defined by the transverse mass M_{T} and the transverse momentum of the leading jet. The resulting event samples for the $\tau_{\mathrm{e}}\tau_{\mathrm{had}}$ and $\tau_{\mu}\tau_{\mathrm{had}}$ final states are statistically combined. These values are to be compared to the nominal value of the scale factor of $r_{t\bar{t}} = 0.88 \pm 0.04$ (stat.).

$t\bar{t}$ background. For each possible combination of the above requirements the scale factor has been re-evaluated for the statistical combination of the $\tau_{\mathrm{e}}\tau_{\mathrm{had}}$ and $\tau_{\mu}\tau_{\mathrm{had}}$ final state event samples and compared to the nominal value. The results are given in Table 7.8. Good agreement of the resulting scale factors and the nominal value is observed, however, within large statistical uncertainties.

7.6.4. b-Jet Selection in Simulated W+jets and $Z/\gamma^* \to \ell^+\ell^-$+jets Events

A precise description of the b-jet properties in simulated events is important for the Higgs boson searches in the b-tagged final states. For two backgrounds with simulated jet content, the $W+$jets and $Z/\gamma^* \to \ell^+\ell^-$+jets backgrounds, methods have been developed to validate or correct the b-jet selection efficiencies in simulated event samples.

b-Jet Selection in Simulated $Z/\gamma^* \to \ell^+\ell^-$+jets Events

A correction for the b-jet selection efficiency in simulated $Z/\gamma^* \to \ell^+\ell^-$+jets events has been derived by comparing the same efficiency in a simulated $Z/\gamma^* \to \tau^+\tau^-$ event sample to that in the τ-embedded $Z/\gamma^* \to \mu^+\mu^-$ data. For this comparison both criteria on the leading jet are applied, the b-jet identification requirement and the restriction to transverse momenta below 50 GeV. The ratio in selection efficiencies results in a correction for the efficiency in the simulated event sample as the jet content in the τ-embedded sample originates from real p–p collisions. For the $\tau_{\mu}\tau_{\mathrm{had}}$ and $\tau_{\mathrm{e}}\tau_{\mathrm{had}}$ final states factors of $f_{Zb}^{\mu} = 1.11 \pm 0.13$ (stat.) and $f_{Zb}^{e} = 1.08 \pm 0.23$ (stat.), respectively, are observed. Although these values are consistent with unity, the factors are applied

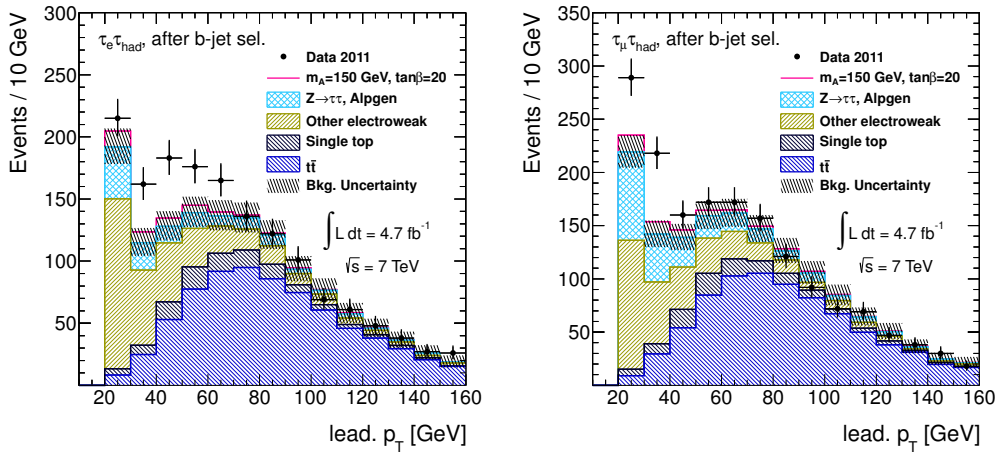

(a) $\tau_e\tau_{\text{had}}$ (b) $\tau_\mu\tau_{\text{had}}$

Figure 7.11.: Transverse momentum of the selected b-jet for the b-tagged $\tau_e\tau_{\text{had}}$ (a) and $\tau_\mu\tau_{\text{had}}$ (b) final state event samples, but without restricting the transverse mass to low values. The data are compared to the background expectation and a hypothetical MSSM signal (m_A=150 GeV and $\tan\beta$=20). The normalisations of the W+ jets and $t\bar{t}$ backgrounds have been corrected. The contributions of the di-boson. W+ jets and $Z/\gamma^* \to \ell^+\ell^-$ background processes are combined and labelled "Other electroweak". The disagreement at low transverse momenta is interpreted to result from the missing multi-jet background contributions that are not included in the background expectations.

to the contributions of simulated $Z/\gamma^* \to \ell^+\ell^-$ processes to the b-tagged signal regions. This is valid as the same Monte Carlo event generator, AlpGen, has been employed to simulate the different Z boson decays and hence the properties of simulated b-jets in the resulting events are expected to be identical.
A potential contamination of the τ-embedded $Z/\gamma^* \to \mu^+\mu^-$ data, especially with events from $t\bar{t}$ production processes, might lead to a bias in the correction factors derived above. The magnitude of this bias has been studied by removing the upper threshold of 50 GeV on the transverse momentum of the leading jet. This leads to a significant increase in the potential contamination and hence any bias would be enhanced. The correction factors resulting from the modified comparison are $f_{Zb}^{\mu\prime} = 1.13 \pm 0.10$ and $f_{Zb}^{e\prime} = 1.27 \pm 0.19$. These values are compatible with the nominal correction factors quoted above, given the large statistical uncertainties.

b-Jet Selection in Simulated *W*+jets Events

Normalisation corrections for simulated $W+$ jets event samples were already derived in Section 7.6.2. However, the efficiency of the subsequent b-jet selection criteria might differ in simulated $W+$ jets events from the true efficiency in data. To validate the $W+$ jets background normalisation in the signal regions of the b-tagged samples the scale factor measurements of Section 7.6.2 have been repeated in an additional control region. The corresponding control samples of events containing either selected electrons or muons are obtained from the data entering the b-tagged samples, but without restricting the transverse mass M_{T} to low values. Instead the latter is required to lie within the range of 70 – 110 GeV. Both criteria on the leading jet are applied, the b-jet identification requirement and the restriction to transverse momenta below 50 GeV. Events containing a second identified b-jet are rejected to reduce the contamination from the $t\bar{t}$ background processes. The $W+$ jets normalisation correction factors that can be derived from the resulting event samples are $f_{Wb}^{e} = 0.55 \pm 0.10$ (stat.) and $f_{Wb}^{\mu} = 0.61 \pm 0.10$ (stat.). The scale factors quoted above are to be compared to the correction factors derived in the nominal $W+$ jets control regions, $f_{W}^{e} \approx 0.59 \pm 0.01$ (stat.) and $f_{W}^{\mu} \approx 0.54 \pm 0.01$ (stat.). Good agreement within the statistical uncertainties is observed.

7.6.5. Multi-jet Background Estimation from Data

The multi-jet production processes are an important source of background that mainly contribute as a consequence of their large production cross sections. These cross sections in combination with the expected low efficiencies of the previously defined selection criteria require a very large

amount of simulated events to acquire conclusive predictions for the expected multi-jet contributions to the signal regions. In addition, such predictions using Monte Carlo simulation techniques are subject to very large uncertainties. For these reasons the contributions of the multi-jet background processes to the signal regions are estimated from the data using a background estimation technique denoted as the *ABCD method*.

The *ABCD* Method

Two variables used in the event selection are chosen to split the data into four orthogonal samples. One of these regions, labelled *A*, is the signal region that is obtained by applying the default selection criteria. The other three data regions, labelled *B*, *C* and *D*, are control regions for which the imposed criteria on either one (regions *B* and *C*) or both (region *D*) of the two selected variables are inverted. All other event selection criteria are applied as for the signal region. The two variables are chosen such that the resulting control regions are predominantly populated by events from multi-jet production processes.

If the two selected variables are uncorrelated, the contribution of the multi-jet background to the signal region, n_A, can be estimated from the number of data events observed in one of the control regions *B* or *C* scaled by the ratio of the numbers of observed events in the remaining two control regions:

$$n_A = n_C \times \frac{n_B}{n_D} \equiv n_C \times r_{B/D} \,, \tag{7.5}$$

where n_B, n_C and n_D denote the numbers of events in data regions *B*, *C* and *D*, respectively. If furthermore an additional variable is not correlated to the two selected ones, the shape of this variable can be extracted from one of the data regions *B* or *C* to approximate the corresponding shape for the multi-jet background in the signal region.

Choice of Variables and Resulting Control Regions

One of the two variables used to split the event sample for the search presented here is the charge product the selected light lepton and the τ_{had} jet. Hence, two of the four resulting data regions contain electrons or muons and τ_{had} jets of opposite sign electric charges, the other two regions such with same sign charges.

As a second set of variables the relative calorimeter and track isolation criteria imposed on the selected light leptons have been chosen, i.e. $E_{\text{T}}^{\Delta\text{R}=0.2}/E_{\text{T}}^{\text{Cluster}}$ and $p_{\text{T}}^{\Delta\text{R}=0.4}/E_{\text{T}}^{\text{Cluster}}$ for selected electons and $E_{\text{T}}^{\Delta\text{R}=0.2}/p_{\text{T}}$ and $p_{\text{T}}^{\Delta\text{R}=0.4}/p_{\text{T}}$ for selected muons. Therefore, two of the four resulting data regions are populated by isolated electrons or muons and the two other control regions with anti-isolated

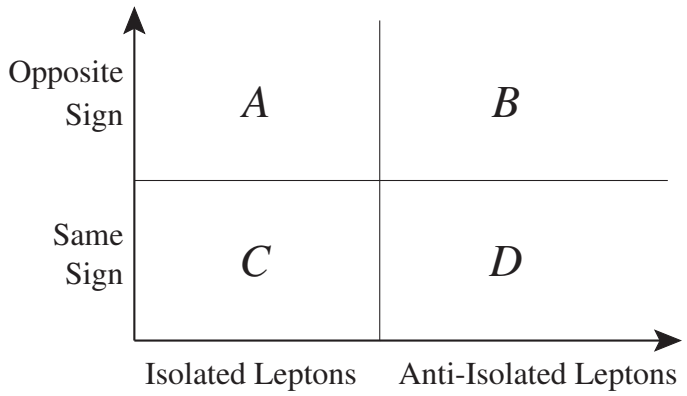

Figure 7.12.: Definition of the four data regions A (the signal region), B, C and D (control regions) obtained by imposing orthogonal requirements on the two selected variables. These variables are the product of electric charges of the selected light lepton and the τ_{had} jet and the isolation criteria applied to the light lepton.

leptons.

The resulting data samples and their labelling with respect to the criteria imposed on the selected variables are illustrated in Fig. 7.12. The numbers of observed events in these regions and the corresponding Monte Carlo predictions for processes other than multi-jet production are presented in Tables 7.9 and 7.10 for the $\tau_\mu \tau_{\text{had}}$ and $\tau_{\text{e}} \tau_{\text{had}}$ final states, respectively. The appropriate correction factors for the $W+$jets, $Z/\gamma^* \to e^+e^-$, $Z/\gamma^* \to \mu^+\mu^-$ and $t\bar{t}$ processes have been applied according to the correction techniques presented in the previous sections.

Results

The numbers of events in the signal regions originating from the multi-jet production processes are estimated according to Equation (7.5). However, the residual contamination of the data from processes other than multi-jet production might introduce a bias in this estimate. Especially in the control regions C a significant contribution from Z/γ^*+jets and $W+$jets processes is expected. Therefore, the predicted contaminations of all non-multi-jet production processes are subtracted from the data in all control regions before Equation (7.5) is applied. A possible contamination from a hypothetical signal in the data control regions is found to be negligible, even for large values of the parameter $\tan\beta$. Given the event yields of Tables 7.9 and 7.10, the estimated

$\tau_\mu\tau_{\text{had}}$ final state, b-vetoed sample			
	B	C	D
	Opposite Sign	Same Sign	Same Sign
	Anti-Isolated	Isolated	Anti-Isolated
$Z/\gamma^*\to\tau^+\tau^-$	1.1 ± 0.8	59.3 ± 6.1	0.7 ± 0.5
$W+$jets	41 ± 5	310 ± 18	13.2 ± 2.8
$Z/\gamma^*\to\ell^+\ell^-$	2.6 ± 1.2	130 ± 10	3.0 ± 1.2
Top	92 ± 5	26.6 ± 1.4	70 ± 4
di-boson	0.42 ± 0.15	2.2 ± 0.4	0.07 ± 0.04
Total	137.0 ± 6.9	528 ± 21	87 ± 5
$h/A/H\to\tau_{\text{lep}}\tau_{\text{had}}$	5.0 ± 0.8	2.4 ± 0.5	0.10 ± 0.08
Data	23979	1025	20635

$\tau_\mu\tau_{\text{had}}$ final state, b-tagged sample			
	B	C	D
	Opposite Sign	Same Sign	Same Sign
	Anti-Isolated	Isolated	Anti-Isolated
$Z/\gamma^*\to\tau^+\tau^-$	0 ± 0	2.7 ± 1.2	0 ± 0
$W+$jets	1.30 ± 0.92	6.5 ± 1.7	0.6 ± 0.6
$Z/\gamma^*\to\ell^+\ell^-$	0 ± 0	4.5 ± 1.5	0 ± 0
Top	2.9 ± 0.8	1.6 ± 0.4	1.6 ± 0.4
di-boson	0 ± 0	0.15 ± 0.07	0 ± 0
Total	4.2 ± 1.2	15.6 ± 2.6	2.2 ± 0.7
$h/A/H\to\tau_{\text{lep}}\tau_{\text{had}}$	0.75 ± 0.26	0.14 ± 0.10	0 ± 0
Data	2751	66	2692

Table 7.9.: Observed numbers of events in data and the predicted event yields for processes other than multi-jet production in the three control regions used by the *ABCD* method for the $\tau_\mu\tau_{\text{had}}$ final state. The upper part shows the event yields for the b-vetoed sample, the lower part those for the b-tagged sample. The predictions for the $W+$jets, $Z/\gamma^*\to\ell^+\ell^-$ and $t\bar{t}$ processes are corrected as described in the previous sections. The potential signal contamination includes the contributions of both production mechanisms and is given for the parameters m_A=150 GeV and $\tan\beta$=20. The quoted errors are of statistical nature.

$\tau_e\tau_{had}$ final state, b-vetoed sample			
	B	C	D
	Opposite Sign	Same Sign	Same Sign
	Anti-Isolated	Isolated	Anti-Isolated
$Z/\gamma^* \to \tau^+\tau^-$	0 ± 0	46 ± 7	0 ± 0
$W+$jets	7 ± 4	321 ± 20	0 ± 0
$Z/\gamma^* \to \ell^+\ell^-$	1.7 ± 0.8	322 ± 14	0.6 ± 0.4
Top	2.6 ± 1.0	26.5 ± 1.3	3.0 ± 1.0
di-boson	0.14 ± 0.10	3.8 ± 0.6	0 ± 0
Total	12 ± 4	720 ± 25	3.6 ± 1.1
$h/A/H \to \tau_{lep}\tau_{had}$	1.01 ± 0.32	2.4 ± 0.5	0.18 ± 0.13
Data	1832	1579	1710

$\tau_e\tau_{had}$ final state, b-tagged sample			
	B	C	D
	Opposite Sign	Same Sign	Same Sign
	Anti-Isolated	Isolated	Anti-Isolated
$Z/\gamma^* \to \tau^+\tau^-$	0 ± 0	0 ± 0	0 ± 0
$W+$jets	0 ± 0	6.6 ± 1.8	0 ± 0
$Z/\gamma^* \to \ell^+\ell^-$	0 ± 0	8.4 ± 2.2	0 ± 0
Top	0.19 ± 0.08	1.78 ± 0.32	0.16 ± 0.07
di-boson	0 ± 0	0.1 ± 0.1	0 ± 0
Total	0.19 ± 0.08	16.9 ± 2.8	0.16 ± 0.07
$h/A/H \to \tau_{lep}\tau_{had}$	0.10 ± 0.10	0 ± 0	0 ± 0
Data	168	80	172

Table 7.10.: Observed numbers of events in data and the predicted event yields for processes other than multi-jet production in the three control regions used by the *ABCD* method for the $\tau_e\tau_{had}$ final state. The upper part shows the event yields for the b-vetoed sample, the lower part those for the b-tagged sample. The predictions for the $W+$jets, $Z/\gamma^* \to \ell^+\ell^-$ and $t\bar{t}$ processes are corrected as described in the previous sections. The potential signal contamination includes the contributions of both production mechanisms and is given for the parameters m_A=150 GeV and $\tan\beta$=20. The quoted errors are of statistical nature.

contributions of the multi-jet production processes to the four signal regions are

$$\begin{aligned} n_{\tau_e\tau_{\text{had}},\, b-tagged} &= 60 \pm 9\,, \\ n_{\tau_e\tau_{\text{had}},\, b-vetoed} &= 920 \pm 50\,, \\ n_{\tau_\mu\tau_{\text{had}},\, b-tagged} &= 51 \pm 9\,, \\ n_{\tau_\mu\tau_{\text{had}},\, b-vetoed} &= 580 \pm 50\,. \end{aligned} \tag{7.6}$$

All uncertainties are of statistical nature, systematic uncertainties on the numbers are discussed in Section 7.8.3.

Different multi-jet background predictions for the $\tau_e\tau_{\text{had}}$ and $\tau_\mu\tau_{\text{had}}$ final states are observed. These are consequences of the different transverse momenta and isolation requirements imposed on the selected leptons and the very different probabilities for a jet to be misidentified as either an electron or muon. Furthermore, different transfer factors $r_{B/D}$, i.e. ratios of multi-jet background events in the regions with opposite sign and same sign electric charges for the selected lepton and τ_{had} jet, are observed in the b-tagged and b-vetoed event samples. For multi-jet events entering the b-vetoed sample a large fraction of $q\bar{q}$ production processes are expected in which the quark jets are selected as the light lepton and the τ_{had} jet. Hence, a large fraction of events with opposite sign electric charges is observed, resulting in values of $r_{B/D}$ above one. In the b-tagged sample, on the other hand, mainly $b\bar{b}$ processes contribute in which additional gluon jets are misidentified as the τ_{had} jet or the light lepton – a b-quark jet is unlikely to be selected as such, which is consistent with the observations made for the study on the $t\bar{t}$ background normalisation. Therefore, no preference for the charge product is expected in multi-jet events entering the b-tagged event samples and a ratio close to one is observed.

The reconstructed invariant $\tau^+\tau^-$ mass $m_{\tau\tau}^{\text{MMC}}$ and several other variables describing event and particle properties are assumed to be uncorrelated to the isolation criteria on the light lepton and the product of the lepton and τ_{had} jet charges. The shapes of these variables are therefore extracted from the control region C and extrapolated to the signal region using Equation (7.5). Again the contamination from processes other than multi-jet production is taken into account by subtracting the corresponding Monte Carlo predictions from the distributions in data.

Important Properties of the *ABCD* method

The subtraction of the Monte Carlo predictions for non-multi-jet backgrounds from the data has several important consequences. An inaccurate Monte Carlo prediction in the signal region is

to some extent compensated with the multi-jet background estimate of the *ABCD* method. If, for example, the predicted contribution of the di-boson background is underestimated in the signal region, the same is very likely in the control regions B, C and D. Hence, by subtracting the low di-boson event yield from the observed data in control region C, the multi-jet background is overestimated in that region. The resulting estimate for the multi-jet production processes in the signal region will therefore compensate for the underestimated contribution of di-boson events. This mechanism is especially important as any bias that might have been introduced by neglecting the multi-jet background contributions to control regions for other processes is compensated to a large degree. A fully correct estimate of all backgrounds without any bias would require a simultaneous fit of all background contributions to the control regions. An equivalent fit, however, is performed when the final results for this search are derived: the expected background contributions to the signal and the multi-jet control regions are simultaneously fit to the observed data, taking into account the statistical and systematic uncertainties on the background predictions and the uncertainties on the shapes of the corresponding $m_{\tau\tau}^{\mathrm{MMC}}$ mass distributions (see Section 7.9).

A further consequence of the background subtraction from the data is that the predicted multi-jet event yields are subject to systematic uncertainties on the predictions for simulated processes. However, due to the mechanism described above, the resulting uncertainties on the multi-jet background estimate are fully anti-correlated to those on the subtracted processes.

It is important to note that a potential signal present in data cannot be compensated with the multi-jet background estimate of the *ABCD* method. The expected contribution of the signal processes to all control regions are negligible and therefore no impact on the background prediction is expected.

Method Validation

The *ABCD* method relies on the assumption that the two selected variables are uncorrelated. The assumption that this is the case for the variables chosen in this search can be validated by comparing the distributions of further uncorrelated variables in the half-planes *AB* and *CD* or the half-planes *AC* and *BD*. Hence, multi-jet events containing leptons and τ_{had} jets with opposite signed electric charges are compared to such containing candidates with same sign charges, and events in which the selected light leptons are isolated to those containing anti-isolated leptons. If the two variables and the third that is to be compared are uncorrelated for multi-jet production processes, the resulting distributions in the half-planes are expected to agree in shapes. The normalisation, however, might differ.
As the Monte Carlo predictions for multi-jet production processes are not reliable this compari-

son is performed using real p–p collision data. For this purpose the predicted contributions from processes other than multi-jet production are subtracted from the data distributions. This results in an estimate for the shape resulting from the multi-jet background only. A potential signal present in data might bias these comparisons. However, the expected event yields for both Higgs boson production modes to the combined data regions are small and especially for the comparison of the half-planes *AB* and *CD* the contamination would be negligible.
The comparison of several variables – the transverse momenta of the selected lepton and the τ lepton and the missing transverse momentum $E_{\text{T}}^{\text{miss}}$ – in the half-planes *AB* and *CD*, i.e. opposite sign versus same sign electric charges, and *AC* and *BD*, i.e. isolated versus non-isolated leptons, are shown in Figs. 7.13 and 7.14 for the b-tagged and b-vetoed samples, respectively. Supplementary comparisons are shown in Appendix A. All distributions show the data observed in these half-planes of which the expected contributions from non-multi-jet production processes have been subtracted. The corrections discussed in the previous sections have been taken into account for the corresponding processes. As the event yields in the half-planes differ strongly in some cases, the histograms are normalised to each other. An overall adequate agreement of the distributions in the half-planes is observed and therefore the variables selected for the *ABCD* method are assumed to be uncorrelated.

An additional validation study has been performed by testing the stability of the transfer factor $r_{B/D}$ (see Equation (7.5)) against a looser and a tighter variation of the anti-isolation criteria on the light leptons. Given that the two selected variables are uncorrelated, the ratio of multi-jet events in the regions with opposite and same sign electric charges is expected to be independent on such variations.
For the looser and tighter criteria the relative calorimeter anti-isolation requirements on electrons (muons) have been changed from the nominal thresholds of 8% (4%) to 6% (2%) and 10% (6%), respectively. The relative track anti-isolation criteria have been changed from the nominal threshold of 6% to 4% and 8% for both leptons types. For these choices the transfer factors $r_{B/D}$ have been re-evaluated and compared to their nominal values. The results are presented in Table 7.11. The observed variations of $r_{B/D}$ are always lower than the corresponding statistical uncertainty. Therefore, the ratio of events in regions *C* and *D* can be assumed stable in general. However, the ratio varies with the reconstructed $\tau^+\tau^-$ mass $m_{\tau\tau}^{\text{MMC}}$ within the considered mass range. The deviations are studied in Section 7.8.3 and systematic uncertainties on the ratios $r_{B/D}$ are derived.

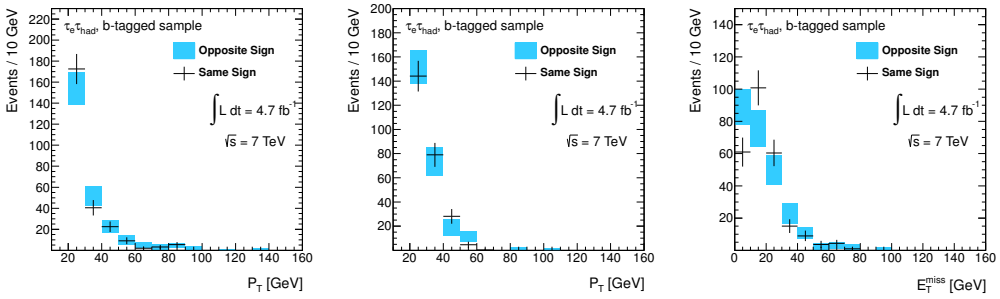

(a) p_T of the τ_{had} (b) p_T of the lepton (c) E_T^{miss}

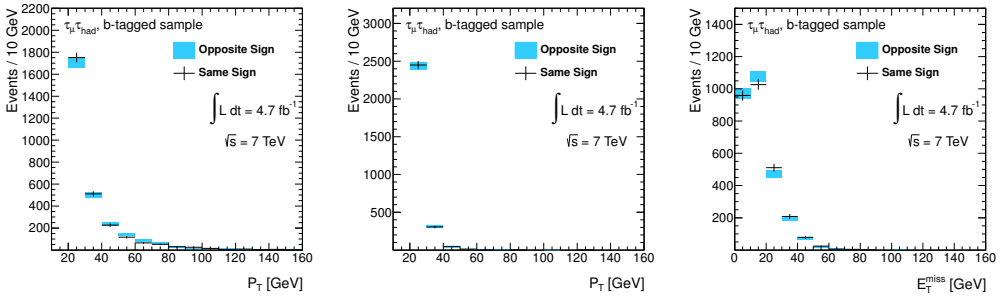

(d) p_T of the τ_{had} (e) p_T of the lepton (f) E_T^{miss}

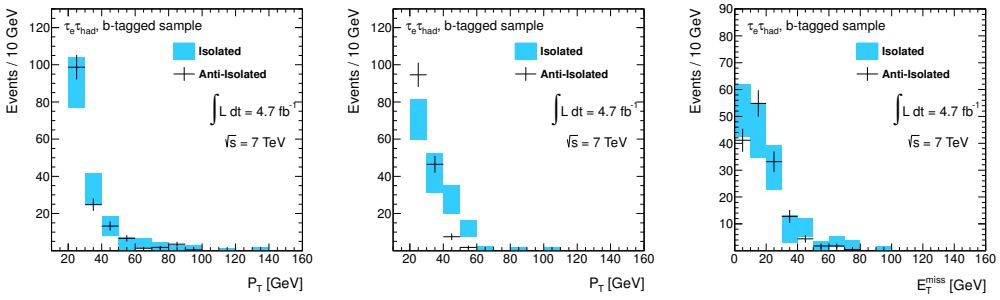

(g) p_T of the τ_{had} (h) p_T of the lepton (i) E_T^{miss}

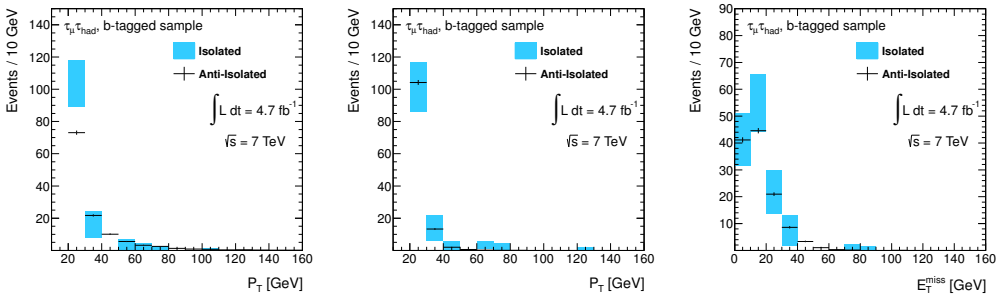

(j) p_T of the τ_{had} (k) p_T of the lepton (l) E_T^{miss}

Figure 7.13.: ***b*-Tagged Sample:** Comparison of the transverse momenta of the selected lepton and the τ_{had} jet and the missing transverse momentum E_T^{miss} in the half-planes *AB* and *CD (opposite vs. same sign charges)* in the upper two rows and *AC* and *BD (isolated vs. anti-isolated leptons)* in the lower rows as the data of which the non-multi-jet background expectations have been subtracted. Figures (a) – (c) and (g) – (i) show the $\tau_e\tau_{had}$ final state, the $\tau_\mu\tau_{had}$ final state is shown in Figures (d) – (f) and (j) – (l).

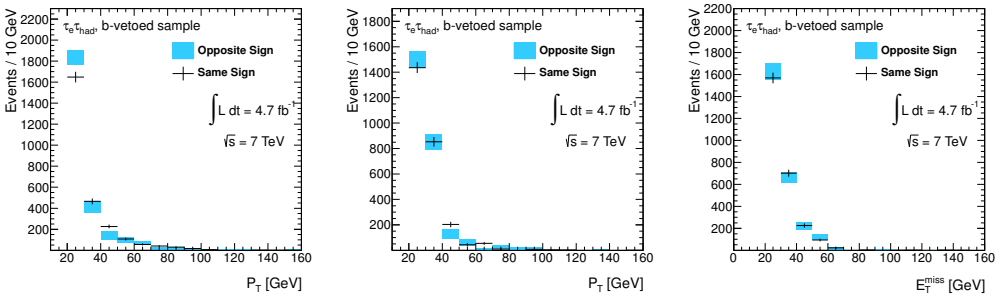

(a) p_{T} of the τ_{had} (b) p_{T} of the lepton (c) $E_{\text{T}}^{\text{miss}}$

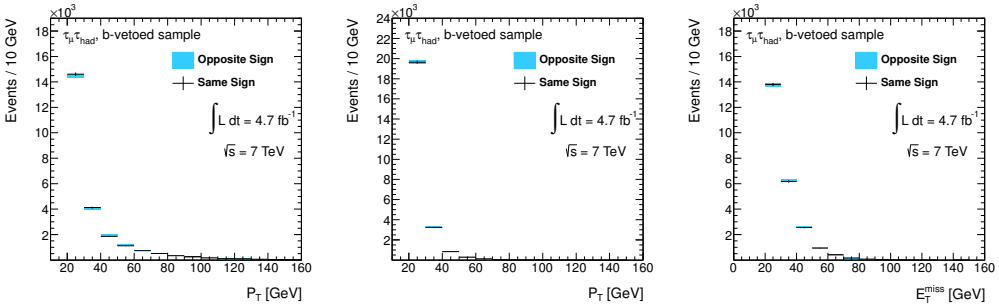

(d) p_{T} of the τ_{had} (e) p_{T} of the lepton (f) $E_{\text{T}}^{\text{miss}}$

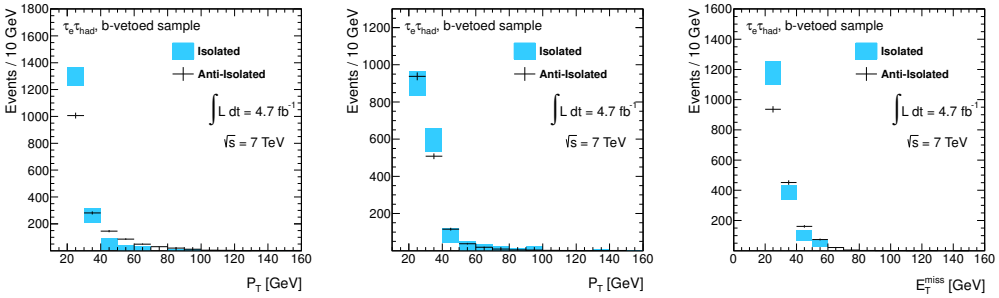

(g) p_{T} of the τ_{had} (h) p_{T} of the lepton (i) $E_{\text{T}}^{\text{miss}}$

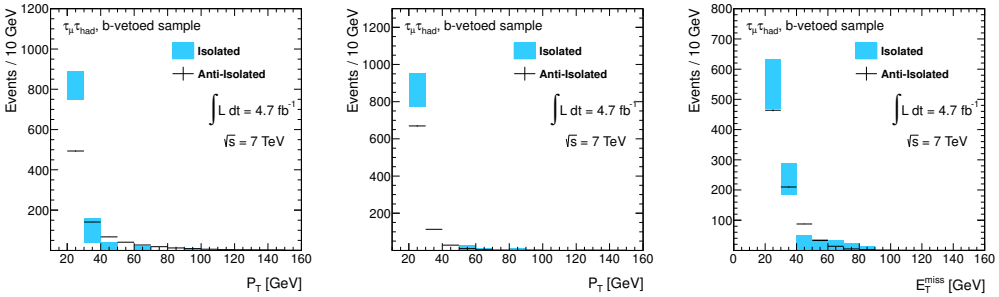

(j) p_{T} of the τ_{had} (k) p_{T} of the lepton (l) $E_{\text{T}}^{\text{miss}}$

Figure 7.14.: ***b*-Vetoed Sample:** Comparison of the transverse momenta of the selected lepton and the τ_{had} jet and the missing transverse momentum $E_{\text{T}}^{\text{miss}}$ in the half-planes *AB* and *CD (opposite vs. same sign charges)* in the upper two rows and *AC* and *BD (isolated vs. anti-isolated leptons)* in the lower rows as the data of which the non-multi-jet background expectations have been subtracted. Figures (a) – (c) and (g) – (i) show the $\tau_{\text{e}}\tau_{\text{had}}$ final state, the $\tau_\mu\tau_{\text{had}}$ final state is shown in Figures (d) – (f) and (j) – (l).

	Anti-Isolation			Maximum	
Final state	Looser	Default	Tighter	Uncert.	Deviation
$\tau_\mu \tau_{\text{had}}$, b-tagged	1.03 ± 0.03	1.03 ± 0.03	1.02 ± 0.03	3%	1%
$\tau_e \tau_{\text{had}}$, b-tagged	0.94 ± 0.09	0.98 ± 0.11	0.96 ± 0.11	11%	4%
$\tau_\mu \tau_{\text{had}}$, b-vetoed	1.16 ± 0.01	1.16 ± 0.01	1.17 ± 0.01	1%	1%
$\tau_e \tau_{\text{had}}$, b-vetoed	1.08 ± 0.03	1.07 ± 0.04	1.08 ± 0.04	4%	1%

Table 7.11.: Transfer factor $r_{B/D}$ (see Equation (7.5)) derived from event samples with looser, nominal and tighter anti-isolation criteria on electrons and muons. Details on the individual thresholds are given in the text. All quoted errors are of statistical nature.

7.7. Results with the Background Estimates

Using the predictions from Monte Carlo simulations and the data-driven estimation and correction techniques discussed in the previous sections, the observed data can be compared to the expectations. Several distributions of important particle and event properties are shown in Fig. 7.15 for the signal regions of the *b*-tagged sample. The variables shown are the transverse momenta of jets, the selected lepton and the τ_{had} jet, the number of jets, the missing transverse momentum $E_{\text{T}}^{\text{miss}}$ and the scalar sum of transverse energies of all calorimeter energy depositions and muons ($\sum E_{\text{T}}$). The same distributions for the signal regions of the *b*-vetoed sample are shown in Fig. 7.16. In all comparisons the contributions resulting from $Z/\gamma^{*}\rightarrow\tau^{+}\tau^{-}$ background processes have been estimated using the τ-embedded $Z/\gamma^{*}\rightarrow\mu^{+}\mu^{-}$ data (Section 7.6.1). The normalisation of the $W+$ jets and $t\bar{t}$ backgrounds have been corrected to data in dedicated control regions (Sections 7.6.2 and 7.6.3). In all comparisons for the *b*-tagged event samples the *b*-jet selection efficiency in simulated $Z/\gamma^{*}\rightarrow\ell^{+}\ell^{-}$ event samples have been corrected (Section 7.6.4). The contributions from multi-jet production processes have been estimated using the *ABCD* method (Section 7.6.5). The corresponding shapes have been extracted from control region *C*, i.e. from the data event sample containing isolated light leptons and same sign electric charges for the selected lepton and τ_{had} jet. The remaining small contributions from other processes, i.e. the single top and di-boson backgrounds, have been estimated using the corresponding Monte Carlo predictions. Further comparisons of the data to the expectations are shown in Appendix B.

The observed and expected event yields are given in Table 7.12 for all signal regions. The table includes the systematic uncertainties on the individual background expectations. The sources for these and their magnitude are discussed in Section 7.8. Small deviations of the systematic uncertainties on the expected event yields from those presented in Ref. [114] originate from a slightly different treatment of the uncertainties and their correlations. In the numbers presented in Table 7.12 the systematic uncertainties on the total background expectations take into account the correlations among the individual contributions: the uncertainties on each background derived from a single source of uncertainty, like the contributions from all $+1\,\sigma$ variations of the jet energy scale, are treated fully correlated and are added linearly. The resulting uncertainties on the total background prediction for the various sources are added in quadrature. This is done separately for contributions that either increase or decrease the total expected event yield. Furthermore, this procedure takes into account the anti-correlations of the uncertainties on simulated backgrounds and those on the multi-jet background predictions (see Section 7.6.5).

The numbers presented in the table show a deficit in the nominal background expectations for

the *b*-tagged samples when compared to the numbers of events observed in data. In contrast, the expectations for the *b*-vetoed event samples exceed the numbers of observed events. Considering the quoted statistical and systematic uncertainties, however, the expectations agree with the observations. In particular, no significant excess of data above the Standard Model background predictions is observed in all signal regions. This is also reflected in the distributions presented in Figs. 7.15 and 7.16 that show an adequate agreement of the data and the expectations, even without considering the systematic uncertainties on the predicted background distributions which are not shown in the figures.

	$\tau_e\tau_{\text{had}}$ Final State	
	b-tagged sample	b-vetoed sample
$Z/\gamma^* \to \tau^+\tau^-$	$42 \pm 6 \pm 19$	$2730 \pm 50 \pm 500$
$W+$jets	$18 \pm 8\ ^{+3}_{-4}$	$740 \pm 20\ ^{+100}_{-150}$
$Z/\gamma^* \to \ell^+\ell^-$	$19 \pm 4\ ^{+8}_{-6}$	$700 \pm 20\ ^{+350}_{-270}$
Top	$15.1 \pm 0.8\ ^{+2.7}_{-3.3}$	$106 \pm 2\ ^{+19}_{-20}$
Di-boson	$0.95 \pm 0.35\ ^{+0.14}_{-0.32}$	$29 \pm 2\ ^{+5}_{-4}$
Multi-Jet	$60 \pm 9 \pm 12$	$920 \pm 50\ ^{+220}_{-230}$
Total	$156 \pm 14\ ^{+24}_{-23}$	$5220 \pm 80\ ^{+680}_{-670}$
Signal (m_A=150 GeV, $\tan\beta$=20)		
$b\bar{b}\,h/A/H \to \tau_{\text{lep}}\tau_{\text{had}}$	$15 \pm 1\ ^{+3}_{-5}$	$138 \pm 4\ ^{+23}_{-30}$
$gg \to h/A/H \to \tau_{\text{lep}}\tau_{\text{had}}$	$1.2 \pm 0.4\ ^{+0.6}_{-0.3}$	$99 \pm 3 \pm 17$
Data	175	5034

	$\tau_\mu\tau_{\text{had}}$ Final State	
	b-tagged sample	b-vetoed sample
$Z/\gamma^* \to \tau^+\tau^-$	$86 \pm 7 \pm 13$	$4760 \pm 50 \pm 740$
$W+$jets	$19 \pm 4\ ^{+4}_{-5}$	$781 \pm 26\ ^{+100}_{-140}$
$Z/\gamma^* \to \ell^+\ell^-$	$8 \pm 2\ ^{+4}_{-2}$	$351 \pm 16\ ^{+100}_{-90}$
Top	$14.5 \pm 0.8\ ^{+2.9}_{-3.0}$	$105 \pm 2\ ^{+20}_{-19}$
Di-boson	$0.75 \pm 0.33\ ^{+0.23}_{-0.18}$	$38 \pm 2\ ^{+5}_{-4}$
Multi-Jet	$51 \pm 9\ ^{+7}_{-6}$	$580 \pm 50\ ^{+130}_{-120}$
Total	$180 \pm 12\ ^{+17}_{-16}$	$6610 \pm 70\ ^{+810}_{-820}$
Signal (m_A=150 GeV, $\tan\beta$=20)		
$b\bar{b}\,h/A/H \to \tau_{\text{lep}}\tau_{\text{had}}$	$20 \pm 1\ ^{+4}_{-6}$	$174 \pm 4\ ^{+28}_{-37}$
$gg \to h/A/H \to \tau_{\text{lep}}\tau_{\text{had}}$	$1.2 \pm 0.4\ ^{+0.6}_{-0.3}$	$115 \pm 4\ ^{+20}_{-19}$
Data	202	6424

Table 7.12.: Numbers of observed events in data and predicted event yields in the four signal regions. The event yields for the two Higgs boson production mechanisms are given for $m_A = 150$ GeV and $\tan\beta$=20. Statistical uncertainties are treated symmetric. Systematic uncertainties are shown separately for up- and down-variations if they differ significantly. Uncertainties on the total background expectations are computed as explained in the text.

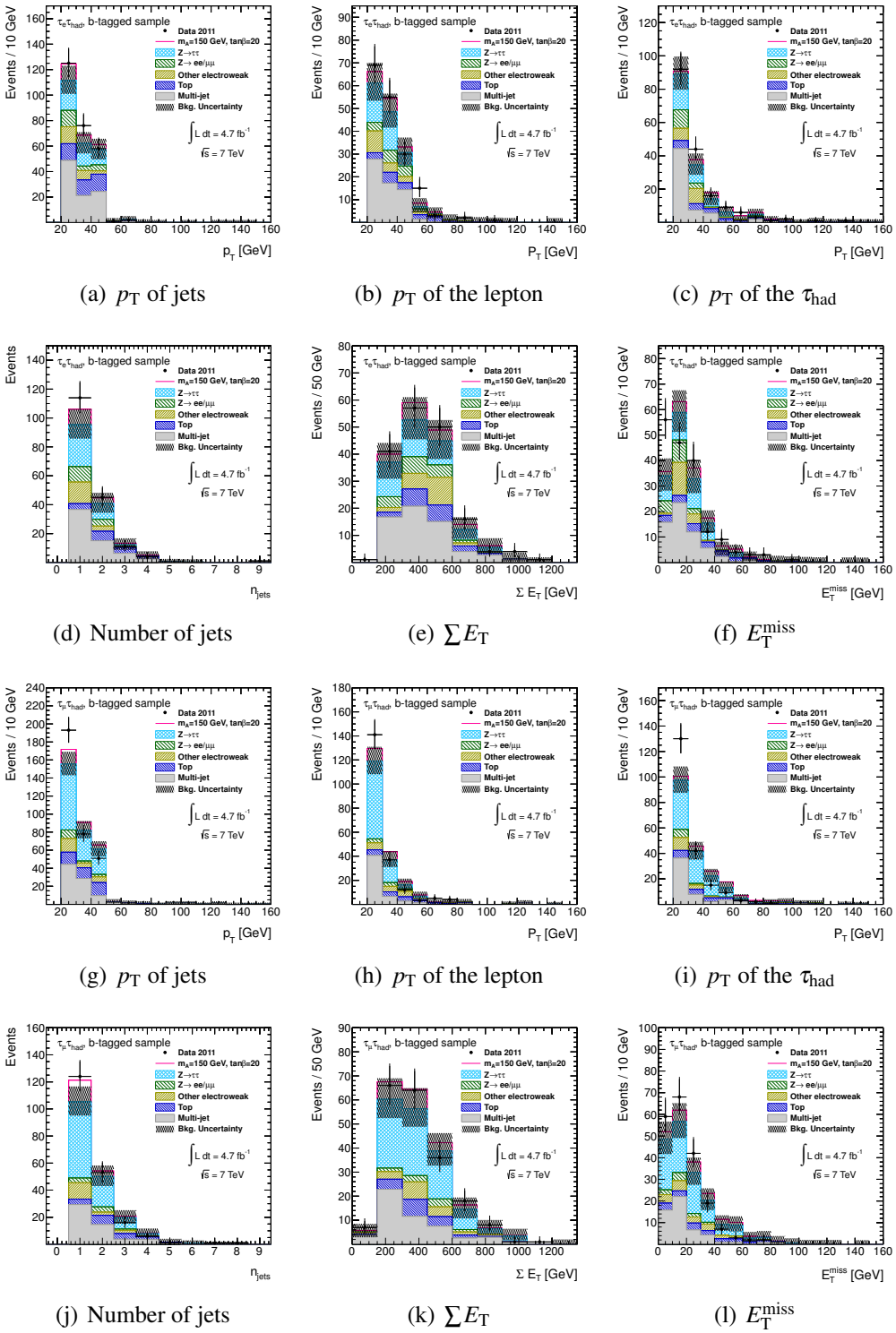

(a) p_{T} of jets (b) p_{T} of the lepton (c) p_{T} of the τ_{had}

(d) Number of jets (e) $\sum E_{\mathrm{T}}$ (f) $E_{\mathrm{T}}^{\mathrm{miss}}$

(g) p_{T} of jets (h) p_{T} of the lepton (i) p_{T} of the τ_{had}

(j) Number of jets (k) $\sum E_{\mathrm{T}}$ (l) $E_{\mathrm{T}}^{\mathrm{miss}}$

Figure 7.15.: The p_{T} of jets, the selected lepton and the τ_{had} jet, the number of jets, the sum of transverse energies $\sum E_{\mathrm{T}}$ and the missing transverse momentum $E_{\mathrm{T}}^{\mathrm{miss}}$ in data in the ***b*-tagged** sample compared to the background expectations and a hypothetical signal (m_A =150 GeV, $\tan\beta$=20) for the $\tau_{\mathrm{e}}\tau_{\mathrm{had}}$ ((a) – (f)) and $\tau_{\mu}\tau_{\mathrm{had}}$ ((g) – (l)) final states. The contributions of the di-boson and W+jets backgrounds are combined and labelled "Other electroweak". The uncertainties shown are of statistical nature.

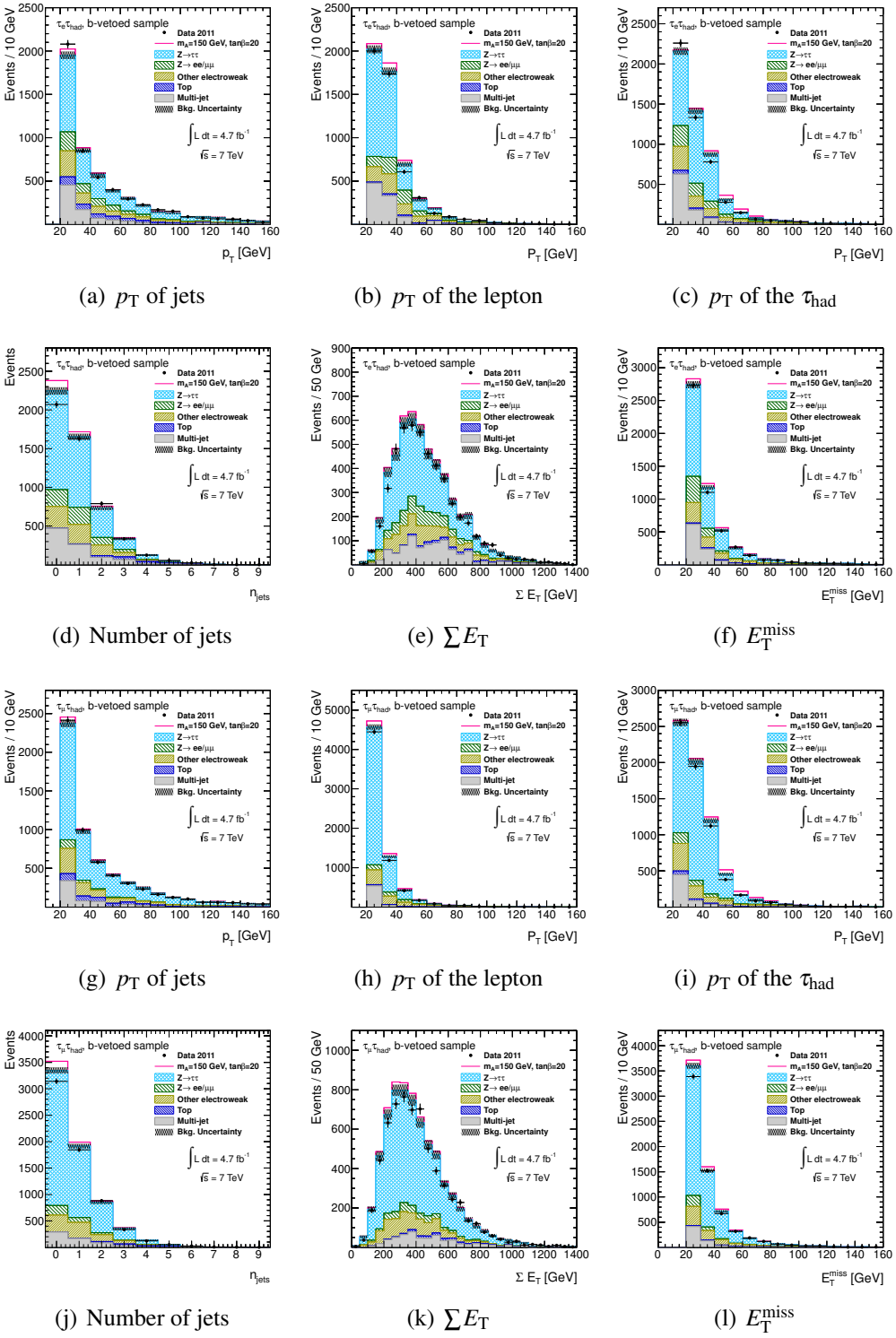

(a) p_{T} of jets (b) p_{T} of the lepton (c) p_{T} of the τ_{had}

(d) Number of jets (e) $\sum E_{\text{T}}$ (f) $E_{\text{T}}^{\text{miss}}$

(g) p_{T} of jets (h) p_{T} of the lepton (i) p_{T} of the τ_{had}

(j) Number of jets (k) $\sum E_{\text{T}}$ (l) $E_{\text{T}}^{\text{miss}}$

Figure 7.16.: The p_{T} of jets, the selected lepton and the τ_{had} jet, the number of jets, the sum of transverse energies $\sum E_{\text{T}}$ and the missing transverse momentum $E_{\text{T}}^{\text{miss}}$ in data in the ***b*-vetoed** sample compared to the background expectations and a hypothetical signal (m_A =150 GeV, $\tan\beta$=20) for the $\tau_{\text{e}}\tau_{\text{had}}$ ((a) – (f)) and $\tau_\mu\tau_{\text{had}}$ ((g) – (l)) final states. The contributions of the di-boson and W+jets backgrounds are combined and labelled "Other electroweak". The uncertainties shown are of statistical nature.

7.8. Systematic Uncertainties

The predicted contributions of the background processes to the signal regions are subject to systematic uncertainties. These can be grouped into several categories that apply to different background sources, depending on whether the backgrounds are estimated using Monte Carlo predictions or from the data.
Those backgrounds estimated using Monte Carlo predictions suffer from an imperfect simulation of p–p collisions and the underlying processes, and a limited precision of the corresponding cross section calculations that are required to normalise the simulated event samples. Such uncertainties on the *predictions of the theory models* and their effect on the event selection are discussed in Section 7.8.1.
Further uncertainties on simulated event samples arise from an imperfect simulation of the ATLAS detector. Several correction techniques aim to compensate for the resulting effects on particle and event properties, but the underlying measurements used to derive these corrections are performed with limited precision. The same applies to the luminosity measured for the considered data set which affects the final normalisation of all simulated event samples. These uncertainties, summarised as *experimental uncertainties*, are discussed in Section 7.8.2.
Backgrounds estimated completely from the data or validated using data suffer from uncertainties on the background estimation methods themselves. These uncertainties and their impact on the search presented here are discussed in Section 7.8.3.

Methodology

The impact of each individual systematic uncertainty described below on the final search results is studied using the following procedure. The corresponding parameter or property is varied from its nominal value by $\pm 1\,\sigma$ of the assigned uncertainty. The complete event selection is applied to the event samples of all processes with these modified conditions and the contributions to the signal regions are re-evaluated. For each process the difference of the re-evaluated event yield and the nominal one defines the $\pm 1\,\sigma$ systematic uncertainty on the expectations due to this parameter or property variation.

7.8.1. Systematic Uncertainties on Theory Predictions

Uncertainties on the predicted event yields arise from the uncertainties on the cross sections that the simulated event samples are normalised to. These are computed with limited precision and

the corresponding uncertainties directly affect the signal and background sample expectations in all signal regions.
In addition, the simulation of p–p collisions and the hard interaction processes with Monte Carlo event generators relies on complex models and techniques of which several were briefly discussed in Chapter 2.3.4. Many of the underlying model parameters have been tuned to existing measurements performed with finite precision. In addition, the involved models are approximations and hence limited in their predictive power. For these reasons studies have been performed to estimate the effect of variations of relevant model parameters employed in the event generation on simulated event and particle properties and hence the acceptance of the event selection. In the following the changes in the event selection efficiency resulting from modifications of the event simulation parameters are denoted as *acceptance uncertainties*.
Both of these sources of uncertainties apply to all processes estimated using simulated event samples, including the signal processes. The $W+$ jets and $t\bar{t}$ event samples, however, are normalised to the data and therefore do not suffer from these uncertainties.

Uncertainties on Signal and Background Cross Sections

The uncertainties on the cross sections of the Higgs boson production in the gluon-fusion and the b-quark associated production modes are discussed in detail in Ref. [44]. For both processes the typical uncertainty ranges from $\pm 10\%$ to $\pm 20\%$, depending on the values of the parameters m_A and $\tan\beta$.

The systematic uncertainty on the cross section of Z boson production is $\pm 5\%$ [129,130]. This estimate includes the uncertainties derived from variations of the parton density functions, the renormalisation and the factorisation scale. For the single top and di-boson production processes relative cross section uncertainties of $\pm 13\%$ and $\pm 7\%$, respectively, are assumed [131].

Acceptance Uncertainties for the b-Quark Associated Higgs Boson Production

As the sensitivity of this search strongly depends on the exact knowledge about the signal expectations, a detailed study of the acceptance uncertainties on the signal processes has been performed.
For the b-quark associated Higgs boson production additional signal event samples have been generated for two masses, $m_A = 120\,\text{GeV}$ and $m_A = 300\,\text{GeV}$, and with varied parameter settings for the Monte Carlo generator Sherpa [78]. The effect of these variations on kinematic properties of electrons, muons, τ_{had} jets and jets and the resulting effects on the event selection efficiencies

have been studied at generator level, i.e. the event information is directly analysed without involving detector simulation and event reconstruction techniques. The following parameter modifications have been applied to the event generator settings:

- The factorisation scale has been varied up and down by a factor of 2.
- In the Sherpa event generator the renormalisation scale does not only affect the matrix element calculation but also the simulation of parton showers. Therefore, large variations of this parameter result in large changes in the calorimeter signatures of jets, for example, which are well constrained by measurements. For these reasons the renormalisation scale has been decreased and increased slightly by $\pm 10\%$ which result in a conservative estimate of the uncertainties on the event acceptance [132].
- The nominal set of parton density functions used by the Sherpa generator is the set *CTEQ6l1* ($\alpha_s(M_Z) = 0.130$) for which no eigenvector PDF sets were available to the time of these studies. Therefore, additional signal samples have been produced using the set *CTEQ6.6m* ($\alpha_s(M_Z) = 0.118$) to approximate the uncertainty on the event acceptance resulting from the limited knowledge on the parton density of the proton.
- The Sherpa event generator employs the CKKW matching scheme. The corresponding matching parameter has been changed from a nominal value of $\sqrt{20.0/E_{CMS}}$ to values of $\sqrt{15.0/E_{CMS}}$ and $\sqrt{30.0/E_{CMS}}$, where E_{CMS} denotes the centre-of-mass energy of the initial partons.
- Further event samples have been generated taking into account the mass of the b-quark, which is neglected for the simulation of the nominal event samples.
- The underlying event activity has been modified by about $\pm 10\%$ in magnitude [132].

The above variations are found to mainly affect the kinematics of the true b-jets produced in the signal events. As a consequence the event yields in the b-tagged final states vary strongly as a function of the acceptance of the transverse momentum thresholds imposed on the b-jet. The largest deviations are observed for modifications of the CKKW matching parameter with changes in the acceptance of about $^{+14}_{-15}\%$ and $^{+12}_{-9}\%$ for signal events with generated Higgs boson masses of m_A=120 GeV and m_A=300 GeV, respectively. Furthermore, the increase of the factorisation scale and the use of the alternative PDF set decrease the event acceptance by about -13% (-7%) and -8% (-8%), respectively, if a Higgs boson mass of m_A=120 GeV (m_A=300 GeV) is assumed. The transverse momenta of the Higgs boson and its decay products and other event properties

are only mildly affected. Given the high thresholds on electron and muon transverse momenta applied in the event selection, only small changes in the event acceptance of the b-vetoed event samples are observed. The largest deviations result from variations of the CKKW matching parameter and the factorisation scale that both affect the expected signal event yields at the level of $\pm 1\%$. Other modifications to the event generation affect the event acceptance by less than 1%.
The systematic uncertainties derived from all variations listed above are summarised in Table 7.13 for both generated mass points and the b-tagged and b-vetoed event samples. The individual contributions sum up to a total uncertainty of $^{+1}_{-2}\%$ on the acceptance of the b-vetoed event sample selection for both generated masses. For the acceptance of the b-tagged event sample selection larger total uncertainties of $^{+14}_{-21}\%$ (m_A=120 GeV) and $^{+12}_{-14}\%$ (m_A=300 GeV) are observed. Uncertainties on signal samples simulated with other Higgs boson masses are obtained by linear interpolation.

Acceptance Uncertainties for the Higgs Boson Production in the Gluon-Fusion Mode

A similar study has been performed to derive acceptance uncertainties for the production of neutral MSSM Higgs bosons in the gluon-fusion mode. For this purpose, additional signal event samples have been generated assuming a Higgs boson mass of m_A=120 GeV [128]. The following parameter settings for the POWHEG event generator have been varied and the impact on the event acceptance has been studied at generator level [128]:

- The initial and final state radiation activities (ISR and FSR) have been increased and decreased independently.
- The renormalisation and factorisation scales have been increased and decreased simultaneously by a factor of 2 and $^1/_2$, respectively.
- The underlying event activity has been varied by modifying the parameter settings of the PYTHIA program that is interfaced with the POWHEG generator ("Perugia 2010 tune").

With these changes to the event simulation small variations in the lepton momenta are observed. The resulting deviations in the acceptance of the b-vetoed event selection are typically below the respective statistical uncertainties. The largest uncertainties are observed for a decrease in the initial and final state radiation activity and the simultaneous downwards variation of the renormalisation and factorisation scales that decrease the event acceptance by (-)2.4 – 2.6%.
In contrast, large deviations are observed for the selection efficiency of the b-tagged sample, however, with large corresponding statistical uncertainties. The modifications in the amount of

$b\bar{b}\,h/A/H$	b-tagged sample		b-vetoed sample	
$m_A=$	120 GeV	300 GeV	120 GeV	300 GeV
CKKW $\sqrt{30.0/E_{CMS}}$	+13.8 ± 1.6	+12.3 ± 0.8	-1.1 ± 0.5	-1.5 ± 0.3
CKKW $\sqrt{15.0/E_{CMS}}$	-14.5 ± 1.5	-8.6 ± 0.8	+0.4 ± 0.5	+1.0 ± 0.3
Fac. scale × 2.0	-13.2 ± 1.5	-6.5 ± 0.8	+1.0 ± 0.5	+1.0 ± 0.3
Fac. scale × 0.5	-1.5 ± 1.5	-1.8 ± 0.8	-0.8 ± 0.5	0.0 ± 0.3
Ren. scale × 1.1	-1.1 ± 1.5	-0.7 ± 0.8	0.0 ± 0.5	0.0 ± 0.3
Ren. scale × 0.9	+1.9 ± 1.5	+0.1 ± 0.8	-0.3 ± 0.5	+0.2 ± 0.3
Underlying Event +10%	+0.3 ± 1.5	0.0 ± 0.8	0.0 ± 0.5	0.0 ± 0.3
Underlying Event −10%	0.0 ± 1.5	0.0 ± 0.8	-0.3 ± 0.5	0.0 ± 0.3
Massive b-quarks	-2.7 ± 1.6	-1.0 ± 0.8	+0.2 ± 0.5	-0.1 ± 0.3
PDF cteq6l1 → cteq6.6m	-7.7 ± 1.5	-8.4 ± 0.8	-0.5 ± 0.5	-0.7 ± 0.3
Total	$^{+13.9}_{-21.3}$	$^{+12.3}_{-13.8}$	$^{+1.1}_{-1.5}$	$^{+1.4}_{-1.7}$

Table 7.13.: Systematic uncertainties on the event acceptance of signal events produced in the b-quark associated production mode. All values are given in percent. The uncertainties have been derived from variations of the parameters involved in the event generation. The samples have been generated for the parameter choice m_A=120 GeV or m_A=300 GeV and $\tan\beta$=20.

initial and final state radiation result in the largest uncertainties on the event acceptance of up to +34%. However, the contribution of the gluon-fusion production mode to the total signal expectations in the b-tagged final states is very small and therefore the large uncertainties do not affect the final results of this search.

A detailed list of uncertainties on the event acceptance derived for the gluon-fusion production mode of the neutral MSSM Higgs bosons is given in Table 7.14. The individual contributions sum up to a total uncertainty of about $^{+48}_{-6}$% and -5% on the acceptance of the b-tagged and b-vetoed event sample selections, respectively. These uncertainties are assigned to the samples for all generated Higgs boson masses.

$gg \to h/A/H$	b-tagged sample	b-vetoed sample
FSR up	+15.7 ± 29.3	-1.9 ± 2.5
FSR down	+19.0 ± 29.2	-2.4 ± 2.5
ISR up	+34.0 ± 28.6	-0.1 ± 2.5
ISR down	+20.2 ± 29.1	-2.6 ± 2.5
Ren./Fac. scales up	+8.0 ± 29.8	-0.7 ± 2.5
Ren./Fac. scales down	+10.4 ± 29.7	-2.4 ± 2.5
Underlying Event	-5.6 ± 30.8	-0.7 ± 2.5
Total	$^{+48.4}_{-5.6}$	$^{+0.0}_{-4.8}$

Table 7.14.: Systematic uncertainties on the event acceptance of signal events produced in the gluon-fusion mode. All values are given in percent. The uncertainties have been derived from variations of the parameters involved in the event generation. All samples have been generated for the parameter choice m_A=120 GeV and $\tan\beta$=20.

Acceptance Uncertainties for Simulated Background Processes

$Z/\gamma^* \to \tau^+\tau^-$ events simulated with the AlpGen event generator are employed to determine the normalisation of the τ-embedded $Z/\gamma^* \to \mu^+\mu^-$ data after selecting the light lepton and the τ_{had} jet. An estimate of the acceptance uncertainty for this sample and for a similar inclusive event selection has been derived in Ref. [128]. The parameters varied in the generation of simulated event samples were the matching parameters of the MLM matching scheme, the renormalisation and factorisation scales and the choice of the parton density functions. A total uncertainty of ±12.5% on the normalisation of the simulated $Z/\gamma^* \to \tau^+\tau^-$ sample has been derived. The largest contribution to this number originates from the variations of the MLM matching parameters that result in uncertainties of approximately ±11%. In the search presented here the quoted uncertainty of ±12.5% is assigned to the event yields of τ-embedded $Z/\gamma^* \to \mu^+\mu^-$ data and the simulated $Z/\gamma^* \to \ell^+\ell^-$ backgrounds in all signal regions. Additional uncertainties on the event acceptance for the latter process originating from potential changes in the b-jet kinematics are not required as the b-jet selection efficiency in simulated $Z/\gamma^* \to \ell^+\ell^-$ events is corrected to the efficiency in data (see Section 7.6.4).

Uncertainties on the event acceptance for the di-boson and single top background processes have been studied in Ref. [128], as well. For both background processes a total systematic uncertainty of ±2% has been derived for an inclusive event selection. The same uncertainty is

assigned in the search presented here and potential deviations in the b-jet selection efficiency originating from modifications to the event generation are neglected. This is expected to not affect the final results of this search as the contributions of these two background processes to the signal regions of the b-tagged event samples are very small.

7.8.2. Experimental Uncertainties

Several corrections to event and particle properties are applied in the search presented here to correct for an imperfect simulation of the ATLAS detector response to traversing particles or the limited precision of energy measurements with the real detector. These corrections have been derived from dedicated measurements and therefore are subject to uncertainties themselves. Variations of the corrections within their assigned uncertainties result in different predictions for the event yields in the signal regions. The shape of the distribution of the reconstructed $\tau^+\tau^-$ mass, $m_{\tau\tau}^{\text{MMC}}$, is assumed to be not affected by these variations, unless stated otherwise.
Further experimental uncertainties are due to the limited precision of the luminosity measurement for the data set taken into account.

Uncertainty on the Measured Luminosity

The simulated event samples are normalised to the integrated luminosity of 4.7 fb^{-1} that has been measured for the data set analysed. The uncertainty on this measurement of $\pm 3.9\%$ [62, 133] is assigned to the expected event yields of the signal processes and those backgrounds that are not estimated from the data.

Uncertainties on the Trigger Selection Efficiency Correction

The uncertainties on the trigger selection efficiency corrections in simulated event samples are approximately $\pm 1\%$ ($\pm 0.5\%$) in magnitude for all electron (muon) triggers used in this search [96, 100].

Uncertainties on Electrons

For energy clusters identified as electrons a scale uncertainty of typically ($\pm$) 0.3 – 1.6% ($\pm 3\%$) is assigned for electron candidates reconstructed in the barrel (end-cap) region of the detector [96]. The systematic uncertainties on the corresponding energy resolution correction are of the order of $\pm 0.4\%$ [96].

The electron reconstruction and identification efficiency corrections have been measured with a precision of the order of $(\pm)\,3$ – 6% [96]. The resulting uncertainties on the event selection efficiencies have been studied and an additional uncertainty of $\pm 2\%$ is added in quadrature to account for an imperfect description of the electron isolation variables.

Uncertainties on Muons

The muon reconstruction and identification efficiencies are correctly reproduced in simulated event samples [100]. The uncertainties on the corresponding measurements are below $\pm 1.8\%$.
The uncertainty on the muon momentum resolution is typically below $\pm 1\%$ [101].
The track and calorimeter isolation variables of muons are correctly modelled by the simulation and no additional uncertainty is assigned [100].

Uncertainties on τ_{had} Jet Properties

The systematic uncertainties on the energy scale of clusters identified as τ_{had} jets have been derived from the data and depend on the kinematic variables p_T and η of the candidates and on their assigned number of reconstructed Inner Detector tracks [107]. The measured uncertainties are typically of the order of $\pm 5\%$. Changes in the τ_{had} energies are expected to not only affect the event yields in the signal regions through the kinematic requirements on the selected τ_{had} jet, but also the reconstructed $\tau^+\tau^-$ mass $m_{\tau\tau}^{\text{MMC}}$ (see Section 7.9.2).
The systematic uncertainties on the τ_{had} jet identification efficiency are $\pm 10\%$ ($\pm 16\%$) and $\pm 5\%$ ($\pm 8\%$) for τ_{had} jets with one (three) associated tracks and transverse momenta below and above 22 GeV, respectively [107].
The τ_{had} misidentification probabilities for electrons have been measured in $Z/\gamma^* \to e^+e^-$ data events [107]. The uncertainties on the derived correction factors for simulated electrons range from values of $\pm 30\%$ up to $\pm 100\%$, depending on the kinematic variable η of the electron.

Uncertainties on Jets

The uncertainties on the jet energy scale has been measured in data and is of the order of $\pm 3\%$ [104]. The uncertainty on the jet energy resolution is measured to be below $\pm 1\%$ [104]. The changes in the energy of jets do not only affect the event acceptance. As these are propagated to the reconstructed missing transverse momentum (see below), the reconstructed $\tau^+\tau^-$ mass $m_{\tau\tau}^{\text{MMC}}$ is affected, as well (see Section 7.9.2).

Uncertainties on the b-Jet Identification

The uncertainties on the identification efficiency correction for true b-jets and the misidentification rates of c- and light quark jets are treated as fully uncorrelated since these have been derived from independent measurements [112, 113]. The uncertainties are typically of the order of $\pm 5\%$ in magnitude for the selection of b-jets and within the range of $(\pm)\,20$ – 30% for the misidentification of jets with different flavour. The resulting variations in the b-jet selection efficiency do not affect the shape of the $m_{\tau\tau}^{\mathrm{MMC}}$ mass distribution in the b-tagged event samples.

Uncertainties on the Missing Transverse Momentum

Uncertainties on the reconstructed missing transverse momentum originate from several sources. The systematic energy variations for electrons, τ_{had} jets and quark and gluon jets are propagated to the reconstructed missing transverse momentum. The resulting uncertainties on the event selection efficiency due to changes in $E_{\mathrm{T}}^{\mathrm{miss}}$ are implicitly included in the uncertainties derived from the individual energy variations.
Further uncertainties on the missing transverse momentum measurement originate from energy mis-measurements in events with a large number of additional pile-up events, denoted as $E_{\mathrm{T}}^{\mathrm{miss}}$ *pile-up* uncertainty in the following. In addition, the $E_{\mathrm{T}}^{\mathrm{miss}}$ measurement is subject to the uncertainties on the energy measurement of cells in topological clusters, that are not associated to the reconstructed objects, and low-p_{T} energy clusters ($p_{\mathrm{T}}<20\,\mathrm{GeV}$), that are not selected as jets in this search. These sources are denoted as $E_{\mathrm{T}}^{\mathrm{miss}}$ *Cluster* uncertainty in the following. Both the $E_{\mathrm{T}}^{\mathrm{miss}}$ Cluster and pile-up uncertainties have been studied in $Z/\gamma^{*}\rightarrow \ell^{+}\ell^{-}$ and $W\rightarrow \ell\nu_{\ell}$ events selected from the data [134]. They are treated independently from each other and from all other uncertainties on the missing transverse momentum.

Modifications in the size of the reconstructed missing transverse momentum affect the results of this search in several ways. The b-vetoed event sample selection restricts the missing transverse momentum to values above 20 GeV and therefore the corresponding event selection efficiency is directly affected. Affected as well is the reconstructed transverse mass M_{T}, which depends on the magnitude and direction of $E_{\mathrm{T}}^{\mathrm{miss}}$and which is restricted to values below 30 GeV. In addition to the effects on the event selection efficiencies, shifts in the reconstructed $m_{\tau\tau}^{\mathrm{MMC}}$ mass distribution might be induced, as this quantity is sensitive to the magnitude and direction of the missing transverse momentum.

Resulting Systematic Uncertainties on the Event Acceptance

The resulting uncertainties on the event yields of the $\tau_e\tau_{\text{had}}$ final states derived from the systematic variations of the electron identification efficiencies are typically of the order of $(\pm)\,3$ – 5% for all signal and background processes. These numbers already include the $\pm 2\%$ systematic uncertainty on the selection efficiency that accounts for the uncertainty on the electron isolation criteria. For changes in the muon reconstruction and identification efficiency lower uncertainties on the event yields in the $\tau_\mu\tau_{\text{had}}$ final states of $(\pm)\,1$ – 2% are observed for all processes. The uncertainties derived from the variations of the electron and muon energy scale and resolution are typically of the order of $\pm 1\%$ and below for all final states and processes.

The uncertainties on the event selection efficiencies of the b-tagged final states derived from variations of the b-jet identification and misidentification efficiency corrections range from absolute values of 3% up to 18%. For processes in which mainly true b-jets are selected, like the single top background or the b-quark associated Higgs boson production, values below $\pm 10\%$ are typical. Backgrounds containing a significant fraction of misidentified light jets are affected by larger uncertainties. In the b-vetoed final states lower uncertainties of typically $\pm 3\%$ and less are observed for all affected processes.

The change in event selection efficiency due to variations of τ_{had} jet identification lies in the range of $(\pm)\,4.1$ – 4.4% for all processes and final states. Only for the $Z/\gamma^* \to e^+e^-$ background larger deviations from the nominal event yields are observed which results from large uncertainties on the $e \to \tau_{\text{had}}$ misidentification rate corrections. For other background processes the fraction of electrons misidentified as τ_{had} jets is negligible. The uncertainty on the τ_{had} jet misidentification rate of muons is negligible, as well. The uncertainty on the rate at which quark and gluon jets are misidentified as τ_{had} jets has not been taken into account for the $Z/\gamma^* \to \mu^+\mu^-$ event sample. However, the contributions of this background to the finally selected event samples are only about 5% in magnitude.

The uncertainty on the event selection efficiency derived from variations of the $E_{\text{T}}^{\text{miss}}$ pile-up and Cluster corrections are typically of the order of $(\pm)\,1$ – 10% and $(\pm)\,1$ – 9%, respectively. For the b-vetoed final states larger uncertainties are observed than for the b-tagged ones, which results from the direct requirement on the missing transverse momentum.

The variations in the jet energy resolution are found to affect the event acceptance at the percent level and below for all samples and final states.

The energy scale uncertainties on clusters identified as τ_{had} jets and quark and gluon jets are treated as fully correlated. These uncertainties affect the event acceptance directly through the requirements on the transverse momenta of the selected b-jet and τ_{had} jet. In case of the τ_{had}

energy scale uncertainty the distribution of the reconstructed $\tau^+\tau^-$ mass is affected, as well. Indirect effects result from the change in the reconstructed missing transverse momentum that the jet and τ_{had} jet energy modifications are propagated to. The jet energy scale uncertainty furthermore affects the corrections to the *b*-jet selection efficiencies of all quark flavours, since these have been measured and applied in dependency on the jet momenta.
The resulting change in the event acceptance due to the fully correlated energy scale variations of jets and τ_{had} jets range from absolute values of 6 – 24% and from 5 – 28% in the *b*-vetoed and *b*-tagged final states, respectively. The former event sample is mainly affected by the requirement imposed on the missing transverse momentum, whereas the latter is mainly affected by the transverse momentum threshold on the selected *b*-jet. The effect of the combined variations of the jet and τ_{had} energy scales on the reconstructed $\tau^+\tau^-$ mass $m_{\tau\tau}^{\text{MMC}}$ are shown in Section 7.9.2 for the signal and background processes.

7.8.3. Systematic Uncertainties on Data-Driven Methods

The background contributions to the signal regions estimated partly or completely from the data are subject to several sources of systematic uncertainties. Most of the methods still depend on the Monte Carlo predictions for other background processes that are subtracted from the data observed in control regions. Hence, the data-driven background estimates indirectly suffer from the same sources of systematic uncertainties as those listed in the previous sections. In addition, the estimation techniques and the underlying assumptions have been tested for potential biases. The deviations from central values observed in these tests are used to derive systematic uncertainties on the background estimates. Details are presented in the following sections, individually for each background estimation technique.

Systematic Uncertainties on the Multi-jet Background Estimation

The background contributions from the multi-jet production processes are estimated using the *ABCD* method as described in Section 7.6.5.

Uncertainties on the predicted multi-jet event yields are due to variations of the subtracted simulated event samples according to the uncertainties presented in Section 7.8.2. Since some of the control regions are heavily contaminated, the resulting uncertainties on the multi-jet background predictions are of the order of $\pm 10\%$ and $\pm 20\%$ for the *b*-tagged and *b*-vetoed final states, respectively. The largest contributions to these numbers originate from the uncertainties on the energy scales of particles and those on the missing transverse momentum which in combination are of

the order of $\pm 6\%$ in magnitude for the b-tagged final state and $\pm 20\%$ for the b-vetoed one. The resulting uncertainties on the multi-jet predictions are fully anti-correlated to the uncertainties on the Monte Carlo predictions of other backgrounds (see discussion in Section 7.6.5).

Further systematic uncertainties on the multi-jet background predictions can be deduced from the stability studies presented in Section 7.6.5. The observed variations of $r_{B/D}$ with different thresholds imposed on the anti-isolation criteria of the selected lepton candidates are found to be smaller than the corresponding statistical uncertainties. Therefore, no systematic uncertainty is assigned to the estimated multi-jet event yields. However, significant deviations of the ratios $r_{B/D}$ from their nominal values are observed in different ranges of the reconstructed $\tau^+\tau^-$ mass $m_{\tau\tau}^{\text{MMC}}$. The dependencies of the ratios $r_{B/D}$ with the mass $m_{\tau\tau}^{\text{MMC}}$ were studied by evaluating these ratios in different bins of the mass. The corresponding $m_{\tau\tau}^{\text{MMC}}$ mass distributions in the data regions in which anti-isolated leptons are selected and the resulting data points for $r_{B/D}$ are shown in Fig. 7.17 for all final states. As these data points show a linear dependence, linear fits were performed. The results of these fits are displayed in Fig. 7.17, as well.
Systematic uncertainties on the nominal values of the ratios $r_{B/D}$ were extracted from each fit based on the difference of the minimum and the maximum of the fit function in the analysed mass range of 0 – 400 GeV. Assuming the measured values of $r_{B/D}$ to be normally distributed around their nominal values, the uncertainty corresponding to the $\pm 1\,\sigma$ uncertainty interval is obtained by multiplying half of this difference by 0.68. For the b-vetoed $\tau_\mu\tau_{\text{had}}$ final state, for example, the fit results in a straight line with maximum and minimum function values of 1.239 and 0.975 for masses of $m_{\tau\tau}^{\text{MMC}} = 0$ GeV and 400 GeV, respectively. Half of the difference of these values, 0.264, is considered the maximum upward (downward) deviation of $r_{B/D}$. The $\pm 1\,\sigma$ uncertainty interval on $r_{B/D}$ is then given by 0.68 times this difference, i.e. ≈ 0.180, which corresponds to a relative uncertainty of approximately $\pm 15\%$ on the nominal value of $r_{B/D}$=1.16 for b-vetoed $\tau_\mu\tau_{\text{had}}$ final state.
The systematic uncertainties on the ratios $r_{B/D}$ obtained with this procedure amount to $\pm 15\%$ and $\pm 17\%$ in the b-vetoed and b-tagged $\tau_e\tau_{\text{had}}$ event samples, respectively, and $\pm 7.7\%$ and $\pm 3\%$ in the b-vetoed and b-tagged $\tau_\mu\tau_{\text{had}}$ event samples. As the uncertainties derived from event samples containing the same selected lepton flavour are of the same order in magnitude, the uncertainties on the ratios $r_{B/D}$ are assumed to be $\pm 15\%$ for the $\tau_e\tau_{\text{had}}$ final state and $\pm 7.5\%$ for the $\tau_\mu\tau_{\text{had}}$ final state.

A complete summary of the systematic uncertainties on the multi-jet background predictions is given in Table 7.15.

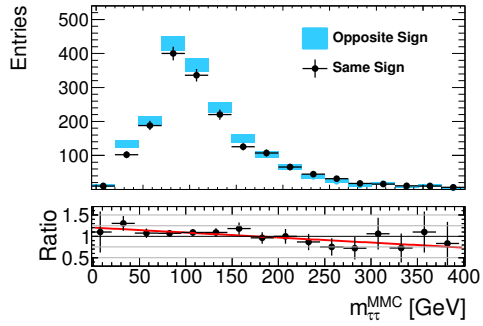

(a) $\tau_e\tau_{had}$, b-vetoed sample

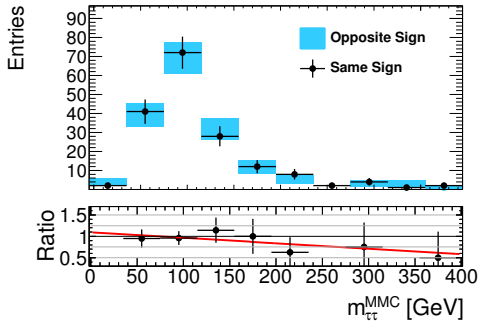

(b) $\tau_e\tau_{had}$, b-tagged sample

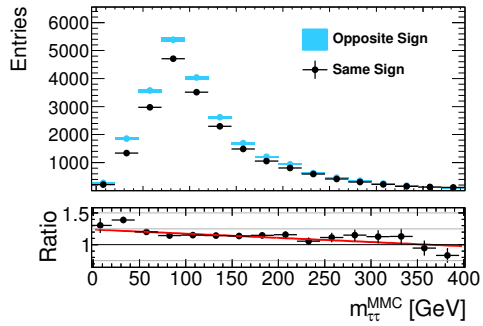

(c) $\tau_\mu\tau_{had}$, b-vetoed sample

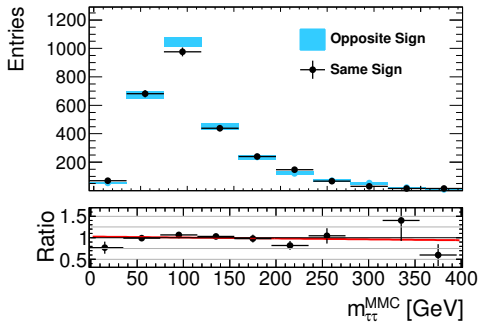

(d) $\tau_\mu\tau_{had}$, b-tagged sample

Figure 7.17.: Comparison of the $m_{\tau\tau}^{\mathrm{MMC}}$ mass distributions in data events in which anti-isolated leptons and τ_{had} jets of either same sign or opposite sign electric charges were selected. The upper (lower) row shows the comparisons for data events containing selected electrons (muons). The left and right column show the distributions for the b-vetoed and b-tagged event samples, respectively. The ratios of the distributions represent the ratios $r_{B/D}$ as a function of the mass $m_{\tau\tau}^{\mathrm{MMC}}$. The straight, red lines show the results of linear fits to the data points for $r_{B/D}$.

	$\tau_e\tau_{\text{had}}$ Final State		$\tau_\mu\tau_{\text{had}}$ Final State	
	b-tagged sample	b-vetoed sample	b-tagged sample	b-vetoed sample
b-jet identification	$^{+6}_{-3}$	$<\pm1$	$^{+7}_{-4}$	$<\pm1$
Energy scales	$^{+6}_{-7}$	$^{+18}_{-19}$	±6	$^{+21}_{-18}$
e/μ identification	±1	±2	$<\pm1$	±1
τ identification	$<\pm1$	±1	$<\pm1$	±1
$\ell\to\tau_{\text{had}}$ misidentification	±1	$^{+1}_{-3}$	$<\pm1$	$<\pm1$
Embedding Shape	±1	±1	±5	±2
Total	$^{+9}_{-8}$	$^{+18}_{-19}$	$^{+11}_{-9}$	$^{+21}_{-18}$
Systematic	±15	±15	±7.5	±7.5

Table 7.15.: Summary of the systematic uncertainties on the predicted event yields of the multi-jet background in percent. Uncertainties on the simulated event samples are propagated to the multi-jet background expectations. "Systematic" denotes the additional uncertainties derived from the stability studies of $r_{B/D}$ as a function of the reconstructed $m_{\tau\tau}^{\text{MMC}}$ mass.

Uncertainties on the $W+$ jets Background Normalisation Correction

Uncertainties on the normalisation correction of the $W+$ jets background originate from the uncertainties on the Monte Carlo predictions for event samples that are subtracted from the data in the high-M_{T} control region and the predictions for the $W+$ jets background in that control region. The largest deviations are observed for variations of the jet energy scale and in case of the $\tau_{\mathrm{e}}\tau_{\mathrm{had}}$ final state the corrections for the τ_{had} misidentification rate of electrons. These variations affect the normalisation correction factor at a level of $(\pm)\,4$ – 6% and $\pm 2\%$, respectively. In total the uncertainties on the $W+$ jets background normalisation derived from the variations of the Monte Carlo predictions sum up to an uncertainty of about $\pm 5\%$ for the $\tau_{\mathrm{e}}\tau_{\mathrm{had}}$ and $\pm 6\%$ for the $\tau_{\mu}\tau_{\mathrm{had}}$ final state event samples.

In addition, small deviations from the nominal normalisation corrections have been observed for the correction factors derived in control regions with varied boundary conditions on the transverse mass M_{T} (see Table 7.6). To account for these, an additional and conservative uncertainty of $\pm 5\%$ is assigned to the normalisation of the $W+$ jets event sample in all signal regions.

An additional uncertainty is assigned to the $W+$ jets background normalisation in the b-tagged event samples. In Section 7.6.4 the normalisation correction measurements were repeated after the b-jet requirements have been applied. This was done in order to validate the b-jet selection efficiency in the simulated $W+$ jets event sample. The corresponding measurements are subject to large statistical uncertainties of approximately $\pm 17\%$ for both final states that are assigned as systematic uncertainties to the normalisation correction of the $W+$ jets background in all b-tagged signal regions.

Systematic Uncertainties on the $t\bar{t}$ Background Estimation

The predicted event yields of the $t\bar{t}$ background processes are corrected as described in Section 7.6.3. The uncertainties on these corrections arise from the subtraction of the small contamination with other background processes from the data observed in the control region and from the uncertainties on the predictions for the $t\bar{t}$ background in this control region. The corresponding simulated samples have been varied within their uncertainties as described above and the effect on the computed $t\bar{t}$ normalisation correction was studied. The largest uncertainties arise from variations of the b-jet identification efficiency corrections and those of the τ_{had} and jet energy scales that result in changes of the $t\bar{t}$ event yields in the signal regions of $\pm 14\%$ and $\pm 3\%$, respectively. Other systematic variations of the simulated event samples result in deviations from the central value at the percent level and below.

The stability studies of the normalisation correction measurement for the combined $\tau_{\mathrm{e}}\tau_{\mathrm{had}}$

and $\tau_\mu\tau_{\text{had}}$ event samples showed good agreement of the scale factors derived in the additional control regions with the nominal value. However, deviations are observed for the factors derived individually for the two final states, ranging from values of 0.82 for the $\tau_e\tau_{\text{had}}$ up to 0.94 for the $\tau_\mu\tau_{\text{had}}$ final state. To account for these deviations a systematic uncertainty of half of the observed range $(0.94-0.82)*0.5=0.06$, i.e. about $\pm 7\%$, is assigned to the normalisation correction factor of the simulated $t\bar{t}$ event sample.

Systematic Uncertainties on the τ-Embedded $Z/\gamma^*\to\mu^+\mu^-$ Data

The $Z/\gamma^*\to\tau^+\tau^-$ background processes are estimated using the τ-embedded $Z/\gamma^*\to\mu^+\mu^-$ data. Since this sample is normalised to the simulated $Z/\gamma^*\to\tau^+\tau^-$ sample after the lepton and the τ_{had} jet are selected, the estimated event yield suffers from the uncertainties on the trigger selection, the energy scales and identification corrections for these particles. The resulting effects on the sample normalisation range from $\pm 1\%$ for variations of the muon identification efficiency up to $\pm 6\%$ for the variation of the τ_{had} energy scale. Further uncertainties arise from the uncertainties on the theory predictions for the simulated $Z/\gamma^*\to\tau^+\tau^-$ sample, i.e. on the production cross section and the event acceptance. Uncertainties on the energy scale and resolution of jets and those on the identification efficiency correction of b-jets do not apply to the τ-embedded sample as the jet content in these events originates from the selected $Z/\gamma^*\to\mu^+\mu^-$ data.

In addition to the uncertainties resulting from the normalisation to the simulated event sample, the τ-embedding procedure itself has been tested for stability in its predictions. The selected $Z/\gamma^*\to\mu^+\mu^-$ data sample has been varied by tightening the isolation criteria imposed on the selected muons. These track isolation criteria have an influence on the average amount of calorimeter energy deposited around the muons and hence on the reconstructed energy of the τ_{had} jets that replace these. Furthermore, variations have been applied to the muon removal procedure in the data. The calorimeter energy deposited by the muons in the simulated $Z/\gamma^*\to\mu^+\mu^-$ event sample has been varied by $\pm 30\%$ before these energy depositions were subtracted from the data event. For both of the previously defined modifications to the embedding procedure, the modified τ-embedded $Z/\gamma^*\to\mu^+\mu^-$ event samples have been analysed and the resulting predictions in the signal regions have been compared to the nominal ones. The systematic uncertainties that have been derived from these comparisons are listed in Table 7.16.
Typical deviations are of the order of $(\pm)\,1$ – 3% for both sources of uncertainties. Larger deviations of up to +40% are observed for the b-tagged sample in the $\tau_e\tau_{\text{had}}$ final state. However, the large deviations are considered to predominantly result from the very limited statistics of the τ-embedded samples used to derive the uncertainties: for these samples the uncertainty of

	$\tau_e\tau_{had}$ Final State		$\tau_\mu\tau_{had}$ Final State	
	b-tagged sample	b-vetoed sample	b-tagged sample	b-vetoed sample
Isolation	± 40	± 3	± 1	± 1
+30% Energy Removed	± 8	± 2	± 3	± 2
-30% Energy Removed	± 14	$< \pm 1$	± 2	± 3
Total	± 42	± 4	± 3	± 3

Table 7.16.: Systematic uncertainties on the event yield of the τ-embedded $Z/\gamma^* \to \mu^+\mu^-$ data in percent that have been derived from variations in the τ-embedding procedure. "Isolation" denotes the uncertainties derived from a τ-embedded sample for which tighter track isolation criteria have been applied to the selected muons in data. For uncertainties labelled "$\pm$30% Energy Removed" the amount of energy in the calorimeters that is removed from the data event has been varied by $\pm$30% for both muons.

+40% is equivalent to less than 1.5 standard deviations of the associated statistical uncertainty. In addition to a change in the sample normalisation, the variations in the calorimeter energy removal procedure are considered to affect the shape of the reconstructed $m_{\tau\tau}^{\mathrm{MMC}}$ mass distribution. A comparison of these shapes in τ-embedded samples obtained with nominal and modified muon removal procedure are shown in Section 7.9.2. Changes to the isolation criteria imposed on the muon candidates, on the other hand, are found to affect the $m_{\tau\tau}^{\mathrm{MMC}}$ mass distribution at a negligible level.

Z/γ^*+jets Background Normalisation Correction

Corrections for the selection efficiency of b-jets in simulated $Z/\gamma^* \to \ell^+\ell^-$ samples were derived in Section 7.6.4 and amount to $f_{Zb}^{e} = 1.08 \pm 0.23$ (stat.) and $f_{Zb}^{\mu} = 1.11 \pm 0.13$ (stat.) for the $\tau_e\tau_{had}$ and $\tau_\mu\tau_{had}$ final states, respectively. A potential bias of these factors originates from a $t\bar{t}$ background contamination in the τ-embedded $Z/\gamma^* \to \mu^+\mu^-$ data, which is strongly enhanced after the b-jet selection criteria are applied. This bias has been studied by removing the upper transverse momentum threshold of 50 GeV that is imposed on the b-jet, which further enhances the contamination with $t\bar{t}$ production processes. For a statistical combination of the $\tau_e\tau_{had}$ and $\tau_\mu\tau_{had}$ final state event samples, the b-jet efficiency scale factors are found to be $f_{Zb}^{combined} = 1.10 \pm 0.12$ (stat.) with and $f_{Zb,no\,p_T}^{combined} = 1.18 \pm 0.08$ (stat.) without applying the upper momentum threshold. The relative difference in these numbers of $\pm$7% is assigned as an additional systematic uncer-

tainty to the simulated $Z/\gamma^* \to \ell^+\ell^-$ background sample normalisation in the b-tagged signal regions.

7.8.4. Summary

A summary of the systematic uncertainties on the event yields of all processes and for all signal regions is given in Table 7.17. The uncertainties on simulated event samples derived from variations of the missing transverse momentum and the energy scales of τ_{had} jets, jets and leptons are combined and labelled "Energy Scales". All numbers are given in percent. Entries showing "–" indicate that the corresponding uncertainty is below $\pm 1\%$ or does not apply to this specific background. The uncertainty on the b-jet identification, for example, only applies to the signal event samples and those of the single top and di-boson backgrounds. The τ-embedded $Z/\gamma^* \to \mu^+\mu^-$ data contains jets from real p–p collisions and for the $W+$ jets and $Z/\gamma^* \to e^+e^-$ backgrounds the uncertainties on the b-jet selection efficiency were derived from control measurements. For similar reasons the lepton and τ_{had} identification efficiency uncertainties, the uncertainty on the luminosity measurement and those on the theory predictions do not apply to the $t\bar{t}$ and $W+$ jets background event yields. The corresponding uncertainties are compensated by the normalisation to the data or included in the uncertainties on the normalisation corrections. The latter are denoted as "Data-driven" uncertainties in the table. These numbers include the statistical uncertainties on the derived corrections, as well as the systematic uncertainties derived from the Monte Carlo event sample subtraction from the data and the stability studies. For all processes the uncertainties derived from energy variations of objects are considered using the Monte Carlo predictions as these uncertainties affect the shape of the reconstructed $\tau^+\tau^-$ mass $m_{\tau\tau}^{\text{MMC}}$ (see Section 7.9.2). The uncertainties on the multi-jet background expectations were already given in Table 7.15.

$\tau_e\tau_{had}$ Final State, b-tagged / b-vetoed sample [%]							
	τ-embedded	W+jets	$Z/\gamma^* \to \ell\ell$	$t\bar{t}$	Other	Signal	
	$Z/\gamma^* \to \mu\mu$					$b\bar{b}h/A/H$	$gg \to h/A/H$
Cross-section	± 5	–	± 5	–	$\pm 12/\pm 9$	$^{+13}_{-19}$	$^{+15}_{-14}$
Acceptance	± 12.5	–	± 12.5	–	$\pm 3/\pm 3$	$^{+14}_{-19}$ / ± 2	$^{+48}_{-6}$ / $^{+0}_{-5}$
e Efficiency	± 5 / ± 8	–	± 4 / ± 4	–	± 3	± 5 / ± 4	± 3 / $^{+5}_{-4}$
τ Efficiency	± 4	–	$^{+25}_{-19}$ / $^{+35}_{-30}$	–	± 4	± 4	± 4
b-jet Id.	–	–	–	–	$^{+9}_{-6}$ / $^{+1}_{-2}$	$^{+3}_{-7}$ / ± 2	$^{+12}_{-18}$ / –
Energy Scales	$^{+6}_{-4}$ / ± 4	$^{+4}_{-14}$ / $^{+11}_{-19}$	$^{+21}_{-3}$ / $^{+32}_{-19}$	$^{+7}_{-13}$ / $^{+8}_{-7}$	$^{+1}_{-20}$ / $^{+12}_{-11}$	$^{+5}_{-13}$ / ± 7	$^{+5}_{-13}$ / ± 7
Data-driven	± 42 / ± 4	± 18 / ± 7	± 22 / –	± 17	–	–	–
Luminosity	± 3.9	–	± 3.9	–	± 3.9	± 3.9	± 3.9
Total	± 45 / ± 18	$^{+18}_{-23}$ / $^{+13}_{-20}$	$^{+42}_{-32}$ / $^{+50}_{-39}$	$^{+18}_{-21}$ / ± 18	$^{+16}_{-25}$ / $^{+17}_{-16}$	$^{+21}_{-32}$ / $^{+17}_{-22}$	$^{+52}_{-28}$ / ± 18

$\tau_\mu\tau_{had}$ Final State, b-tagged / b-vetoed sample [%]							
	τ-embedded	W+jets	$Z/\gamma^* \to \ell\ell$	$t\bar{t}$	Other	Signal	
	$Z/\gamma^* \to \mu\mu$					$b\bar{b}h/A/H$	$gg \to h/A/H$
Cross-section	± 5	–	± 5	–	$\pm 12/\pm 9$	$^{+13}_{-19}$	$^{+15}_{-14}$
Acceptance	± 12.5	–	± 12.5	–	± 2	$^{+14}_{-19}$ / ± 2	$^{+48}_{-6}$ / $^{+0}_{-5}$
μ Efficiency	± 1	–	± 2	–	± 2	± 2	± 2
τ Efficiency	± 4	–	–	–	± 4	± 4	± 4
b-jet Id.	–	–	–	–	$^{+9}_{-6}$ / $^{+3}_{-2}$	$^{+3}_{-7}$ / ± 2	$^{+12}_{-18}$ / –
Energy Scales	± 2 / ± 4	$^{+13}_{-17}$ / $^{+9}_{-15}$	$^{+48}_{-18}$ / $^{+24}_{-22}$	$^{+11}_{-12}$ / $^{+8}_{-6}$	$^{+22}_{-1}$ / $^{+10}_{-7}$	$^{+5}_{-13}$ / ± 7	$^{+5}_{-13}$ / ± 7
Data-driven	± 3 / ± 3	± 18 / ± 8	± 14 / –	± 17	–	–	–
Luminosity	± 3.9	–	± 3.9	–	± 3.9	± 3.9	± 3.9
Total	± 15	$^{+22}_{-25}$ / $^{+12}_{-17}$	$^{+52}_{-27}$ / $^{+28}_{-26}$	$^{+20}_{-21}$ / $^{+19}_{-18}$	$^{+27}_{-15}$ / $^{+15}_{-13}$	$^{+21}_{-31}$ / $^{+16}_{-21}$	$^{+53}_{-27}$ / ± 17

Table 7.17.: Systematic uncertainties in percent on the estimated background and signal event yields (m_A =150 GeV and $\tan\beta = 20$). Entries separated by "/" correspond to the b-tagged sample on the left-hand side and the b-vetoed sample on the right-hand side. If no distinction is made, the uncertainty for both samples is identical. "–" indicates that this uncertainty is below $\pm 1\%$ or does not apply to this specific background. "Other" denotes the uncertainties on the combined single top and di-boson backgrounds. "Energy Scales" denotes the combination of the uncertainties on the τ_{had}, jet and lepton energy scales and the uncertainty on the missing transverse momentum.

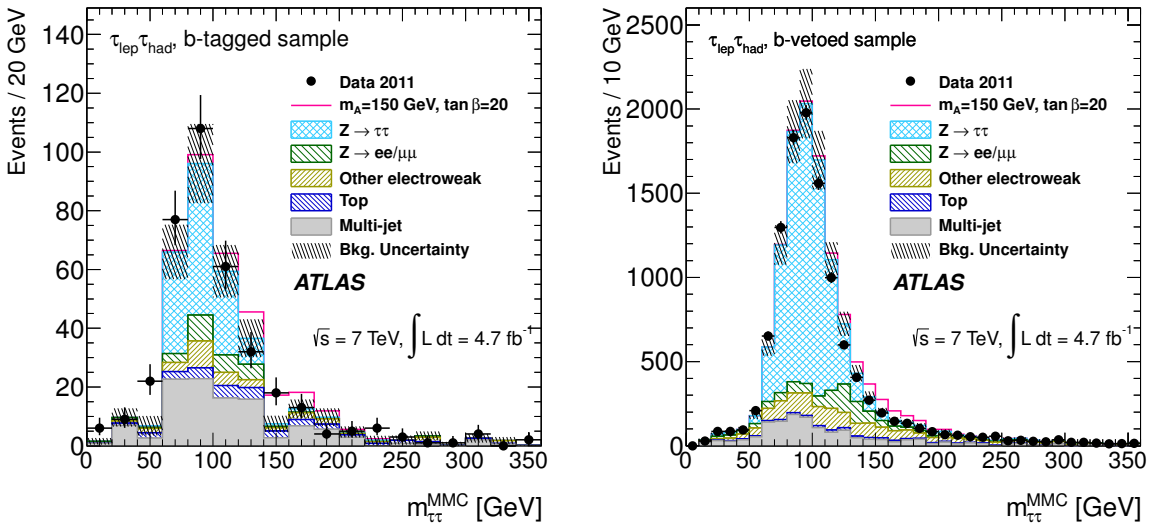

(a) b-tagged sample

(b) b-vetoed sample

Figure 7.18.: Distributions of the reconstructed $\tau^+\tau^-$ mass $m_{\tau\tau}^{\text{MMC}}$ in the b-tagged (a) and b-vetoed (b) samples for the combined $\tau_e\tau_{\text{had}}$ and $\tau_\mu\tau_{\text{had}}$ final states. The data are compared to the background expectation and a hypothetical MSSM signal ($m_A = 150$ GeV and $\tan\beta = 20$). Uncertainties on the background expectation represent the combined statistical and systematic uncertainties. The contributions of the di-boson and $W+$jets background processes are combined and labelled "Other electroweak".

7.9. Statistical Interpretation

The final interpretation of the search results is based on the analysis of the reconstructed $\tau^+\tau^-$ mass distribution, $m_{\tau\tau}^{\text{MMC}}$. This distribution is shown in Fig. 7.18 for the statistical combination of the $\tau_e\tau_{\text{had}}$ and $\tau_\mu\tau_{\text{had}}$ final states and for both the b-tagged and b-vetoed event samples. For reasons given below, rebinned distributions for the individual final states containing either selected electrons or muons are shown in Fig. 7.19. The corresponding event yields have been presented in Table 7.12.

No significant excess of data over the background expectations has been observed. Therefore, upper limits on the value of $\tan\beta$ have been derived as a function of the Higgs boson mass m_A using the CL$_s$ *frequentist approach* [135] and *asymptotic approximation* techniques [136]. The procedure is briefly summarised below.

7.9.1. General Methodology

Two hypotheses are defined to test the observed data against the predicted background and signal expectations. The *background–only hypothesis*, or null hypothesis, assumes that no signal is present in data. In contrast, the *signal–plus–background hypothesis* assumes a signal being present in data. The level of agreement of the observed data with one of the two hypotheses can be quantified by the probability of finding data of lower compatibility with the predictions for that particular hypothesis. If this probability is lower than a certain threshold the hypothesis can be rejected with a certain confidence level.

The probabilities quantifying the level of agreement are calculated from the distributions of a final discriminating observable. In this search this observable is the mass $m_{\tau\tau}^{\mathrm{MMC}}$. For each bin i of the distribution the expected number of events E_i can be expressed as

$$E_i = \mu\, s_i(\theta) + b_i(\theta)\,. \tag{7.7}$$

The s_i and b_i denote the nominal expected number of signal and background entries, respectively, in the ith bin. Since these entries are known to limited precision only, they are defined as functions of a set of *nuisance parameters* θ that parameterise the assigned uncertainties on the entries in units of standard deviations. The parameter μ in Equation (7.7) is the *signal strength* that globally scales the signal contribution to each bin. Therefore, the background–only hypothesis can be defined by choosing $\mu = 0$ and the nominal signal–plus–background hypothesis is defined by $\mu = 1$.

The particular values for the nuisance parameters θ and the signal strength μ for which the expectations and the observed data exhibit the highest level of agreement are unknown a-priory. Hence, these values are fit from the data. Auxiliary measurements may provide additional information to improve the fit results and stability and to constrain some of the nuisance parameters. If such an additional measurement of an observable m has been performed, the expected number of events in bin k in the distribution of this observable can be parameterised analogous to Equation (7.7) as a function of the expected number of signal and background events in bin k, $s'_k(\theta)$ and $b'_k(\theta)$, respectively.

Using these definitions a *profile likelihood* function for the measurements is defined. This likelihood is based on the product of the Poisson probabilities for each bin in the distributions of the final observable and the auxiliary measurement of m

$$\mathscr{L}(\mu,\theta) = \prod_{\theta} G(\theta_i) \times \prod_{i=1}^{N} \frac{(\mu s_i + b_i)^{n_i}}{n_i!} e^{-(\mu s_i + b_i)} \times \prod_{k=1}^{M} \frac{(\mu s'_k + b'_k)^{m_k}}{m_k!} e^{-(\mu s'_k + b'_k)}\,. \tag{7.8}$$

The n_i and m_k in this equation are the observed data in the ith and kth bin of the corresponding distributions. Since the s_i, b_i, s'_k and b'_k depend on the nuisance parameters θ the same statement holds for the likelihood function. The $G(\theta_i)$ in Equation (7.8) are Gaussian functions defined for each nuisance parameter. They represent penalty terms that decrease the likelihood function with increasing deviations of the nuisance parameter from zero, i.e. for large deviations of fit values from the nominal values of the parameters that are fit.

Data-driven predictions derived with an *ABCD* method can be taken into account by including the auxiliary measurements in all control regions according to Equation (7.8). Let $b^k_{A,B,C,D}$ denote the contributions of the backgrounds that are determined using Monte Carlo predictions to the signal region A and the three control regions B, C and D. The contribution b^u of an additional, unknown background – the multi-jet background in this search – to the signal region is to be estimated with and *ABCD* method. For this background the *ABCD* relations between its contributions to all four regions can be described by two additional nuisance parameters τ_B and τ_C, of which the latter corresponds to $(r_{B/D})^{-1}$ of Equation (7.5). Therefore, the estimated rates in the three control regions can be parameterised as $b^u\tau_B$ in region B, $b^u\tau_C$ in region C and $b^u\tau_C\tau_B$ in region D. Given the signal contributions to the four regions s, s_B, s_C and s_D, the expected event yields in all regions $E_{A,B,C,D}$ are defined analogous to Equation (7.7) as

$$\begin{aligned} E_A &= \mu s + b^k_A + b^u\,, \\ E_B &= \mu s_B + b^k_B + b^u\,\tau_B\,, \\ E_C &= \mu s_C + b^k_C + b^u\,\tau_C\,, \\ E_D &= \mu s_D + b^k_D + b^u\,\tau_B\tau_C\,. \end{aligned} \tag{7.9}$$

Using these relations the likelihood function can be defined as

$$\mathscr{L}_{ABCD}\,(n_a,n_b,n_c,n_d|\mu,\theta) = \prod_{\theta} G(\theta_i) \times \prod_{i=A,B,C,D} \frac{e^{-E_i}E_i^{n_i}}{n_i!}\,, \tag{7.10}$$

where the products over the histogram bins are suppressed. The n_A, n_B, n_C and n_D in Equation (7.10) denote the number of observed data events in the four data regions.

To test the data against the signal–plus–background hypothesis for a particular value of the signal strength parameter μ a *profile likelihood ratio* $\lambda(\mu)$ is defined as

$$\lambda(\mu) = \frac{\mathscr{L}(\mu,\hat{\hat{\theta}})}{\mathscr{L}(\hat{\mu},\hat{\theta})}\,. \tag{7.11}$$

The $\hat{\hat{\theta}}$ denotes the particular values of θ that maximise the likelihood $\mathscr{L}$ for a certain signal strength μ. This maximum of $\mathscr{L}$ is denoted as the *conditional maximum-likelihood estimator* (μ fixed). The resulting value for the likelihood is normalised to the *unconditional*, global maximum of the likelihood function $\mathscr{L}(\hat{\mu},\hat{\theta})$ (μ free), obtained with appropriate values $\mu = \hat{\mu}$ and $\theta = \hat{\theta}$.

To compute upper limits on the signal strength parameter a *test statistics* t_μ is defined as

$$t_\mu = \begin{cases} -2\ln \frac{L(\mu,\hat{\hat{\theta}}(\mu))}{L(0,\hat{\hat{\theta}}(0))} & \hat{\mu} < 0\,, \\ -2\ln \frac{L(\mu,\hat{\hat{\theta}}(\mu))}{L(\hat{\mu},\hat{\theta})} & 0 \le \hat{\mu} \le \mu\,, \\ 0 & \hat{\mu} > \mu\,. \end{cases} \tag{7.12}$$

This definition assumes that the signal strength μ is always positive, reflecting the fact that a potential signal only increases the number of observed data. The magnitude of t_μ is a measure for the level of agreement of the observed data with the signal–plus–background hypothesis for the signal strength μ. To quantise this level of agreement a probability, denoted as the *p–value*, is computed as

$$p_\mu = \int_{t_\mu^{obs}}^{\inf} f(t_\mu|\mu)\, dt_\mu\,, \tag{7.13}$$

where t_μ^{obs} denotes the observed value for the test statistics. The functions $f(t_\mu|\mu)$ are the probability density functions of t_μ for a given signal strength μ. They can be determined by performing a sufficiently large number of *pseudo experiments*. However, the corresponding computations are very complex and time consuming. Therefore, the density functions are usually approximated using asymptotic formulae, resulting in an *Asimov data set* of functions [136]. The Asimov data set for a measurement is usually validated against the results of pseudo experiments for a small subset of signal hypotheses.

The existence of a signal in data with signal strength μ' is excluded at the *95% Confidence Level*, if the observed data are incompatible with the signal–plus–background hypothesis with a probability of 95%, i.e. if the corresponding p–value yields $p(\mu') = 0.05$. Consequently larger signal strengths are excluded, as well, since for these the corresponding p–value is lower ($p(\mu) < p(\mu')\ \forall\, \mu > \mu'$).

For very small signals, however, one finds that the above definition is not sufficient as the background–only and the signal–plus–background hypotheses cannot be distinguished. In such cases signal strengths might be excluded for which no experimental sensitivity is at hand. To

avoid such unjustified exclusions the CL_s *statistics* is defined as

$$\text{CL}_s(\mu) = \frac{p_\mu}{1 - p_0}, \tag{7.14}$$

where p_0 denotes the p–value of the background–only hypothesis ($\mu = 0$) [18]. Using this CL_s statistics, signals with strength μ can be excluded at the *95% CL_s Confidence Level*, if $\text{CL}_s(\mu) < 0.05$.

The *expected sensitivity* of a search for new physics can be computed by testing the signal–plus–background hypothesis against the background–only hypothesis using the expectations from simulation. The *median* or *expected significance* is given by the signal strength μ' for which one finds $\text{CL}_s(\mu') = 0.05$. For all signal strengths $\mu > \mu'$ the background–only hypothesis can be excluded at the 95% CL_s Confidence Level and therefore a signal with that strength should be detectable in the data.

The median significance can be evaluated completely without considering the observed data. In this case the expected sensitivity is denoted as the *blinded* expected limit. However, the nominal background expectations might be substantially different from the true background contributions to the data. To better approximate these, the data can be taken into account to constrain the values of the nuisance parameters by evaluating the conditional maximum-likelihood estimator for the background–only hypothesis ($\mu = 0$). In this case the resulting expected sensitivity is denoted as the *unblinded* expected limit. For signal free control regions this procedure does not induce any bias to the fit result. In the signal region, however, the potential signal contribution to the data might affect the fit values of the nuisance parameters. By convention, such effects are neglected.

7.9.2. Application to the Search for the Neutral Higgs Bosons of the MSSM

The procedure described above has been applied to the search for the neutral Higgs bosons of the MSSM in the $\tau_{\text{lep}}\tau_{\text{had}}$ decay mode. The input to the profile likelihood function is the distribution of the reconstructed $\tau^+\tau^-$ mass $m_{\tau\tau}^{\text{MMC}}$. As the asymptotic approximation technique is sensitive to bins containing a low number of events, the $m_{\tau\tau}^{\text{MMC}}$ mass shapes analysed have been defined using variable bin sizes. The corresponding boundaries for the mass histograms in all signal regions were chosen such that the number of events in each bin is sufficient for the approximation technique to be valid[1)]. The resulting histograms are shown in Fig. 7.19 for

[1] For the b-tagged event samples the histograms are defined by six bins with boundaries 0 – 70 – 90 – 100 – 120 – 150 – 600 GeV. The boundaries for the 30 bins of the b-vetoed sample mass histograms are 0 – 20 – 40 – 50 –

the signal regions. The data are compared to the background expectations and a hypothetical signal, assuming MSSM parameter values of m_A=150 GeV and $\tan\beta$=20. The control region measurements of the *ABCD* method that determine the contribution of the multi-jet background processes are included in the likelihood function according to Equation (7.10).

The expected amount of signal in each bin of the $m_{\tau\tau}^{\mathrm{MMC}}$ mass distribution depends on the hypothetical values for the MSSM parameters m_A and $\tan\beta$, assuming production cross sections, branching ratios and widths for the Higgs bosons as computed in the m_h^{max} benchmark scenario. Therefore, the signal strength μ can be expressed as a function of $\tan\beta$ for each mass hypothesis m_A. Accordingly, limits on the free parameters of the MSSM Higgs sector are set as upper 95% CL_s Confidence Limit limits on $\tan\beta$ individually for each mass m_A.

Systematic uncertainties on the background expectations are parameterised by nuisance parameters. Uncertainties common among several backgrounds are assumed to be fully correlated. This includes the uncertainties on the luminosity and the energy scales and acceptances of physics objects. Additional nuisance parameters defined for each bin of the $m_{\tau\tau}^{\mathrm{MMC}}$ distributions take into account the statistical uncertainties on the background predictions. Statistical uncertainties on the signal predictions are not taken into account.

Most systematic uncertainties do not or only mildly affect the shape of the reconstructed $m_{\tau\tau}^{\mathrm{MMC}}$ mass distribution. Hence, the corresponding nuisance parameters are assumed to only affect the expected event yields for the different processes. Exceptions to this treatment are the systematic uncertainties on the jet and τ_{had} energy scales. The corresponding nuisance parameters are used to parameterise shape uncertainties on the $m_{\tau\tau}^{\mathrm{MMC}}$ distribution for all considered backgrounds and the signal processes. While for ordinary nuisance parameters the normalisations of the background expectations are continuously changed, the shapes of the $m_{\tau\tau}^{\mathrm{MMC}}$ mass distributions are changed by nuisance parameters parameterising shapes uncertainties in addition: these shapes are continuously shifted from the nominal ones to the ones obtained from systematic variations, and beyond for absolute values of the parameters greater than one.

For the τ-embedded $Z/\gamma^* \rightarrow \mu^+\mu^-$ data only the uncertainties on the τ_{had} energy scale but not those on the jet energy scale are considered as the jets in this sample originate from the data. Furthermore, the uncertainties on this sample derived from the modifications of the muon calorimeter energy removal procedure in the τ-embedding process are treated as additional shape uncertainties.

A comparison of the nominal $m_{\tau\tau}^{\mathrm{MMC}}$ mass shapes for the two Higgs boson production processes, assuming $m_A = 150$ GeV and $\tan\beta = 20$, to those obtained by simultaneously varying the jet

60 – 65 – 70 – 75 – 80 – 85 – 90 – 95 – 100 – 105 – 110 – 115 – 120 – 125 – 130 – 135 – 140 – 145 – 150 – 160 – 170 – 180 – 200 – 225 – 250 – 300 – 600 GeV

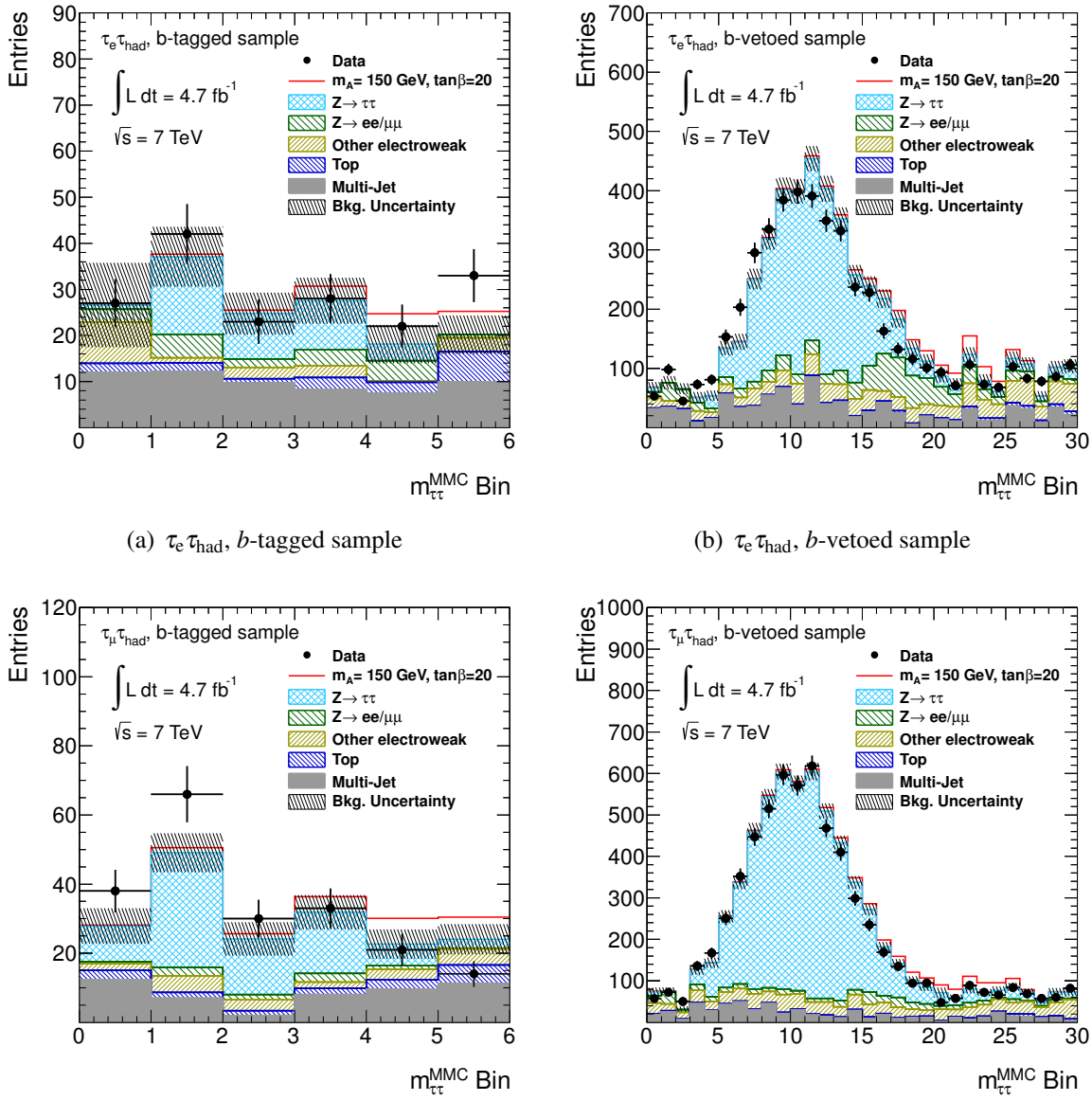

(a) $\tau_e\tau_{\text{had}}$, b-tagged sample

(b) $\tau_e\tau_{\text{had}}$, b-vetoed sample

(c) $\tau_\mu\tau_{\text{had}}$, b-tagged sample

(d) $\tau_\mu\tau_{\text{had}}$, b-vetoed sample

Figure 7.19.: Rebinned distributions of the $\tau^+\tau^-$ mass $m_{\tau\tau}^{\text{MMC}}$ reconstructed from the b-tagged (left column) and b-vetoed (right column) event samples for the $\tau_e\tau_{\text{had}}$ (upper row) and $\tau_\mu\tau_{\text{had}}$ (lower row) final states. The data are compared to the background expectation and a hypothetical MSSM signal ($m_A = 150$ GeV and $\tan\beta = 20$). Statistical uncertainties are shown combined for the background expectation. The contributions of the di-boson and $W+$jets background processes are combined and labelled "Other electroweak".

and τ_{had} jet energy scales are shown in Fig. 7.20 for the b-tagged event sample. Furthermore, the figure shows a comparisons of the nominal $m_{\tau\tau}^{\text{MMC}}$ mass shape for the dominant $Z/\gamma^* \to \tau^+\tau^-$ background to the shapes obtained by varying the τ_{had} jet energy scale and by modifying the muon calorimeter energy removal procedure. The comparison of the shapes for the top, the $Z/\gamma^* \to \ell^+\ell^-$ and the combination of the single top and di-boson backgrounds are shown in Fig. 7.21. The same comparisons are shown in Figs. 7.22 and 7.23 for the b-vetoed event samples.

The exclusion limits obtained with the observed and predicted distributions are shown in Fig. 7.24 for the combination of the searches in all final states. Fig. 7.24 (a) shows the upper 95% CL_s exclusion limits on the MSSM parameter $\tan\beta$ as a function of the Higgs boson mass m_A. An overall good agreement of the observed and expected limits is found. A large area of the $(m_A, \tan\beta)$-parameter plane can be excluded, ranging down to values of $\tan\beta \simeq 10.5$ for a Higgs boson mass of $m_A = 170$ GeV. This is consistent with the expected median of $\tan\beta \simeq 12.5 \pm 2.1$ for the same mass. For higher masses the sensitivity of this search decreases rapidly, which is a consequence of the steeply falling production cross sections for large masses m_A. The lowest local p_0-value observed is 0.067 at a mass of $m_A = 90$ GeV, which corresponds to an excess with a significance of $1.5\,\sigma$.

In addition to the interpretations in the context of the MSSM, a more general interpretation of the search results has been performed. Upper 95% CL_s exclusion limits on the cross section times the branching ratio ($\sigma \times BR$) of a generic resonance ϕ produced in the gluon-fusion mode or in association with b-quarks and decaying into the $\tau_{\text{lep}}\tau_{\text{had}}$ final states have been derived. The results are shown in Fig. 7.24 (b). According to these, the existence of a resonance with a mass of 150 GeV and values of $\sigma \times BR \simeq 3.4$ pb ($\simeq 3.3$ pb) for the production via the gluon-fusion (b-quark associated) production mode and above can be excluded, given that the width of the resonance is below the experimental resolution for the considered final states. These values are consistent with the expected exclusion limit of $\sigma \times BR \simeq 3.8 \pm 1.1$ pb for both production mechanisms.

The expected and observed limits for the two different production modes are very similar, although the b-tagged event sample is only sensitive to the b-quark associated production mode. This is caused by the large systematic and statistical uncertainties on the corresponding signal and background expectations. As a consequence the observed and expected limits presented above are mainly driven by the results derived from the b-vetoed signal regions.

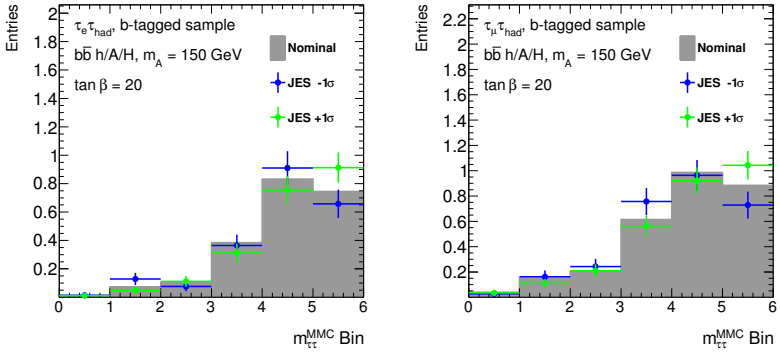

(a) $b\bar{b}\,h/A/H$

(b) $b\bar{b}\,h/A/H$

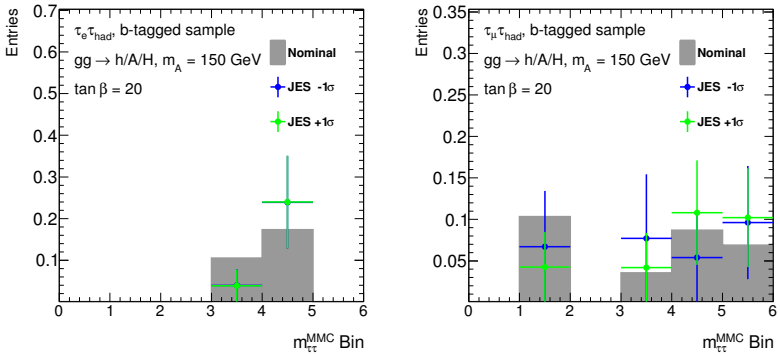

(c) $gg \to h/A/H$

(d) $gg \to h/A/H$

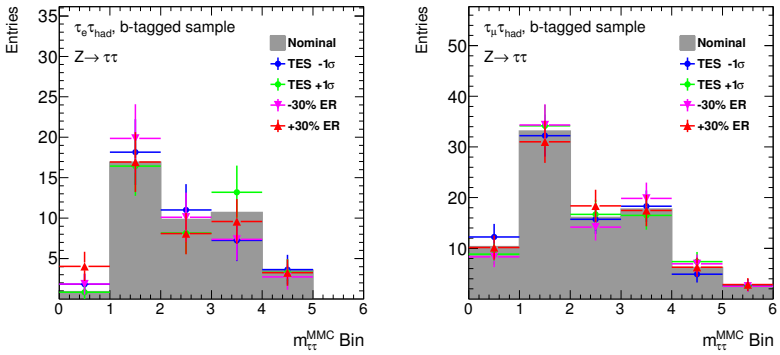

(e) τ-embedded $Z/\gamma^* \to \mu^+\mu^-$

(f) τ-embedded $Z/\gamma^* \to \mu^+\mu^-$

Figure 7.20.: Uncertainties on the $m_{\tau\tau}^{\text{MMC}}$ mass distributions for the Higgs boson production in the b-quark associated (upper row) and gluon-fusion (middle row) modes ($m_A = 150$ GeV and $\tan\beta = 20$) in the ***b*-tagged** sample. Shown are the shape uncertainties obtained from a simultaneous variation of jet and τ_{had} energy scales ("JES $\pm 1\,\sigma$"). The lower row shows the $m_{\tau\tau}^{\text{MMC}}$ distributions for the τ-embedded $Z/\gamma^* \to \mu^+\mu^-$ data and the corresponding uncertainties obtained from variations of the τ_{had} energy scale ("TES $\pm 1\,\sigma$") and the muon calorimeter energy removal procedure ("$\pm$30% ER"). The left and right columns show the distributions for the $\tau_e\tau_{\text{had}}$ and $\tau_\mu\tau_{\text{had}}$ final states, respectively.

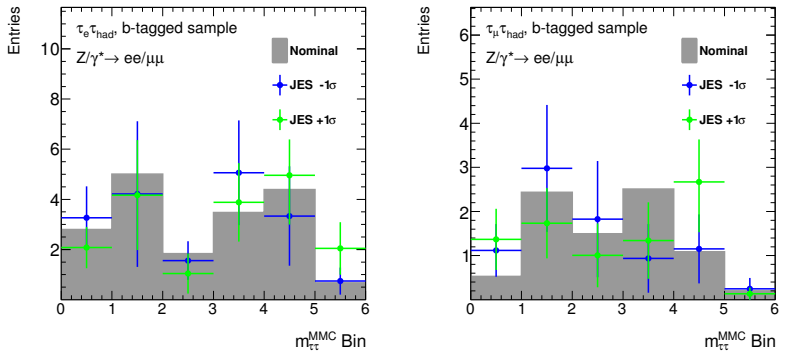

(a) $Z/\gamma^* \rightarrow \ell^+\ell^-$

(b) $Z/\gamma^* \rightarrow \ell^+\ell^-$

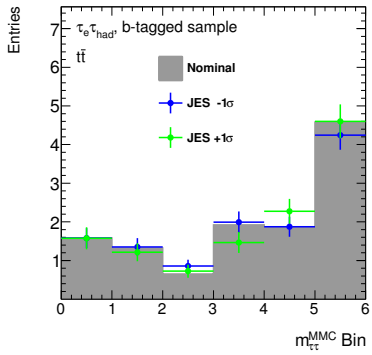

(c) $t\bar{t}$

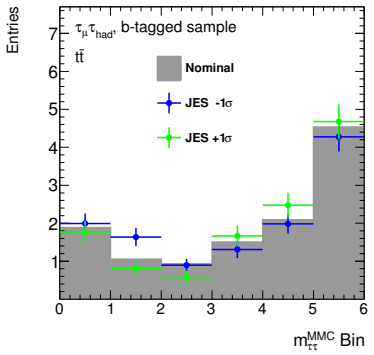

(d) $t\bar{t}$

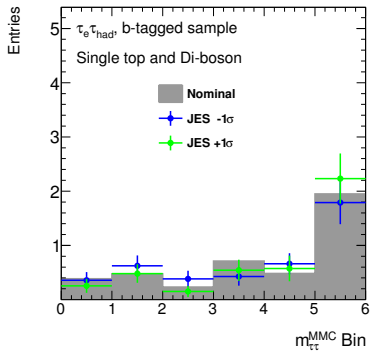

(e) Single top and di-boson

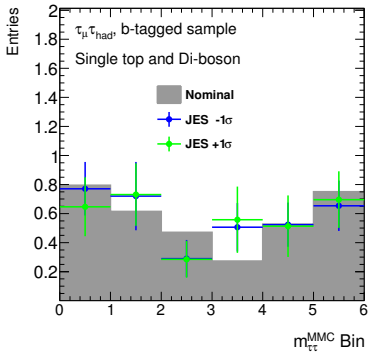

(f) Single top and di-boson

Figure 7.21.: Uncertainties on the $m_{\tau\tau}^{\mathrm{MMC}}$ mass distributions for the $Z/\gamma^* \rightarrow \ell^+\ell^-$ (upper row), $t\bar{t}$ (middle row) and the combination of the single top and di-boson background processes in the *b*-**tagged** sample. Shown are the shape uncertainties obtained from a simultaneous variation of jet and τ_{had} energy scales ("JES $\pm 1\,\sigma$"). The left and right columns show the distributions for the $\tau_{\mathrm{e}}\tau_{\mathrm{had}}$ and $\tau_\mu\,\tau_{\mathrm{had}}$ final states, respectively.

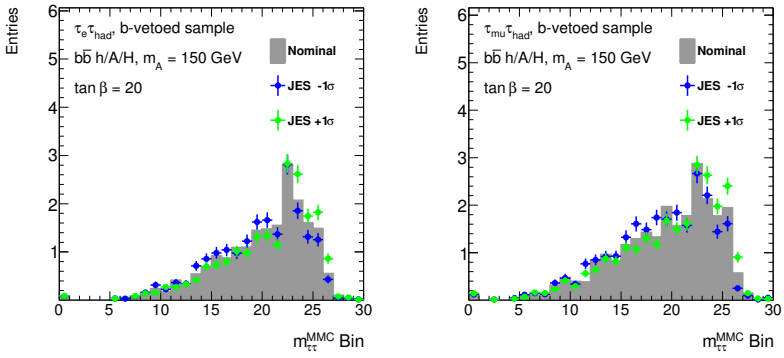

(a) $b\bar{b}\,h/A/H$

(b) $b\bar{b}\,h/A/H$

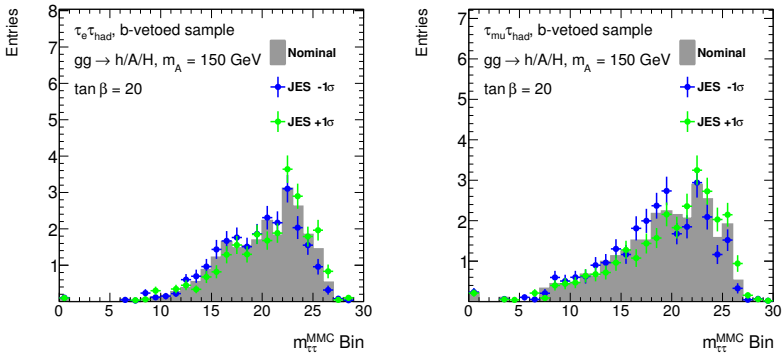

(c) $gg \to h/A/H$

(d) $gg \to h/A/H$

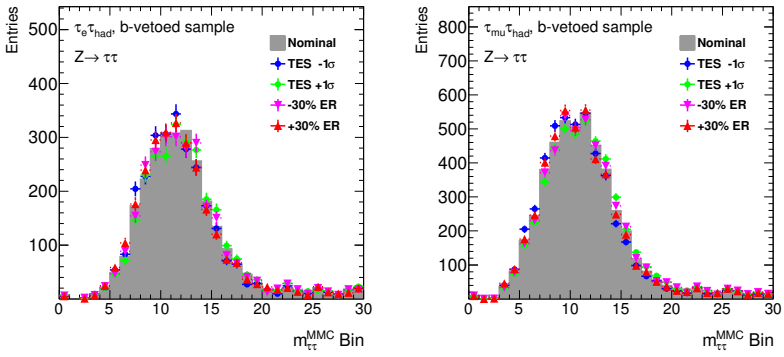

(e) τ-embedded $Z/\gamma^* \to \mu^+\mu^-$

(f) τ-embedded $Z/\gamma^* \to \mu^+\mu^-$

Figure 7.22.: Uncertainties on the $m_{\tau\tau}^{\text{MMC}}$ mass distributions for the Higgs boson production in the b-quark associated (upper row) and gluon-fusion (middle row) modes ($m_A = 150$ GeV and $\tan\beta = 20$) in the ***b*-vetoed** sample. Shown are the shape uncertainties obtained from a simultaneous variation of jet and τ_{had} energy scales ("JES $\pm 1\,\sigma$"). The lower row shows the $m_{\tau\tau}^{\text{MMC}}$ distributions for the τ-embedded $Z/\gamma^* \to \mu^+\mu^-$ data and the corresponding uncertainties obtained from variations of the τ_{had} energy scale ("TES $\pm 1\,\sigma$") and the muon calorimeter energy removal procedure ("$\pm$30% ER"). The left and right columns show the distributions for the $\tau_e\tau_{\text{had}}$ and $\tau_\mu\tau_{\text{had}}$ final states, respectively.

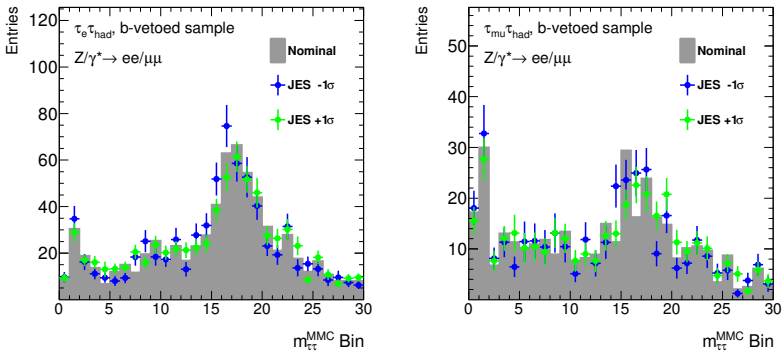

(a) $Z/\gamma^* \rightarrow \ell^+\ell^-$

(b) $Z/\gamma^* \rightarrow \ell^+\ell^-$

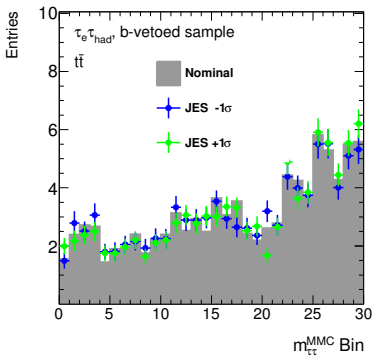

(c) $t\bar{t}$

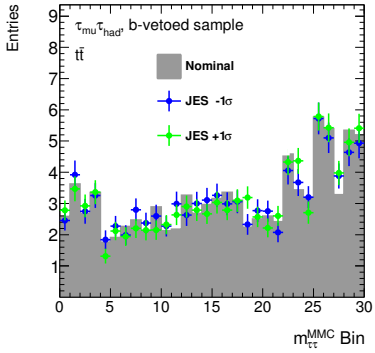

(d) $t\bar{t}$

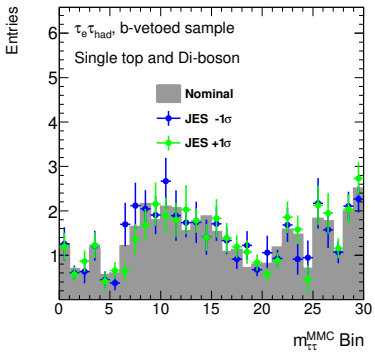

(e) Single top and di-boson

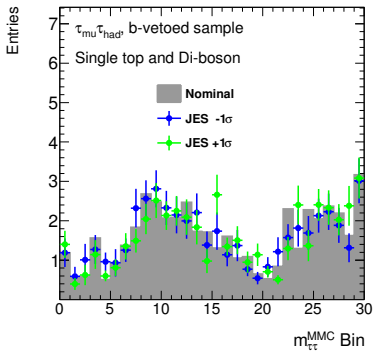

(f) Single top and di-boson

Figure 7.23.: Uncertainties on the $m_{\tau\tau}^{\mathrm{MMC}}$ mass distributions for the $Z/\gamma^* \rightarrow \ell^+\ell^-$ (upper row), $t\bar{t}$ (middle row) and the combination of the single top and di-boson background processes in the *b*-**vetoed** sample. Shown are the shape uncertainties obtained from a simultaneous variation of jet and τ_{had} energy scales ("JES $\pm 1\,\sigma$"). The left and right columns show the distributions for the $\tau_{\mathrm{e}}\tau_{\mathrm{had}}$ and $\tau_{\mu}\tau_{\mathrm{had}}$ final states, respectively.

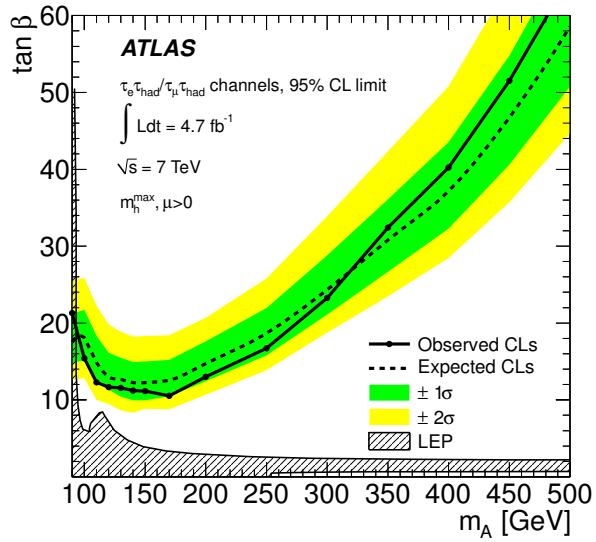

(a)

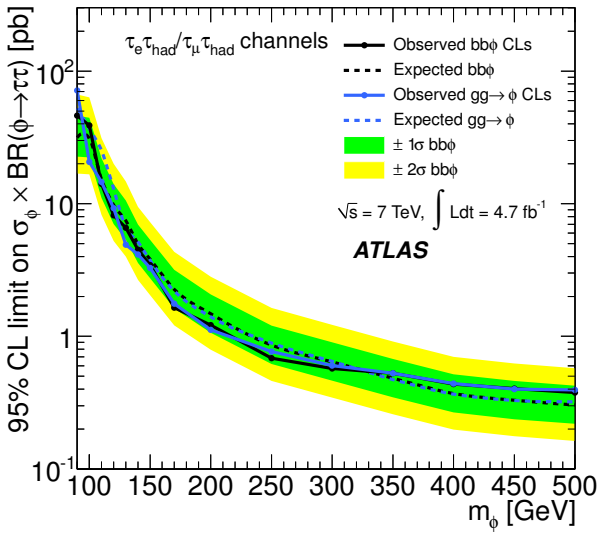

(b)

Figure 7.24.: Upper 95% Confidence Level CL_s exclusion limits for the search for neutral MSSM Higgs bosons decaying to $\tau_{\text{lep}}\tau_{\text{had}}$. Figure (a): Upper limits on $\tan\beta$ as a function of m_A for the combination of all search channels. Figure (b): Upper limits on the cross section times the branching ratio for a generic resonance ϕ produced in the gluon-fusion mode or in association with b-quarks and decaying into $\tau_{\text{lep}}\tau_{\text{had}}$. Expected limits are shown as dashed lines, observed limits as solid lines. The green and yellow bands indicate the $\pm1\sigma$ and $\pm2\sigma$ interval error bands on the expected limits, respectively.

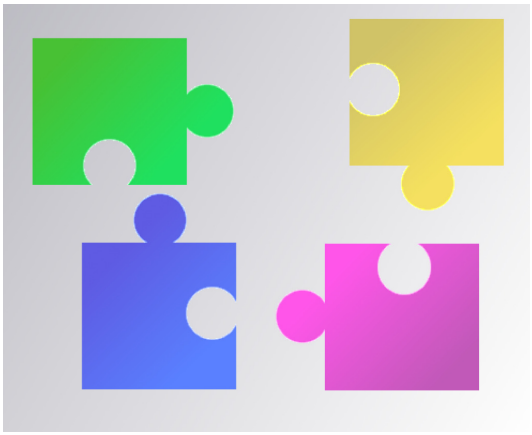

Chapter 8

Statistical Combination with other Searches

In addition to the search presented here, further searches for the neutral Higgs bosons of the MSSM produced the gluon-fusion and the b-quark associated production modes have been performed with the ATLAS experiment [114]. The additional final states considered are the $\tau_e\tau_\mu$, $\tau_{had}\tau_{had}$ and $\mu^+\mu^-$ decay modes of the Higgs bosons. The p–p collision data taken into account have been recorded with the ATLAS detector in 2011 at a centre-of-mass energy of $\sqrt{s} = 7$ TeV. The data set usable for the searches amounts to $4.7 - 4.8\,\text{fb}^{-1}$, depending on the requirements on the data quality that differs for the various final states. Equivalent to the search already presented, all searches assume masses, branching ratios and production cross sections as computed in the m_h^{max} benchmark scenario and have been categorised depending on the presence or absence of an identified b-jet.

In the following sections the additional searches are summarised and the results of the statistical combination of all searches is presented.

8.1. Search for the $h/A/H \to \mu^+\mu^-$ Decay Mode

The signal signature of the $\mu^+\mu^-$ decay mode is a pair of isolated muons with large transverse momenta and opposite sign electric charges [114]. A low missing transverse momentum is required in the reconstructed events since all of the final state particles are detectable. The invariant mass of the di-muon system is used to reconstruct the Higgs boson mass and serves as the final discriminating observable.

The search for this decay mode is very challenging due to the large production cross section of the irreducible $Z/\gamma^* \to \mu^+\mu^-$ background. In addition, the direct decay of the neutral Higgs bosons into two muons occurs with a very low branching ratio of around 0.04%. Consequently, a hypothetical signal would manifest itself as a small resonance on top of a large background. These circumstances require a precise knowledge of the background composition and its di-muon mass distribution in the signal region. To minimise the uncertainties on the corresponding predictions, the total background contribution is estimated completely from the data. At each point of a $(m_A, \tan\beta)$ grid a signal model is used to parameterise the di-muon mass distribution, taking into account all three resonances h, A and H. Using this signal distribution a signal window is defined, outside of which the signal contributes at a negligible level. Furthermore, a background model is used to parameterise the complete background distribution. This model is defined as a convolution of a Breit-Wigner function describing the background from Z/γ^* production and a Gaussian that accounts for the finite resolution for the reconstructed di-muon mass. This model is found to provide a sufficiently good approximation for the shape of the total di-muon background. This is still the case after requiring the presence of a b-jet, which changes the background composition and enhances the contribution of t-quark production processes. The complete background contribution inside a signal window for a particular point in the $(m_A, \tan\beta)$ grid is estimated by fitting the background model to the observed data outside the signal window.

8.2. Searches for the $h/A/H \to \tau_e\tau_\mu$ and $\tau_{had}\tau_{had}$ Decay Modes

The $\tau^+\tau^-$ final states considered for Higgs boson searches in addition to the ones already presented are the $\tau_e\tau_\mu$ and $\tau_{had}\tau_{had}$ decay modes of the di-τ system. The final observable for these searches is the invariant mass of the $\tau^+\tau^-$ pair which is reconstructed using the Missing Mass Calculator technique (see Section 7.4).

Search for the $\tau_e \tau_\mu$ Final State

The decay $\tau^+\tau^- \to \tau_e \tau_\mu$ has a low branching ratio of 6%. This final state is characterised by the presence of exactly one isolated electron and one isolated muon of opposite sign electric charges and a large invariant mass of the di-lepton system [114]. Background suppressing selection criteria are applied with thresholds depending on the presence or absence of an identified b-jet. A large opening angle in the plane transverse to the beam axis is required in between the two leptons. Furthermore, an upper threshold is applied to the scalar sum of the lepton transverse momenta and the missing transverse momentum. The combination of the transverse opening angles in between the lepton directions and the direction of the missing transverse momentum is restricted to large values. With these requirements the contributions from t-quark and di-boson production can be reduced effectively. In case a b-jet is identified in the final state, an upper threshold is applied to the scalar sum of transverse energies of all jets. This criterion further suppresses the background contributions from t-quark production processes.

Search for the $\tau_{had}\tau_{had}$ Final State

The decay $\tau^+\tau^- \to \tau_{had}\tau_{had}$ occurs with a probability of 42%. This final state contains two τ_{had} jets with large transverse momenta and opposite sign electric charges [114]. Events containing identified electrons or muons are rejected to reduce the contributions of several background processes and to preserve orthogonality to the other $h/A/H \to \tau^+\tau^-$ searches. A lower threshold on the missing transverse momentum is imposed to account for the neutrinos produced in the τ decays. In case no b-jet can be identified in an event, the lower threshold on the transverse momentum of the leading τ_{had} is raised in order to gain further background suppression power, especially against multi-jet production processes. In the presence of a b-jet an upper threshold on its transverse momentum is applied to reduce the contributions from t-quark production processes. In both the b-tagged and b-vetoed final states the main background to this search are the multi-jet production processes.

Estimation and Validation of Dominant Background Processes

The $Z/\gamma^* \to \tau^+\tau^-$ background is a largely irreducible background to all searches for the $\tau^+\tau^-$ final states. In the search for the $\tau_e\tau_\mu$ decay mode of the Higgs bosons the $Z/\gamma^* \to \tau^+\tau^-$ background is estimated with a τ-embedded $Z/\gamma^* \to \mu^+\mu^-$ data sample. In the search for the $\tau_{had}\tau_{had}$ decay mode simulated $Z/\gamma^* \to \tau^+\tau^-$ events are used for this purpose and the τ-embedded data is used to validate the simulated $Z/\gamma^* \to \tau^+\tau^-$ events.

In all searches the contributions from multi-jet background processes is estimated from the data using the *ABCD* technique.

For the b-tagged $\tau_e\tau_\mu$ final states the background contributions from $t\bar{t}$ production processes are normalised to the data in a $t\bar{t}$ background dominated control region.

In the search for the $\tau_{had}\tau_{had}$ decay mode a misidentification rate measurement has been performed to derive correction factors for the τ_{had} misidentification rate of quark and gluon jets. The results of these measurements have been applied to misidentified jets in simulated $W+$jets events. These corrections account for the discrepancies in the τ_{had} misidentification rates observed in data and simulation.

8.3. Results of the Combination

No significant excess of data above the predicted Standard Model background has been observed in the signal regions of the searches presented above. Therefore, 95% confidence level upper exclusion limits on $\tan\beta$ have been derived as a function of the mass m_A, using the CL_s frequentist approach as described in Section 7.9. All search channels have been combined statistically. The signal hypotheses assumed Higgs boson masses, production cross sections and branching ratios according to the m_h^{max} benchmark scenario. Nuisance parameters have been grouped in two categories. Those nuisance parameters describing uncertainties common among the search channels, like the uncertainty on the luminosity measurement, are treated fully correlated among the searches. In contrast, uncertainties on several data-driven background estimates are channel specific and therefore the corresponding nuisance parameters are treated fully uncorrelated.
The resulting exclusion limits on the parameter $\tan\beta$ are shown in Fig. 8.1 as a function of the Higgs bosons mass m_A. The lowest value of $\tan\beta$ that can be excluded is $\tan\beta > 9.3$ for a Higgs boson mass of $m_A = 130$ GeV. The corresponding expected exclusion for this mass is $\tan\beta > 10.3$. The lowest local p_0-values per channel are 0.014 (2.2σ) at $m_A = 125$ GeV for the $\mu\mu$ channel, 0.014 (2.2σ) at $m_A = 90$ GeV for the $\tau_e\tau_\mu$ channel, 0.067 (1.5σ) at $m_A = 90$ GeV for the $\tau_{lep}\tau_{had}$ channel and 0.097 (1.3σ) at $m_A = 140$ GeV for the $\tau_{had}\tau_{had}$ channel. The lowest local p_0 for the statistical combination of all channels is 0.004 (2.7σ) at $m_A = 90$ GeV. Taking into account the look-elsewhere effect [137] in the range 90 GeV $\leq m_A \leq$ 500 GeV and $5 \leq \tan\beta \leq 60$, the significance of this excess is below 2σ.
A large fraction of the remaining $(m_A, \tan\beta)$-parameter space that could not be excluded is still compatible with the assumption that the recently discovered particle is one of the neutral MSSM Higgs bosons h or H [55, 138].

Compared to the search in the $\tau_{\text{lep}}\tau_{\text{had}}$ decay modes only, the excluded area could be expanded significantly by combining the different search channels. This is shown in Fig. 8.1 (b) that compares the combined exclusion limits in the $(m_A, \tan\beta)$ plane to the limits derived from the individual search channels. Especially for large masses m_A an improvement is observed since the search for the $\tau_{\text{had}}\tau_{\text{had}}$ decay mode is very sensitive to these parameter configurations.

In addition to the interpretation in the context of the MSSM, a more general interpretation of the search results has been performed. For this purpose, 95% confidence level CL_s upper exclusion limits on the production cross section times the branching ratio for a single scalar boson ϕ produced in the gluon-fusion mode or in association with b-quarks and decaying into $\mu^+\mu^-$ or $\tau^+\tau^-$ have been derived as a function of the bosons mass. The results are shown in Fig. 8.2 for the search for the $\mu^+\mu^-$ decay mode and the combination of searches for the $\tau^+\tau^-$ decay modes.

8.4. Comparison to former Results and those of other Experiments

With the combination of the neutral MSSM Higgs boson searches performed with the ATLAS experiment, a large area in the $(m_A, \tan\beta)$ plane can be excluded with the observed data. A comparison of these results to the areas excluded by the CMS collaboration and the combined effort of the experiments DØ and CDF is shown in Fig. 8.3. In addition, the results are compared to former results presented by the ATLAS collaboration.

The results presented in this thesis represent a large improvement compared to the previous exclusion limits set by the ATLAS Collaboration which were derived using a subset of the data recorded in 2011 ($1.06\,\text{fb}^{-1}$) [56, 128]. This is a consequence not only of the increased data set analysed, but also results from the refined analysis techniques, like the categorisation of the search depending on the presence or absence of an identified b-jet in the final state.

The two Tevatron experiments DØ and CDF combined their searches for the neutral Higgs bosons of the MSSM, using data sets corresponding to integrated luminosities of about $2.2\,\text{fb}^{-1}$ (DØ) and $1.8\,\text{fb}^{-1}$ (CDF) [139]. The results of this combination could be outperformed by far, as well.

Furthermore, the results derived here are compared to those presented by the CMS collaboration using about the same amount of data ($4.6\,\text{fb}^{-1}$) [57]. Assuming a Higgs boson mass of $m_A = 130$ GeV, the observed (expected) upper 95% confidence level CL_s exclusion limit on $\tan\beta$ set by the CMS collaboration is $\tan\beta > 9.0$ ($\tan\beta > 7.9$). These results are similar to the upper

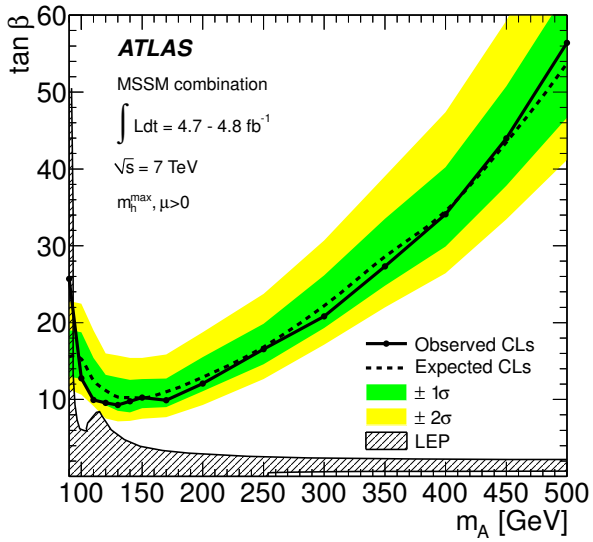

(a)

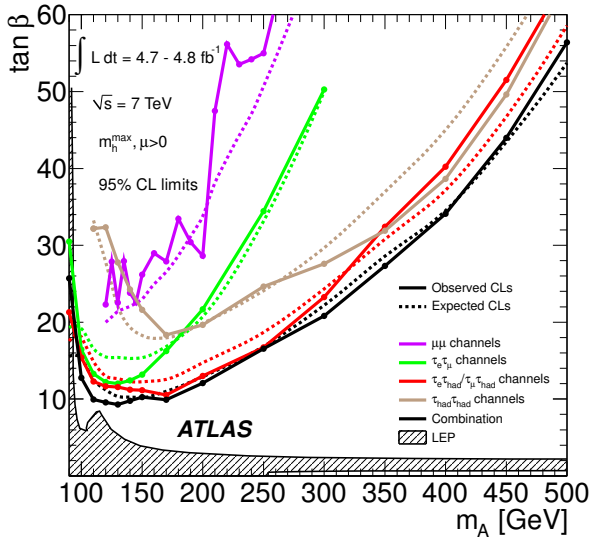

(b)

Figure 8.1.: Upper 95% confidence level CL_s exclusion limits derived from the combination of all searches for the neutral MSSM Higgs bosons performed with the ATLAS experiment. Figure (a) shows the upper limits on $\tan\beta$ as a function of the mass m_A. Expected limits are shown as dashed lines, the observed limits as solid line. The green and yellow bands indicate the $\pm 1\sigma$ and $\pm 2\sigma$ error bands for the expected limit, respectively. Figure (b) compares the same limits to the limits derived for the individual search channels.

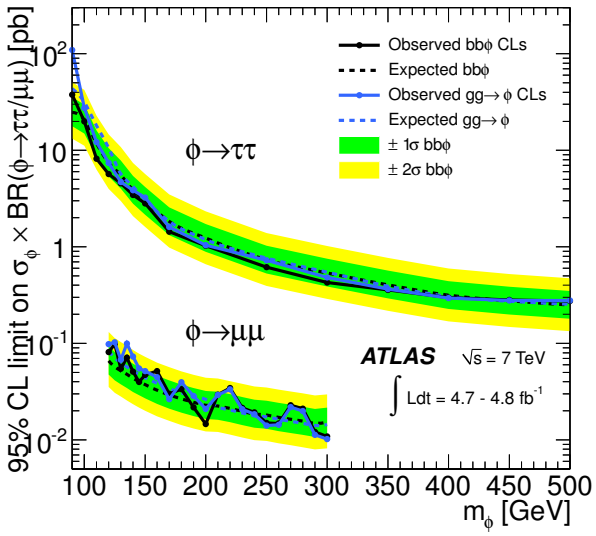

Figure 8.2.: Upper 95% confidence level CL_s exclusion limits on the cross section times the branching ratio of a generic resonance ϕ produced in the gluon-fusion mode or in association with b-quarks and decaying into τ and μ pairs. All searches for neutral MSSM Higgs bosons performed with the ATLAS experiment have been combined. Expected limits are shown as dashed lines, the observed limits as solid line. The green and yellow bands indicate the $\pm 1\sigma$ and $\pm 2\sigma$ error bands for the expected limits, respectively.

limit of $\tan\beta > 9.3$ ($\tan\beta > 10.3$) obtained for the combined search with the ATLAS experiment when assuming the same the mass m_A, with a slightly higher expected sensitivity of the searches presented by the CMS collaboration.

8.5. Prospects for future Searches

The good performance of the LHC and the ATLAS experiment lead to a large amount of accumulated data over the past few months. The data recorded with the ATLAS detector in 2012 correspond to an integrated luminosity of about $13\,\text{fb}^{-1}$, which exceeds the data set recorded in 2011 by far ($\approx 4.8\,\text{fb}^{-1}$). In addition, the increase in the centre-of-mass energy of the p–p collisions from $\sqrt{s} = 7\,\text{TeV}$ to $\sqrt{s} = 8\,\text{TeV}$ is expected to improve the sensitivity of the Higgs boson searches. This is a consequence of the rapidly growing cross sections for the MSSM Higgs boson production as a function of $\sqrt{s}$. Both the large increase of the data set and the higher centre-of-mass energy of the p–p collisions will improve the sensitivity of the MSSM Higgs boson searches with the ATLAS detector significantly. This effect was already observed by the CMS colaboration, who presented their updated searches in Ref. [140], using the complete data set recorded in 2011 ($\sqrt{s} = 7\,\text{TeV}$, $\int L\,\text{dt} = 4.9\,\text{fb}^{-1}$) and most of the data recorded in 2012 ($\sqrt{s} = 8\,\text{TeV}$, $\int L\,\text{dt} = 12.1\,\text{fb}^{-1}$). By including the data set of 2012, the observed (expected) upper 95% confidence level CL_s exclusion limit on $\tan\beta$ could be lowered from values of $\tan\beta > 9.0$ ($\tan\beta > 7.9$) to values of $\tan\beta > 4.9$ ($\tan\beta > 5.0$) for a Higgs boson mass hypothesis of $m_A = 130$ GeV.

In addition, further developments of the analysis strategies might increase the sensitivity of the search presented here. The limit setting procedure summarised in Section 7.9, for example, provides a powerful tool to constrain the uncertainties on the background expectations. Including further control region measurements in the profile likelihood function definition might improve the sensitivity of future searches, despite the fact that large uncertainties on the background expectations are possibly observed. The auxiliary measurements performed to derive the normalisation corrections for the $t\bar{t}$ and W+ jets backgrounds, for example, are not included in the profile likelihood definition for the search presented here.

Furthermore, a refined categorisation of the search might improve the sensitivity. A categorisation defined by the number of tracks associated to the selected τ_{had} jet, for example, could be used to separate the background contributions in which leptons are erroneously selected as the τ_{had} jet from those in which quark or gluon jets are selected as such. In that case, dedicated control region measurements might be included in the profile likelihood to constrain the uncertainties

on the individual misidentification probabilities.

Further developments of the τ-embedding procedure might significantly reduce the large uncertainties observed for the dominant background of this search, the $Z/\gamma^* \to \tau^+\tau^-$ background. In the search presented here, the most important sources of uncertainties on the estimates for this background originate from the uncertainties on the theory predictions. These sum up to a total uncertainty of about $\pm 13.5\%$ on the predicted event yields of the $Z/\gamma^* \to \tau^+\tau^-$ background. If it were possible to emulate the trigger decision in the τ-embedded $Z/\gamma^* \to \mu^+\mu^-$ data these uncertainties could eventually be avoided.

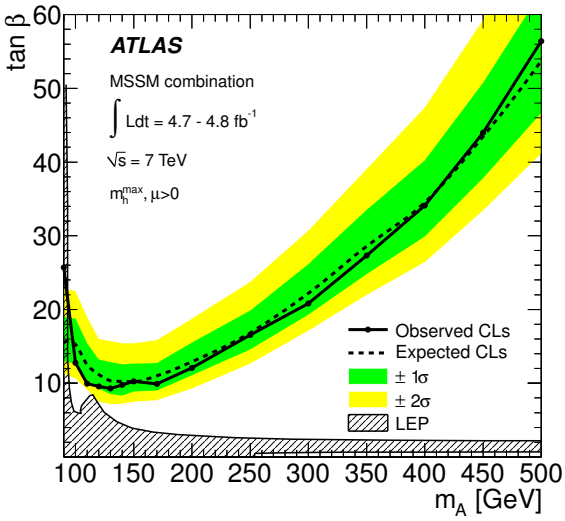

(a) **ATLAS Collaboration (current results)**

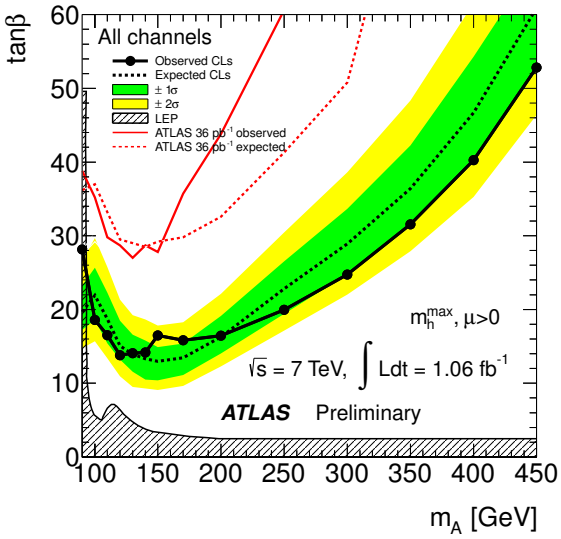

(b) ATLAS Collaboration (former results)

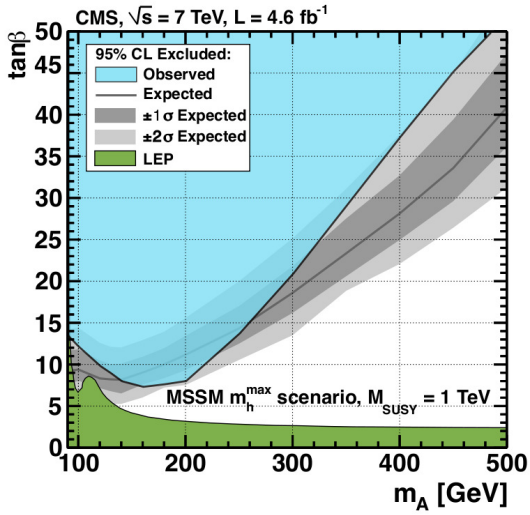

(c) CMS Collaboration

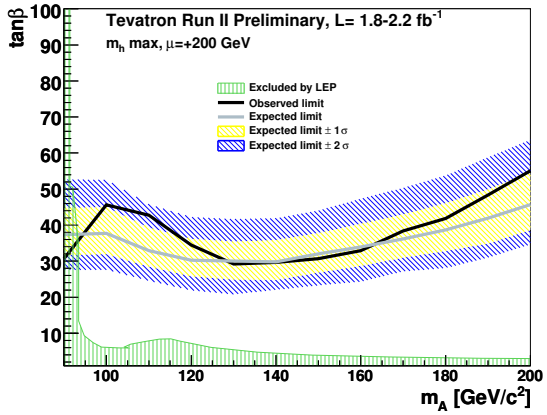

(d) CDF and DØ Collaborations

Figure 8.3.: Upper 95% confidence level CL_s exclusion limits on $\tan\beta$ as a function of the parameter m_A set by the ATLAS collaboration (Figures (a) and (b)), the CMS collaboration (c) and the two experiments located at the Tevatron (d), CDF and DØ. Figure (a) shows the current limits set by the ATLAS collaboration for which the full data set recorded in 2011 was analysed ($4.7 - 4.8\,\text{fb}^{-1}$). Figure (b) shows the former results that were derived using a subset of the data recorded in 2011 ($1.06\,\text{fb}^{-1}$) [56]. The limits set by the CMS collaboration were derived by analysing the complete data set recorded in 2011 ($4.6\,\text{fb}^{-1}$) [57]. The combined searches performed with the DØ and CDF experiments [139] used data sets corresponding to integrated luminosities of about $2.2\,\text{fb}^{-1}$ and $1.8\,\text{fb}^{-1}$, respectively.

Combined ATLAS 95% CL_s exclusion limits

(Search for $h/A/H \to \mu\mu$, $\tau_e\tau_\mu$, $\tau_e\tau_{had}$, $\tau_\mu\tau_{had}$ and $\tau_{had}\tau_{had}$)

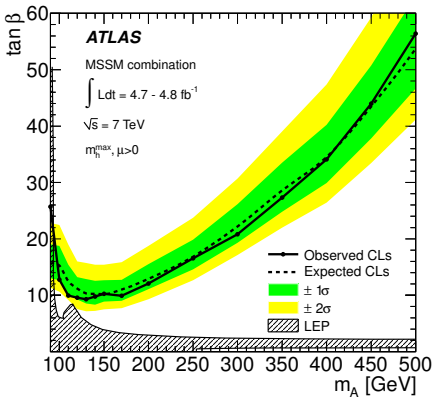

Chapter 9

Summary

In the light of the recent discovery of a new boson at the LHC [51,52], experimental high energy particle physics currently focusses on the precise measurement of its properties. These information are required in order to determine if the new particle is the Standard Model Higgs boson or a Higgs boson of a more complex Higgs sector. In the Minimal Supersymmetric Standard Model (MSSM), for example, two Higgs doublets are postulated to provide masses to up- and down-type fermions, resulting in five observable Higgs bosons. Three of these, denoted as h, A and H, are electrically neutral and massive. Depending on the actual values of the MSSM parameters m_A and $\tan\beta$, the boson A and either h or H might feature enhanced couplings to down-type fermions. Given these properties, a discovery of the $\tau^+\tau^-$ decay mode of the recently discovered boson or the evidence for an additional new particle decaying in this mode will provide essential information for the interpretation of the recent results.

In this context, a search for the neutral Higgs bosons of the MSSM produced in the gluon-fusion and the b-quark associated production modes and decaying into $\tau^+\tau^-$ has been presented in this thesis. The final states considered are the $\tau_e\tau_{had}$ and $\tau_\mu\tau_{had}$ decay modes of the two τ leptons, where τ_e and τ_μ denote the processes $\tau \to e\nu_e\nu_\tau$ and $\tau \to \mu\nu_\mu\nu_\tau$, respectively, and τ_{had} the decay of a τ lepton into hadrons. The p–p collision data analysed have been recorded with the ATLAS detector in 2011 at a centre-of-mass energy of $\sqrt{s} = 7\,\text{TeV}$ and correspond to an integrated luminosity of $4.7\,\text{fb}^{-1}$. The search strategy exploits the particular properties of

the two main production mechanisms of Higgs bosons in the MSSM, the gluon-fusion and the b-quark associated production modes. For this purpose, the searches for the $\tau_e\tau_{had}$ and $\tau_\mu\tau_{had}$ decay modes have been categorised depending on the presence or absence of an identified b-jet in the reconstructed events. The signal regions of the b-tagged event sample would be mainly populated with Higgs bosons produced in the b-quark associated production mode, whereas in the b-vetoed event sample both production mechanisms would contribute at a similar level, depending on the actual values of the parameters m_A and $\tan\beta$.

Several Standard Model processes contribute as sources for background events to this search. The expectations for the most important ones have been estimated from the data themselves. The largest background contributions to all signal regions originate from irreducible $Z/\gamma^* \to \tau^+\tau^-$ decays. Therefore, an exact knowledge of these is essential for the correct interpretation of the observed data. The τ-embedding technique has been employed to use modified $Z/\gamma^* \to \mu^+\mu^-$ decays selected from the data to mimic $Z/\gamma^* \to \tau^+\tau^-$ events. From these data events the muons have been removed and replaced by simulated τ leptons, resulting in a hybrid event sample in which most event properties, e.g. the underlying event structure, the jet activity and the pile-up conditions, originate from real p–p collisions.

The multi-jet production processes represent the second most important source of background events. These processes are characterised by large production cross sections and low expected selection efficiencies. Given these properties and the large uncertainties on the corresponding predictions, a reliable estimate of this background cannot be derived from simulated event samples. Instead, the corresponding contributions to the signal regions have been estimated completely from the data using an *ABCD* technique that extrapolates the multi-jet background contributions from dedicated control regions to the signal regions. In this procedure simulated event samples are only employed to take into account the contributions of other Standard Model background processes to the control regions.

The contributions from other background processes have been estimated from the Monte Carlo predictions. The expectations for the $W+$jets and $t\bar{t}$ backgrounds have been corrected for the discrepancy in the τ_{had} misidentification rate of quark and gluon jets observed between simulated event samples and the data. For both processes these corrections have been derived by comparing the data observed in dedicated control regions dominated by the respective background process to the expectations from the simulation.

The contributions from $Z/\gamma^* \to \ell^+\ell^-$ ($\ell = e, \mu$) processes have been tested for a potential difference in the b-jet selection efficiency in event samples simulated with the AlpGen event generator compared to the same efficiency in data. This test has been performed by comparing the b-

jet selection efficiency in the τ-embedded $Z/\gamma^* \to \mu^+\mu^-$ data to the efficiency in a simulated $Z/\gamma^* \to \tau^+\tau^-$ sample.

Good agreement of the observed data and the background predictions within the statistical and systematic uncertainties has been observed in all final states considered. In particular, no significant excess of data above the predicted background event yields has been found. These search results have been interpreted in the context of the MSSM, assuming masses, branching ratios and decay widths of the Higgs bosons as computed in the m_h^{max} benchmark scenario. For this purpose, the invariant $\tau^+\tau^-$ mass, reconstructed using the Missing Mass Calculator technique, has been analysed to derive 95% confidence level CL_s upper exclusion limits on the parameter $\tan\beta$ as a function of the assumed Higgs boson mass m_A. As a result of this interpretation a large area in the $(m_A, \tan\beta)$ plane can be excluded, ranging down to values of $\tan\beta \simeq 10.5$ for a Higgs boson mass hypothesis of $m_A = 170$ GeV.
A more general interpretation of the search results assumes the existence of a single boson that can be produced in the b-quark associated or the gluon-fusion production mode, and which decays into $\tau_{\text{e}}\tau_{\text{had}}$ and $\tau_\mu\tau_{\text{had}}$. Since no significant excess of the data above the Standard Model expectations has been observed, 95% confidence level CL_s upper exclusion limits on the cross section times the branching ratio for such a boson have been derived as a function of its mass. Assuming a mass of the boson of 150 GeV, values of $\sigma \times BR \gtrsim 3.4\,\text{pb}$ and $\gtrsim 3.3\,\text{pb}$ can be excluded for the production via the gluon-fusion and the b-quark associated modes, respectively.

Furthermore, the results of the search presented here have been statistically combined with the results of other searches for the neutral MSSM Higgs bosons performed with the ATLAS experiment. The additional Higgs boson decay modes considered are $h/A/H \to \tau_{\text{e}}\tau_\mu$, $\tau_{\text{had}}\tau_{\text{had}}$ and $\mu^+\mu^-$. These searches also analysed the data recorded with the ATLAS detector in 2011, which corresponds to an integrated luminosity of 4.7–4.8 fb^{-1}, depending on the data quality requirements for the individual final states. All searches have been categorised depending on the presence or absence of an identified b-jet in the reconstructed event in order to account for the two dominant MSSM Higgs boson production modes.
No significant excess of data above the predicted Standard Model background has been observed in the signal regions for all final states. Therefore, 95% confidence level CL_s upper limits on $\tan\beta$ have been derived as a function of the mass m_A. The combination of the different search channels expands the excluded area in the $(m_A, \tan\beta)$ plane significantly compared to the area excluded by the individual search channels. The strongest constraint could be derived for a mass hypoth-

esis of $m_A = 130$ GeV at which the expected median is $\tan\beta \simeq 10.3$ and values of $\tan\beta > 9.3$ are excluded by the observed data. The largest deviation of the data from the Standard Model expectations is observed at a mass of $m_A = 90$ GeV. The global significance of this excess is below two standard deviations when taking into account the "look-elsewhere" [137] effect in the range $90\ \text{GeV} \leq m_A \leq 500\ \text{GeV}$ and $5 \leq \tan\beta \leq 60$.

Given the refined analysis techniques presented in this thesis, the additional categorisation of the search and the large data set accumulated in 2011, a large area in the $(m_A, \tan\beta)$ plane of the MSSM can be excluded with the observed data. Especially with the combination of all neutral MSSM Higgs boson searches performed with the ATLAS experiment a significant increase in the experimental sensitivity was achieved compared to former results presented by the ATLAS Collaboration [56, 128]. The combined limits on the $(m_A, \tan\beta)$ plane are comparable to those presented by the CMS collaboration that have been derived from about the same amount of data [57].
The results presented here provide important information to further improve the analysis strategies for the search for the neutral Higgs bosons of the MSSM. In addition, these information can be used to refine those theory models that are still consistent with the observations.
Although a large part of the $(m_A, \tan\beta)$ plane could be excluded, a large fraction of the remaining parameter space is still compatible with the assumption that the recently discovered particle is one of the MSSM Higgs bosons h or H – since the CP–odd Higgs boson A does not couple to WW and ZZ, it cannot be the observed particle. Further investigations are therefore required to reveal the nature of this particle and to confirm or exclude whether the MSSM is realised in nature. Given the good performance of the LHC and the ATLAS experiment, leading to a large amount of accumulated data over the past few months, exciting and important results might be presented in the near future.

Appendix A

Further Validation Comparisons for the Multi-jet Background Estimation

The *ABCD* method presented in Section 7.6.5 relies on the selection of two uncorrelated variables. This assumption has been validated by comparing the distributions of other uncorrelated variables in the half-planes *AB* and *CD* or the half-planes *AC* and *BD*. Additional comparison in the half-planes *AB* and *CD*, i.e. opposite sign versus same sign electric charges, are shown in Figs. A.1 and A.2 for the *b*-tagged and *b*-vetoed samples, respectively. Further comparisons of the half-planes *AC* and *BD*, i.e. isolated versus non-isolated leptons, are presented in Figs. A.3 and A.4. All comparisons show the observed data from which the contamination from processes other than the multi-jet background were subtracted. The respective corrections to simulated event samples have been applied prior to the subtraction. As the event yields in the half-planes differ, the distributions are normalised to each other.

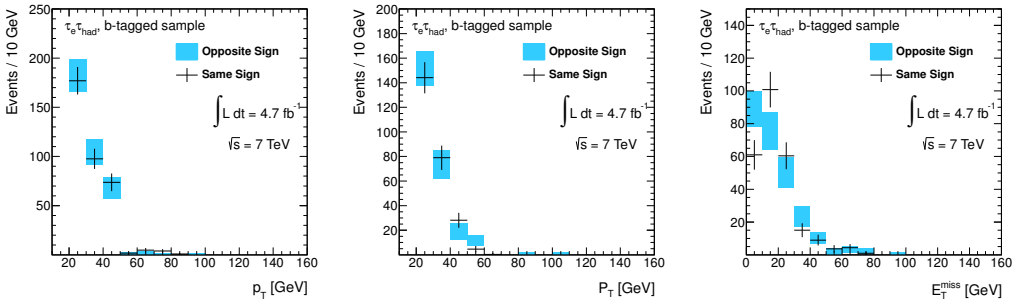

(a) p_{T} of jets

(b) p_{T} of the lepton

(c) $E_{\mathrm{T}}^{\mathrm{miss}}$

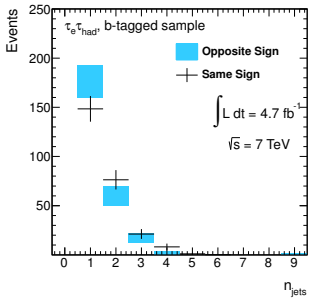

(d) Number of jets

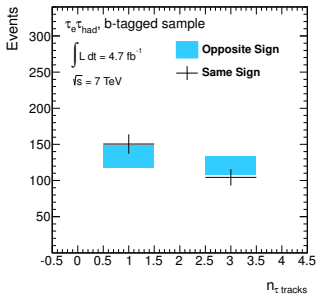

(e) Number of τ_{had} tracks

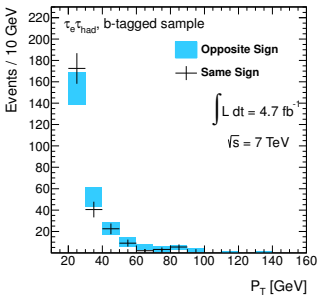

(f) p_{T} of the τ_{had}

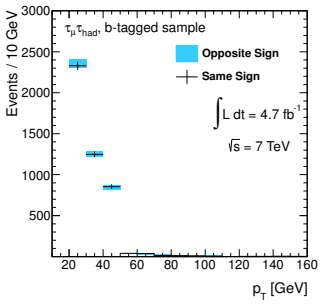

(g) p_{T} of jets

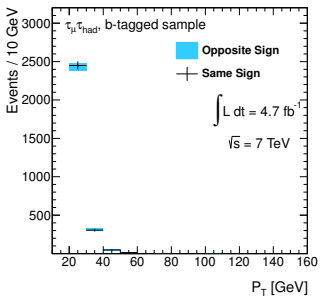

(h) p_{T} of the lepton

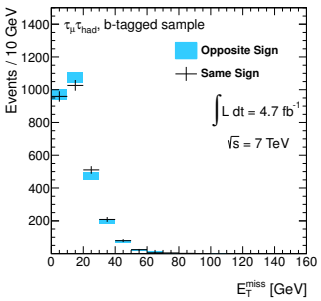

(i) $E_{\mathrm{T}}^{\mathrm{miss}}$

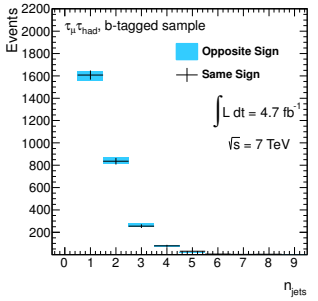

(j) Number of jets

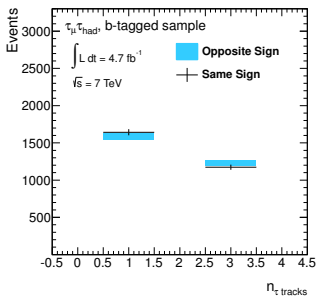

(k) Number of τ_{had} tracks

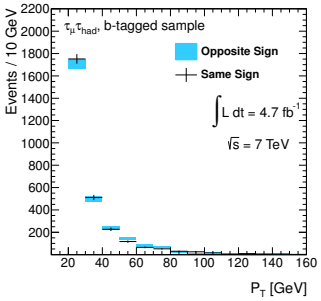

(l) p_{T} of the τ_{had}

Figure A.1.: Comparison of the p_{T} of jets, the selected lepton and τ_{had} jet, the missing transverse momentum $E_{\mathrm{T}}^{\mathrm{miss}}$, the number of jets and the number of tracks associated to the selected τ_{had} jet in the half-planes ***AB (opposite sign charges)*** and ***CD (same sign charges)*** as the data of which the expectations from non-multi-jet production processes have been subtracted for the ***b*-tagged** event samples. Figures (a) – (f) show the comparisons for the $\tau_{\mathrm{e}}\tau_{\mathrm{had}}$ final state, the $\tau_\mu\tau_{\mathrm{had}}$ final state is shown in Figures (g) – (l).

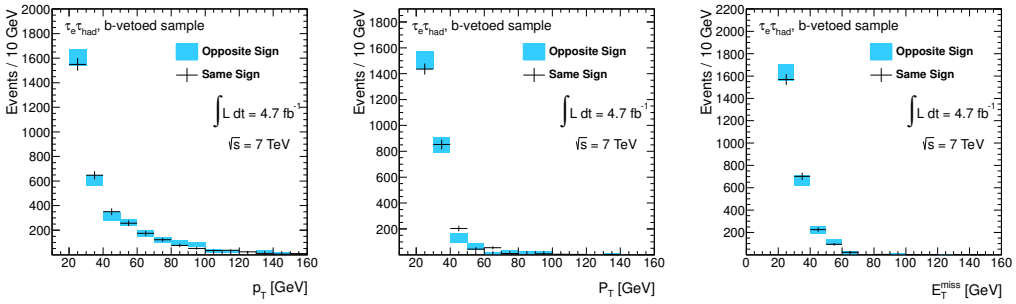

(a) p_{T} of jets (b) p_{T} of the lepton (c) $E_{\mathrm{T}}^{\mathrm{miss}}$

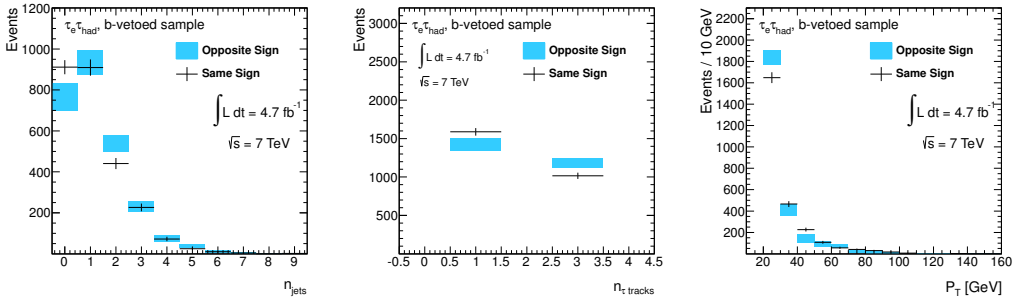

(d) Number of jets (e) Number of τ_{had} tracks (f) p_{T} of the τ_{had}

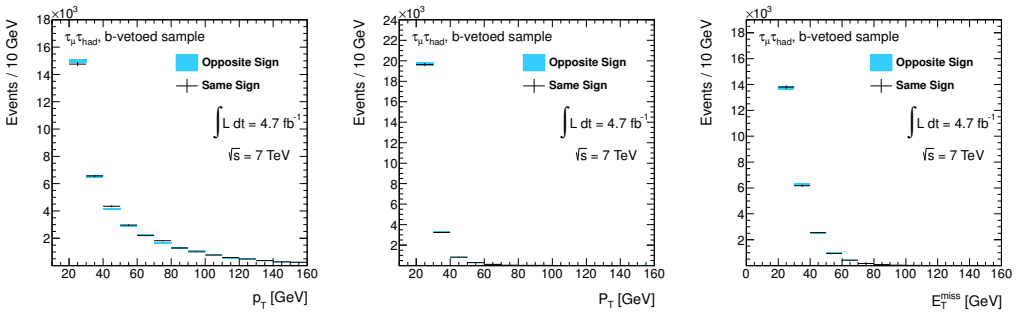

(g) p_{T} of jets (h) p_{T} of the lepton (i) $E_{\mathrm{T}}^{\mathrm{miss}}$

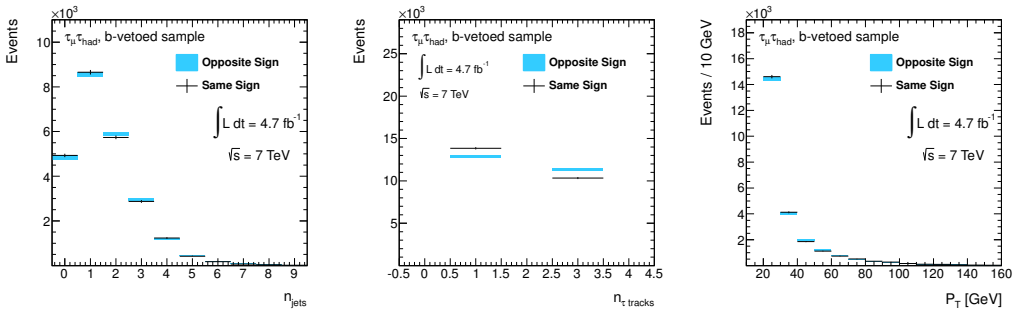

(j) Number of jets (k) Number of τ_{had} tracks (l) p_{T} of the τ_{had}

Figure A.2.: Comparison of the p_{T} of jets, the selected lepton and τ_{had} jet, the missing transverse momentum $E_{\mathrm{T}}^{\mathrm{miss}}$, the number of jets and the number of tracks associated to the selected τ_{had} jet in the half-planes ***AB (opposite sign charges)*** and ***CD (same sign charges)*** as the data of which the expectations from non-multi-jet production processes have been subtracted for the ***b*-vetoed** event samples. Figures (a) – (f) show the comparisons for the $\tau_{\mathrm{e}}\tau_{\mathrm{had}}$ final state, the $\tau_{\mu}\tau_{\mathrm{had}}$ final state is shown in Figures (g) – (l).

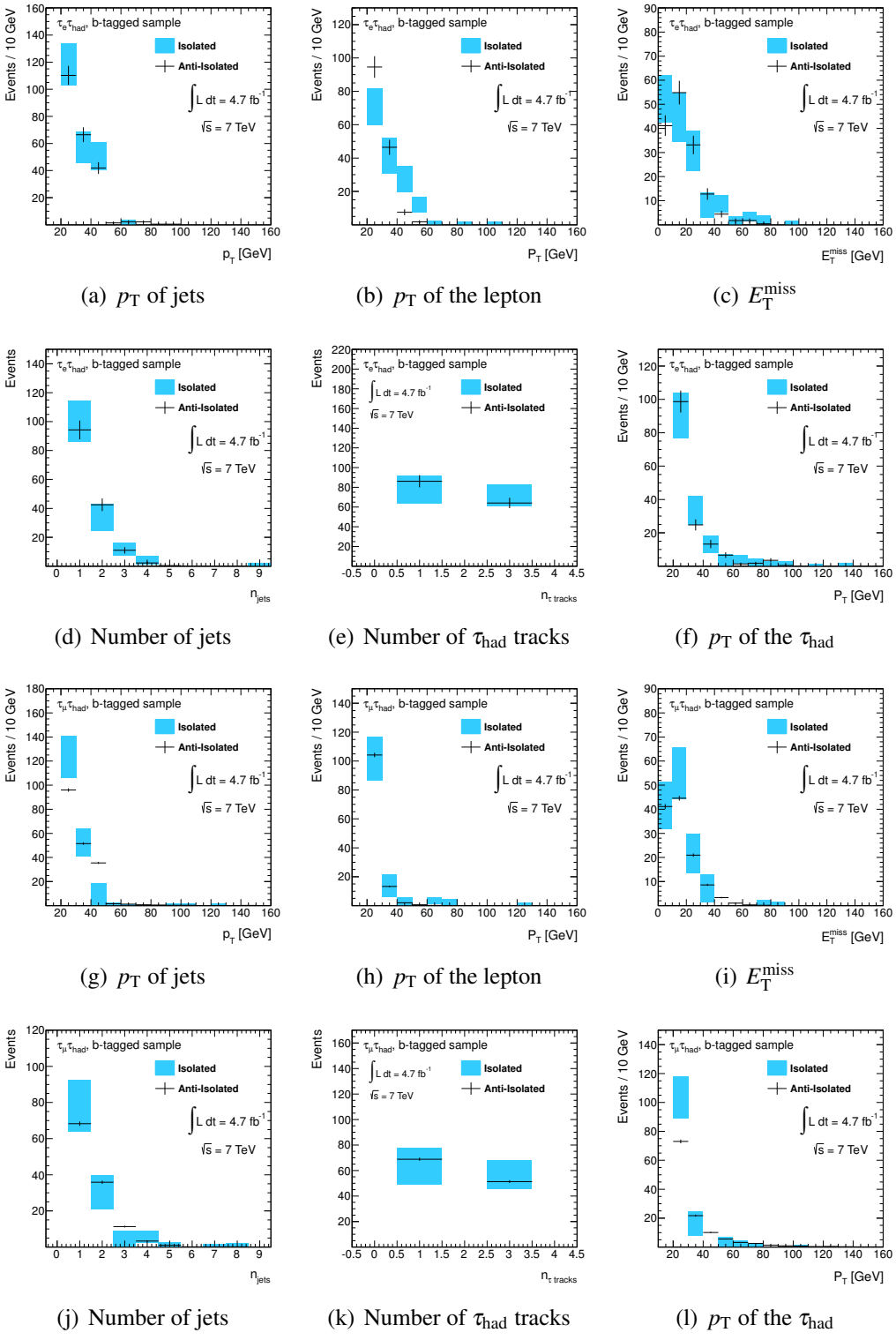

(a) p_{T} of jets (b) p_{T} of the lepton (c) $E_{\mathrm{T}}^{\mathrm{miss}}$

(d) Number of jets (e) Number of τ_{had} tracks (f) p_{T} of the τ_{had}

(g) p_{T} of jets (h) p_{T} of the lepton (i) $E_{\mathrm{T}}^{\mathrm{miss}}$

(j) Number of jets (k) Number of τ_{had} tracks (l) p_{T} of the τ_{had}

Figure A.3.: Comparison of the p_{T} of jets, the selected lepton and τ_{had} jet, the missing transverse momentum $E_{\mathrm{T}}^{\mathrm{miss}}$, the number of jets and the number of tracks associated to the selected τ_{had} jet in the half-planes ***AC (isolated leptons)*** and ***BD (anti-isolated leptons)*** as the data of which the expectations from non-multi-jet production processes have been subtracted for the ***b*-tagged** event samples. Figures (a) – (f) show the comparisons for the $\tau_{\mathrm{e}}\tau_{\mathrm{had}}$ final state, the $\tau_{\mu}\tau_{\mathrm{had}}$ final state is shown in Figures (g) – (l).

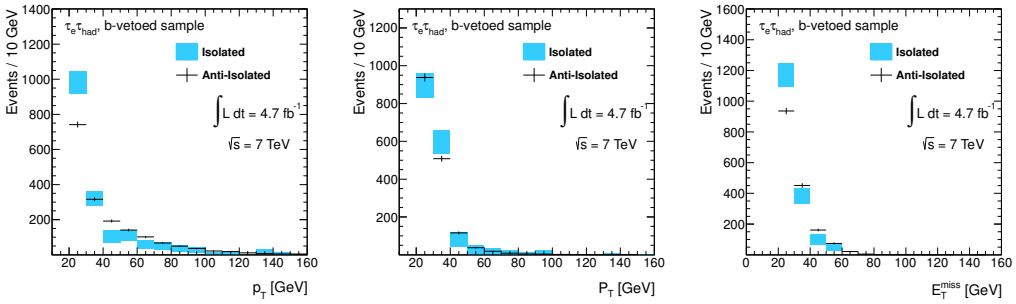

(a) p_{T} of jets (b) p_{T} of the lepton (c) $E_{\mathrm{T}}^{\mathrm{miss}}$

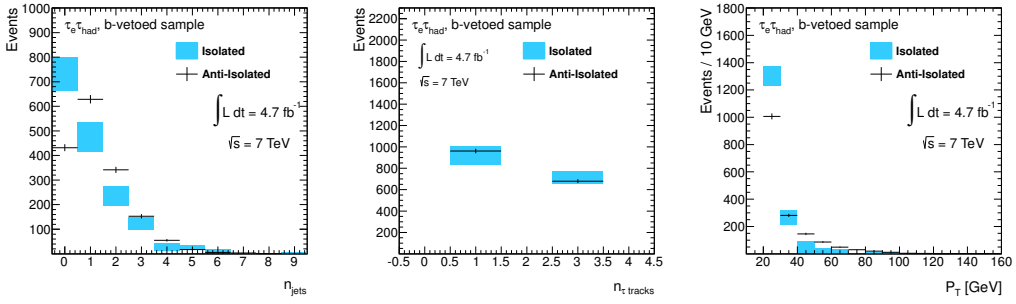

(d) Number of jets (e) Number of τ_{had} tracks (f) p_{T} of the τ_{had}

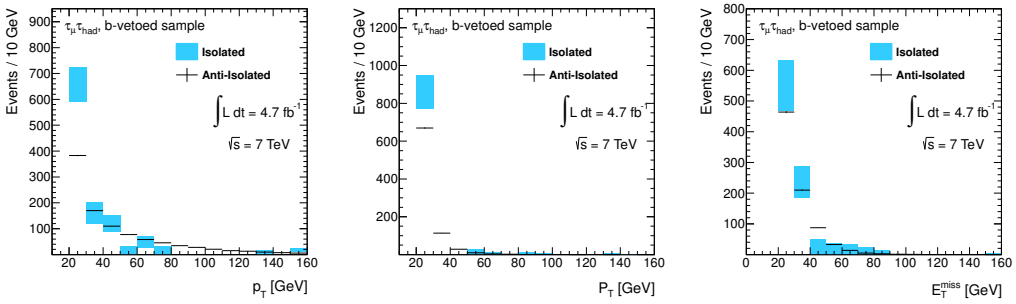

(g) p_{T} of jets (h) p_{T} of the lepton (i) $E_{\mathrm{T}}^{\mathrm{miss}}$

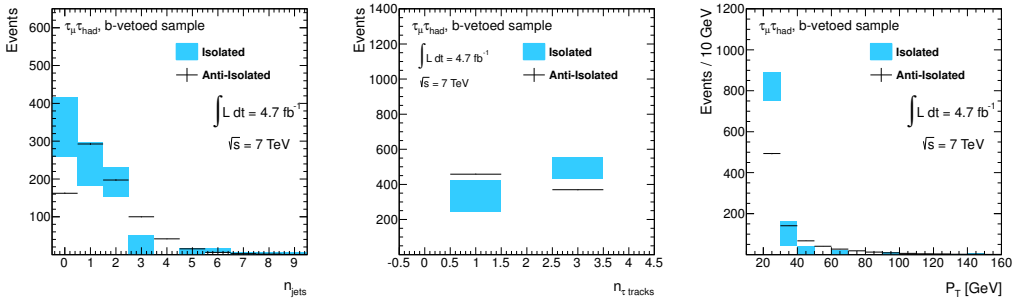

(j) Number of jets (k) Number of τ_{had} tracks (l) p_{T} of the τ_{had}

Figure A.4.: Comparison of the p_{T} of jets, the selected lepton and τ_{had} jet, the missing transverse momentum $E_{\mathrm{T}}^{\mathrm{miss}}$, the number of jets and the number of tracks associated to the selected τ_{had} jet in the half-planes ***AC (isolated leptons)*** and ***BD (anti-isolated leptons)*** as the data of which the expectations from non-multi-jet production processes have been subtracted for the ***b*-vetoed** event samples. Figures (a) – (f) show the comparisons for the $\tau_{\mathrm{e}}\tau_{\mathrm{had}}$ final state, the $\tau_\mu\tau_{\mathrm{had}}$ final state is shown in Figures (g) – (l).

Appendix B

Further Results with the Background Estimates

The background estimation techniques employed for this search were discussed in Section 7.6. In this chapter additional comparisons of the observed data to the background expectations are presented. Several additional distributions of important particle and event properties are shown in Fig. B.1 and Fig. B.2 for the signal regions of the b-tagged and b-vetoed samples, respectively. The τ-embedded $Z/\gamma^* \to \mu^+\mu^-$ data represents the contributions resulting from $Z/\gamma^* \to \tau^+\tau^-$ background processes (Section 7.6.1). The normalisation of the $W+$jets and $t\bar{t}$ backgrounds are corrected to data (Sections 7.6.2 and 7.6.3) for all final states. For comparisons of the b-tagged event samples the b-jet selection efficiency in simulated $Z/\gamma^* \to \ell^+\ell^-$ event samples is corrected (Section 7.6.4). The contributions from multi-jet production processes are estimated using an *ABCD* method (Section 7.6.5). The contributions from the single top and di-boson backgrounds are estimated using the corresponding Monte Carlo predictions.

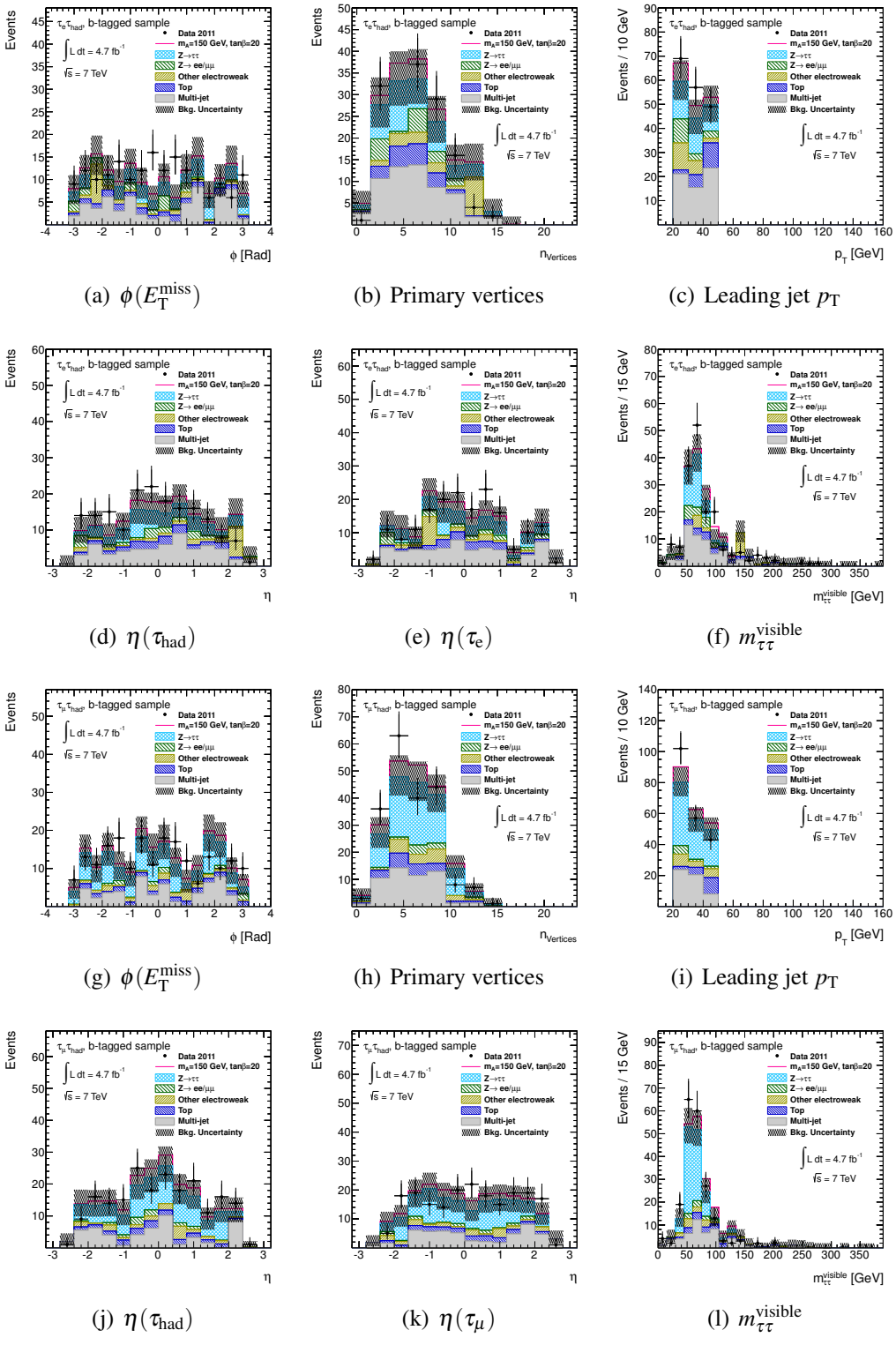

(a) $\phi(E_{\mathrm{T}}^{\mathrm{miss}})$ (b) Primary vertices (c) Leading jet p_{T}

(d) $\eta(\tau_{\mathrm{had}})$ (e) $\eta(\tau_{\mathrm{e}})$ (f) $m_{\tau\tau}^{\mathrm{visible}}$

(g) $\phi(E_{\mathrm{T}}^{\mathrm{miss}})$ (h) Primary vertices (i) Leading jet p_{T}

(j) $\eta(\tau_{\mathrm{had}})$ (k) $\eta(\tau_{\mu})$ (l) $m_{\tau\tau}^{\mathrm{visible}}$

Figure B.1.: The ϕ-coordinate of $E_{\mathrm{T}}^{\mathrm{miss}}$, the number of primary vertices, p_{T} of the leading jet, the η-coordinates of the τ_{had} jet and the lepton and the invariant mass of the visible τ decay products $m_{\tau\tau}^{\mathrm{visible}}$ in the observed data compared to the background expectations and a hypothetical signal (m_A =150 GeV, $\tan\beta$=20) in the ***b*-tagged** sample for the $\tau_{\mathrm{e}}\tau_{\mathrm{had}}$ ((a) – (f)) and $\tau_{\mu}\tau_{\mathrm{had}}$ ((g) – (l)) final states. The di-boson and W+ jets backgrounds are combined and labelled "Other electroweak". Only statistical uncertainties are shown.

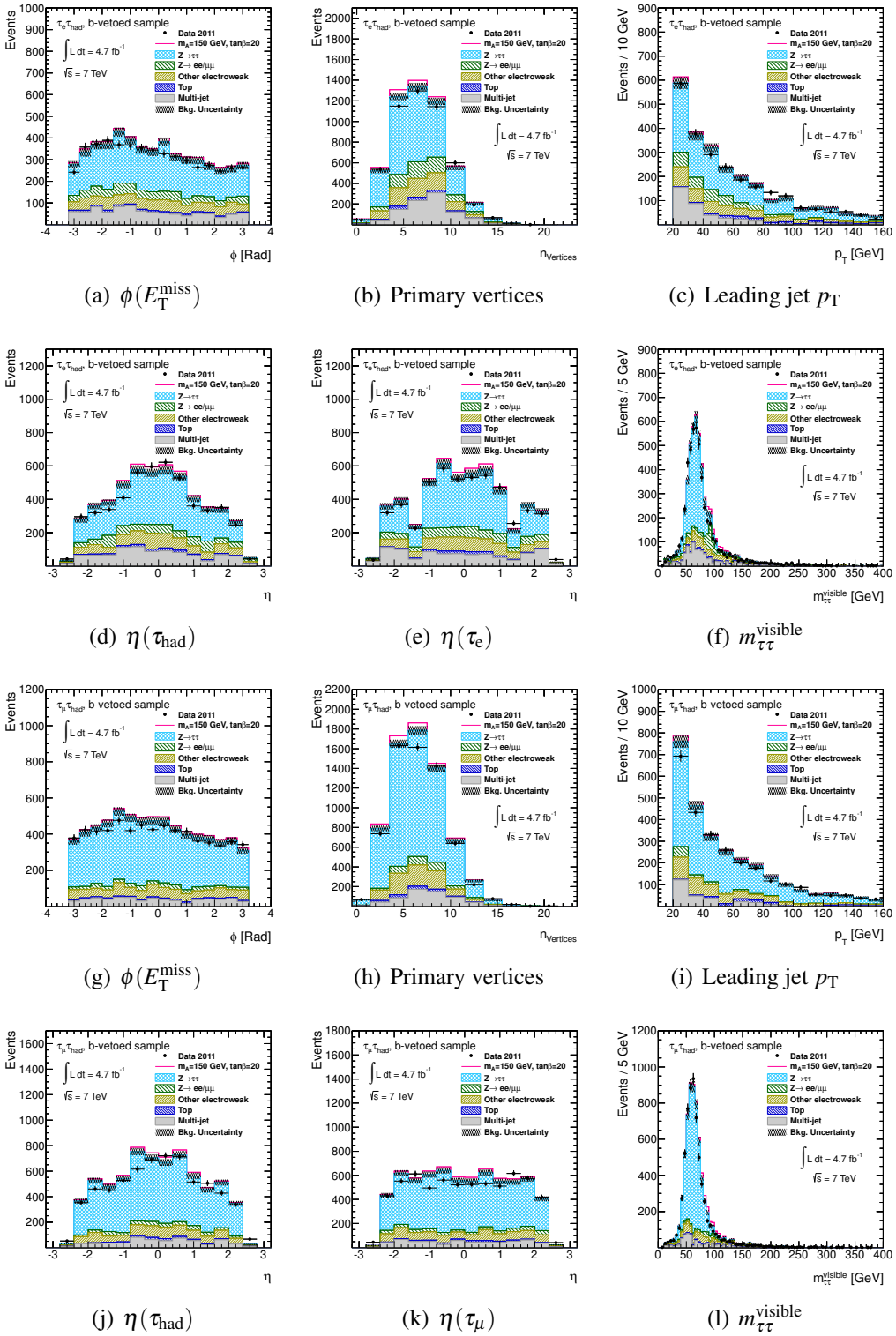

(a) $\phi(E_{\mathrm{T}}^{\mathrm{miss}})$ (b) Primary vertices (c) Leading jet p_{T}

(d) $\eta(\tau_{\mathrm{had}})$ (e) $\eta(\tau_{\mathrm{e}})$ (f) $m_{\tau\tau}^{\mathrm{visible}}$

(g) $\phi(E_{\mathrm{T}}^{\mathrm{miss}})$ (h) Primary vertices (i) Leading jet p_{T}

(j) $\eta(\tau_{\mathrm{had}})$ (k) $\eta(\tau_{\mu})$ (l) $m_{\tau\tau}^{\mathrm{visible}}$

Figure B.2.: The ϕ-coordinate of $E_{\mathrm{T}}^{\mathrm{miss}}$, the number of primary vertices, p_{T} of the leading jet, the η-coordinates of the τ_{had} jet and the lepton and the invariant mass of the visible τ decay products $m_{\tau\tau}^{\mathrm{visible}}$ in the observed data compared to the background expectations and a hypothetical signal (m_A =150 GeV, $\tan\beta$=20) in the ***b*-vetoed** sample for the $\tau_{\mathrm{e}}\tau_{\mathrm{had}}$ ((a) – (f)) and $\tau_{\mu}\tau_{\mathrm{had}}$ ((g) – (l)) final states. The di-boson and W+jets backgrounds are combined and labelled "Other electroweak". Only statistical uncertainties are shown.

List of Tables

List of Figures

Bibliography

[1] The WMAP Collaboration, C. L. Bennett et al., *Seven-year Wilkinson Microwave Anisotropy Probe (WMAP) Observations: Cosmological Interpretation*, Astrophys. J. Suppl. 192 (2011) p. 18, arXiv:1001.4538 [astro-ph.CO].

[2] The CMS Collaboration, S. Chatrchyan et al., *Combination of standard model Higgs boson searches and measurements of the properties of the new boson with a mass near 125 GeV*, CMS-PAS-HIG-12-045, CERN, Geneva, Nov, 2012.

[3] The ATLAS Collaboration, G. Aad et al., *An update of combined measurements of the new Higgs-like boson with high mass resolution channels*, ATLAS-CONF-2012-170, CERN, Geneva, Dec, 2012.

[4] M. Carena et al., *Suggestions for benchmark scenarios for MSSM Higgs boson searches at hadron colliders*, Eur. Phys. J. C26 (2003) pp. 601–607, hep-ph/0202167.

[5] F. Halzen and A. Martin, *Quarks and leptons: an introductory course in modern particle physics*. Wiley, New York, USA, 1984.

[6] S. P. Martin, *A Supersymmetry primer*, hep-ph/9709356.

[7] G. 't Hooft and M. Veltman, *Regularization and renormalization of gauge fields*, Nucl. Phys. B44 (1972), no. 1 pp. 189–213.

[8] P. W. Higgs, *Broken symmetries, massless particles and gauge fields*, Phys. Lett. 12 (1964) pp. 132–133.

[9] P. W. Higgs, *Broken Symmetries and the Masses of Gauge Bosons*, Phys. Rev. Lett. 13 (1964) p. 508.

[10] P. W. Higgs, *Spontaneous Symmetry Breakdown without Massless Bosons*, Phys. Rev. 145 (1966) p. 1156.

[11] F. Englert and R. Brout, *Broken Symmetry and the Mass of Gauge Vector Mesons*, Phys. Rev. Lett. 13 (1964) p. 321.

[12] G. S. Guralnik et al., *Global Conservation Laws and Massless Particles*, Phys. Rev. Lett. 13 (1964) pp. 585–587.

[13] J. Goldstone et al., *Broken Symmetries*, Phys. Rev. 127 (1962) pp. 965–970.

[14] S. L. Glashow, *Partial-symmetries of weak interactions*, Nucl. Phys. 22 (1961), no. 4 pp. 579–588.

[15] S. Weinberg, *A Model of Leptons*, Phys. Rev. Lett. 19 (1967) pp. 1264–1266.

[16] A. Salam, *Weak and Electromagnetic Interactions*, Conf. Proc. C680519 (1968) pp. 367–377.

[17] S. Glashow et al., *Weak Interactions with Lepton-Hadron Symmetry*, Phys. Rev. D2 (1970) pp. 1285–1292.

[18] Particle Data Group, J. Beringer et al., *Review of Particle Physics, 2012-2013. Review of Particle Properties*, Phys. Rev. D86 (2012), no. 1 p. 010001.

[19] T. van Ritbergen and R. G. Stuart, *On the precise determination of the Fermi coupling constant from the muon lifetime*, Nucl. Phys. B564 (2000) pp. 343–390, hep-ph/9904240.

[20] T. van Ritbergen and R. G. Stuart, *Complete two loop quantum electrodynamic contributions to the muon lifetime in the Fermi model*, Phys. Rev. Lett. 82 (1999) pp. 488–491, hep-ph/9808283.

[21] M. Steinhauser and T. Seidensticker, *Second order corrections to the muon lifetime and the semileptonic B decay*, Phys. Lett. B467 (1999) pp. 271–278, hep-ph/9909436.

[22] The MuLan Collaboration, D. M. Webber, *A New part-per-million measurement of the positive muon lifetime and determination of the Fermi Constant*, arXiv:1109.6689 [hep-ex].

[23] C. Rubbia, *The Discovery of the W and Z bosons*, Phys. Rept. 239 (1994) pp. 241–284.

[24] E. Radermacher, *The Experimental Discovery of the Intermediate Vector Bosons W+, W- and Z0 at the CERN p anti-p Collider*, Prog. Part. Nucl. Phys. 14 (1985) pp. 231–328.

[25] D. Gross and F. Wilczek, *Ultraviolet Behavior of Nonabelian Gauge Theories*, Phys. Rev. Lett. 30 (1973) pp. 1343–1346.

[26] H. D. Politzer, *Reliable Perturbative Results for Strong Interactions?*, Phys.Rev.Lett. 30 (1973) pp. 1346–1349.

[27] G. Altarelli and G. Parisi, *Asymptotic freedom in parton language*, Nucl. Phys. B126 (1977) p. 298.

[28] V. Gribov and L. Lipatov, *Deep inelastic e p scattering in perturbation theory*, Sov. J. Nucl. Phys. 15 (1972) pp. 438–450.

[29] Y. L. Dokshitzer, *Calculation of the Structure Functions for Deep Inelastic Scattering and e+ e- Annihilation by Perturbation Theory in Quantum Chromodynamics.*, Sov. Phys. JETP 46 (1977) pp. 641–653.

[30] B. Andersson et al., *Parton Fragmentation and String Dynamics*, Phys. Rept. 97 (1983) pp. 31–145.

[31] D. Amati and G. Veneziano, *Preconfinement as a Property of Perturbative QCD*, Phys. Lett. B83 (1979) p. 87.

[32] T. Sjöstrand et al., *PYTHIA 6.4 physics and manual*, JHEP 0605 (2006) p. 026, hep-ph/0603175.

[33] J. M. Butterworth et al., *Multiparton Interactions in Photoproduction at HERA*, Z. Phys. C72 (1996) pp. 637–646, hep-ph/9601371.

[34] The Super-Kamiokande Collaboration, Y. Fukuda et al., *Evidence for oscillation of atmospheric neutrinos*, Phys. Rev. Lett. 81 (1998) pp. 1562–1567, hep-ex/9807003.

[35] The Super-Kamiokande Collaboration, K. Abe et al., *Solar neutrino results in Super-Kamiokande-III*, Phys. Rev. D83 (2011) p. 052010, arXiv:1010.0118 [hep-ex].

[36] The KamLAND Collaboration, S. Abe et al., *Precision Measurement of Neutrino Oscillation Parameters with KamLAND*, Phys. Rev. Lett. 100 (2008) p. 221803, arXiv:0801.4589 [hep-ex].

[37] The MINOS Collaboration, P. Adamson et al., *An improved measurement of muon antineutrino disappearance in MINOS*, Phys. Rev. Lett. 108 (2012) p. 191801, arXiv:1202.2772 [hep-ex].

[38] S. Dimopoulos and D. W. Sutter, *The Supersymmetric flavor problem*, Nucl. Phys. B452 (1995) pp. 496–512, hep-ph/9504415.

[39] A. Djouadi, *The anatomy of electroweak symmetry breaking Tome II: The Higgs bosons in the Minimal Supersymmetric Model*, Phys. Rep. 459 (2008) p. 1.

[40] The Super-Kamiokande Collaboration, K. Abe et al., *Search for Proton Decay via $p \to \mu^+ K^0$ in Super-Kamiokande I, II, and III*, Phys. Rev. D86 (2012) p. 012006, arXiv:1205.6538 [hep-ex].

[41] S. L. Glashow and S. Weinberg, *Natural Conservation Laws for Neutral Currents*, Phys. Rev. D15 (1977) p. 1958.

[42] N. P. Nilles, *Supersymmetry, supergravity and particle physics*, Phys. Rept. 110 (1984) pp. 1–162.

[43] H. E. Haber and G. L. Kane, *The search for supersymmetry: Probing physics beyond the standard model*, Phys. Rept. 117 (1985) pp. 75–263.

[44] LHC Higgs Cross Section Working Group, S. Dittmaier et al., *Handbook of LHC Higgs Cross Sections: 1. Inclusive Observables*, arXiv:1101.0593 [hep-ph].

[45] The ATLAS Collaboration, G. Aad et al., *Search for the Standard Model Higgs boson produced in association with a vector boson and decaying to a b-quark pair with the ATLAS detector*, arXiv:1207.0210 [hep-ex].

[46] D. Stockinger, *The Muon Magnetic Moment and Supersymmetry*, J. Phys. G34 (2007) pp. R45–R92, hep-ph/0609168.

[47] The BABAR Collaboration, J. Lees et al., *Evidence for an excess of* $\bar{B} \to D^{(*)}\tau^-\bar{\nu}_\tau$ *decays*, arXiv:1205.5442 [hep-ex].

[48] The Belle Collaboration, K. Hara et al., *Evidence for* $B^- \to \tau^-\bar{\nu}$ *with a Semileptonic Tagging Method*, Phys. Rev. D82 (2010) p. 071101, arXiv:1006.4201 [hep-ex].

[49] The BABAR Collaboration, B. Aubert et al., *Search for* $B^+ \to \ell^+\nu_\ell$ *recoiling against* $B^- \to D^0\ell^-\overline{\nu}X$, Phys. Rev. D81 (2010) p. 051101.

[50] The ALEPH, DELPHI, L3 and OPAL Collaborations and the LEP Working Group for Higgs Boson Searches, S. Schael et al., *Search for neutral MSSM Higgs bosons at LEP*, Eur. Phys. J. C47 (2006) pp. 547–587, hep-ex/0602042.

[51] The ATLAS Collaboration, G. Aad et al., *Observation of a new particle in the search for the Standard Model Higgs boson with the ATLAS detector at the LHC*, arXiv:1207.7214 [hep-ex].

[52] The CMS Collaboration, S. Chatrchyan et al., *Observation of a new boson at a mass of 125 GeV with the CMS experiment at the LHC*, arXiv:1207.7235 [hep-ex].

[53] The CDF and DØ Collaborations, T. Aaltonen et al., *Evidence for a particle produced in association with weak bosons and decaying to a bottom-antibottom quark pair in Higgs boson searches at the Tevatron*, arXiv:1207.6436 [hep-ex].

[54] J.-J. Cao et al., *A SM-like Higgs near 125 GeV in low energy SUSY: a comparative study for MSSM and NMSSM*, JHEP 1203 (2012) p. 086, arXiv:1202.5821 [hep-ph].

[55] S. Heinemeyer et al., *Interpreting the LHC Higgs Search Results in the MSSM*, Phys. Lett. B710 (2012) p. 201, arXiv:1112.3026 [hep-ph].

[56] The ATLAS Collaboration, G. Aad et al., *Search for neutral MSSM Higgs bosons decaying to tau+tau- pairs in proton-proton collisions at $\sqrt{s} = 7$ TeV with the ATLAS detector*, ATLAS-CONF-2011-132, CERN, Geneva, Sep, 2011.

[57] The CMS Collaboration, S. Chatrchyan et al., *Search for neutral Higgs bosons decaying to tau pairs in pp collisions at $\sqrt{s}$=7 TeV.*, Phys. Lett. B713 (2012) pp. 68–90, arXiv:1202.4083 [hep-ex].

[58] CERN Press Office, *First beam in the LHC – Accelerating science*, http://press.web.cern.ch/press-releases/2008/09/first-beam-lhc-accelerating-science, 2008.

[59] CERN Press Office, *The LHC is back*, http://press.web.cern.ch/press-releases/2009/11/lhc-back, 2009.

[60] CERN Press Office, *Two circulating beams bring first collisions in the LHC*, http://press.web.cern.ch/press-releases/2009/11/two-circulating-beams-bring-first-collisions-lhc, 2009.

[61] BBC News, *CERN LHC sees high-energy success*, http://news.bbc.co.uk/2/hi/science/nature/8593780.stm, 2010.

[62] The ATLAS Collaboration, G. Aad et al., *Luminosity Determination in pp Collisions at $\sqrt{s} = 7$ TeV using the ATLAS Detector in 2011*, ATLAS-CONF-2011-116, CERN, Geneva, Aug, 2011.

[63] The ATLAS Collaboration, G. Aad et al., *The ATLAS Experiment at the CERN Large Hadron Collider*, JINST 3 (2008) p. S08003.

[64] The ATLAS Collaboration, G. Aad et al., *Expected Performance of the ATLAS Experiment - Detector, Trigger and Physics*, arXiv:0901.0512 [hep-ex].

[65] D. Froidevaux and P. Sphicas, *General-Purpose Detectors for the Large Hadron Collider*, Annu. Rev. Nucl. Part. Sci. 56 (2006) pp. 375–440.

[66] E. Abat et al., *Combined performance studies for electrons at the 2004 ATLAS combined test-beam*, JINST 5 (2010) p. P11006.

[67] The ATLAS Electromagnetic Liquid Argon Calorimeter Group Collaboration, B. Aubert et al., *Performance of the ATLAS electromagnetic calorimeter end-cap module 0*, Nucl. Instrum. Meth. A500 (2003) pp. 178–201.

[68] The ATLAS Collaboration, G. Aad et al., *Atlas Experiment – Public results*, https://twiki.cern.ch/twiki/bin/view/AtlasPublic/WebHome.

[69] Calafiura, P. et al., *The athena control framework in production, new developments and lessons learned*, 2005.

[70] The GEANT4 Collaboration, S. Agostinelli et al., *Geant4: a simulation toolkit*, Nucl. Instrum. Meth. A506 (2003) pp. 250–303.

[71] The ATLAS Collaboration, G. Aad et al., *The ATLAS Simulation Infrastructure*, Eur. Phys. J. C70 (2010) pp. 823–874, arXiv:1005.4568 [physics.ins-det].

[72] R. Brun and F. Rademakers, *ROOT: An Object Oriented Data Analysis Framework*, Nucl. Instrum. Meth. A389 (1997) pp. 81–86.

[73] J. Alwall et al., *Comparative study of various algorithms for the merging of parton showers and matrix elements in hadronic collisions*, Eur. Phys. J. C53 (2008) pp. 473–500, arXiv:0706.2569 [hep-ph].

[74] A. Buckley et al., *General-purpose event generators for LHC physics*, Phys. Rept. 504 (2011) pp. 145–233, arXiv:1101.2599 [hep-ph].

[75] E. Barberio et al., *Photos – a universal Monte Carlo for QED radiative corrections in decays*, Comput. Phys. Commun. 66 (1991) pp. 115–128.

[76] S. Jadach et al., *TAUOLA – a library of Monte Carlo programs to simulate decays of polarized τ leptons*, Comput. Phys. Commun. 64 (1990) pp. 275–299.

[77] S. Alioli et al., *NLO Higgs boson production via gluon fusion matched with shower in POWHEG*, JHEP 0904 (2009) p. 002, arXiv:0812.0578 [hep-ph].

[78] T. Gleisberg et al., *Event generation with SHERPA 1.1*, JHEP 0902 (2009) p. 007, arXiv:0811.4622 [hep-ph].

[79] M. L. Mangano et al., *ALPGEN, a generator for hard multiparton processes in hadronic collisions*, JHEP 0307 (2003) p. 001, hep-ph/0206293.

[80] S. Frixione and B. R. Webber, *Matching NLO QCD computations and parton shower simulations*, JHEP 0206 (2002) p. 029, hep-ph/0204244.

[81] T. Binoth et al., *Gluon-induced W-boson pair production at the LHC*, JHEP 0612 (2006) p. 046, hep-ph/0611170.

[82] G. Corcella et al., *HERWIG 6: an event generator for hadron emission reactions with interfering gluons (including supersymmetric processes)*, JHEP 0101 (2001) p. 010, hep-ph/0011363.

[83] S. Catani et al., *QCD matrix elements + parton showers*, JHEP 0111 (2001) p. 063, hep-ph/0109231.

[84] H.-L. Lai and others, *New parton distributions for collider physics*, Phys. Rev. D82 (2010) p. 074024, arXiv:1007.2241 [hep-ph].

[85] J. Pumplin,, *New Generation of Parton Distributions with Uncertainties from Global QCD Analysis*, JHEP 0207 (2002) p. 012, hep-ph/0201195.

[86] M. Frank et al., *The Higgs Boson Masses and Mixings of the Complex MSSM in the Feynman-Diagrammatic Approach*, JHEP 0702 (2007) p. 047, hep-ph/0611326.

[87] M. Spira, *HIGLU: A program for the calculation of the total Higgs production cross-section at hadron colliders via gluon fusion including QCD corrections*, hep-ph/9510347.

[88] R. V. Harlander and W. B. Kilgore, *Next-to-next-to-leading order Higgs production at hadron colliders*, Phys. Rev. Lett. 88 (2002) p. 201801, hep-ph/0201206.

[89] R. Harlander et al., *Bottom-quark associated Higgs-boson production: reconciling the four- and five-flavour scheme approach*, arXiv:1112.3478 [hep-ph].

[90] S. Dittmaier et al., *Higgs radiation off bottom quarks at the Tevatron and the LHC*, Phys. Rev. D70 (2004) p. 074010, hep-ph/0309204.

[91] S. Dawson et al., *Higgs production in association with bottom quarks at hadron colliders*, Mod. Phys. Lett. A21 (2006) pp. 89–110, 0508293.

[92] R. V. Harlander and W. B. Kilgore, *Higgs boson production in bottom quark fusion at next-to-next-to leading order*, Phys. Rev. D68 (2003) p. 013001, hep-ph/0304035.

[93] M. Cacciari et al., *The anti-k_t jet clustering algorithm*, JHEP 0804 (2008) p. 063, arXiv:0802.1189 [hep-ph].

[94] The ATLAS Collaboration, G. Aad et al., *Performance of the ATLAS Inner Detector Track and Vertex Reconstruction in the High Pile-Up LHC Environment*, ATLAS-CONF-2012-042, CERN, Geneva, Mar, 2012.

[95] The ATLAS Collaboration, G. Aad et al., *Performance of primary vertex reconstruction in proton-proton collisions at $\sqrt{s}$ =7 TeV in the ATLAS experiment*, ATLAS-CONF-2010-069, CERN, Geneva, Jul, 2010.

[96] The ATLAS Collaboration, G. Aad et al., *Electron performance measurements with the ATLAS detector using the 2010 LHC proton-proton collision data*, Eur. Phys. J. C72 (2012) p. 1909, arXiv:1110.3174 [hep-ex].

[97] M. Aharrouche et al., *Measurement of the response of the ATLAS liquid argon barrel calorimeter to electrons at the 2004 combined test-beam*, Nucl. Instrum. Meth. A614 (2010) pp. 400–432.

[98] M. Aharrouche et al., *Response uniformity of the ATLAS liquid argon electromagnetic calorimeter*, Nucl. Instrum. Meth. A582 (2007) pp. 429–455, arXiv:0709.1094 [physics.ins-det].

[99] M. Aharrouche et al., *Energy linearity and resolution of the ATLAS electromagnetic barrel calorimeter in an electron test-beam*, Nucl. Instrum. Meth. A568 (2006) pp. 601–623, physics/0608012.

[100] The ATLAS Collaboration, G. Aad et al., *Muon reconstruction efficiency in reprocessed 2010 LHC proton-proton collision data recorded with the ATLAS detector*, ATLAS-CONF-2011-063, CERN, Geneva, Apr, 2011.

[101] The ATLAS Collaboration, G. Aad et al., *Muon Momentum Resolution in First Pass Reconstruction of pp Collision Data Recorded by ATLAS in 2010*, ATLAS-CONF-2011-046, CERN, Geneva, Mar, 2011.

[102] W. Lampl et al., *Calorimeter Clustering Algorithms: Description and Performance*, , CERN, Geneva, Apr, 2008.

[103] The ATLAS Collaboration, G. Aad et al., *Properties of Jets and Inputs to Jet Reconstruction and Calibration with the ATLAS Detector Using Proton-Proton Collisions at* $\sqrt{s} = 7$ *TeV*, ATLAS-CONF-2010-053, CERN, Geneva, Jul, 2010.

[104] The ATLAS Collaboration, G. Aad et al., *Jet energy scale and its systematic uncertainty in proton-proton collisions at* $\sqrt{s} = 7$ *TeV in ATLAS 2010 data*, arXiv:1112.6426 [hep-ex].

[105] The ATLAS Collaboration, G. Aad et al., *Validating the measurement of jet energies with the ATLAS detector using Z+jet events from proton-proton collisions at* $\sqrt{s}$ *= 7 TeV*, ATLAS-CONF-2011-159, CERN, Geneva, Dec, 2011.

[106] Particle Data Group, K. Nakamura et al., *Review of Particle Physics*, J. Phys. G37 (2010) p. 075021.

[107] The ATLAS Collaboration, G. Aad et al., *Performance of the Reconstruction and Identification of Hadronic Tau Decays in ATLAS with 2011 Data*, ATLAS-CONF-2012-142, CERN, Geneva, Oct, 2012.

[108] The ATLAS Collaboration, G. Aad et al., *Performance of the Reconstruction and Identification of Hadronic Tau Decays with ATLAS*, ATLAS-CONF-2011-152, CERN, Geneva, Nov, 2011.

[109] The ATLAS Collaboration, G. Aad et al., *Performance of Missing Transverse Momentum Reconstruction in Proton-Proton Collisions at 7 TeV with ATLAS*, Eur. Phys. J. C72 (2012) p. 1844, arXiv:1108.5602 [hep-ex].

[110] The ATLAS Collaboration, G. Aad et al., *Commissioning of the ATLAS high-performance b-tagging algorithms in the 7 TeV collision data*, ATLAS-CONF-2011-102, CERN, Geneva, Jul, 2011.

[111] G. Piacquadio and C. Weiser, *A new inclusive secondary vertex algorithm for b-jet tagging in ATLAS*, J. Phys. Conf. Ser. 119 (2008) p. 032032.

[112] The ATLAS Collaboration, G. Aad et al., *Measurement of the b-tag Efficiency in a Sample of Jets Containing Muons with 5 fb^{-1} of Data from the ATLAS Detector*, ATLAS-CONF-2012-043, CERN, Geneva, Mar, 2012.

[113] The ATLAS Collaboration, G. Aad et al., *Measurement of the Mistag Rate with 5 fb^{-1} of Data Collected by the ATLAS Detector*, ATLAS-CONF-2012-040, CERN, Geneva, Mar, 2012.

[114] The ATLAS Collaboration, G. Aad et al., *Search for the neutral Higgs bosons of the Minimal Supersymmetric Standard Model in p–p collisions at $\sqrt{s}$ =7 TeV with the ATLAS detector*, Submitted to JHEP (2012) arXiv:1211.6956 [hep-ex].

[115] The ATLAS Collaboration, G. Aad et al., *Data-Quality Requirements and Event Cleaning for Jets and Missing Transverse Energy Reconstruction with the ATLAS Detector in Proton-Proton Collisions at a Center-of-Mass Energy of $\sqrt{s} = 7$ TeV*, ATLAS-CONF-2010-038, CERN, Geneva, Jul, 2010.

[116] The ATLAS Collaboration, G. Aad et al., *Measurement of the $W \to \ell\nu$ production cross-section and observation of $Z \to \ell\ell$ production in proton-proton collisions at $\sqrt{s} = 7$ TeV with the ATLAS detector*, ATLAS-CONF-2010-051, CERN, Geneva, Jul, 2010.

[117] R. Gavin, Y. Li, F. Petriello, and S. Quackenbush, *FEWZ 2.0: A code for hadronic Z production at next-to-next-to-leading order*, Comput. Phys. Commun. 182 (2011) pp. 2388–2403, arXiv:1011.3540 [hep-ph].

[118] The ATLAS Collaboration, G. Aad et al., *Measurement of the $Z \to \tau\tau$ cross section with the ATLAS detector*, Phys. Rev. D84 (2011) p. 112006, arXiv:1108.2016 [hep-ex].

[119] M. Cacciari et al., *Top-pair production at hadron colliders with next-to-next-to-leading logarithmic soft-gluon resummation*, Phys. Lett. B710 (2012) pp. 612–622, arXiv:1111.5869 [hep-ph].

[120] M. Aliev et al., *HATHOR: HAdronic Top and Heavy quarks crOss section calculatoR*, Comput. Phys. Commun. 182 (2011) pp. 1034–1046, arXiv:1007.1327 [hep-ph].

[121] N. Kidonakis, *NNLL resummation for s-channel single top quark production*, Phys. Rev. D81 (2010) p. 054028, arXiv:1001.5034 [hep-ph].

[122] N. Kidonakis, *Next-to-next-to-leading-order collinear and soft gluon corrections for t-channel single top quark production*, Phys. Rev. D83 (2011) p. 091503, arXiv:1103.2792 [hep-ph].

[123] N. Kidonakis, *Two-loop soft anomalous dimensions for single top quark associated production with a W- or H-*, Phys. Rev. D82 (2010) p. 054018, arXiv:1005.4451 [hep-ph].

[124] J. M. Campbell et al., *Vector boson pair production at the LHC*, JHEP 1107 (2011) p. 018, arXiv:1105.0020 [hep-ph].

[125] A. Elagin et al., *A New Mass Reconstruction Technique for Resonances Decaying to di-tau*, Nucl. Instrum. Meth. A654 (2011) pp. 481–489, arXiv:1012.4686 [hep-ex].

[126] The DØ Collaboration, V. M. Abazov et al., *Measurement of the $p\bar{p} \to t\bar{t}$ production cross section at $\sqrt{s}$ = 1.96 TeV in the fully hadronic decay channel.*, Phys. Rev. D76 (2007) p. 072007, hep-ex/0612040.

[127] The ATLAS Collaboration, G. Aad et al., *Measurement of the inclusive $W^{\pm}$ and Z/gamma cross sections in the electron and muon decay channels in pp collisions at $\sqrt{s} = 7$ TeV with the ATLAS detector*, Phys. Rev. D85 (2012) p. 072004, arXiv:1109.5141 [hep-ex].

[128] The ATLAS Collaboration, G. Aad et al., *Search for neutral MSSM Higgs bosons decaying to tau+ tau- pairs in proton-proton collisions at $\sqrt{s} = 7$ TeV with the ATLAS detector*, Phys. Lett. B705 (2011) pp. 174–192, arXiv:1107.5003 [hep-ex].

[129] R. Hamberg et al., *A Complete calculation of the order $\alpha - s^2$ correction to the Drell-Yan K factor*, Nucl. Phys. B359 (1991) pp. 343–405.

[130] C. Anastasiou et al., *High precision QCD at hadron colliders: Electroweak gauge boson rapidity distributions at NNLO*, Phys. Rev. D69 (2004) p. 094008, hep-ph/0312266.

[131] Private Communication, J.M. Butterworth et al., *Single Boson and Diboson Production Cross Sections in p–p Collisions at $\sqrt{s}$ =7 TeV*, ATL-COM-PHYS-2010-695, CERN, Geneva, Aug, 2010.

[132] Private Communication, F. Siegert et al.

[133] The ATLAS Collaboration, G. Aad et al., *Luminosity Determination in pp Collisions at $\sqrt{s}$ =7 TeV Using the ATLAS Detector at the LHC*, Eur. Phys. J. C71 (2011) p. 1630, arXiv:1101.2185 [hep-ex].

[134] The ATLAS Collaboration, G. Aad et al., *Reconstruction and Calibration of Missing Transverse Energy and Performance in Z and W events in ATLAS Proton-Proton Collisions at $\sqrt{s}$=7 TeV*, ATLAS-CONF-2011-080, CERN, Geneva, Jun, 2011.

[135] A. L. Read,, *Presentation of search results: the CL_s technique*, J. Phys. G28 (2002) pp. 2693–2704.

[136] G. Cowan et al., *Asymptotic formulae for likelihood-based tests of new physics*, Eur. Phys. J. C71 (2011) p. 1554, arXiv:1007.1727 [hep-ex].

[137] E. Gross et al., *Estimating the significance of a signal in a multi-dimensional search*, Astropart. Phys. 35 (2011) pp. 230–234, arXiv:1105.4355 [astro-ph.IM].

[138] A. Arbey and others, *The Higgs sector of the phenomenological MSSM in the light of the Higgs boson discovery*, JHEP 1209 (2012) p. 107, arXiv:1207.1348 [hep-ph].

[139] The CDF, DØ Collaborations and the Tevatron New Physics Higgs Working Group, D. Benjamin et al., *Combined CDF and DØ upper limits on MSSM Higgs boson production in $\tau - \tau$ final states with up to 2.2 fb^{-1}*, arXiv:1003.3363 [hep-ex].

[140] The CMS Collaboration, S. Chatrchyan et al., *Search for MSSM Neutral Higgs Bosons Decaying to Tau Pairs in pp Collisions*, CMS-PAS-HIG-12-050, CERN, Geneva, Nov, 2012.

Danksagung / Acknowledgements

Zuallererst möchte ich meiner Familie danken. Meinen Eltern dafür, dass sie mich stets und mit vollen Einsatz unterstützt und immer an mich geglaubt haben. Ohne Eure Hilfe hätte ich mein Studium nie verwirklichen oder diese Arbeit fertigstellen können. Auch meinem Bruder Christian danke ich dafür, dass er mich immer unterstützt hat. Vor allem aber auch für die gelegentliche Ablenkung, sei es mit Fußball oder anderen Freizeitaktivitäten, die während eines Studiums oder der Anfertigung dieser Arbeit hin und wieder einfach notwendig ist.

Vielen Dank, Vesela, für deine Unterstützung, deine Geduld und dein Verständis, auch und gerade in den anstrengenden Monaten dieser Promotion.

A big and warm “Thank you” goes to my family in Australia, Ingrid, Sue, Katie, Nicole and Andrew. Thanks for the great time in Melbourne.

Prof. Karl Jakobs danke ich für die Möglichkeit, diese Arbeit in seiner Arbeitsgruppe und unter seiner Leitung anfertigen und ein Teil der ATLAS Kollaboration werden zu können.

Weiterhin danke ich Prof. Karl Jakobs, Prof. Jochen Dingfelder und Prof. Markus Schumacher für die vielen nützlichen und lehrreichen Diskussionen rund um die Inhalte dieser Arbeit.
Der gleiche Dank geht ebenso an meine vielen inoffiziellen Mitbetreuer, Inga Ludwig, Michael Dührssen, Michael Heldmann, Stan Lai, Henrik Nilsen und Christian Weiser, ohne die diese Arbeit sicherlich nicht zustande gekommen wäre. Danke auch an Christoph Anders und Julian Glatzer. Mit Euch hat die Arbeit einfach Spaß gemacht.

Ein großer Dank geht natürlich auch an meine vielen, fleißigen “Test-Leser”, allen voran Prof. Karl Jakobs und Kristin Lohwasser. Danke auch an Susanne Kühn, Georges Aad, Thomas Barber, Ulrich Parzefall, Iacopo Vivarelli und Christian Weiser.

Christina Skorek danke ich für ihre Hilfsbereitschaft und das Erledigen von unzähligen kleinen Gefallen, die sie nicht nur für mich, sondern für die ganze Arbeitsgruppe unentbehrlich macht.

Meinen Bürokollegen Johanna Nagel, Helge Hass und Nils Ruthmann danke ich für ihre moralische Unterstützung und die angenehme Büroatmosphäre.

Der ganzen Arbeitsgruppe danke ich für ihre Freundschaft und Unterstützung während der letzten Jahre, Besonders erwähnen möchte ich an dieser Stelle Evelyn Schmidt, Christoph Anders, Markus Dambacher, Julian Glatzer, Michel Janus und Matthias Werner.

Many thanks to my colleagues at CERN, John Stakely Keller and Nikolaos Rompotis, for their help with the search for the neutral MSSM Higgs bosons.

An alle oben Erwähnten und jene, die ich versehentlich vergessen habe, ein herzliches

Danke & Thank You!